LBL-37886
UC-401

Center for Advanced Materials

CAM

Surface Structures from Low Energy Electron Diffraction: Atoms, Small Molecules and an Ordered Ice Film on Metal Surfaces

N.F. Materer
(Ph.D. Thesis)

September 1995

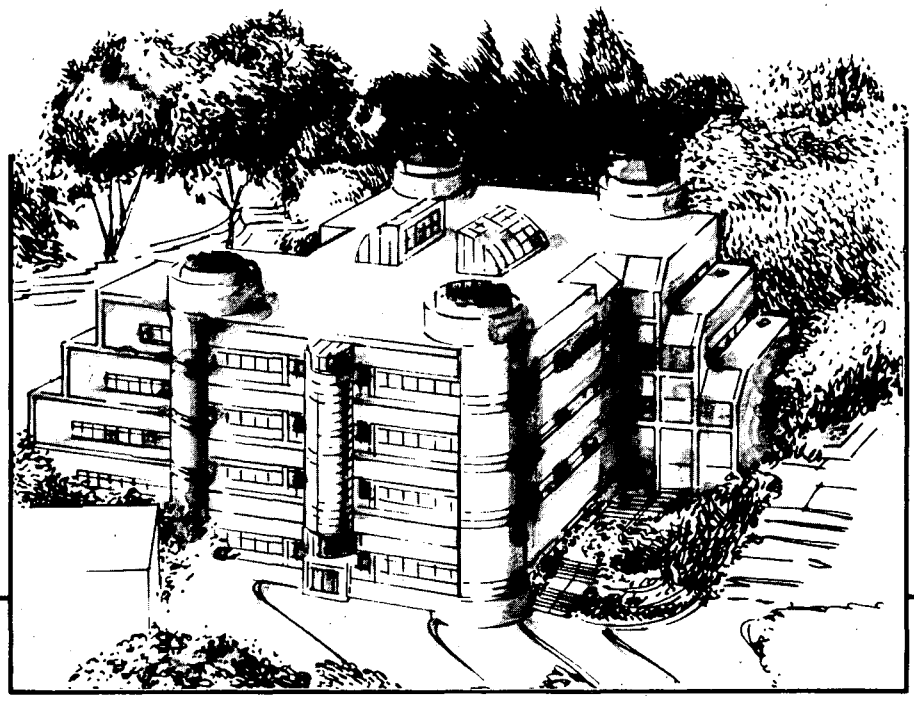

REFERENCE COPY
Does Not
Circulate
Bldg. 50 Library.
LBL-37886
Copy 1

Materials and Chemical Sciences Division
Lawrence Berkeley Laboratory • University of California
ONE CYCLOTRON ROAD, BERKELEY, CA 94720 • (415) 486-4755

Prepared for the U.S. Department of Energy under Contract DE-AC03-76SF00098

DISCLAIMER

This document was prepared as an account of work sponsored by the United States Government. While this document is believed to contain correct information, neither the United States Government nor any agency thereof, nor the Regents of the University of California, nor any of their employees, makes any warranty, express or implied, or assumes any legal responsibility for the accuracy, completeness, or usefulness of any information, apparatus, product, or process disclosed, or represents that its use would not infringe privately owned rights. Reference herein to any specific commercial product, process, or service by its trade name, trademark, manufacturer, or otherwise, does not necessarily constitute or imply its endorsement, recommendation, or favoring by the United States Government or any agency thereof, or the Regents of the University of California. The views and opinions of authors expressed herein do not necessarily state or reflect those of the United States Government or any agency thereof or the Regents of the University of California.

LBL-37886

Surface Structures from Low Energy Electron Diffraction: Atoms, Small Molecules and an Ordered Ice Film on Metal Surfaces

Nicholas F. Materer

(Ph.D. Thesis)

Department of Chemistry
University of California

and

Materials Sciences Division
Ernest Orlando Lawrence Berkeley National Laboratory
University of California
Berkeley, California 94720

This work was supported by the Director, Office of Energy Research, Office of Basic Energy Sciences, Materials Sciences Division, of the US Department of Energy under Contract No. DE-AC03-76SF00098.

Surface Structures from Low Energy Electron Diffraction: Atoms, Small Molecules and an Ordered Ice Film on Metal Surfaces

by

Nicholas F. Materer

B.S. (University of Missouri at Columbia) 1990

A dissertation submitted in partial satisfaction of the
requirements for the degree of
Doctor of Philosophy

in

Chemistry

in the

GRADUATE DIVISION
of the
UNIVERSITY of CALIFORNIA at BERKELEY

Committee in charge:

Professor Gabor A. Somorjai, Chair
Professor Ignacio Tinoco
Professor Doros N. Theodorou

1995

Surface Structures from Low Energy Electron Diffraction: Atoms, Small Molecules and an Ordered Ice Film on Metal Surfaces

Copyright © 1995

by

Nicholas F. Materer

The U.S. Department of Energy has the right to use this document
for any purpose whatsoever including the right to reproduce
all or any part thereof

Surface Structures from Low Energy Electron Diffraction: Atoms and Small Molecules and an Ordered Ice Film on Metal Surfaces

by

Nicholas F. Materer

Abstract

We investigated the surface bonding of various adsorbates (O, S, C_2H_3 and NO) along with the resulting relaxation of the Pt(111) surface using low energy electron diffraction (LEED). LEED experiments have been performed on these ordered overlayers along with theoretical structural analysis using automated tensor LEED (ATLEED). The resulting surface structures of these ordered overlayers exhibit similar adsorbate-induced relaxations. In all cases the adsorbate occupies the fcc hollow site and induces an approximately 0.1 Å buckling of the metal surface. The three metal atoms directly bonded to the adsorbate are "pulled" out of the surface and the metal atom that is not bound to the adsorbate is "pushed" inward. In order to understand the reliability of such details, we have carried out a comprehensive study of various non-structural parameters used in a LEED computation.

We also studied the adsorption of water on the Pt(111) surface. We ordered an ultra thin ice film on this surface. The film's surface is found to be the (0001) face of hexagonal ice. This surface is apparently terminated by a full-bilayer, in which the uppermost water molecules have large vibrational amplitudes even at temperatures as low as 90 K.

We examined two other metal surfaces besides Pt(111): Ni(111) and Fe(111). On Ni(111), we have studied the surface under a high coverage of NO. On both Ni(111) and Pt(111) NO molecules occupy the hollow sites and the N-O bond distances are practically identical. The challenging sample preparation of an Fe(111) surface has been investigated and a successful procedure has been obtained. The small interlayer spacing found on Fe(111) required special treatment in the LEED calculations. A new ATLEED program has been developed to handle this surface.

Contents

List of Figures vii

List of Tables x

1 Introduction 1
- 1.1 The Need for Surface Structures . . . 2
- 1.2 Historical Overview of LEED . . . 4
- 1.3 Relationship to Other Surface Structure Techniques . . . 6
- 1.4 Thesis Summary . . . 6

2 LEED: Experiment and Theory 9
- 2.1 Introduction to LEED . . . 10
  - 2.1.1 Basic Principles . . . 10
  - 2.1.2 Nomenclature . . . 12
  - 2.1.3 Ideal Diffraction Conditions . . . 14
  - 2.1.4 Real Surfaces and Instrumentation . . . 16
  - 2.1.5 I-V Measurements and Structural Determinations . . . 17
- 2.2 Instrumentation and Experimental Preparations . . . 20
  - 2.2.1 UHV Requirement and Equipment . . . 20
  - 2.2.2 Sample Preparation . . . 22
- 2.3 LEED Image Recording . . . 25
  - 2.3.1 Video LEED . . . 25
  - 2.3.2 Digital LEED . . . 29
- 2.4 The LEED I-V Experiment . . . 32
  - 2.4.1 Sample Alignment . . . 33
  - 2.4.2 Image Collection . . . 33
  - 2.4.3 I-V Curve Generation . . . 34
- 2.5 LEED Theory and Computational Methods . . . 35
  - 2.5.1 Muffin-Tin Potential . . . 36
  - 2.5.2 Atomic Phase Shifts . . . 37
  - 2.5.3 Dynamical LEED Calculations . . . 38
  - 2.5.4 TLEED Approximation . . . 39
- 2.6 Search Techniques . . . 41

2.6.1 R-Factors 41
2.6.2 Conventional LEED Analysis 43
2.6.3 ATLEED Implementations 44
2.6.4 Other Methods and the Global Minimum 46

3 Clean and Oxygen Covered Pt(111) 47
3.1 Background 48
3.2 Experiment 48
3.3 Clean Pt(111) 50
3.3.1 LEED Computations 50
3.3.2 Results 51
3.3.3 Conclusions 58
3.4 Pt(111)-$p(2 \times 2)$-O: Structural Analysis 59
3.4.1 LEED Computations 60
3.4.2 Results 60
3.4.3 Conclusions 65
3.5 Pt(111)-$p(2 \times 2)$-O: Non-structural Parameters 67
3.5.1 Phase Shifts and the Muffin-Tin Potential 67
3.5.2 Additional Factors 69
3.5.3 The Final Structure 70
3.5.4 Conclusions 70
3.6 Summary 72

4 Sulfur on Pt(111): A Combined LEED and STM Study. 74
4.1 Background 75
4.2 Experiments 76
4.2.1 Pt(111)-$p(2 \times 2)$-S 77
4.2.2 Pt(111)-$(\sqrt{3} \times \sqrt{3})$R30°-S 78
4.2.3 Pt(111)-Oblique-3S 80
4.3 LEED Theory 81
4.4 LEED Analyses 82
4.4.1 Coarse Searches 83
4.4.2 Effects of Buckling on the $p(2 \times 2)$ Model 84
4.4.3 Lateral Displacements and Symmetry-Breaking Models 87
4.4.4 Summary of Initial Results 88
4.5 LEED Results 89
4.5.1 Final $p(2 \times 2)$ Structure 89
4.5.2 Final $(\sqrt{3} \times \sqrt{3})$R30° Structure 91
4.6 Conclusions 91

5 Ethylidyne on Pt(111): Structure and Coverage 96
5.1 Background 97
5.2 Experiment 97
5.3 Theory 99
5.4 Structural Analysis 100

5.4.1 Symmetry-Preserving Structures 100
5.4.2 Addition of Hydrogen 107
5.4.3 Symmetry-Breaking Features 111
5.5 Conclusions 113

6 Surface Structures of NO on Pt(111) and Ni(111) 115
6.1 Introduction 116
6.2 Experiments 117
6.2.1 NO Adsorption on Pt(111) 117
6.2.2 NO Adsorption on Ni(111) 118
6.3 Theory 120
6.4 Results 121
6.4.1 Clean Surfaces: Pt(111) and Ni(111) 121
6.4.2 Pt(111)-$p(2 \times 2)$-NO 123
6.4.3 Ni(111)-$c(4 \times 2)$-2NO 127
6.4.4 Unexpected Sensitivity of the (1/4,1/4) Beam 132
6.5 Discussion 134
6.6 Conclusions 136

7 Molecular Surface Structure of Ice(0001) 138
7.1 Motivation and Background 139
7.2 The LEED Experiment 140
7.3 Theory 142
7.3.1 LEED Theory 142
7.3.2 Total Energy Theory 142
7.3.3 MD Theory 143
7.4 Initial LEED Results 145
7.4.1 Surface Models 145
7.4.2 Single Termination Models 146
7.4.3 Coexistence of Two Terminations 148
7.4.4 Possible Models 150
7.5 Total Energy Calculations 150
7.5.1 Lattices with Hexagonal Symmetry 151
7.5.2 Distorted Hexagonal Lattices 153
7.5.3 Conclusions from Total Energy Computations 156
7.6 Molecular Dynamics Simulations 157
7.7 Refinements to the LEED Structure 160
7.7.1 Refinement of the Lattice Parameters 163
7.7.2 Enhanced Vibrations 164
7.7.3 Addition of Hydrogen 164
7.7.4 The Final Structure 166
7.8 Conclusion 168

8 Iron Surface: A First Step **169**
8.1 Background 169
8.2 Cleaning 170
8.2.1 UHV Cleaning 170
8.2.2 High-Pressure Cell 172
8.2.3 Hydrogen Furnace 172
8.2.4 UHV Sample Mounting 174
8.3 LEED Computations 175
8.3.1 Layer Doubling 175
8.3.2 Generation of the Tensor 176
8.4 General Conclusions 176

9 General Conclusions **177**
9.1 Reliability of a LEED Structure 177
9.2 General Features of Pt(111)-$p(2 \times 2)$ Overlayers 179
9.3 Tilting of Molecules 181
9.4 Coverage-Dependent Relaxations and Clustering 182
9.5 NO on Ni(111) and Pt(111) 183
9.6 The Ordered Ice Film 184
9.7 Iron Surfaces 184
9.8 Future Directions 185

Bibliography **186**

List of Figures

2.1 A simple representation of the LEED process 11
2.2 Scattering of a plane-wave off a one-dimensional lattice. 12
2.3 Real space lattice vectors 13
2.4 A (1×1) surface and LEED pattern. 15
2.5 A $p(2 \times 2)$ surface and LEED pattern. 16
2.6 Flow-chart for a LEED structural determination 19
2.7 AES spectra of the Pt(111) surface. 24
2.8 VLEED image of the Pt(111)-(1x1) LEED pattern at 120 eV. 26
2.9 VLEED image of the Pt(111)-(1x1) LEED pattern at 270 eV. 26
2.10 Conventional LEED optics 27
2.11 DLEED image of the Pt(111)-(1x1) LEED pattern at 80 eV. 29
2.12 DLEED image of the Pt(111)-(1x1) LEED pattern at 120 eV. 30
2.13 The digital LEED detector 31
2.14 Wedge and strip anode 31
2.15 Flow-chart for I-V curve generation 34
2.16 Muffin-tin potential model. 36
2.17 Contour plot of the R_p-factor hypersurface for clean Pt(111)-(1×1). 43

3.1 The Pt(111)-$p(2 \times 2)$-O LEED pattern at 84 eV. 49
3.2 I-V curves for the best-fit clean Pt(111)-(1×1) surface. 52
3.3 Side view of the best-fit clean Pt(111)-(1×1) surface. 52
3.4 Phase shifts for Pt computed using different potentials. 53
3.5 Theoretical I-V curves for the ideally terminated Pt(111)-(1×1) surface . . 56
3.6 Top view of the Pt(111)-$p(2 \times 2)$-O structure. 62
3.7 Side view of the Pt(111)-$p(2 \times 2)$-O structure. 62
3.8 Improvements in the Pt(111)-$p(2 \times 2)$-O I-V curves for the fcc-hollow site model with increasing degrees of freedom. 63
3.9 R_p-factor vs. coordinate plots for Pt(111)-$p(2 \times 2)$-O. 66
3.10 I-V curves of the final best-fit Pt(111)-$p(2 \times 2)$-O structure. 72

4.1 The LEED pattern of the Pt(111)-$p(2 \times 2)$-S overlayer 77
4.2 The STM image of the Pt(111)-$p(2 \times 2)$-S overlayer 78
4.3 The LEED pattern of the Pt(111)-$(\sqrt{3} \times \sqrt{3})$R30°-S overlayer 79

4.4 The STM image of the Pt(111)-($\sqrt{3} \times \sqrt{3}$)R30°-S overlayer 79
4.5 The LEED pattern of the Pt(111)-Oblique-3S overlayer. 80
4.6 The STM image of the Pt(111)-Oblique-3S overlayer 81
4.7 Top view of the Pt(111)-$p(2 \times 2)$-S structure. 84
4.8 Side view of the Pt(111)-$p(2 \times 2)$-S structure. 85
4.9 Top view of the Pt(111)-($\sqrt{3} \times \sqrt{3}$)R30°-S structure. 85
4.10 Side view of the Pt(111)-($\sqrt{3} \times \sqrt{3}$)R30°-S structure. 86
4.11 Improvements in the Pt(111)-$p(2 \times 2)$-S I-V curves for the fcc-hollow site model with increasing degrees of freedom. 86
4.12 I-V curves of the best-fit Pt(111)-$p(2 \times 2)$-S structure. 91
4.13 I-V curves of the best-fit Pt(111)-($\sqrt{3} \times \sqrt{3}$)R30°-S structure. 93

5.1 The Pt(111)-(2×2)-C_2H_3 LEED pattern at 120 eV. 99
5.2 Possible unit cells compatible with the (2×2)-C_2H_3 LEED pattern on the Pt(111) surface 100
5.3 Pt(111)-(2×2)-C_2H_3 I-V curves of the (1,0), (1/2,0) and (0,1/2) beams obtained for various models. 102
5.4 Pt(111)-(2×2)-C_2H_3 I-V curves showing the effect of a tilted carbon-carbon bond in the $p(2 \times 1)$ and $p(2 \times 2)$ fcc hollow-site models. 105
5.5 Side view of the best-fit, symmetry-preserving, Pt(111)-$p(2 \times 2)$-C_2H_3 fcc hollow-site model 106
5.6 Top view of the best-fit, symmetry-preserving, Pt(111)-$p(2 \times 2)$-C_2H_3 fcc hollow-site model. 107
5.7 Pt(111)-$p(2 \times 2)$-C_2H_3 I-V curves of the (1,0) and (1/2,0) beams for different degrees of relaxation 108
5.8 Orientation of the carbon-hydrogen bond in each Pt(111)-$p(2 \times 2)$-C_2H_3 model used as a reference structure to analyze hydrogen presence and position. 109
5.9 Pt(111)-$p(2 \times 2)$-C_2H_3 fractional (1/2,0) and (0,1/2) beam I-V curves with and without hydrogen included in the calculations. 110

6.1 The LEED pattern of the Pt(111)-$p(2 \times 2)$-NO overlayer at 120 eV 118
6.2 Initial LEED pattern for NO on Ni(111) at 83 eV. 119
6.3 The LEED pattern of the Ni(111)-$c(4 \times 2)$-2NO overlayer at 82 eV. 119
6.4 The LEED pattern for NO on Ni(111) after heating to 420 K. 120
6.5 I-V curves for best-fit the clean Ni(111)-(1×1) surface 122
6.6 Side view of the best-fit clean Ni(111)-(1×1) surface 122
6.7 Top view of the Pt(111)-$p(2 \times 2)$-NO surface structure. 124
6.8 Side view of the Pt(111)-$p(2 \times 2)$-NO structure 124
6.9 I-V curves for the Pt(111)-$p(2 \times 2)$-NO surface 125
6.10 Suggested models for the Ni(111)-$c(4 \times 2)$-2NO structure 127
6.11 Top view of the Ni(111)-$c(4 \times 2)$-2NO surface structure. 128
6.12 Side view of the Ni(111)-$c(4 \times 2)$-2NO structure. 130
6.13 I-V curves for the Ni(111)-$c(4 \times 2)$-2NO surface 131

6.14 The variations in the Ni(111)-$c(4 \times 2)$-2NO overlayer's (1/4,1/4) beam R_p-factor when the two NO molecules are displaced symmetrically and antisymmetrically. 133

7.1 The LEED pattern of the Ih(0001) film 141
7.2 Perspective grazing view of the ice Ih (0001) surface. 145
7.3 R_p-factor for mixed Ih(0001) terminations. 149
7.4 Top view of the $cm11$ ice model. 154
7.5 Resulting density profiles of the Ih(0001) surface from MD. 159
7.6 The resulting MD distribution of $\cos\theta$ for the first two layers of Ih(0001). . 161
7.7 The resulting MD distribution of ϕ for the first two layers of Ih(0001). . . . 162
7.8 R_p-factor variation of Ih(0001) with the 2D and 3D lattice constants 163
7.9 The R_p-factor variation of the topmost water layer in Ih(0001) vs. the inverse rms amplitude. 165
7.10 The best-fit intensity vs. energy (I-V) curves for the full-bilayer model of the Ih(0001) surface. 166

8.1 AES spectrum of a sulfur covered iron sample. 171
8.2 AES spectrum of an oxygen covered Fe sample. 171
8.3 Time dependence of the surface segregation of sulfur monitored by AES. . . 173
8.4 Design of the hydrogen furnace 173

List of Tables

3.1 The best-fit R_p- and R_2-factor values for the clean Pt(111)-(1 × 1) surface . 52
3.2 R-factor values for clean Pt(111)-(1 × 1) surface generated using different muffin-tin potentials. 56
3.3 R_2- and R_p-factor values for theoretical Pt(111)-(1 × 1) I-V curves generated from I-V curves computed with different muffin-tin potentials. 57
3.4 The resulting R_p-factor values for various Pt(111)-p(2 × 2)-O models. . . . 61
3.5 Error bars for the Pt(111)-p(2 × 2)-O structure computed with either the fractional order, integer order, or both beam sets. 69
3.6 Optimal atomic coordinates for the best-fit Pt(111)-p(2 × 2)-O fcc-hollow site model 71

4.1 R_p-factor values for various high symmetry Pt(111)-p(2 × 2)-S and ($\sqrt{3}$ × $\sqrt{3}$)R30°-S models 83
4.2 Error bars for the best-fit Pt(111)-p(2 × 2)-S model computed with either the fractional order, integer order, or both beam sets. 87
4.3 Optimal atomic coordinates for the Pt(111)-p(2 × 2)-S fcc hollow-site model 90
4.4 Optimal atomic coordinates for the Pt(111)-($\sqrt{3}$ × $\sqrt{3}$)R30°-S fcc-hollow site model 92
4.5 Comparison of various geometrical parameters for the Pt(111)-p(2 × 2)-S and the ($\sqrt{3}$ × $\sqrt{3}$)R30°-S overlayers. 94

5.1 Resulting R_p-factor values for various Pt(111)-C_2H_3 models. 103
5.2 Cartesian coordinates of the symmetry-preserving best-fit Pt(111)-p(2 × 2)-C_2H_3 model. 106
5.3 Cartesian coordinates of the symmetry-breaking best-fit ethylidyne on Pt(111) model. 112

6.1 R_p-factor values for various Pt(111)-p(2 × 2)-NO models 123
6.2 Atomic coordinates of the best-fit geometry of Pt(111)-p(2 × 2)-NO 125
6.3 R_p-factor values for various Ni(111)-c(4 × 2)-2NO models 129
6.4 Atomic coordinates of the best-fit geometry of Ni(111)-c(4 × 2)-2NO 130

7.1 R_p-factor values obtained for Ice(0001) 147
7.2 Total energies computed with the 631G* basic set for various bilayer models 152

7.3 Total energies computed with the 631G** basic set for various distorted ($cm11$) bilayer models. 155
7.4 MD simulation results for the ice Ih(0001) surface. 157
7.5 Oxygen coordinates for the best-fit structure of ice Ih (0001) 167

9.1 Comparison of vertical relaxations for $p(2 \times 2)$ overlayers on Pt(111). 180
9.2 Comparison of lateral relaxations for $p(2 \times 2)$ overlayers on Pt(111) 181

Acknowledgements

I would like to thank my research advisor, Gabor Somorjai, for the opportunity to work in his research group. The large number of people working on a diverse range of projects has given me exposure to many aspects of surface science which would not be available anywhere else. Gabor's willingness to attempt the "impossible" and succeed has been an educational experience. Through him, I have learned that if one does not push the conventional limits, one cannot advance science. I would also like to thank Michel van Hove (staff scientist at LBL) for his effort in leading the surface structure group. Our weekly meetings on this topic have provided a focus that could not be duplicated in the large meetings of Gabor's group. In addition, Michel's careful reading and support of my work has been appreciated during my stay.

Dr. Uli Starke and Dr. Angelo Barbeiri are two post-docs who have contributed much to my success in graduate school. I would like to thank Dr. Uli Starke for the large quantity of experimental knowledge which he imparted to me in my early years of graduate school. Angelo has guided my introduction to the theoretical aspects of science. His thorough explanations of the use of limits and symmetry operations to quickly determine if an equation or a piece of code is correct have been invaluable.

The group has undergone many changes as students and post-docs flowed through; I have enjoyed interacting with the great variety of individuals. Glenn and Dave provided both entertainment and enjoyable conversations during my first few years. Later, Alex and Zaf have been good friends. During the end of my stay, Howard, Chris and Rudy have added a bit of sanity and moral support as I completed my studies.

I thank my parents for their support throughout my education and, last but not least, I must thank my wife, Lonnajean, for her support during my time in Berkeley. Her help in editing my papers and this work has been invaluable to me. I would not have "made it" without her.

Chapter 1

Introduction

In this work, the geometrical positions of atoms and molecules on various metal surfaces have been determined using low energy electron diffraction (LEED). In the past, surface crystallography by LEED has been limited in the complexity of solvable structures due to the time-consuming computational task of solving the quantum mechanical multiple scattering problem required in order to fit the experimental data. We used the newly developed tensor LEED (TLEED) approximation coupled with an automated search[1] to determine complex surface structures on the platinum, nickel and rhenium surfaces. This work represents the first determinations of adsorbate-induced relaxations, or displacements of the metal atoms away from their ideal locations, for the close-packed face of platinum (the Pt(111) surface). We also present the first successful structural analysis of the molecular surface of an ordered ice film grown on Pt(111).

For the number of systems examined in this study, it would not have been computationally possible to determine adsorbate-induced relaxations without the TLEED approximation. The addition of relaxation to the computational analysis, as we will show, significantly improves the agreement between experiment and theory. This was of particular importance for ethylidyne on Pt(111) (Chapter 5) where older structural results were challenged due to alternate models based on other surface science techniques.

In this chapter, we first discuss the importance of structural information in understanding both the physical and chemical properties of metal surfaces. In the next two sections, we provide a short historical overview of LEED and its relationship to other surface science techniques. The final section is a short guide to this work.

1.1 The Need for Surface Structures

Between any two phases of matter, there is an interface. This interface can be a lipid bilayer of a cell, a junction in an electronic device, or a metal surface in a catalytic reactor. To understand basic interactions that occur between different bulk phases, one must understand the surface region. It is only through the interface that two "bulk" phases can communicate. Because of the reduced dimensionality of the interface, it can have unique physical and chemical properties. It is hoped that the understanding of these properties will in turn generate additional technologies. The electronic device industry has already benefited greatly from surface science studies of the electronic properties of the clean silicon surface and layer-by-layer growth.

Experimentally determined surface structures provide a database (for example the SSD database[2]) which can be used to form models of surface bonding. This is analogous to early X-ray diffraction work on organic and inorganic compounds. Examination of such a database can yield empirical models to predict surface structures. The following are three important uses of surface structure determinations: first, they complement current theoretical efforts to understand and predict surface bonding; second, they are invoked in the formation of models in the study of heterogeneous catalysis; third, they provide calibration for other non-structural techniques.

A large amount of information is known regarding the interaction of a gas with a surface. Many basic models have been developed to describe physical and chemical adsorption and desorption[3]. What is not well understood is the nature of the surface chemical bond. To form models which describe a chemical reaction, one must have a detailed understanding of this bond. Theoretical studies have contributed much to our understanding of surface bonding and reactivity[3–5] but, due to the complexity of the problem, have not advanced to the needed level. Total energy calculations are still too computationally expensive to examine adsorbate-induced relaxations or the influence of the adsorbate on the metal surface. The structural database provides calibration for the total energy researchers. By comparing the resulting total energy structures with those in the database, one can begin to evaluate the level of theory required to obtain the desired accuracy. This judgment is of prime importance because accurate calculations can help develop an understanding of the energetics and pathways of surface reactions.

Such experimentally determined structures play an additional role in the ongo-

ing theoretical development. Theoretical studies are driven by the imagination of the researcher; however, nature unfortunately provides surprises that are beyond our imagination. The complex reconstruction (when the surface unit cell is larger than that expected from the ideal bulk termination) of clean Ir, Au and Pt metal surfaces is one such example.[6] More recently, the high temperature reconstruction of the Pt(111) surface[7] has surprised researchers. Nature has also surprised researchers with molecular systems. When the molecular structure of ethylidyne on Pt(111) was first examined by LEED and other surface science techniques in the late 1970s, the initial site determinations were controversial.[6] In this work, more than a decade later, we examine another controversial system: the adsorption site of NO on Pt(111) and Ni(111) (see Chapter 6). There is a clear need for experimentally determined surface structures to add to the ongoing theoretical effort to understand and predict surface bonding.

The second use of structural determinations is in the formation of models for catalytic reactions. Most catalysis uses expensive metals; thus, understanding the catalytic reaction is critical from a technological viewpoint. The growing concern for the environment is another driving force for new catalytic technologies which provide reaction pathways that are more selective and have lower energy barriers. Qualitative research in the area of heterogeneous catalysis began in 1833 when Michael Faraday proposed a qualitative theory for Döbereiner's low temperature reaction of hydrogen and oxygen in the presence of platinum[3]. One goal of modern surface science is to relate catalytic reaction rates, like the one formulated by Michael Faraday, to elementary surface processes. To formulate these processes, one must understand how catalytically important molecules bond to the surface. It has been suggested by G. A. Somorjai[8] that the small relaxations of the metal surface induced by the adsorbate are responsible for bond breaking. Knowledge of surface structures are required in the formulation and the testing of such theories.

Structural results also provide a means for interpreting non-structural experiments performed under conditions in which structural studies are not possible. Most surface science laboratories are equipped to perform qualitative LEED experiments. To interpret vibrational spectra, one needs to compare the experimental spectra to those of known structures. These spectra can come from organometallic compounds or preferably from known surface structures. As another example, surface structures can also be used to calibrate coverage determinations found by other methods. Although these uses of surface structure seem more mundane than those above, they still represent an important function.

They extend the experimental usefulness of static determinations in pristine environments to the messy and difficult to interpret experimental investigations of surface dynamics and reactivity.

1.2 Historical Overview of LEED

LEED is one of the most common techniques used in studies of single crystal surfaces. It is also one of the oldest, dating back to a paper by Davisson and Germer from April 1927[9]. Although LEED dates back to 1927, it was in the 1960s, when modern surface science began to be assisted by commercially available UHV equipment, that LEED started to attract attention from both experimental and theoretical perspectives. Before 1960, LEED provided only one notable scientific discovery. It was found that two faces of silicon and germanium have a different unit cell than that expected from the ideal bulk termination[6]. In the 1960s and 1970s, LEED's progress as a tool for structural analysis was limited. By the late 1970s, some detailed LEED analyses had been performed, but only for simple structures. In the 1980s, through painstaking work, a few high-symmetry structures containing adsorbate-induced relaxations were solved by LEED[2]. More recently, as evident in this work, the situation has changed drastically thanks to major advances in both theory and experiment.

The theoretical development has mainly focused on efficient solutions to the multiple scattering problem. Between the late 1960s and early 1970s much of the theoretical development required to solve this problem was completed[6]. Because of multiple scattering, it is not possible to obtain the structural parameters directly from diffraction data; therefore, LEED structural determinations require a trial-and-error approach. One must guess a model, perform a computation and compare the results to the experiment, then iterate these steps. In the 1970s, R-factors[6] were developed to provide a figure of merit or quantitative measure of the agreement between experiment and theory. Armed with these developments, LEED analyses have solved a large number of unreconstructed clean surfaces. Some atomic adsorption systems have also been solved by LEED. Many of these systems have high symmetry unit cells and only in rare cases were any metal relaxations investigated. Molecular systems are even rarer and must be done with great computational and human effort. Further advances in structural determinations required a solution to the painstaking structural search problem. Additional historical details related to adsorbate-induced

relaxations can be found in Reference 10. With the development of tensor LEED (TLEED) and other similar techniques[1] in the late 1980s and early 1990s, the LEED practitioner has been given a partial solution to this search problem. In 1991, the TLEED method was used to determine the relaxation of metal atoms underneath an ethylidyne molecule on the Ru(111) surface[11]. This structure is the first example of an molecular adsorbate-induced relaxations. Additional problems related to the information content of experimental data and issues surrounding global optimizations are yet to be solved. As the number of fit-parameters increases, these unsolved issues become increasingly important.

In contrast to the theoretical development, the LEED experiment has undergone relatively few changes over the years. Most qualitative LEED studies are still performed using a detection system developed in the 1960s[6]. This system detects the diffracted electrons by accelerating them into a fluorescent screen. For LEED measurements relevant to structural analysis, most experimental changes have involved improvements in both the speed and accuracy of the data collection. Even though the basic elements of the LEED experiment have not changed, the recent advances in structural determination have put increasing demands on the experimentalist. Modern structural analysis requires a large amount of data. The experimentalist must measure a large number of diffraction spots at many different energies, with a sizable signal-to-noise ratio. In the 1970s, experimental data was painstakingly recorded utilizing either a Faraday cup or a spot photometer[6]. Photographic cameras were introduced in the mid-1970s[6]. This method allowed rapid data collection, but required a difficult and time consuming film processing step. In the 1980s and 1990s, advancements in video cameras, computer interfacing and the development of rear-view LEED optics have made possible the rapid collection of high quality data without a painful post-processing step. In addition, the rapid computer controlled data collection now possible allows one to examine overlayers which are sensitive to background gas adsorption. Another experimental improvement is the ability to reduce the electron beam current in order to prevent damage to the sample. The use of multichannel plates and electron position sensing, referred to as digital LEED,[12] has reduced the beam current required to obtain a diffraction pattern into the picoampere range. The LEED study of an ordered ice film in Chapter 7 would not have been possible without this reduction in beam current. Even with these advances, LEED structural studies are still limited by the creativity of the experimentalist. It is this creativity or in some cases perseverance that enables one to finally tame the surface.

1.3 Relationship to Other Surface Structure Techniques

LEED has the advantage that it does not require nearly as much specialized equipment as other techniques. When compared to glancing angle X-ray diffraction, which requires synchrotron radiation and a high-precision goniometer, LEED seems relatively simple. The major drawback in LEED (as discussed above) is the complexity of fitting the experimental data. Other synchrotron-based techniques, photoelectron diffraction and the multitude of fine structure techniques, have the advantage, in most cases, of simpler data analysis. Ion scattering experiments have less equipment constraints than the techniques above, but still more than LEED, and also offer simpler data interpretation. The drive for more direct surface structure determinations has seemed to lead to more complex experimental setups. At some point the complexity of the experiment becomes so great that it does not justify the simpler data analyses. More information regarding different structural techniques can be found in a number of books on the subject.[13,14]

The use of other techniques in surface determinations is important as a check on the LEED results. It is through the comparison of LEED results with other determinations that one can convince scientists outside the field, for example, scientists who do total energy calculations with surfaces, of the validity of ones results. In addition, one should not forget that non-structural techniques give valuable information for structural determination. The structural analyses in this work have been assisted by coverage determinations using thermal desorption spectroscopy and radiotracers. Vibrational spectroscopy of molecular adsorbates gives clues to the molecular orientations. Because LEED structural determinations require a trial-and-error approach, any additional clues to the surface structure from non-structural techniques prove to be valuable. As structures become more and more complex, LEED determinations will increasingly rely on this additional information.

1.4 Thesis Summary

We begin Chapter 2 with a brief description of the principles of LEED, after which we provide details of the experiment. The procedures required to obtain the experimental data are delineated next. For our analyses, we measure LEED intensity vs. voltage curves or I-V curves for various diffraction beams. Formal LEED theory and various approximations are described next. In particular, we will spend some time discussing the

TLEED approximation. We complete this chapter with an outline of a LEED structural determination.

We present our first results in Chapter 3. In this chapter, we describe and compare independent dynamical LEED analyses of the Pt(111)-$p(2 \times 2)$-O system, using three different optimization schemes based on different implementations of TLEED[1]. These independent dynamical LEED analyses illustrate the reliability of different approaches to LEED analysis in the similar structural results obtained with each. In addition, we examine various factors which affect structural analysis. One important factor is various non-structural parameters, particularly those involved in the construction of the phase shifts. This chapter's results for both the clean Pt(111) and the Pt(111)-$p(2 \times 2)$-O surfaces play a critical role in the subsequent structural determinations in the chapters which follow.

Examined in Chapter 4 are the effects of different coverages of sulfur on the relaxation of the Pt(111) surface. Sulfur is an ideal adsorbate for the study of adsorbate-induced reconstruction, because it forms a relatively large number of stable ordered overlayers[15]. This allows one to examine metal-adsorbate and nearest neighbor interactions. The possibility of many different ordered overlayers suggests a delicate balance of forces between the adsorbates and the metal surface, as well as between the adsorbates themselves. LEED provides structural information that can be used to elucidate these interactions. Sulfur adsorption on platinum is also of interest because sulfur acts as a poison in some catalytic reactions. An understanding of the binding site of sulfur as a function of coverage may be helpful in the study of catalytic properties and in studies of the interaction of sulfur with other adsorbates.

In the next two chapters, we move away from atomic systems to molecular systems. In Chapter 5, we examine ethylidyne, the relatively stable decomposition product of ethylene on Pt(111); while in Chapter 6, we address the controversial adsorption site for ordered nitric oxide (NO) overlayers on the Pt(111) and Ni(111) surfaces. The determination of the surface structure of ethylidyne on Pt(111) returns us to "chemistry." Ethylene is probably the most intensively studied hydrocarbon on metal surfaces because both hydrogenation and dehydrogenation of this hydrocarbon serve as model systems for understanding the interactions involved in heterogeneous catalytic reactions of hydrocarbons over metal catalysts. The next molecule, NO, is often an environmentally harmful byproduct of combustion reactions using air as a source of oxygen. The environmentally important oxidation of NO to NO_2 (a harmless gas) over platinum has been studied using vibrational spectroscopy.

However, a SEXAFS study[16] has called the generally assumed site assignments of NO on the Ni(111) surface into question. Because of this, we utilized the sensitivity of LEED to the position of the atomic cores to unambiguously assign the adsorption sites for NO on both Pt(111) and Ni(111).

In Chapter 7, we collected LEED patterns of an ordered ice film grown on Pt(111) using multichannel plates and electron position sensing. There has been relatively few studies of the surface structure of the ice surface. This is surprising because ice plays such a pervasive role in many daily phenomena. For example, the unusual slipperiness of ice is possibly due to surface premelting, i.e. the melting of the surface below the bulk melting point. One question which is addressed in this chapter is to what extent ice surfaces may show either disordering or larger amplitudes of vibrations at temperatures as low as 90 K. The issues of surface disorder and enhanced vibrational amplitudes are especially important for structural determinations of molecular surfaces in which the bonding is much weaker than in metals or semiconductors.

The clean iron surfaces have been studied in great detail by the group of F. Jona and P. M. Marcus[17]. However, very little work has been done with adsorbates on any iron surface. For Fe(111), there have been no structural determinations for any adsorbate system. In Chapter 8, we describe our initial attempts to investigate this surface. We will examine two of the major problems with this surface. First, the spacing between the atomic planes in the (111) direction is too small for our "standard" LEED code. Second, the bcc to fcc phase transition creates technical problems with the conventional cleaning procedures. Solutions to both these problems along with some initial results will be reported.

In the final chapter, Chapter 9, we will step back and examine general features which connect the various surface structures in this work. Although this final chapter will contain a brief account of our results obtained in the previous chapters, we will also present some new information. Now that we have examined four different $p(2 \times 2)$ overlayers on the Pt(111) surface, we can examine similarities in the surface relaxations. One additional structural feature of molecules is a possible tilt. We will summarize our evidence for either an anharmonic wagging vibration or a static tilt for both C_2H_3 and NO. The next two sections summarize the work done with sulfur on Pt(111) and with NO on Ni(111). We present our results for the ordered ice film and our ongoing investigation of the Fe(111) surface. Finally, we end this work with a discussion of future directions.

Chapter 2

LEED: Experiment and Theory

Low energy electron diffraction (LEED) from single crystal surfaces has three important applications in surface science studies. LEED can quickly determine the surface unit cell. For the clean surface, this determination allows the crystal face to be identified. For adsorbate covered surfaces, one can tell if an ordered overlayer has been formed. The second use is the characterization of the degree of surface order through "spot profile" analysis. Valuable information regarding surface imperfections and average sizes of ordered domains can be obtained through this type of analysis. The third application of LEED is the determination of the geometrical positions of atoms in the surface unit cell. This work focuses on this third application. In the most simplified view, the LEED experiment used in this work for structural analysis involves the measurement of integrated diffraction spot intensities as a function of energy. In an iterative fashion, the intensity vs. energy curves (I-V curves) are compared to theoretical diffraction intensities computed from different model structures; in this way, the best-fit surface structure is determined.

In this chapter we examine both experimental and theoretical aspects of LEED as it applies to structural determinations. This chapter is divided into three main parts: first, in Section 2.1, we outline some basic principles of LEED and LEED structural determinations; second, in Sections 2.2 to 2.4, we describe the experimental techniques and equipment; third, in Sections 2.5 to 2.6, we detail the theory and the computational approaches for fitting the experimental data.

2.1 Introduction to LEED

LEED involves scattering electrons elastically off a surface to generate a diffraction pattern. At energies between 20 and 300 eV, the electron has a wavelength between 2.7 and 0.7 Å, as given by the de Broglie relationship, $\lambda = h/\sqrt{2mE}$. Because this wavelength is of the same order as a typical lattice constant, a monoenergetic beam of electrons will diffract from an ordered surface. Assuming the electron can be approximated by a plane-wave in the scattering process and the surface as an infinite two dimensional (2D) lattice, the situation is similar to that found in X-ray diffraction. There is one very important exception: electrons interact strongly with the surface. In a typical LEED experiment, more than 90% of the incidence electrons scatter inelastically and do not contribute to the diffraction pattern. This strong interaction has two effects. First, it limits the electron's mean free path to a few atomic layers, thus, giving LEED surface sensitivity. The electron's mean free path vs. energy has been measured for many materials and the resulting curves tend to follow a "universal curve"[13] with a minimum of only a few Å between 40 and 100 eV. Second, this strong interaction results in multiple scattering of the electron. It is this factor that has prevented LEED structural determinations from becoming as routine as X-ray diffraction studies of crystal structures.

In this section, we attempt to give a short introduction to LEED. This section ends with a brief overview of the I-V curve measurement and the subsequent analysis of this information using "automated" tensor LEED (ATLEED) (Section 2.1.5). This brief introduction provides the knowledge required for a basic understanding of the structural determinations found in the subsequent chapters. In addition, we provide the knowledge needed to understand both the experimental and theoretical descriptions that follow. References 13 and 14 provide a more complete introduction to LEED, while Reference 6 is a recent book devoted to LEED.

2.1.1 Basic Principles

In analogy to the relationship of the X-ray diffraction pattern to the three dimensional (3D) unit cell of a crystal, the LEED pattern formed is related to the 2D surface unit cell. The LEED pattern is a projection in reciprocal space of the real space 2D unit cell. The quantum mechanical wave-like properties of electrons combined with the translational symmetry of the substrate restricts momentum transfer to values that are integer multiples

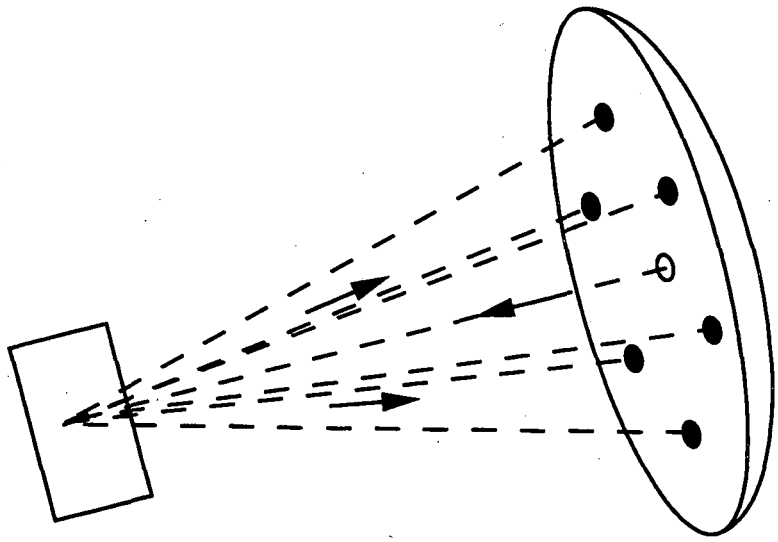

Figure 2.1: A simple representation of the LEED process to illustrate the scattering process. Electrons first pass through the hole in the center of the detector. After elastically scattering off the sample, their impact position is recorded by the detector. The arrows represent possible paths taken by the scattered electron.

of a reciprocal lattice vector[18]. Figure 2.1 is a simplified illustration of the LEED scattering process. The electrons first pass through a hole in the detector and strike the sample with a certain $\vec{k}_{\parallel}$ and $\vec{k}_{\perp}$. The elastically backscattered electrons then travel back to the detector (after having their parallel momentum changed by integer multiples of a reciprocal lattice vector) and their impact position and intensity is recorded by the detector.

To understand this process, we will first consider scattering from a one dimensional (1D) infinite line of scatterers, as shown in Figure 2.2. In this figure, a plane-wave, represented by lines, scattering off a 1D lattice with a periodicity of d. The circles in the figure represent the scattering atoms. Each atom scatters the incident wavefield into spherical-waves, which, far from the source, merge into the outgoing plane-waves. To have an outgoing plane-wave, one must have constructive interference between the outgoing waves; thus, the path difference between waves generated by each scatterer must be an integer multiple of the electron's wavelength. If the incident wave makes an angle of ϕ_o with the surface normal and the outgoing wave an angle of ϕ_f, the difference in path length between scattering events at two adjacent lattice points must equal $n\lambda$. From Figure 2.2, one can derive the

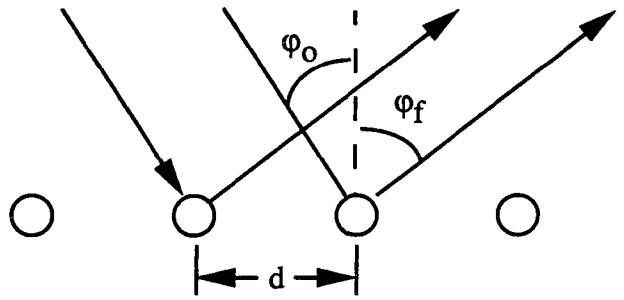

Figure 2.2: Scattering of a plane-wave off a one-dimensional lattice. ϕ_o and ϕ_f are the incidence and scattered angles, respectively. The 1D lattice has a periodicity of d.

following expression:

$$d \cdot (\sin\phi_f - \sin\phi_o) = n\lambda \tag{2.1}$$

In the 2D case, the process is the same with one exception: scattering takes place in a plane and not a line. The condition for constructive interference now depends on θ and ϕ of both the incident and the outgoing waves. Because of the additional complexity, a vector representation has been developed to simplify the diffraction conditions.

2.1.2 Nomenclature

Before we delve into the diffraction conditions, let us first examine the nomenclature for a 2D lattice. The real space lattice vectors, $\vec{a}_1$ and $\vec{a}_2$, define the sides of the smallest parallelogram from which the surface can be constructed using only translation operations. The resulting parallelogram describes the primitive surface unit cell and contains the geometrical positions of the atoms. These real space lattice vectors define the Bravais lattice. Figure 2.3a illustrates these lattice vectors ($\vec{a}_{s1}$ and $\vec{a}_{s2}$) for a clean unreconstructed surface. A clean surface is labeled S(hkl)-$(m \times n)$[6]. In this notation, the (hkl) are the Miller indices of the surface; S is the chemical identity of the substrate; and, $(m \times n)$ is the resulting Wood notation.[19] Figure 2.4 shows a Pt(111)-(1 × 1) surface.

In the case of an ordered overlayer or a reconstruction, an additional unit cell is formed. This unit cell is defined by the vectors $\vec{a}_{o1}$ and $\vec{a}_{o2}$ shown in Figure 2.3b. The relationship between these vectors and those of the substrate ($\vec{a}_{s1}$ and $\vec{a}_{s2}$) can be described by a matrix and the notation is of the following form: S(hkl)-M-ηA. S(hkl) is as before; A is the chemical identity of the overlayer and η is the number of overlayer atoms in the

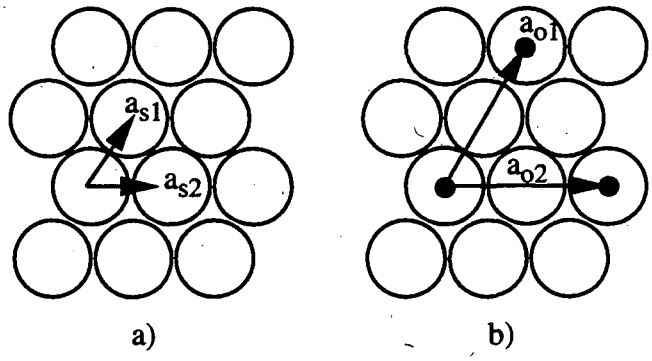

Figure 2.3: Real space lattice vectors representing the substrate and an overlayer. In a) the vectors $\vec{a}_{s1}$ and $\vec{a}_{s2}$ define the substrate unit cell; while in b) the vectors a_{o1} and a_{o2} define the overlayer's unit cell. The black dots in b) represent overlayer atoms arbitrarily placed on top sites.

primitive unit cell. The matrix M is defined by

$$\begin{pmatrix} a_{o1} \\ a_{o2} \end{pmatrix} = \begin{pmatrix} M_{11} & M_{12} \\ M_{21} & M_{22} \end{pmatrix} \begin{pmatrix} a_{s1} \\ a_{s2} \end{pmatrix} \tag{2.2}$$

As an example, the matrix notation for the overlayer illustrated in Figure 2.3b is

$$\mathrm{Pt(111)} - \begin{pmatrix} 2 & 0 \\ 0 & 2 \end{pmatrix} - \mathrm{O} \tag{2.3}$$

assuming the substrate is Pt and the adsorbate O.

The matrix notation can be simplified using the Wood notation[19]. This notation takes the following form:

$$\mathrm{S(hjk)} - \mathrm{B}\left(\frac{a_{o1}}{a_{s1}} \times \frac{a_{o2}}{a_{s2}}\right) \mathrm{R}\alpha - \eta\mathrm{A} \tag{2.4}$$

In this equation, B is equal to "p" in the case where the vectors $\vec{a}_{o1}$ and $\vec{a}_{o2}$ represent a primitive unit cell, or "c" in the case of a centered unit cell. If omitted, one assumes that the unit cell defined by these vectors is a primitive unit cell. Rα describes any rotation of the overlayer vectors with respect to the substrate vectors and if equal to zero, is dropped. As an example, the Wood notation for the overlayer illustrated in Figure 2.3b is Pt(111)-$p(2 \times 2)$-O. Rα is dropped because the angle between $\vec{a}_{o1}$ and $\vec{b}_{o1}$ and the angle between $\vec{a}_{o2}$ and $\vec{b}_{o2}$ are zero (see Figure 2.3). Other examples can be found throughout this work.

All overlayers in this work can be described by either the matrix or the Wood notation.[19] However, there are many cases where neither the matrix nor the Wood notation

are convenient or even possible. One example is overlayers in which the substrate and the overlayer vectors have non-rational ratios. Another case is when the surface is stepped or kinked. In this case, one prefers either a step or a microfacet notation. Reference 6 contains a detailed description of both the standard and these more exotic notation systems.

2.1.3 Ideal Diffraction Conditions

The reciprocal lattice vectors, $\vec{b}_1$ and $\vec{b}_2$, are determined from the real space lattice vectors, $\vec{a}_1$ and $\vec{a}_2$, by the following relationship:

$$\vec{a}_i \cdot \vec{b}_j = 2\pi\delta_{ij} \qquad (i,j = 1,2) \tag{2.5}$$

In this equation, δ_{ij} is the Kronecker delta function and $\vec{a}_1 \perp \vec{b}_2$ and $\vec{a}_2 \perp \vec{b}_1$. In order to have constructive interference between the incoming and outgoing waves, the parallel component of an elastically scattered electron's momentum can only change by integer multiples of a reciprocal lattice vector.[6] Given this, we obtain the following restriction for the parallel momentum transfer.

$$\Delta\vec{k}_{\parallel} = n_1\vec{b}_1 + n_2\vec{b}_2 \tag{2.6}$$

$\vec{k}_{\parallel}$ is the change in parallel momentum and n_1 and n_2 are integers. In an elastic process, the total energy of the incoming electron must be equal to the total energy of the outgoing electron; thus, we require the perpendicular component of the electron's momentum to be equal to

$$\vec{k}_{\perp} = \sqrt{k^2 - k^2_{initial\ \parallel} - \Delta k^2_{\parallel}} \tag{2.7}$$

Each spot in a LEED pattern can be associated with values of $\vec{b}_1$ and $\vec{b}_2$ such that the perpendicular component of the electron's momentum, $\vec{k}_{\perp}$ is real. The direction of the backscattered electron is also determined by $\vec{b}_1$ and $\vec{b}_2$ through Equation 2.6. In this way, three Laue conditions of X-ray diffraction are replaced by only two conditions

$$\vec{a}_1 \cdot (\vec{k}_{backscattered} - \vec{k}_{initial}) = 2\pi n_1 \tag{2.8a}$$

$$\vec{a}_2 \cdot (\vec{k}_{backscattered} - \vec{k}_{initial}) = 2\pi n_2 \tag{2.8b}$$

due to the loss of transitional symmetry perpendicular to the surface. Again, n_1 and n_2 are integers. Each Laue condition is identical to the Equation 2.1 obtained in the 1D case.

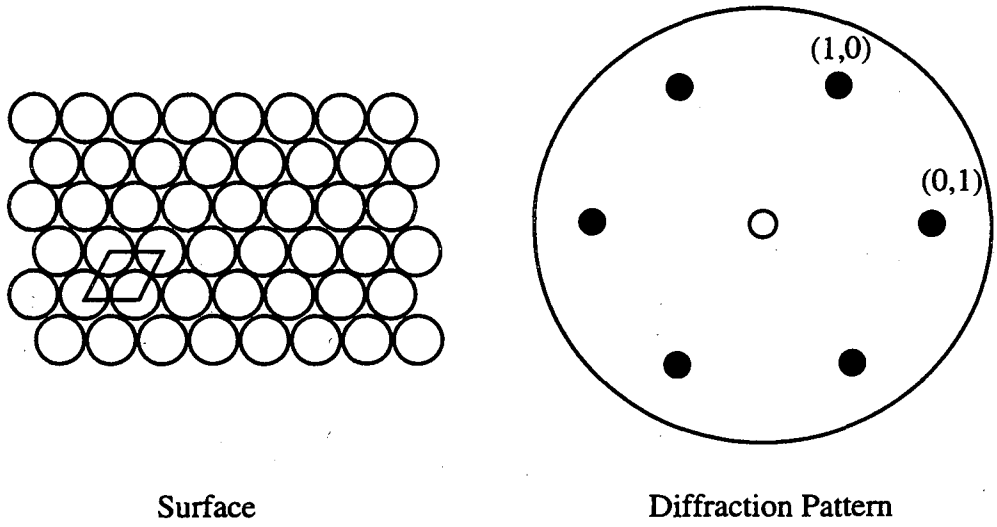

Figure 2.4: An fcc(111)-(1 × 1) surface is shown along with the resulting diffraction pattern at normal incidence. The real space unit cell is represented by the parallelogram; the diffraction spots are labeled in the LEED pattern.

Figure 2.4 illustrates both the surface and the resulting diffraction pattern at normal incidence ($\vec{k}_{initial\ \parallel} = 0$) for an fcc(111)-(1 × 1) crystal face. In this figure, the labels of the diffraction spots correspond to the two numbers, n_1 and n_2, of Equation 2.6. The formation of a typical ordered overlayer generates additional spots in the diffraction pattern. From Equation 2.5, it is clear that the overlayer reciprocal lattice vectors will be smaller than those of the substrate. The presence of the ordered overlayer results in spots between those present when the surface is clean. Figure 2.5 shows a $p(2 \times 2)$ overlayer on an fcc(111) surface along with the diffraction pattern. The additional spots present in the diffraction pattern after the overlayer has been formed are lightly shaded. Also in this figure, the black dots on the surface represent overlayer atoms in arbitrary high symmetry positions. From the location of the diffraction spots it is not possible to determine atomic positions in the overlayer's unit cell. Since intensities of the "(1×1)" spots are also changed by the overlayer, it is impossible to separate out the contribution of the substrate from that of the overlayer. Because the real space unit vectors for the overlayer are two times that of the substrate, the additional spots appear at "half-order" positions with respect to the substrate spots. In Figures 2.4 and 2.5, only the symmetry inequivalent diffraction spots are labeled. For example, in Figure 2.4, the $(\bar{1},0)$ is not labeled although it is located directly across from the (1,0) beam. This labeling convention is used throughout this work.

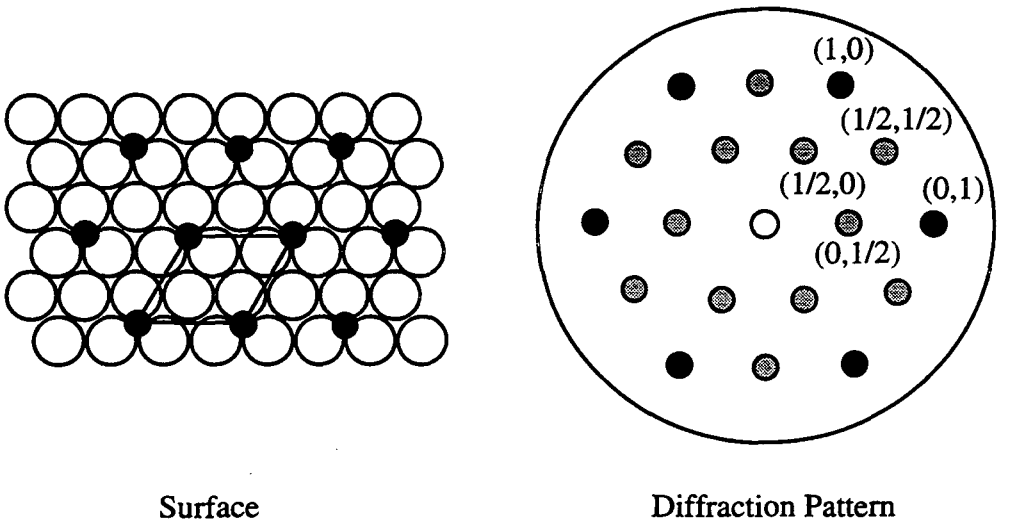

Figure 2.5: An fcc(111)-$p(2\times2)$ surface is shown along with the resulting diffraction pattern at normal incidence. The real space unit cell is represented by the parallelogram; the diffraction spots are labeled in the LEED pattern. The location of the black dot in each unit cell represents an overlayer atom placed in an arbitrary high symmetry position. The additional diffraction spots which appear when the overlayer is present are lightly shaded.

In the case of fcc(111) surfaces, the $p3m1$ symmetry of the surface results in three-fold rotational and mirror plane symmetry in the LEED pattern at normal incidence. However, the symmetry of the LEED pattern is not necessarily the symmetry of the overlayer. In the case of a bridge bound adsorbate in a $p(2\times2)$ overlayer, the unit cell has only a mirror plane symmetry. Symmetry is regained in the LEED pattern because domains, or patches of the ordered overlayer, can form with an angle of 120° or 240° between their respective unit cells. Another case is that of a $p(2\times1)$ overlayer. This overlayer has only mirror plane symmetry; but, again, it can form three different domains on the fcc(111) surface and would result in the same diffraction pattern as the $p(2\times2)$ overlayer. One must consider these possibilities when one proposes a structural model.

2.1.4 Real Surfaces and Instrumentation

Up to this point we have assumed the electron can be approximated by a plane wave and the surface by an infinite two dimensional (2D) lattice at $T=0$ K. The possibility of domain boundaries, defects in the overlayer and steps all lead to a break in the periodicity of the overlayer. In addition, thermal vibrations reduce the scattered intensities

of the diffraction spots. Both surface defects and thermal vibrations result in an increased background and a reduction in the diffraction intensities. However, these factors do not affect the width of the diffraction spots. Because defects influence the signal-to-noise ratio, one must carefully prepare the overlayer in order to minimize them. The effect of thermal vibrations is reduced by cooling the sample. Intensity losses due to thermal vibrations are taken into account when the theoretical intensities are computed.

In addition to sample difficulties, the instrument is not perfect. The electron beam is not perfectly monoenergetic and the detector spreads the diffracted intensity out in k-space. We have also assumed that the electron can be modeled by plane-waves and the surface as an infinite two dimensional (2D) lattice. To address these approximations, the concept of an instrumental response function has been developed[20]. From ideal samples, the diffraction conditions (Equation 2.8) result in diffraction spots with delta function shapes. In the real instrument, these ideal diffraction spots are spread out by this response function. The convolution of the ideal diffraction intensities $I(\vec{k})$ with instrumental response function $T(\vec{k})$ give the resulting width of the diffraction spots $J(\vec{k})$.

$$J(\vec{k}) = I(\vec{k}) * J(\vec{k}) \tag{2.9}$$

The half-width of the approximately Gaussian function which results from the Fourier transform of $T(\vec{k})$ is called the transfer width and has a value of a few hundred Å. Loosely, the value represents the range over which one can detect the resulting interference of the electron's wavefunction. The reader is referred to an article by G. Comsa[21] for more information regarding the various meanings and conceptual difficulties associated with the transfer width. Although the resolving power of a LEED experiment is of great importance for experiments aimed at studying surface ordering or imperfections,[22] it is of less importance for structural experiments. The diffraction intensities depend on the atomic positions in the unit cell and not on the long range order.

2.1.5 I-V Measurements and Structural Determinations

I-V Measurements

There are several different experiments that can be performed to obtain structural information[6]. One can measure intensities of the diffracted beams as a function of the incident and scattering angles, of the electron's energy, or even as a function of the momen-

tum transfer. Experiments performed in this work measured the diffraction intensities as a function of the beam energy for each diffraction spot. This results in a set of intensity vs. voltage curves or I-V curves. Due to the limitations of both the instrument and the sample, the intensities are obtained by integrating the measured intensity over the size of the diffraction spot. This is similar to the procedure used in X-ray diffraction.[23] In the I-V curve measurement, information regarding the direction of each diffracted beam is not implicitly used and the incident angle is fixed. These curves have several advantages over other forms of experimental data acquisition. The experiments are easier to perform than those that require one to vary both the incident and scattering angles. Because the incident angle is fixed, it is possible to use the symmetry of the LEED pattern to align the sample for an I-V curve experiment. In addition, a large data base can be quickly measured because of the experimental ease of changing the electron energy. I-V curves represent the most efficient method of obtaining experimental information that can be used in a structural analysis.

Details on the experimental method used to record the LEED pattern can be found in Section 2.3. The actual procedure used to obtain I-V curves is described in Section 2.4.

Structural Analysis: Trial and Error

A LEED structural analysis is based on a trial and error procedure. The multiple scattering which gives LEED its surface sensitivity prevents the direct inversion of the experimental data to give the geometrical positions of the surface atoms. Figure 2.6 is a flow-chart which represents this trial-and-error process. The first box ("Model") represents the first component of the coarse search. The outermost loop is a trial-and-error search over distant surface models. In the case of a $p(2\times2)$ overlayer on Pt(111) with one atom per unit cell, this could represent models based on the high symmetry sites: top, bridge, fcc-hollow and hcp-hollow. With more complex models, this step represents a careful delineation of the possible models based on other experimental and theoretical information. Because this loop contains a full dynamical calculation, it represents a major computational investment. This calculation is discussed in Section 2.5.

The inner loop represents the automated TLEED search. As discussed in the introduction, this search represents a major advance in LEED structural determinations. The search is directed by R-factors which quantify the agreement between experimental and

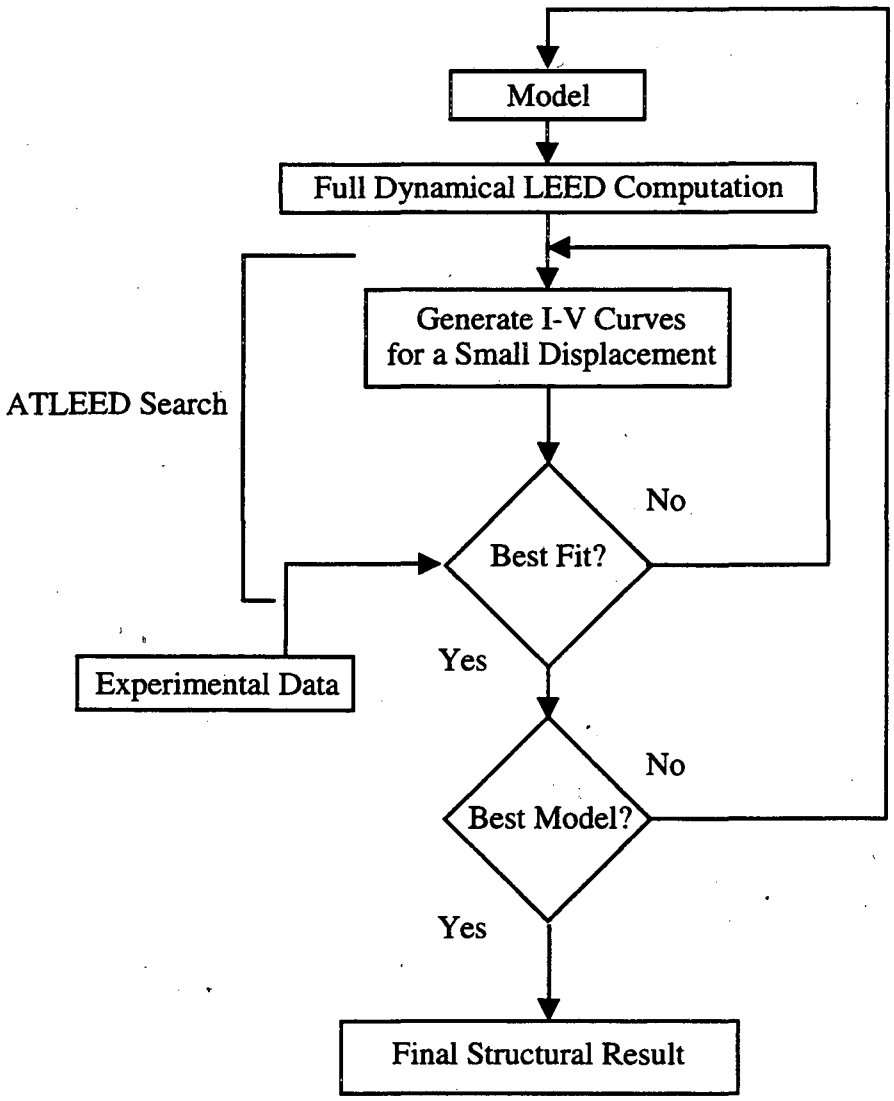

Figure 2.6: Flow-chart illustrating the various steps in a LEED structural determination. The outer loop represents a coarse search over different adsorption sites; while the inner loop is the automated TLEED search which refines each crude model.

theoretical I-V curves. Before the automated TLEED search was available, one was required to manually program a grid search over a limited number of parameters. Relaxations, or buckling, of a metal surface were not possible in this limited grid search, because it represented a major modification which required one to return to the time-consuming outer loop. The automated TLEED search eliminates the painstaking human effort and time consuming outer loop. Because the TLEED approximation is valid for small changes from the initial model for which the full dynamical calculation was performed, one needs to verify that this condition is maintained throughout the search. See Section 2.6 for details on the TLEED approximation and on the implementation of the search.

After the best-fit model has been determined, refinements need to be made. These refinements include not only the addition of more parameters, but, what is more important, a careful examination of the model and the quality of the fit. Once error bars are assigned to the best-fit structure, one finally completes the analysis. At this point the modeling work ends and the science begins again as one attempts to understand the structure and its implications.

2.2 Instrumentation and Experimental Preparations

2.2.1 UHV Requirement and Equipment

Experimental surface science requires a well-characterized surface for at least the duration of the experiment. Most clean metal surfaces are highly reactive with oxygen- and carbon-containing contaminants present in the laboratory environment. A good vacuum is required not only for the electron diffraction experiment, but also for sample cleanliness. The necessary quality of the vacuum can be approximated by considering the arrival rate of molecules to the surface. The estimated arrival rate (P in torr, T in K, and M in atomic mass units) of molecules to the surface using simple kinetic theory of gases is:

$$r = 3.51 \times 10^{22} \frac{P}{(TM)^{1/2}} \tag{2.10}$$

N_2 molecules at room temperature and 1 torr have an arrival rate of 3.88×10^{20} molecules $cm^{-2}s^{-1}$. If all of these molecules stick to the approximately 1 cm^2 area of the sample, they form a monolayer in about 3×10^{-6}s. It is from these considerations that the unit of one Langmuir is derived. One Langmuir is 10^{-6} torr/second and is used experimentally to

measure the exposure of a sample to gas molecules. To have a contamination rate of only a few percent of a monolayer per hour, a pressure of approximately 10^{-10} torr or less is required. This range of pressures is referred to as ultra-high vacuum or UHV.

Modern surface science has benefited greatly from the development of commercially available UHV equipment in the 1960s[14]. Early work was carried out in glass vacuum systems using liquid N_2 trapped Hg diffusion pumps. Modern surface science is performed in stainless steel chambers or bell jars. The instrumentation is mounted on stainless steel flanges which are connected to the chamber using Cu gasket seals. The chamber is typically pumped with an ion pump that requires little attention as compared to diffusion pumps with liquid N_2 traps. The base pressure, or the lowest pressure obtainable, is limited by the desorption of adsorbed gasses from the walls of the chamber. The system must be baked, or the walls of the chamber must be heated, to increase the desorption rate and remove the species which have adsorbed there. Only after baking can a base pressure of 10^{-10} torr be obtained. Baking does impose many limitations on the materials which can be used in UHV chambers. Additional information regarding the methods of UHV can be found in Reference 24.

Our LEED studies were conducted in standard, ion-pumped, bakeable, stainless steel UHV chambers. All the LEED data, with the exception of clean and NO-covered Ni(111) (Chapter 6), and sulfur on Pt(111) (Chapter 4), were collected using a UHV chamber equipped with a UTI quadrupole mass spectrometer for residual gas analysis and thermal desorption spectroscopy (TDS), an ion sputter gun along with an auxiliary turbo-molecular pump for sputtering, and a cylindrical mirror analyzer and electron gun for Auger electron spectroscopy (AES). LEED experiments were performed using either conventional 4-grid LEED optics with a fluorescent screen or a digital LEED detector. The chambers utilized for the clean and NO-covered Ni and for sulfur on Pt(111) did not have a cylindrical mirror analyzer, but instead used the 4-grid LEED optics as a retarding field analyzer for AES. The chamber utilized in the sulfur work was also equipped with a scanning tunneling microscope (STM) capable of obtaining atomic resolution, real space images of the sample. The base pressure of these chambers was approximately 10^{-10} torr.

This thesis will focus on both experimental and theoretical practices of LEED as they relate to surface structure determinations. Additional information on many of the surface science techniques mentioned here can be found in a number of recent books.[13,14]

2.2.2 Sample Preparation

The sample preparation procedures can be divided into two parts: the non-UHV and the UHV preparations. The first part involves the preparation of the desired crystal face and its mounting to the UHV manipulator. After transferring the crystal into UHV, it must first be cleaned and annealed before it can be used for surface science experiments. We discuss this procedure following our discussion of the non-UHV preparations.

Non-UHV Preparation

Single crystal rods were obtained from commercial venders. These single crystal rods were grown from high purity zone-refined material and are typically 8 *mm* in diameter and several *cm* long. Laue X-ray back-diffraction was used to align the desired face and a 1 *mm* slice was cut with either a diamond saw or an electric discharge machine. The single crystal slice was polished using diamond paste, and the orientation of the crystal face was checked again with Laue X-ray back-diffraction. The sample preparation procedures are described in the LBL publication by Wini Heppler [25].

The Pt(111) single crystal was mounted using Ta strips spot welded to a Mo sample holder pressed between two Cu blocks. The Cu blocks are fixed to the manipulator which allows accurate positioning in three orthogonal directions, as well as rotation around two axes. Cooling to 90 K was accomplished by flowing liquid-N_2-cooled N_2 gas through the Cu blocks. The sample could be heated using an e-beam filament placed 1 *mm* under the metal sample through a hole in the Mo sample holder. The sample temperature was measured using a chromel-alumel thermocouple spot welded to the side of the sample.

The Ni(111) single crystal used in the LEED study of Chapter 6 was mounted on an on-axis sample manipulator which, as in the case of the Pt(111) sample manipulator, is capable of positioning the sample normal to the LEED optics. Heating was accomplished by resistive heating and cooling via Cu braids connecting a liquid N_2 reserve to the Cu support rods of the manipulator. The sample could be cooled only to approximately 170 K due to the limited heat transfer through the Cu braids. A chromel-alumel thermocouple spot welded to the side of the sample was used to measure the temperature.

The Fe crystals required additional non-UHV cleaning procedures. These procedures along with details of the sample mounting are described in Chapter 8.

UHV Preparation

Before one can perform a surface science experiment, one must clean the sample to obtain an atomicly clean surface. Surface contamination comes from two main sources: adsorption and surface segregation of bulk impurities. Two different surface science techniques are used in cleaning a single crystal sample in UHV; iron sputtering and AES. An ion sputter gun along with an auxiliary turbomolecular pump is used for sputtering the sample. AES is used as an analytical tool to determine the surface composition.

After introducing a sample to UHV, one must initially sputter it. An Ar^+ ion beam, generated in the ion sputter gun, with energies between 600 and 1000 eV is focused on the sample for about 10 minutes in order to remove the first few atomic layers. After this process, the surface must be annealed to between 500° and 1000° C in order to repair the beam-damaged surface which was damaged in the sputtering process. The annealing process brings to the surface various bulk impurities. The sputtering and annealing cycle is repeated until one can obtain an AES spectrum showing peaks due to metal Auger transitions. For some metal surfaces, such as Cu and Ni, this process should be repeated until the crystal is free of impurities. Carbon contamination can be removed from Pt by heating the sample in an oxygen environment. Reference 26 contains a large number of different UHV cleaning techniques for many different elements.

As a specific example, we will now describe the cleaning process for our Pt(111) sample, that was used for many of the experiments in this work. For this sample, we found that calcium and carbon were the major impurities. We found that calcium segregates to the surface when the sample is heated to around 1000° C and is enhanced by the presence of oxygen, possibly due to the formation of CaO on the surface. This segregation behavior was used to pull calcium from the bulk to the surface. Once on the surface, it can be removed by sputtering for about 10 minutes at room temperature. Carbon is a constant problem due to its large concentration in both the bulk of the crystal and in the background gases which adsorb on the sample. Initially, we burned the carbon in oxygen at approximately 750° C. However, carbon has a high solubility in Pt at elevated temperatures. Because of this, we found for the final cleaning, that annealing the sample from 250° to 500° C followed by burning in oxygen was required to remove the carbon from the crystal. Before the LEED experiment, the sample was annealed to 250° for 10 minutes followed by an oxygen exposure of 1 Langmuir and an additional annealing to 500° C, in order to obtain a clean surface.

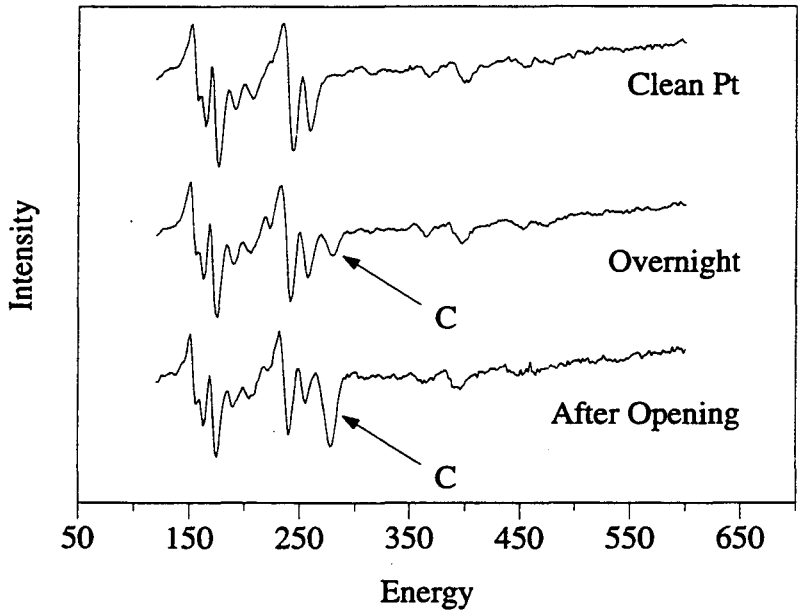

Figure 2.7: AES spectrum of the Pt(111) surface. The spectrum labeled "clean Pt" was measured after the sample was cleaned in oxygen and annealed. It is representative of the surface cleanliness before the LEED experiments were performed. The two other spectra were taken following an overnight exposure to the UHV background gases, and after opening the chamber for repair.

An AES spectrum of the clean Pt(111) surface is shown in Figure 2.7. The spectrum is representative of the surface cleanliness before the LEED experiments were performed. This figure also shows AES spectra of typical surface compositions after an overnight exposure to the UHV environment, and after opening the chamber for repair. The CO background is the source of the carbon in the spectrum obtained following overnight exposure and can be removed either by heating the sample or by burning in oxygen. The carbon in the spectrum obtained after opening the chamber usually has to be removed by ion sputtering. Because this crystal has already gone through the UHV cleaning procedure, carbon is the only contaminant on the surface.

2.3 LEED Image Recording

Two different techniques were used to record images of the LEED pattern during an experiment. First, we review the video LEED technique which utilizes conventional LEED optics coupled with a high sensitivity video camera. Two books (References 13 and 14) contain detailed descriptions of the conventional LEED technique. Second, we examine a more specialized detector, the digital LEED detector, developed recently in the group of G. A. Somorjai. Additional details regarding this detector can be found in References 27 and 12.

2.3.1 Video LEED

Conventional LEED optics produce light at the impact positions of the diffracted electrons. This light can be detected in many ways and for most qualitative studies the detector is the human eye. Quantitative work requires an accurate measurement of the diffraction intensities. This was accomplished in the 1970s with Faraday cup assemblies and spot photometers.[6] In the mid-1970s, a photographic method was developed to overcome the long data collection times that the above methods imposed.[6] Although this technique allowed faster data collection, it was limited by a time consuming film processing. High sensitivity video cameras and computer acquisition have overcome many of these disadvantages. Data collection can be performed quickly (approximately 30 minutes) under computer control, and the signal-to-noise of resulting LEED patterns can be determined immediately. Early video LEED systems coupled the video camera to a video tape recorder for image storage.[6] The data was later digitized from the video tape, along with any addi-

Figure 2.8: VLEED image of the Pt(111)-(1x1) LEED pattern at 120 eV and normal incidence.

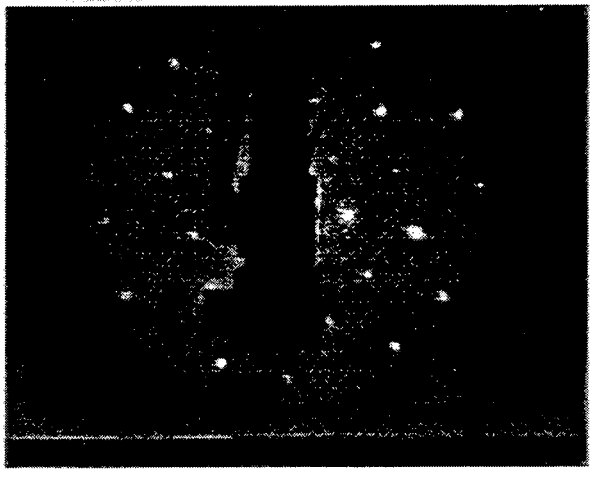

Figure 2.9: VLEED image of the Pt(111)-(1x1) LEED pattern at 270 eV and normal incidence.

tional noise from the recording process. The system we currently use digitizes the pattern during the experiment and records it in digital form on a hard disk. Figures 2.8 and 2.9 are the clean Pt(111)-(1x1) LEED patterns, at 120 and 270 eV, respectively, obtained at normal incidence using our video LEED system.

We used the Varian 4-grid LEED optics with an off-axis electron gun to produce a visible image which could be measured with the camera. Figure 2.10 shows a typical arrangement of the electron gun, the grids, the screen, and the video camera, with respect to the sample. The conventional LEED optics have three or four (for the AES option)

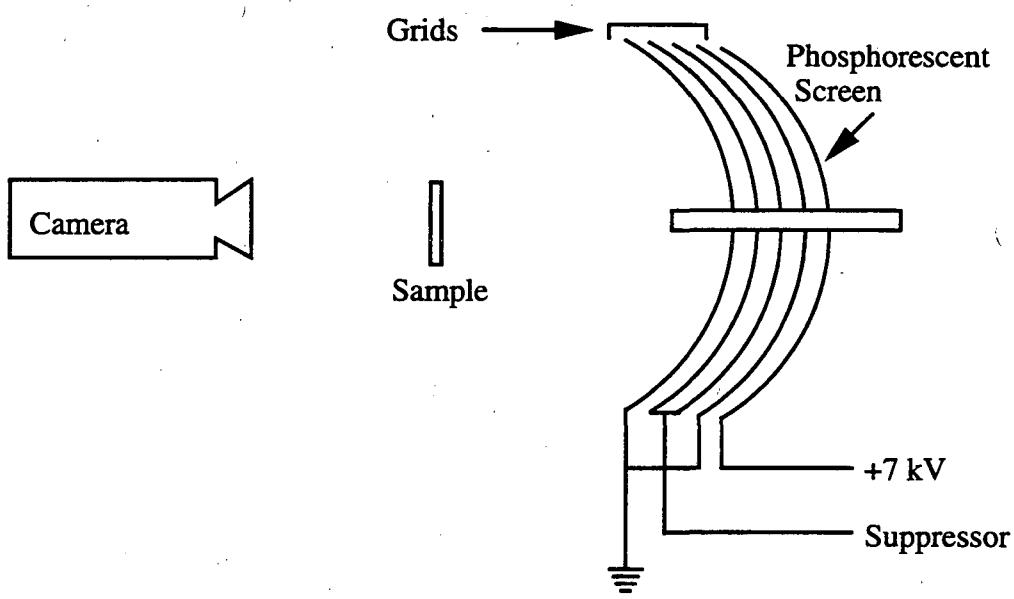

Figure 2.10: The arrangement of the conventional LEED optics, the sample and the camera.

concentric spherical grids. These grids are used as a retarding field energy analyzer (RFA) to select only the quasielastically scattered electrons, because the energy resolution of the RFA is not sufficient enough to separate out the electrons which scatter off a phonon or a vibrational mode of an adsorbed species. Directly behind the grids lies a fluorescent screen, P-11 coated, biased at approximately 7 keV. The light generated is proportional to the number of electron impacts.

A Dage-MTI SIT-68 high-sensitivity video camera was used to produce the video signal which was then digitized. This camera utilizes a silicon intensified target (SIT) to store the image charge pattern. Light from the fluorescent screen is imaged through a simple lens onto a photoemissive cathode. The resulting electrons impact a silicon-diode array and produce a large number of electron-hole pairs. As in a standard vidicon tube, the back of the array is charged by a scanning electron beam, and these electron-hole pairs cause a short which discharges the array. As the scanning electron gun passes over the discharged region, a current is measured as the area is recharged. This current is equal to the total number of charge pairs produced by the light source during the interval between scans. Also, because the location of the scanning electron gun is known, the resulting current can be converted into the video signal. One problem with this type of video camera is that thermally produced hole-pairs result in a constant background which limits the overall signal-to-noise of the camera. This background must be subtracted when the I-V curves are generated.

This camera technology represents only one level above the original low sensitivity vidicon tube. Intensified SIT cameras and cameras with multichannel plates can provide much greater sensitivity. Newer video LEED systems are now using cooled charge-coupled devices. These devices offer higher sensitivity and larger dynamic ranges than cameras based on the vidicon tube. One commercially available system can image LEED patterns with primary beam current as low as 1 nA[28]. Our video LEED system requires hundreds of nA to mA.

The video output of our camera is connected to a Matrox MVP-AT video digitizer. The digitizer occupies two expansion slots in an IBM compatible PC. The Matrox digitizer came with routines which we used in our specialized programs to collect LEED images at different energies under computer or manual control. The board's 8-bit A/D converter digitizes one image consisting of 480 horizontal lines with 512 pixels. Data collection normally requires the averaging of 128 images which is done in the 16-bit video memory of the Matrox

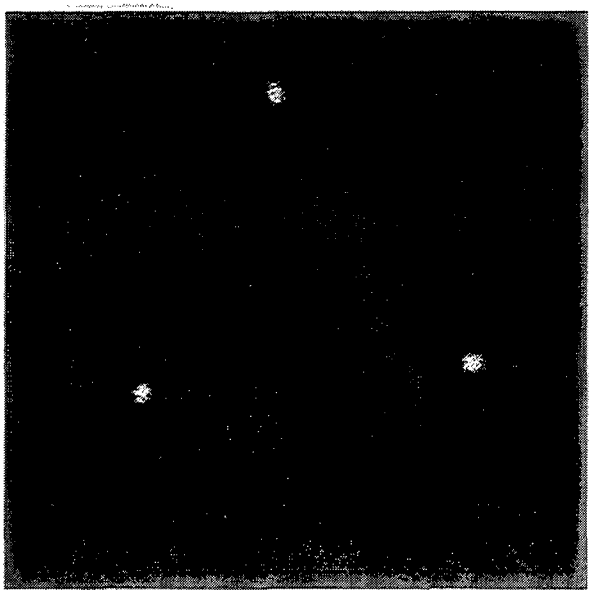

Figure 2.11: DLEED image of the Pt(111)-(1x1) LEED pattern at 80 eV and normal incidence.

board. The resulting image in the video memory is divided by 128 to convert back to an 8-bit representation and subsequently downloaded to disk.

2.3.2 Digital LEED

The digital LEED detector is designed to measure the impact position of single electrons in order to digitally generate the diffraction pattern. Additional details can be found in References 27 and 12. This detector eliminates the background problem found in video LEED systems, thus, increasing the overall signal-to-noise ratio. Another, important feature of the detector is its picoampere primary beam current as compared to the beam current of microamperes from commercial LEED optics. During the acquisition of a LEED pattern with the digital LEED detector, the charge deposition is typically only about 10^{-5} electrons per surface unit cell. About 100 LEED patterns, at different energies, are necessary for a complete LEED experiment involving measurements of I-V curves. The LEED patterns are recorded as images under automatic computer control for primary energy, electron gun and detector parameters. Figures 2.11 and 2.12 are the clean Pt(111)-(1x1) LEED patterns, at 80 and 120 eV, obtained at normal incidence with this detector.

The overall layout is similar to that of the conventional LEED optics of Figure 2.10,

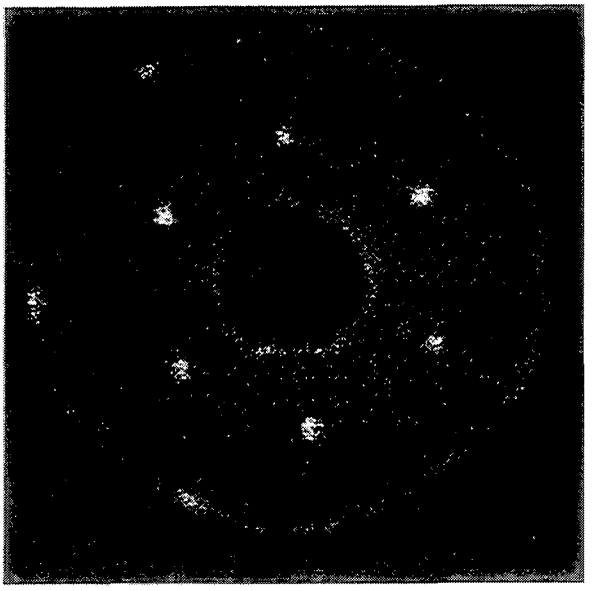

Figure 2.12: DLEED image of the Pt(111)-(1x1) LEED pattern at 120 eV and normal incidence.

but the fluorescent screen is replaced by a pair of multichannel plates (MCP) and a position sensitive detector. A schematic diagram of the digital detector is illustrated in Figure 2.13. In this case, only three concentric spherical grids are used as a retarding field energy analyzer to select only the quasielastically scattered electrons. Directly behind the grids is the front face of the first channel plate which is biased at approximately $V_{beam}+700$ eV. The constant 700 eV forces the electrons to impact the channel plate normal to its surface. The MCP are configured in a chevron-type stack and are used to generate a charge pulse from each electron impact. "Chevron" stack refers to a configuration in which the channels of the two plates are aligned 8° off normal to prevent any ion feedback caused by ions traveling back through the channels. In this arrangement, electron amplifications of up to 5×10^7 with background count rates below 1 Hz/cm^2 can be obtained. In the LEED experiment the count rate is limited to about 15 kHz due to local saturation of individual channels.

The resulting charge cloud formed by a single electron impact on the first MCP is detected by the wedge and strip anode. This detection system has many advantages over other electron position sensing detectors[12]. The wedge and strip anode uses three metal conductors in an interlocking pattern with a spatial periodicity of approximately $1\mu m$ to determine the impact position of the charge cloud and thereby determine the position of

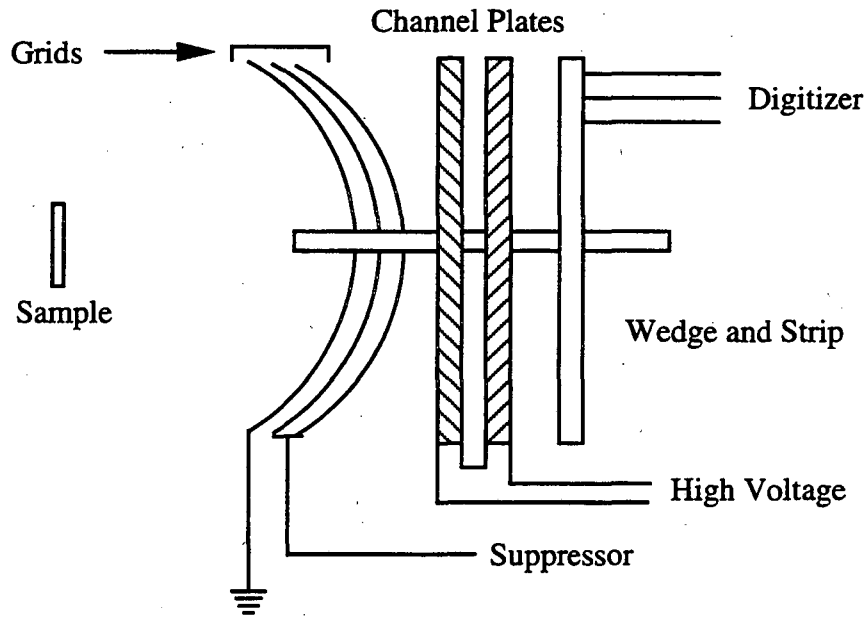

Figure 2.13: The arrangement of the optics, sample, channel plates, and the wedge and strip anode in the digital LEED detector.

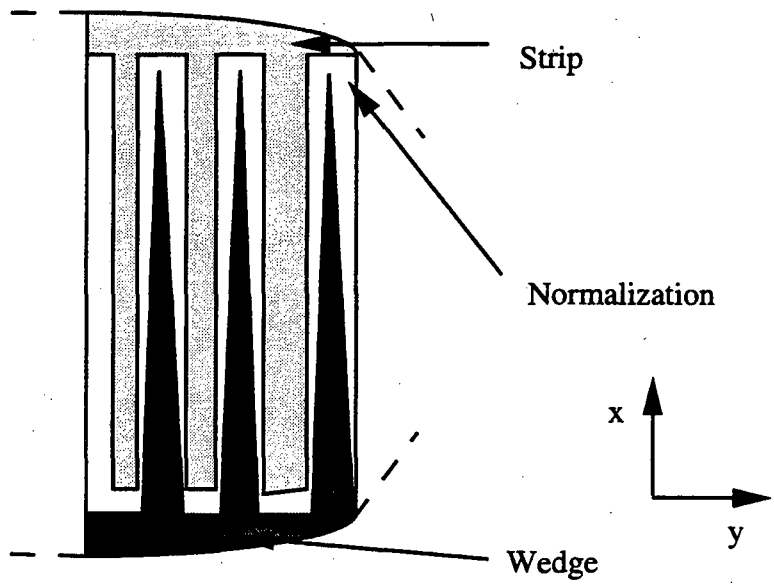

Figure 2.14: A top view of a section of the wedge and strip anode showing the variation in size of the wedge and of the strip at various positions on the anode.

the LEED electron (Figure 2.14). One of the three conductors is a wedge which narrows as one moves in the y direction. The second conductor is the strip which varies in size as one moves in the x direction. The third conductor covers the remaining area and, along with

the other two, provides information about the total charge of the cloud. From the division of charge between these three conductors the position can be computed by

$$x = \frac{Q_{strip}}{Q_{wedge} + Q_{strip} + Q_{remain}} \tag{2.11a}$$

$$y = \frac{Q_{wedge}}{Q_{wedge} + Q_{strip} + Q_{remain}} \tag{2.11b}$$

Equations 2.11a and 2.11b are only true for an ideal anode. In practice, one needs to correct for capacitance coupling between the conductors, which is the limiting factor in the detector's special resolution. To determine the total charge on each conductor, the current pulses which result from the impacting charge clouds, are integrated by fast charge sensitive preamplifiers and digitalized by fast analog-to-digital converters. The computation of x and y is done by hard-wired digital circuits and stored in a 256×256 histogram memory. Additional amplifiers are involved in the rejection of current pulses from multiple charge impacts. The collection is controlled by a PC, and the images are downloaded to the PC after data collection.

Both the detector and the position sensitive anode have a hole through the center for the LEED electron gun. The electron gun is of a conventional design with the exception of a $37\mu m$ beam-limiting aperture attached to the anode at the first crossover point. This aperture limits the beam current to the picoampere range and keeps the detector's count rate in the kHz range. The rest of the gun consists of a thoriated iridium filament with a Wehnelt electrode and anode. A three element Einzel lens provides focusing.

2.4 The LEED I-V Experiment

After the sample has been cleaned and the ordered overlayer formed, the LEED I-V experiments consist of three main parts. First, the sample must be placed at a known angle of incidence with respect to the electron beam. Second, LEED images are taken over a suitable energy range. Third, the I-V curves must be generated from the LEED images. In most LEED I-V experiments, it is the preparation of an ordered overlayer that poses the difficulty; for sufficient signal-to-noise, this overlayer must be well-ordered.

2.4.1 Sample Alignment

Once the ordered overlayer has been formed, the crystal must be positioned such that the incidence of the electron beam is known. The experimental LEED data in this work were taken at normal incidence; we used the three-fold symmetry and mirror plane of the LEED pattern at normal incidence to position the sample normal to the electron beam. Normal incidence was then checked by comparing the resulting I-V curves. By examination of the different symmetry equivalent I-V curves, one can also find energy ranges where the I-V curves are particularly sensitive to the angle of incidence. Once these have been found, it is possible to quickly align the sample. In our work, we used the clean surface to initially calibrate the manipulator, allowing faster sample positioning when the overlayer had been formed.

For proper energy selection, the sample must also be positioned in the center of curvature of the LEED optics. In practice however, this may not be the ideal location. For instance, for dense overlayers, one may want to move the sample further away from the optics to expand the image, or, if one wants to examine higher order diffraction spots, one may wish to move the sample closer. Because we are interested in the integrated intensities, distortion of the LEED pattern resulting from sample positioning off the center of curvature of the optics is not a major difficulty. Also, because most of the inelastically scattered electrons are at lower energies, the errors introduced by the inaccurate energy selection process are negligible. However, if one is interested in spot profiles, such distortions are a problem, so the sample must be positioned in the center of curvature.

2.4.2 Image Collection

After determining the optimal sample position in front of the LEED optics, one can proceed with the experiment using either the digital LEED detector or the video LEED camera to record the LEED patterns as a function of energy. In both video and digital LEED, one must take the time to adjust various collection parameters. For both detectors, one needs to verify that the incident beam current is constant or known as a function of energy before one proceeds with the experiment. The video camera's lens must be focused on the pattern, and the f-stop must be adjusted to maximize the signal without overloading the detector. For digital LEED, the computer-controlled lens in the electron gun must be optimized and the number of seconds required to collect the image must be adjusted. One

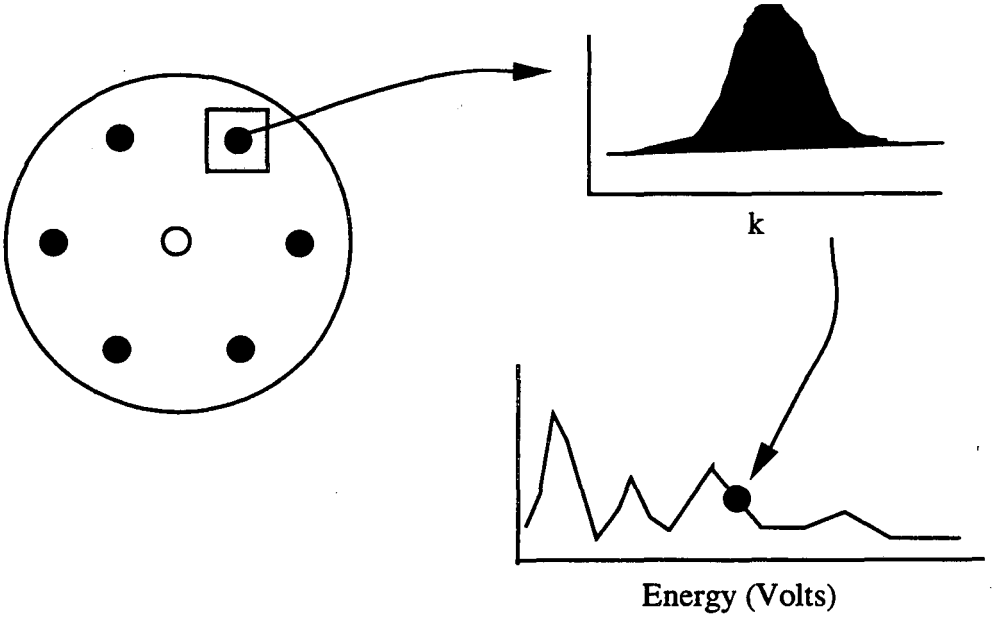

Figure 2.15: Flow-chart showing the steps required to generate an I-V curve.

should check the sensitivity of the overlayer to either background gases or electron beam damage. By remeasuring a few of the first images, one can check to see if the pattern has deteriorated. In addition, one should prepare a new overlayer and take the LEED images in the reverse order. Aside from this, this step in the process is relatively painless.

2.4.3 I-V Curve Generation

In both digital and video LEED, the resulting LEED images at each energy point are stored on a hard disk during data acquisition. To generate I-V curves the integrated spot intensities must be measured for each individual diffraction spot at each energy point. In our work, this was done using software developed by Dr. Ulrich Starke. Figure 2.15 illustrates the typical sequence of events in the generation of I-V curves. Each image is read into the computer and the spot intensity is integrated for each measured energy within a square or octagonal window, the integration area being determined by the borders of the window. A background correction which subtracts the intensity averaged over the window frame is included. In addition to the background correction, two additional factors should be accounted for. The first factor is any changes in the electron beam current as a function of energy. Our electron guns were operated such that this correction was not required; however, a linear increase in beam current as a function of energy would have provided

greater signal-to-noise due to the increasing number of diffraction spots with increasing beam energy. The second factor applies only to video LEED systems. In this system, the light generated by the diffracted electrons passes through the grids before being collected by the video camera. Because transmission of the light through the grids changes as a function of the diffraction beam's position, one should in principle take this into account[29,30]. This effect was not taken into account and is believed to be small. The clean Pt(111) I-V curves measured on either the video LEED system or the digital LEED system, which does not rely on the transmission of the light through the grids, were found to be identical.

As images of increasing energy are analyzed, the positions of the diffraction spots change. The is due to the contraction of the projection of reciprocal space on the detector with increasing energy. The movement of the integration frame to follow the diffraction spots can be controlled manually; automatically by following the first moment of the intensity distribution within the window frame; or with a semiautomatic interpolation scheme. The resulting I-V curves can be obtained quickly using this software. After each I-V curve is generated, the symmetry-equivalent beams are compared and averaged to reduce noise. This procedure also removes, to the first order, any error in the sample position away from normal incidence. The beam intensities are then written to disk in an ASCII format suited to the LEED analysis programs. In some cases, the experimental I-V curves from more than one preparation of the overlayer may be averaged together to increase the signal-to-noise before the final experimental results are written in ASCII format.

2.5 LEED Theory and Computational Methods

In this section, we discuss the theory and computational methods used in dynamical LEED calculations in this work. Reference 6 describes many different theoretical and computational approaches while Reference 31 contains a very formal description.

The dynamical LEED calculations used in this work divide the crystal into a stack of 2D layers. The layers are further subdivided into atoms which are treated as spherically symmetric scatterers. The combined-space method[6] uses both plane-waves and spherical-waves to describe the LEED wavefunction. Within the layers spherical-waves are used to take advantage of the spherical scatters. Between the layers, plane-waves are utilized in effective perturbation methods which stack the layers to form the semi-infinite crystal. The combined-space approach facilitates a very effective "divide and conquer" strategy. In this

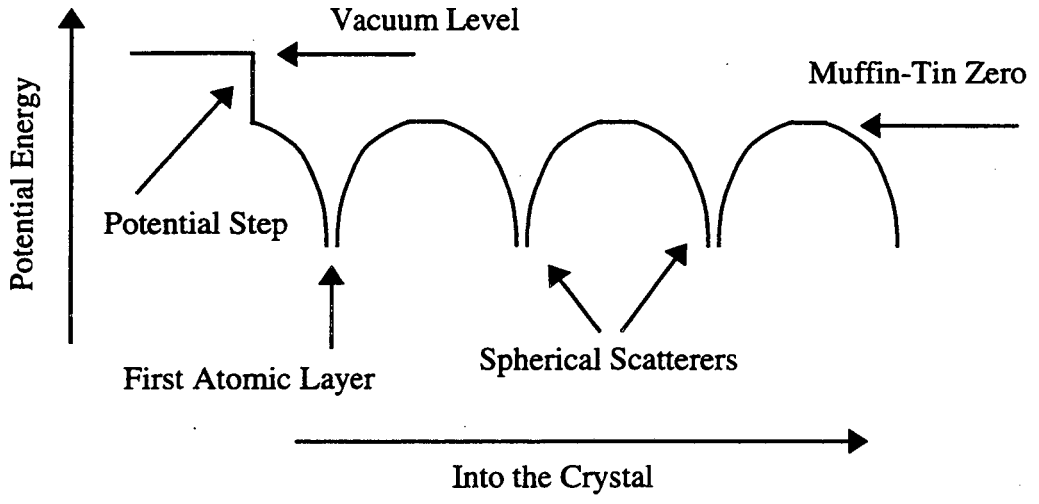

Figure 2.16: The muffin-tin potential at a surface. As one moves from left to right, the transition from the vacuum to the substrate is shown.

section, we work backwards through the scattering problem: atoms to layers to crystal.

2.5.1 Muffin-Tin Potential

We use a muffin-tin potential model shown in Figure 2.16 for the semi-infinite crystal[6]. In this model, the potential can be separated into two regions. A flat potential between each muffin-tin sphere and a spherical potential within each sphere representing the actual atoms. This approximation has been found to well describe the low energy electron scattering process[6,18]. The potential at the interface between muffin-tins of the semi-infinite crystal and the vacuum is modeled by a potential step function. In the LEED programs, this step function does not reflect the incoming plane-wave and has unity transmission for the outgoing plane-waves.

The muffin-tin potential is computed from the atomic wavefunctions as described in Loucks.[32,33] First, the atomic potentials are obtained from atomic wave-functions computed by numerical integration of either the Dirac-Fock or Hartree-Fock (see References 34 and 35) equation with electron exchange treated exactly. In this calculation the population of the atomic orbitals is such that the resulting charge density is spherical. Second, the atomic charge densities are corrected for the effects of the surrounding atoms in the crystal lattice. In the last step, the total potential within the muffin-tin is computed by adding the coulombic potential, which results from the spherically symmetrized charge densities,

to the exchange correlation potential determined by the local density approximation. This final charge density was checked against the self-consistent results of V. L. Moruzzi et al.[36] and found to be almost identical. This was especially true for the density within the atomic cores which is responsible for the scattering in LEED.

2.5.2 Atomic Phase Shifts

Scattering from a spherical potential can be described in terms of partial waves. At each energy, one can compute phase shifts for each partial wave of angular momentum l. The phase shifts used in our LEED computations were obtained by requiring the radial solution within the muffin-tin to smoothly match the spherical-wave solution outside the muffin-tin. For the phase shift calculations the muffin-tin zero was set equal to zero by subtracting the constant potential due to both the coulombic and the exchange correlation potentials from the muffin-tin potential. This is done so that the real part of the inner potential used in the LEED codes properly references the effective muffin-tin zero.

The phase shifts were computed by numerically integrating either the Schrödinger or the relativistic Dirac equation using methods outlined by Loucks.[33] Only a small modification has been made to Loucks' code to insure greater accuracy. The relativistic phase shifts were spin-averaged (which we call quasi-relativistic) before they were used in the LEED computation.[37] For the LEED codes, the phase shifts are a function of energy and of orbital angular momentum l. Additional discussions of the phase shift treatment can be found in Section 3.3.

Within our LEED program the atomic phase shifts are converted to the atomic t-matrix

$$t_l = -\frac{\hbar^2}{2m}\frac{1}{k}\sin\delta_l \exp(i\delta_l) \tag{2.12}$$

t_l represents the amplitude for scattering from an incoming spherical-wave with a unit amplitude equal to that of an outgoing wave, where both waves are of angular momentum l. Temperature effects are taken into account by multiplication of a Debye-Waller factor into the atomic t-matrix. As shown by C. B. Duke et al.,[38,39] this procedure correctly models the lowering of intensities due to thermal vibrations with the assumption of independent vibrations. Because the Debye-Waller factor depends on $\vec{k}_{in} - \vec{k}_{out}$, most of the effects will be in the weaker backscattering events; thus, this approximation of independent vibrations is not too bad for isotropic vibrations. In Chapters 5 and 6, we examine the wagging vibrations

of molecules which are poorly described by this model, following the investigation of CO on Ru(0001) by H. Over et al.[40]. Recent work on this topic has also been done in other groups to address correlated vibrations using TLEED.[41,42]

2.5.3 Dynamical LEED Calculations

Scattering in two dimensional layers is solved in the spherical-wave representation by matrix inversion similar to the Korringa-Kohn-Rostoker method of band structure calculations.[6] This procedure requires the majority of the total computer time. Once the solutions have been obtained for each inequivalent layer, they are used to generate diffraction matrices which describe the transmission and reflectivity of the layer.

The basic idea can be understood by considering layers containing only one inequivalent atom (a 2D Bravais lattice). Given G^{12} as a spherical-wave propagator from atom 1 to atom 2 in another unit cell; t^1 as the atomic t-matrix of atom 1; and τ^i as the total spherical-wave scattering amplitude from each atom i in the lattice. τ^1 can be computed by the following series:

$$\tau^1 = t^1 + t^1 \sum_{i=2,\infty} G^{1i} t^i + t^1 \sum_{i,j=1,\infty}^{i\neq j, i\neq 1} G^{1i} t^j G^{ij} t^j + \cdots \tag{2.13}$$

Because all the atoms are equivalent, the superscript can be dropped, and this equation can be reduced to

$$\tau = t + t \left(\sum_{i=2,\infty} G^{1i} \right) \tau \tag{2.14}$$

which, once the lattice sum is computed, can be solved by matrix inversion (the elements of t and τ are indexed by lm).

$$\tau = t \left[1 - (\sum_{i=2,\infty} G^{1i}) t \right]^{-1} \tag{2.15}$$

For more than one inequivalent atom in a layer (a so-called composite layer) similar equations can be written by letting t equal τ and τ equal T, thereby representing the total scattering of a "sublayer." Thus, in a composite layer, the τ's must be computed for each sublayer followed by another matrix inversion to determine the T's. Once τ or T is computed, one converts τ into the plane-wave diffraction matrix, $M_{out,in}$, of the layer.[6,18]

$$M_{out,in} = -\frac{8\pi^2 i}{A\, k_{out,z}} \frac{2m}{\hbar^2} \sum_{LL'} Y_L(\vec{k_{out}})\, \tau_{LL'}\, Y^*_{L'}(\vec{k_{in}}) \tag{2.16}$$

where A is the two dimensional area of the unit cell and the Y's are spherical harmonics. L represents the sum over l and m. As in Section 2.1, $\vec{k}_{out\,\|}$ and $\vec{k}_{in\,\|}$ must differ only by integer multiples of the reciprocal lattice vectors. $M_{out,in}$ for a composite layer is obtained by changing τ to a summation over the T's of the sublayers with the proper phases.

The reflectivity of a stack of layers can be quickly solved using either the Layer-Doubling (LD) or the Renormalized-Forward-Scattering (RFS)[6,18] both of which use the plane-wave representation for describing the electron propagation between the layers. LD is computationally more intensive than RFS and is used only when the spacing between the layers becomes smaller than 1.0 Å. This method is discussed in Chapter 8 where it was needed to compute the diffraction intensities of an Fe(111) surface. For Pt(111) and Ni(111), RFS was utilized to compute the diffracted amplitudes. This method computes the diffracted amplitudes for each beam in a series over backscattering events, thus, relying on the fact that backscattering is weak compared to forward scattering. Typically, the resulting beam intensities do not change more than 1 % after 5 to 7 backscattering events, and the series can be truncated. The theoretical I-V curves are then obtained by multiplying the square of the absolute value of each beam amplitude by the ratio of the incoming to the outgoing beam areas to account for charge in flux[6].

2.5.4 TLEED Approximation

The TLEED approximation[43] allows one to quickly compute the change in intensity of a diffracted beam for a structure in which the atomic positions of the atoms have been displaced by a small amount with respect to a reference structure. If the scattering is weak or the displacements are small enough, it has been observed that the resulting I-V curves of the two structures are similar. Thus, for small displacements, the change in the amplitude of a diffracted beam can be treated using first order perturbation theory. This change in amplitude can be written as

$$\delta A \approx \sum_n < \Psi(n, \vec{k}_{out}) \mid \delta t^n \mid \Psi(n, \vec{k}_{in}) > \tag{2.17}$$

or explicitly in the spherical-wave representation as

$$\delta A \approx \sum_n \mathcal{F}^n \, \delta t^n \tag{2.18}$$

The quantity $\mathcal{F}^n$ is a Cartesian tensor giving the method its name. This tensor is evaluated during the full dynamical calculation of the reference structure and is analogous to the

form factor in X- ray diffraction. δt^n is the change in the atomic t-matrix when an atom n is displaced by $\delta\vec{r}$. $\mid \Psi(n, \vec{k}_{in}) >$ is the incoming wavefield. It contains all paths from the incident beam to the atom n and can be computed from the plane-wave amplitudes incident on the top and bottom of the atomic layer which contains the atom. The quantity $< \Psi(n, \vec{k}_{out}) \mid$ is the LEED state which takes the scattered wavefield around atom n and carries it out of the crystal.

The quantity δt^n can be written as

$$\delta t^n = G(-\delta\vec{r}_n) t^n G(\delta\vec{r}_n) - t^n \delta_{ll'} \tag{2.19}$$

This equation represents exact propagation of the incoming spherical-waves by $\delta\vec{r}_n$, scattering by t, propagating the outgoing wave back by $\delta\vec{r}_n$. G is a spherical-wave propagator which converts a set of spherical-waves at the origin to ones centered at $\delta\vec{r}_n$.

In the tensor LEED approximation, scattering paths which contain more than one scattering event from the displaced atom are not included. Neglecting these paths results in failure of the TLEED approximation for displacements larger than 0.2 to 0.4 Å.

In Chapter 8, we discuss the computation of the tensor when the LD method is used in the dynamical calculation. As background to this discussion, we outline the procedure, described in References 44 and 45, to obtain the quantities $\mid \Psi(n, \vec{k}_{in}) >$ and $< \Psi(n, \vec{k}_{out}) \mid$ from the RFS calculation. In the spherical representation, the amplitude of the wavefield around each atom in a layer is equal to

$$A^0_{j,lm} = 4\pi i \sum_{\vec{g}} B^+_{n,\vec{g}} Y^*_{lm}(\vec{g}^{\,+}) + B^-_{n,\vec{g}} Y^*_{lm}(\vec{g}^{\,-}) \tag{2.20}$$

$B^+_{n,\vec{g}}$ and $B^-_{n,\vec{g}}$ are the plane-wave amplitudes with their phases referenced to the top and bottom of layer n and are obtained by suitable propagation of the converged plane-wave amplitudes determined by RFS. However, one needs to take into account intralayer scattering. This scattering information is contained in the τ or T computed during the layer diffraction matrix calculation. With this included, $< lm \mid \Psi(n, \vec{k}_{in}) >$ is equal to the amplitude of the wavefield $A_{j,lm}$ determined by

$$A_{j,L} = \sum_{L'} t_L^{-1} \tau_{LL'} A^0_{j,L'} \tag{2.21}$$

where L represents lm. In the case of a composite layer, τ is replaced by T. $< \Psi(n, \vec{k}_{out}) \mid$ is computed using the reciprocity principle[44–46]. From time reversal invariance, we can write

$$< \Psi(n, \vec{k}_{out}) \mid lm >= \frac{-i}{A\, k_{out,z}} < lm \mid \Psi(n, -\vec{k}_{out\,\parallel}, \vec{k}_{out\,\perp}) >^* \tag{2.22}$$

The pre-factor results from the projection of the spherical-wave basis on the plane-wave basis required when the reciprocity principle is invoked. Once this is done the solution can be obtained as before for $\mid \Psi(n, \vec{k}_{in} >$. It does require an additional full-dynamical LEED calculation for an incident beam with parallel momentum $-k_{\|}$. However, with RFS this can be done very quickly as neither the atomic positions nor the energies change.

2.6 Search Techniques

A LEED structural analysis is based on the trial-and-error procedure described briefly in Section 2.1.5. The multiple scattering prevents the direct inversion of the experimental data to give the geometrical positions of the surface atoms. The flow-chart shown in Figure 2.6 and described in Section 2.1.5 represents this trial-and-error procedure. The outermost loop describes a trial-and-error search over distant surface models; because the large structural differences between the models, the ATLEED search cannot be applied. The ATLEED search addresses the second loop over trial structures which are related to a reference structure (the structure for which a full dynamical calculation has been performed). In this second loop, we test trial structures which are closely related to the reference structure. Before we begin our discussion of the search methods, we first examine the R-factors which are used to judge the fit between the computed and the experimental I-V curves.

2.6.1 R-Factors

Many different R-factor definitions have been used in LEED structure determinations,[6] and there has been no general agreement as to which is the most appropriate. The complexity of the R-factors ranges from the simple R_1 (which equals the sum, over all available experimental beams, of the energy integral over the absolute value of the theoretical minus the weighted experimental I-V curves) to the very complex Zanazzi-Jona R-factor. Each theoretical I-V curve is normalized before comparison with the corresponding experimental curve. The normalization used can either be an average over the beams or an independent normalization of each beam. In practice, the fractional order beams have, on average, large normalization constants as compared to the integer order beams. The formation of a partially ordered overlayer on the metal surface can expose additional clean or otherwise disordered areas. Because of this factor we usually normalize each beam separately; however, the normalization constants are written to disk. In additional to the

normalization, to eliminate experimental noise the experimental I-V curves were smoothed before being compared to the theoretical I-V curves. Because this smoothing changes the underlying peak shapes, the theoretical I-V curves are also smoothed in an identical fashion. In all cases, the amount of smoothing was kept to a minimum. This is important because the error bars are determined by the curvature of the R-factor values at the minimum.

This work used both the R_2-factor and the R_p-factor[47]. The R_2-factor is defined by

$$R_2 = \left(\frac{\int (I_e - cI_t)^2 dE}{\int I_e dE} \right)_{average} \tag{2.23a}$$

with

$$c = \left(\frac{\int I_e dE}{\int I_t dE} \right)_{average} \tag{2.23b}$$

The average over the I-V curves of each diffraction beam is weighted to take into account any differences in the energy ranges of the beams. The R_p-factor is defined by

$$R_p = \left(\frac{\int (Y_e - Y_t)^2 dE}{\int (Y_e + Y_t)^2 dE} \right)_{average} \tag{2.24a}$$

$$Y = \frac{L}{1 + V_{oi}^2 L^2} \tag{2.24b}$$

$$L = \frac{I'}{I} \tag{2.24c}$$

where V_{oi} is the imaginary part of the inner potential. This R-factor was designed to have high sensitivity to structural information and low sensitivity to non-structural parameters. We found this R-factor, which is the only one designed with enhanced sensitivity for specific features in the I-V curves, to be the most reliable in determining surface structures. Because of the additional complexity and the sensitivity to numerical noise, this R_p-factor is computed after interpolating the I-V curves onto a 0.25 eV grid. In addition, because the logarithmic derivatives are sensitive to low-intensity points, the I-V curves are shifted upward by 5% of the average intensity. This shift is computed prior to the structural search.

Error bars were determined by Pendry's method.[47] Pendry computes a range of R-factor values around the best-fit R-factor. This is done by considering the effect of noise on the R-factor and making a crude estimation of the amount of information in the I-V curves. The result is the following expression of the range ($\pm varR$) of R-factors:

$$varR = R_{p,best-fit} \sqrt{\frac{8V_{oi}}{\Delta E}} \tag{2.25}$$

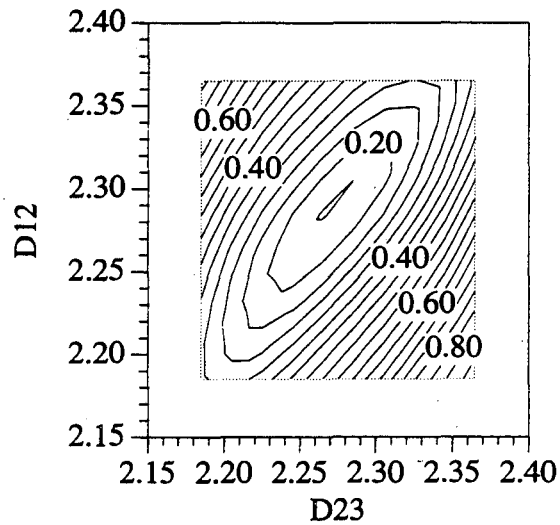

Figure 2.17: Contour plot of the R_p-factor hypersurface for clean Pt(111)-(1 × 1). In this plot, the first two interlayer spacings were varied (D_{12} and D_{23} of Figure 3.3) with all other parameters fixed. The elliptical shape of the R-factor surface is due to correlation between the two interlayer spacings.

This normally allows one to rule out all but the correct structural models tried in the outer loop of Figure 2.6. For variations of the best-fit model, i.e. changes in the interlayer spacings, one varies each parameter to compute a range of values in which the resulting R_p-factor is contained. Correlations are normally not computed; however, one can see in the R_p-factor hypersurface of Figure 2.17 that such correlations do exist. Error bars obtained by this method are normally considered to be conservative estimates.

2.6.2 Conventional LEED Analysis

To understand the great advantage that ATLEED provides, we must first discuss the conventional LEED analysis which contains only the outer loop. The required computational effort is the most apparent limitation of the conventional LEED analysis. In a full dynamical LEED calculation, the multiple-scattering problem requires summations over all multiple scattering paths between the N non-equivalent atoms in the surface. Each calculation scales as N^3 or at best as N^2. Techniques which speed up this calculation of various trial geometries require one to store many energy dependent quantities and thus are not very amiable to automatic search routines.

In the case of Pt(111), RFS[6] provides a very efficient solution to the multiple

scattering problem. It is possible, using conventional methods, to program a grid search which is very effective at finding the minimum of the R-factor hypersurface. In this type of search, the LEED intensities for all points in the grid are computed at each energy; thus, the problem scales as a hypercube of N^p dimensions, were N is the number of steps along each edge and p is the dimensionality of the cube. Figure 2.17 shows the results for the case of clean Pt(111)-(1 × 1). The eliptical shape of the R-factor surface is due to correlation between the values of D_{12} and D_{23}. A poor D_{12} can be "fixed" by a change in D_{23}.

Although this form of analysis is efficient enough for simple systems, it rapidly becomes too computationally intensive. For the Pt(111)-p(2 × 2)-O overlayer, it took approximately 5 hours (IBM RS6000 520) to do one full dynamical LEED computation using a single layer for the oxygen atom and two composite layers for two metal layers of four atoms each. Using conventional methodology to fit the interlayer spacings, buckling, and lateral expansions of the two metal layers, one needs to do a full calculation for each trial structure for each model containing a different buckling of the metal atoms. The interlayer spacings would be easily fit using RFS; and thus, would not be considered as a time constraint. Assuming that we vary each buckling and lateral displacements between -0.20 and 0.20 Å in 0.04 Å steps, we arrive at 11^4 dynamical computations at 5 hours apiece, or approximately 8 years. The use of symmetry dramatically reduces the total time for each dynamical computation by a factor of ten for this particular computation. However, a reduction of the total time to a little less than one year is still not completely satisfactory. This total time becomes even less satisfying when one considers that it may have to be repeated for each adsorption model.

It is also important to realize that this computational limitation still exists with today's computers and will not likely be solved by simply increasing computation power. It is a barrier which must be met with a theoretical approach and not brute force. TLEED coupled with an automated search algorithm provides an effective solution.

2.6.3 ATLEED Implementations

This stage of the structural search, represented by the inner loop in Figure 2.6, is basically a minimization of the R-factor with respect to the structural parameters. After one full-dynamical computation has been made, Equation 2.18 is combined with an R-factor routine to provide a function which returns R-factor values. Many search algorithms are

available and we tried several of the algorithms described in Reference 48 to minimize the R-factor value. The most effective algorithm was found to be the direction-set method which is a modification of Powell's original method. In this method the R-factor is minimized along a set of independent directions which are updated as the search proceeds. The minimization along each direction is done independently by either parabolic interpolation or by simple bracketing if the function is not found to be parabolic. The algorithm updates the directions by trying to converge on a set of so-called conjugate directions, which are defined as directions in which minimization along one does not spoil the subsequent minimizations along another. Some care must be taken that the directions do not "fold up on each other." One advantage of this method is that it does not require the numerical computation of derivatives. As one approaches the minimum, the program reduces the step size. Once the minimum has been obtained, the directions are reset and the step size increased as the search is continued. This is done to help insure that the program does not fall into a local minimum, but does not insure that the global minimum will be found.

In our structural searches, we first search over the most sensitive coordinates by keeping the highest symmetry and allowing only vertical coordinates to be optimized. The R-factor is more sensitive to vertical coordinates than to lateral coordinates, because, for normal incidence LEED data, most of the momentum transfer is normal to the surface. As the symmetry is reduced, one must average over different equivalent displacements generated by the symmetry of the surface. One must also be careful that the displacements are small enough that the location of the minimum in the R-factor hypersurface is left unchanged. This is very difficult to quantify, however, it can be solved in practice by starting the search over with a full-dynamical calculation to obtain a new reference structure and tensor. A majority of this work is concerned with the search procedure used to optimize the I-V curves.

The number of R-factor evaluations required by this search algorithm scales as cN^2 where c is approximately 10 and N is the number of parameters. For the Pt(111)-(2 × 2)-O example, N is equal to 7 structural and one 1 non-structural (the real part of the inner potential is also fit in a LEED analysis) parameters, and the R-factor evaluation takes under a second. The search then takes about 10 minutes, not one year as in the case of a conventional analysis discussed above. Even if several full-dynamical calculations are required to insure that the TLEED approximation holds for the resulting displacements, one can still complete the analysis with only several hours of computer time.

2.6.4 Other Methods and the Global Minimum

Reference 1 contains additional methods used to fit the theoretical and experimental I-V curves. Some, like the direct method,[49,50] rely on the basic foundations of TLEED. Although the relative merits of the various methods are yet to be quantified, TLEED seems to be the most efficient for optimizations as described above. There is still a need to address the outer loop in Figure 2.6. If the structure is very complex or if additional information is not available, this process becomes tedious and time consuming. In addition, our search schemes find a local not a global minimum. Because TLEED can accurately describe only a small segment of the parameter space, one cannot explore the complete space. Some progress has been made using simulated annealing,[51] however this remains too time consuming for any routine structure determination. This problem has very important practical aspects for complex surface structures with many parameters and awaits further research.

Chapter 3

Clean and Oxygen Covered Pt(111)

The objective of this work is to determine the detailed surface structure of atoms and molecules on metal surfaces using low energy electron diffraction (LEED). With the development of tensor LEED (TLEED) and other similar techniques,[1] LEED analysis has become increasingly capable of extracting detailed geometric information from experimental I-V curves. Information not only about adsorbate position, but also regarding its effect on the metal surface can be routinely determined. This effect, commonly called adsorbate-induced relaxations, shows up only when the fine details of the surface structure are investigated. As a result, when detailed relaxations of a surface structure are reported, the reliability of these fine details becomes an important issue.

In this chapter, which is based on Reference 52, we describe and compare independent dynamical LEED analyses of the Pt(111)-$p(2 \times 2)$-O system, using three optimization schemes based on different implementations of TLEED[1]. These independent dynamical LEED analyses illustrate the reliability of different approaches to LEED analysis in the similar structural results obtained with each. We have also investigated the effects of various non-structural parameters, particularly those involved in the construction of the phase shifts, on the resulting structures of the clean Pt(111) and the Pt(111)-$p(2 \times 2)$-O surfaces.

After a brief description of the experiment, this chapter is divided into three main sections. In Section 3.3, we examine different approximations in the phase shift computations and their effects on both the quality of fit between experimental and theoretical I-V

curves and the resulting structure of the clean Pt(111) surface. In Section 3.4, we report the structural results of the dynamical LEED analyses of the Pt(111)-$p(2 \times 2)$-O structure obtained by different search schemes. In Section 3.5, we describe the effect on the optimal O/Pt(111) structure of the various non-structural parameters discussed in Section 3.3 for clean Pt(111). Following these three main sections, we draw conclusions in Section 3.6.

3.1 Background

The Pt(111)-$p(2 \times 2)$-O system has been well studied using other techniques[53–55] due to the importance of Pt as a catalyst for oxidation reactions. Our sharp $p(2 \times 2)$ LEED pattern had an exceptionally large signal-to-noise ratio, which permitted the measurement of experimental I-V curves for many higher order diffraction spots. With only one O atom per unit cell (as established earlier[53–55]), different surface Pt atoms must have different O coordination. Due to this and in view of the strong chemisorption of O on Pt(111), considerable surface relaxations are expected. Correspondingly O/Pt(111) is an ideal system for use in investigating the extent to which the resulting relaxations (including interlayer spacings, buckling and lateral atomic displacements) are affected by the methodology used in the LEED analysis.

In addition, the surface geometry of clean Pt(111) has been the subject of earlier LEED investigations using R-factor analysis.[56,57] These investigations have never yielded satisfactory R-factors as compared to other clean surfaces. Because clean Pt(111) normally has an unreconstructed bulk-periodic surface, these unsatisfactory R-factor values could not be caused by neglecting structural parameters. Using I-V curves taken for clean Pt(111), we have investigated how non-structural parameters influence the LEED analysis. In particular, we have examined different parameters involved in obtaining the atomic phase shifts which describe the electron-atom scattering process. The consequences of varying these parameters on the resulting phase shifts and, in turn, on the quality of fit for both the clean surface and for the O overlayer are considered.

3.2 Experiment

The experiments were carried out in a stainless steel ultrahigh vacuum (UHV) chamber. The sample was cleaned with repeated cycles of ion bombardment and annealing

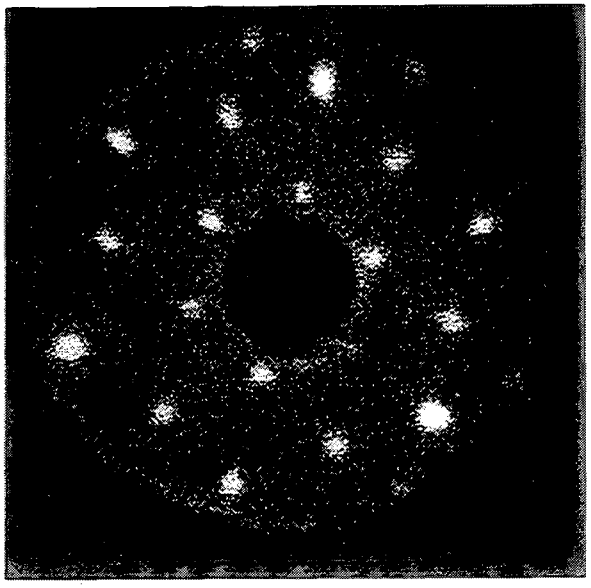

Figure 3.1: The Pt(111)-$p(2 \times 2)$-O LEED pattern at 84 eV and normal incidence.

in oxygen until no impurities could be detected by Auger electron spectroscopy (AES), and the LEED pattern of the clean surface was sharp and free of diffuse background intensities. The UHV instrumentation and sample preparations are described in Section 2.2. LEED measurements were taken with a digital LEED detector[12](see Section 2.3.2). After flashing to 1000 K, the crystal was cooled to 90 K and the I-V curves of the clean surface were measured. See Section 2.4 for additional experimental details related to the I-V curve measurements. During the measurements, sharp (1×1) LEED patterns were obtained from the Pt(111) crystal (see Figure 2.12). The (1,0), (0,1), (1,1), (2,0) and (0,2) beams were measured from 50 to 250 eV at normal incidence for a total energy range of 690 eV. In addition, the (1,0), (0,1) and (1,1) beams were measured at 300 K. These experiments were repeated several times in order to insure the reproducibility of the I-V curves. The experimental I-V curves agree well with other work[56–58] and are reproducible.

The O chemisorption phase was prepared by exposing the clean surface to 7.5 Langmuir (L) of molecular O at 270 K, followed by flashing the crystal to 300 K. This procedure resulted in the sharp (2×2) LEED pattern shown in Figure 3.1. After preparation of the O overlayer, the crystal was cooled to 90 K and the I-V curves for the $p(2 \times 2)$ LEED structure were measured from 20 to 350 eV at normal incidence. Five different LEED experiments were performed and resulted in nearly identical I-V curves. Normal incidence

was confirmed by the good visual agreement between symmetry equivalent beams. A total of five integer order, symmetry-averaged beams, the (1,0), (0,1), (1,1), (2,0) and (0,2), and nine fractional order, symmetry-averaged beams, the (1/2,0), (0,1/2), (1/2,1/2), (3/2,0), (0,3/2), (1/2,1), (1,1/2), (1/2,3/2) and (3/2,1/2), was obtained by averaging the I-V curves from the two LEED experiments having the highest signal-to-noise ratios for a cumulative energy range of 3415 eV. The total energy range of the integer order beams was 1214 eV, and that of the fractional order beams was 2201 eV.

3.3 Clean Pt(111)

The surface structure of the clean Pt(111) surface has been investigated with both dynamical LEED[56–58] and ion scattering.[59,60] Two LEED studies quantified the agreement between the experimental and theoretical I-V curves by computing reliability factors, or R-factors,[6] which represent the quality of the fit. Ion scattering experiments[59,60] support the LEED results. Adams et al.[56] found the first interlayer spacing to be possibly expanded by 0.04 ± 0.10 Å with a relatively large R_2-factor[6] of 0.16, while Hayek et al.[57] found an unrelaxed surface within 0.05 Å with a high R_p-factor[47] of 0.43. In addition, Adams et al.[56] noticed almost no change between the R_2-factor value obtained using non-relativistic phase shifts and that obtained using spin-averaged, or quasi-relativistic, phase shifts. In contrast, we observe large differences in the R-factor values obtained utilizing phase shifts computed in different ways. This prompted us to re-examine the effects of the phase shift computation not only on the structure, but also on the quality of the fit between experimental and theoretical I-V curves.

3.3.1 LEED Computations

We used the TLEED approximation combined with an automated search algorithm directed by R-factor values[1] to analyze the experimental I-V curves obtained for the clean Pt(111) surface. A brief introduction to LEED structural analysis can be found in Section 2.6. Nine phase shifts at each energy were used to describe atomic scattering within a layer. Scattering between the layers and towards the bulk was modeled using renormalized forward scattering (RFS) with up to 37 plane waves.

The phase shifts used in our LEED computations were obtained, within the muffin-tin approximation, by requiring the radial solution within the muffin-tin to smoothly match

the spherical wave solution outside the muffin-tin. The muffin-tin approximation has been found to well describe the low energy electron scattering process.[6,18] The phase shifts were computed by numerically integrating either the Schrödinger or the relativistic Dirac equation using methods outlined by Loucks.[33] The relativistic phase shifts were spin-averaged (which we call quasi-relativistic) before they were used in the LEED computation.[37] The potential utilized in the integration was obtained from atomic wave-functions computed by numerical integration of either the Dirac-Fock or Hartree-Fock equation with electron exchange treated exactly. A muffin-tin potential was then computed, as in Loucks,[32,33] after correcting the atomic charge densities for the effects of the surrounding atoms in the fcc crystal lattice. The total potential within the muffin-tin was computed by adding the coulombic potential, which resulted from the spherically symmetrized charge densities, to the exchange correlation potential determined by the local density approximation. The muffin-tin zero was set equal to zero by subtracting the constant potential due to both the coulombic and the exchange correlation potentials from the muffin-tin potential.

3.3.2 Results

Relativistic Effects

Using a muffin-tin potential obtained from the bulk Pt lattice and a muffin-tin radius of 0.95 Å, the choice of which will be discussed later, phase shifts were generated starting from either relativistic or non-relativistic atomic charge density. Although with five experimental beams measured at 90 K over an energy range of 100 to 250 eV a similar final structure is obtained using both quasi-relativistic and non-relativistic phase shifts, the quasi-relativistic phase shifts improved both the R_2-factor and the R_p-factor considerably. A smaller but significant improvement in both R-factors is observed if the experimental range is increased to 50 to 250 eV. These results are summarized in Table 3.1, and the I-V curves generated with the quasi-relativistic phase shifts are shown in Figure 3.2. A side view of this best-fit structure is shown in Figure 3.3. Using non-relativistic phase shifts, the R_2-factor is comparable to the result of 0.18 obtained by Adams et al.[56] Likewise, with non-relativistic phase shifts, the R_p-factor is in agreement with the result of 0.48 found by Hayek et al.[57]

The phase shift computation is naturally separated into two parts: determining the muffin-tin potential and dealing with scattering from each atomic sphere in the muffin-

Table 3.1: The best-fit R_p- and R_2-factor values and corresponding first interlayer relaxations (d_{12} in Å) for the clean Pt(111)-(1 × 1) surface analyzed with non-relativistic or quasi-relativistic phase shifts over two energy ranges.

	100-250 eV				50-250 eV			
	R_p	d_{12}	R_2	D_{12}	R_p	d_{12}	R_2	D_{12}
Non-Relativistic	0.34	-0.01	0.13	-0.02	0.38	-0.01	0.14	-0.01
Quasi-Relativistic	0.15	-0.01	0.126	-0.02	0.22	-0.01	0.14	-0.01

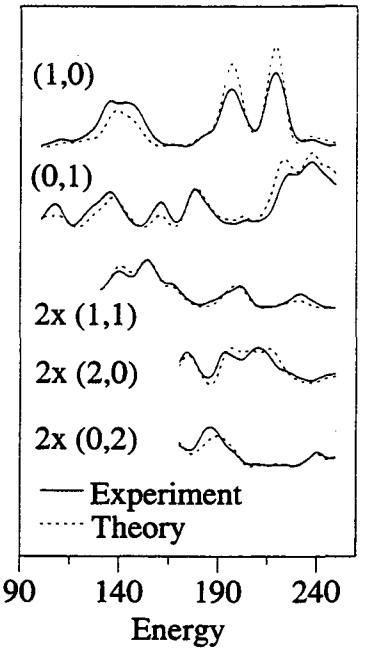

Figure 3.2: Experimental and theoretical I-V curves for the best-fit clean Pt(111)-(1 × 1) surface with an R_p-factor of 0.15. The side view of this surface is shown in Figure 3.3.

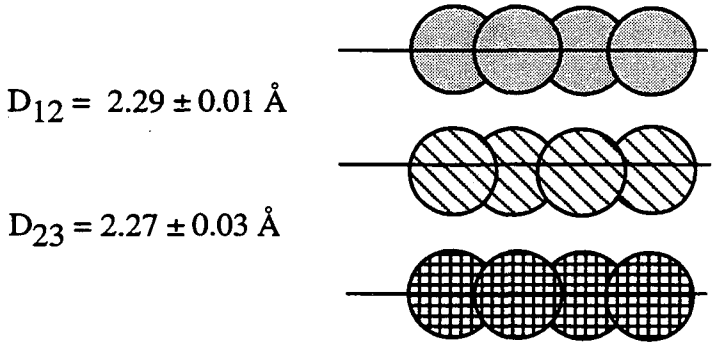

Figure 3.3: The side view of the best-fit clean Pt(111)-(1 × 1) surface with an R_p-factor of 0.15. The I-V curves for this surface are shown in Figure 3.2.

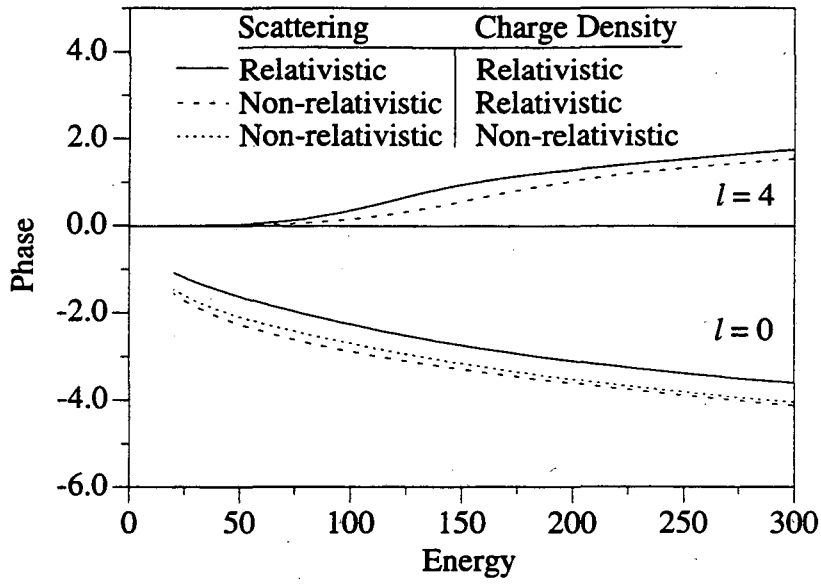

Figure 3.4: Energy dependence of the $l = 0$ and $l = 4$ phase shifts for Pt. For each l the shift was computed using relativistic or non-relativistic charge density and either relativistic or non-relativistic scattering. The solid line was computed using relativistic charge density and the Dirac equation. The dashed line was computed using relativistic charge density and the Schrödinger equation. Finally, the dotted line was computed using the non-relativistic charge density and the Schrödinger equation. Note that for $l = 4$ the dotted line lies on top of the solid line.

tin. The most important ingredient in the computation of the muffin-tin potential is the electron charge density, which is determined by a self-consistent atomic calculation.[34,35] Since relativistic effects make the potential in the atomic calculation more attractive in the core region as compared to the non-relativistic case, the self-consistent atomic charge density is pulled inward, or close to the core, thereby more effectively screening the nucleus. Therefore, the effective muffin-tin potential resulting from the relativistic charge density is weaker than that from the non-relativistic density.

Ignoring relativistic effects in the scattering portion for the moment, by numerically integrating the Schrödinger equation at each energy, we find that the phase shifts computed from the relativistic charge density lie beneath the phase shifts computed from the non-relativistic charge density. In Figure 3.4, the phase shifts for $l = 0$ computed using the relativistic charge density are shifted downward with respect to the phase shifts computed with the non-relativistic charge density. In addition, for $l = 4$, the non-relativistic phase shift computed using the relativistic charge density is also shifted downward with

respect to that computed with the non-relativistic charge density, which coincides with the spin-averaged, fully-relativistic phase shift. These downward shifts are a direct result of the weaker relativistic scattering potential which results in a smaller phase difference between incoming and outgoing spherical waves. A LEED analysis of the clean Pt(111) surface using the non-relativistic phase shifts generated from the relativistic potential results in an R_p-factor close to the fully non-relativistic R_p-factor in Table 3.1. Incorporation of relativistic effects into the scattering portion of the phase shift computations increases the strength of the scattering potential. Ignoring these effects in the phase shift computations gives rise to phase shifts which reflect an unrealistically weak atomic scatterer. The addition of relativistic effects in the scattering portion effectively increases the atomic scattering power; thus, relativistic effects produce a large upward shift of the phase shifts. This large upward shift is illustrated in Figure 3.4 for $l = 0$ and $l = 4$. At each energy, the phase shifts computed from the Dirac equation lie above the phase shifts computed from the Schrödinger equation. This effect also exists for the non-relativistic phase shifts computed with a non-relativistic muffin-tin potential. However, for $l = 4$, the non-relativistic phase shifts computed using the non-relativistic charge density are almost identical to spin-averaged, fully-relativistic phase shifts, as can be seen in Figure 3.4. This is due to the fact that the inner core region, where relativistic effects are most important, is probed progressively less by the scattered electrons with increasing values of l. An important point is illustrated in Figure 3.4: the non-relativistic phase shifts computed using the relativistic charge density lie beneath both the spin-averaged, fully- relativistic and the non-relativistic phase shifts computed with the non-relativistic charge density. This is due to unrealistic screening of the nuclear charge. Inclusion of relativistic effects in only the atomic charge density portion of the computations and not the scattering portion yields a poorer R-factor than do fully non-relativistic computations. A LEED analysis of the clean Pt(111) surface using quasi-relativistic phase shifts produced a low R_p-factor value of 0.15. Relativistic effects must be included in the scattering portion of the phase shift computations in order to obtain an improvement in the quality of fit between theory and experiment.

Although the introduction of relativistic effects improved the R-factor values, these effects have only a small influence on the final structure of the clean Pt(111) surface. The features, or peaks and valleys, of an I-V curve are caused by interference between different scattering paths. In the single scattering, or kinematic, limit the relative values of the atomic phase shifts are important. Because of this, one would expect the R-factor hypersur-

face to depend strongly on the relative values–not the absolute values–of the phase shifts. Therefore, the resulting best-fit surface structure is not usually affected by this introduction of relativistic effects. However, the Pt(111)-$p(2 \times 2)$-O system is a different case. In this system, even in the single scattering limit, the differences in the atomic phase shifts between O and Pt influence scattering paths between these atoms. This will be discussed in more detail later.

The addition of experimental data between 50 and 100 eV caused the R_p-factor value to increase from 0.15 to 0.22. Though the addition of these data increased the energy range by only 18%, giving a cumulative energy range of 560 eV, it increased the R_p-factor by 50%. One possible explanation for this large increase in the R-factor could lie in the neglect of spin in the LEED computations. By spin-averaging the phase shifts, one assumes that the LEED I-V curves reflect a surface in which the LEED electron feels a spin-averaged interaction with the atomic scatterers. This is certainly not true even in the single scattering, or kinematic, limit where interference exists between the direct scattered wave and the spin-flip wave.[61,62] Examining the phase shifts between 50 and 100eV, one sees large differences between the spin-up ($j = l + 1/2$) and spin-down ($j = l - 1/2$) phase shifts. Figure 3.5 shows the resulting I-V curves for the (1,0) and (0,1) beams computed using the spin-up, the spin-down, and the spin-averaged, or quasi-relativistic, phase shifts. The large differences between these I-V curves in the low energy range support the suspicion that the neglect of the effect of spin in the LEED computations is partly responsible for the discrepancy between experimental and theoretical I-V curves in the energy range between 50 and 100 eV, which was not fitted in the final structural analysis.

Role of the Muffin-Tin Radius

Another factor in the phase shift computations is the choice of the muffin-tin radius. For LEED computations in which scattering occurs primarily in the atomic cores, it is not obvious that the muffin-tin radius should equal one half the interatomic distance, as is the case in lower energy band structure computations in which the crystal potential is solved self-consistently. Examination of the charge density for Pt shows the bulk of the charge density to be within 0.95 Å from the origin. Table 3.2 shows the optimal first interlayer spacing and both the R_2- and R_p-factor values obtained with phase shifts generated from different muffin-tin radii. In this table, one can see a slow decrease in the R-factor value with

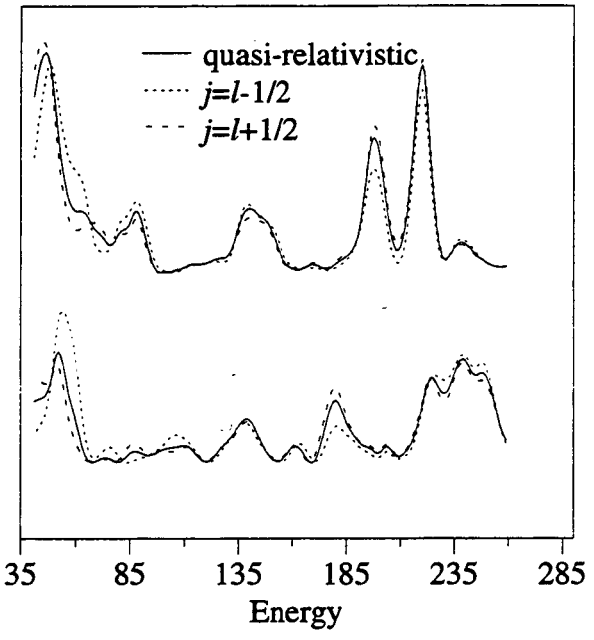

Figure 3.5: Theoretical I-V curves for the (1,0) and (0,1) beams of the ideally terminated clean Pt(111)-(1 × 1) surface. Both beams are computed using only the "spin-up," "spin-down," or quasi-relativistic (spin-averaged) phase shifts.

Table 3.2: Variation in the R-factor values when the first interlayer spacing (d_{12} in Å) and the real part of the inner potential (V_o in eV) for the clean Pt(111) surface are optimized with relativistic phase shifts generated from muffin-tin potentials computed with different muffin-tin radii for the Pt atoms. Independent fitting has been done for each R-factor.

Radius	R_p	d_{12}	V_o	R_2	d_{12}	V_o
1.38	0.18	-0.03	7.5	0.06	-0.05	6.8
1.16	0.18	-0.03	8.5	0.06	-0.04	8.0
0.95	0.15	-0.02	10.5	0.06	-0.03	10.4
0.74	0.30	-0.02	14.2	0.13	-0.02	15.7

Table 3.3: R_2- and R_p-factor values and the real part of the inner potential, for theoretical I-V curves computed for the Pt(111)-(1 × 1) surface with a muffin-tin radius of 1.38 Å obtained with relativistic phase shifts generated from muffin-tin potentials computed with different muffin-tin radii for the Pt atoms. Independent fitting is done for each R-factor. Because the "experimental" I-V curves were generated using a muffin-tin radius of 1.38 Å the resulting R-factors must be 0.00.

Radius	R_p	V_o	R_2	V_o
1.28	0.00	10.0	0.00	10.0
1.16	0.02	12.0	0.00	11.0
0.95	0.09	13.2	0.04	13.0
0.74	0.38	16.4	0.20	16.6

decreasing radius, followed by a rapid increase. In addition, correlation between the inner potential and the muffin-tin radius is evident. This is due to the displacement of more charge density from the muffin-tin spheres into the flat region as the muffin-tin radius becomes smaller. Possibly due to the relative insensitivity of the R_p-factor to absolute intensities in the I-V curves, we find that the variation of the first interlayer spacing is smaller for the R_p-factor than for the R_2-factor. A computer experiment designed to quantify the effective size of the computed atomic scattering potential shows that most of the scattering is contained within 0.95 Å from the origin. R_2- and R_p-factor values of the fit between I-V curves generated with a muffin-tin radius of 1.38 Å (one half the interatomic distance) and I- V curves generated with a muffin-tin radius of 1.38 to 0.74 Å show a rapid rise only when the muffin-tin radius is reduced below 0.95 Å (see Table 3.3). This supports the assumption that the scattered electron at typical LEED energies effectively feels the atomic charge density only out to about 0.95 Å. By increasing the muffin-tin radius, one adds charge density which is possibly inaccurate because the muffin-tin potential was not solved self-consistently. In a LEED computation, this charge density is better described by a constant, the real part of the inner-potential, which is then fit in the analysis. An additional important benefit of reducing the muffin-tin radius is a decrease in the number of phase shifts required in the LEED computations. The computational time decreases proportional to the sixth power of the number of phase shifts. The muffin-tin radius should be viewed as an adjustable non-structural parameter in the LEED analysis, and we have found that a muffin-tin radius which excludes the valence charge density results in an improved R-factor value for other metals in addition to Pt (Ni and Rh for example).

The Effect of Other Parameters

The resulting structure and R-factor were found to be relatively insensitive to the other non-structural parameters: the Debye temperature (Θ_D), the imaginary part of the inner potential (V_{oi}), and the muffin-tin statistical exchange coefficient (α). Θ_D and V_{oi} were found to be the same as in Reference 56. Varying α within a reasonable range of 0.5 to 0.9 results in only small changes in the R_p-factor value. The optimal α value of 0.72 is similar to that determined in atomic structure computations for Pt[63]. The small effect of this parameter contrasts with findings from work done on the Mo(100) surface[64] but is in agreement with results from the clean Cu(100) and Ag(111) surfaces.[65]

Finally, we have examined the influence on the final structure of smoothing the experimental I-V curves. The effect of smoothing was quantified by examining the resulting error bars given by Pendry's method.[47] Because Pendry's method depends both on the overall R-factor and on R-factor sensitivity to variation of the coordinate, an optimal amount of smoothing can be found by minimizing the error bar of a coordinate vs. the amount of smoothing. As smoothing is increased, experimental noise is removed, thus reducing the overall R-factor. However, if it is increased until information is lost from the I-V curves, R-factor sensitivity to changes in a coordinate will be indirectly decreased. By minimizing the error bars vs. amount of smoothing, we can decrease the amount of information lost and lower the final R-factor. For our experimental clean Pt(111) I-V curves, we find that one initial three-point smoothing of the experimental I-V curves on a 2 eV grid followed by one additional smoothing of both the experimental and theoretical I-V curves, after interpolating onto a common 0.25 eV energy grid, minimizes the R_p-factor value and maximizes the curvature of the R-factor vs. the first layer distance.

3.3.3 Conclusions

The identification of the relative importance of various factors in the phase shift computations establishes a foundation which can be applied to different systems. A detailed examination of the scattering potential in our study of this system leads to a large improvement in agreement between theoretical and experimental I-V curves; the agreement represents a 50% improvement over older LEED results.[56,57] In addition, the averaging of spin-dependent phase shifts (as usually practiced) to correctly model the scattering properties is brought into question for the low energy range between 50 and 100 eV for Pt.

This limitation of spin-averaged, or quasi-relativistic, phase shifts for Pt is supported by the excellent agreement in both peak position and height obtained for the clean Ni(111) I-V curves below 100 eV[66] (see Figure 6.5). Unfortunately, fully relativistic LEED analysis has not been applied to intensity-only Pt(111) I-V curves, but only to spin polarization experiments[67]. However, the R-factor improvement for clean Pt(111) using the optimized spin-averaged phase shifts increases our confidence in the resulting clean surface structure and carries over to the analysis of overlayers on this surface.

I-V analysis of the clean surface shows excellent agreement with other experimental results.[57–60] We estimate the error bars using Pendry's method.[47] The first and second interlayer spacings of the clean Pt(111) surface were determined to be 2.29 ± 0.01 and 2.27 ± 0.03 Å, respectively, with an R_p-factor of 0.15. This corresponds to a 0.03 ± 0.01 Å expansion of the first metal layer spacing of the ideally terminated, clean Pt(111) surface. I-V analysis of the I-V curves measured at 300 K gives identical conclusions. Within its error bars, the second interlayer spacing of the clean Pt surface agrees with the bulk value of 2.265 Å. It is plausible that the reorganization of electronic charge density at the surface is such that it is energetically more favorable to weaken the interlayer bonding in order to strengthen the intralayer bonding. If this is true, then it is quite possible that it would lead to both an expansion of the interlayer distance and an increase in surface stress. An examination of the computed surface stresses of the Ir(111), Pt(111) and Au(111) surfaces shows they are much greater than those of the equivalent $3d$ metals,[68] which have a small contraction of the first interlayer spacing. The same surface forces which are also believed to cause the high temperature reconstruction of the Pt(111) surface[68,69] seen with X-ray diffraction[7] and scanning tunneling microscopy,[70] may explain the anomalous expansion of the clean Pt(111) surface.

3.4 Pt(111)-$p(2 \times 2)$-O: Structural Analysis

In this section, the structural results of the Pt(111)-$p(2\times2)$-O system are discussed. First we describe the computational details of the LEED calculations. This is followed by a description of a coarse search over the high symmetry adsorption sites using both TLEED and conventional methods. Next, the surface relaxations of the first two metal layers for the best model found in the coarse search determined with three different search schemes (a regular grid search, an automated search, and a direct method) are compared. Opti-

mization of non-structural parameters relating to the O/Pt(111) system will be discussed in Section 3.5.

3.4.1 LEED Computations

The dynamical LEED computations and the search schemes used in the LEED analyses of the Pt(111)-$p(2 \times 2)$-O structure are described in Section 2.6. Three different search schemes were used in the analyses. The first search scheme among our different approaches used TLEED to explore relaxations on a regular grid of displacement values. The second scheme combined TLEED with an automated optimization algorithm.[1] The third scheme used a direct method based on TLEED in which a system of non-linear equations was solved iteratively for displacement parameters.[49,50] All analyses in this section used the same Pt and O phase shifts. A Debye temperature of 230 K was used for the Pt atoms ($\langle r^2 \rangle = 0.01$ Å^2), implying a Debye temperature of 800 K for the O atoms, in order to match the vibrational amplitude of the O atoms to that of the Pt surface. The first and third search schemes used an imaginary inner potential of -6 eV and 11 phase shifts, while the second used -5 eV and 9 phase shifts. The first and third schemes used layer doubling with up to 200 beams to compute the total reflectivity of the surface. A 3 eV grid was used for calculating the theoretical I-V curves. Both the experimental and theoretical I-V curves were interpolated onto a 0.5 eV grid. The second search scheme used up to 200 beams between layers stacked by RFS. Theoretical I-V curves for this scheme were computed on a 4 eV grid and interpolated onto a 0.25 eV grid along with symmetry-averaged experimental I-V curves. Error bars for the first and second search schemes were estimated using Pendry's method.[47]

3.4.2 Results

The Pt(111)-$p(2 \times 2)$-O system has been well studied using other techniques.[53–55] High resolution electron loss spectroscopy (HREELS)[53] of the $p(2 \times 2)$ overlayer shows only one vibrational peak corresponding to the O-Pt vibration. In addition, results from transmission channeling of protons through the crystal detected by a nuclear reaction with the adsorbed O support both the fcc site adsorption and 0.25 ML coverage.[53] Detailed relaxations of the metal surface due to O adsorption have not been reported. Given only one O atom in the $p(2 \times 2)$ unit cell, four high symmetry adsorption sites are possible: top,

Table 3.4: The resulting R_p-factor values for the best-fit structure of each adsorption site and for various degrees of freedom. The "Bulk" heading refers to automated TLEED searches (scheme 2) in which only the O height above the ideally terminated substrate was varied. "Planar" refers to additional automated TLEED searches (scheme 2) which varied only vertical displacements of the O and the first two metal layers. "Buckled" refers to all vertical relaxations in the first two metal layers allowed by the local symmetry of the site and determined by automated TLEED searches (scheme 2). Finally, "Conventional" refers to a grid search that allowed only vertical displacements of the O and the first two metal layers by conventional LEED methods. "Conventional" is similar to "Planar," but includes a search grid and a larger experimental data base.

Site	Bulk	Planar	Buckled	Conventional
fcc-hollow	0.40	0.40	0.19	0.49
hcp-hollow	0.58	0.54	0.48	0.75
top	0.66	0.65	0.57	0.64
bridge	0.55	0.50	0.45	0.68

bridge, fcc-hollow and hcp-hollow.

We determined the adsorption site by a conventional analysis and by a TLEED analysis coupled with an automated search algorithm, both restricted to the high symmetry sites. The conventional analysis, using all 14 non-equivalent experimental I-V curves from 30 to 350 eV, i.e. a 3355 eV total energy range, optimized O heights and the first two interlayer spacings on a regular grid for each model. The R_p-factors obtained for each adsorption site are shown in Table 3.4 under the heading "Conventional." In the analysis using TLEED combined with an automated search algorithm an energy range of 30 to 260 eV, i.e. a 2579 eV total energy range, was used for the fcc-, hcp- and top-site models. For the bridge-site model the initial TLEED search was restricted to the (1,0), (0,1), (1,1), (1/2,0), (0,1/2) and (1/2,1/2) beams, giving an energy range of 100 to 250 eV for a total range of 882 eV. These beams have the lowest experimental noise and the largest total energy range. For each high symmetry site, automated searches were carried out over trial geometries with varying degrees of freedom (see Table 3.4 and Figures 3.6 and 3.7). The fcc-hollow site model clearly yields the best fit to the experimental data. Figure 3.8 illustrates the improvements in the I-V curves of the fcc-hollow site model with increasing degrees of freedom. The resulting R_p-factors for the other sites were obtained from structures which have large, possibly unrealistic displacements from the reference structures. Due to the growing inaccuracy of the TLEED approximation for larger displacements, the R_p-factor

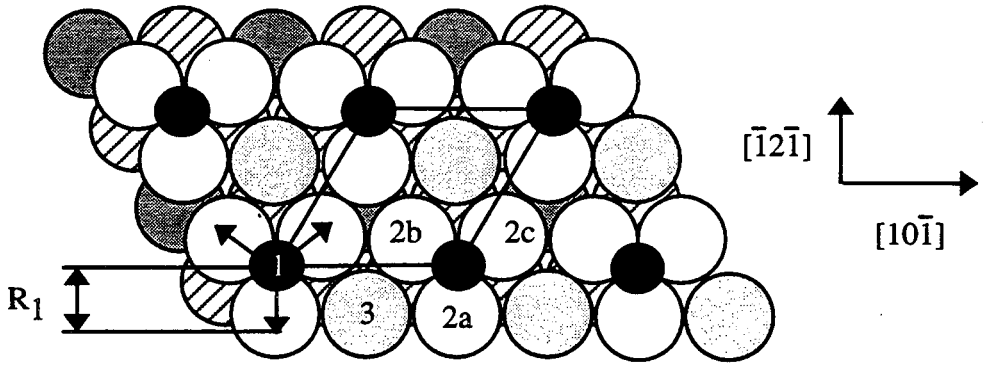

Figure 3.6: Top view of the Pt(111)-$p(2 \times 2)$-O structure. Geometrical parameters are labeled. The parameter which characterizes the second layer lateral expansion of the triangle of three metal atoms directly below the O (R_2) is not shown. Inequivalent atoms are shaded differently and numbered; the numbering corresponds to that in Table 3.6. The unit cell is outlined.

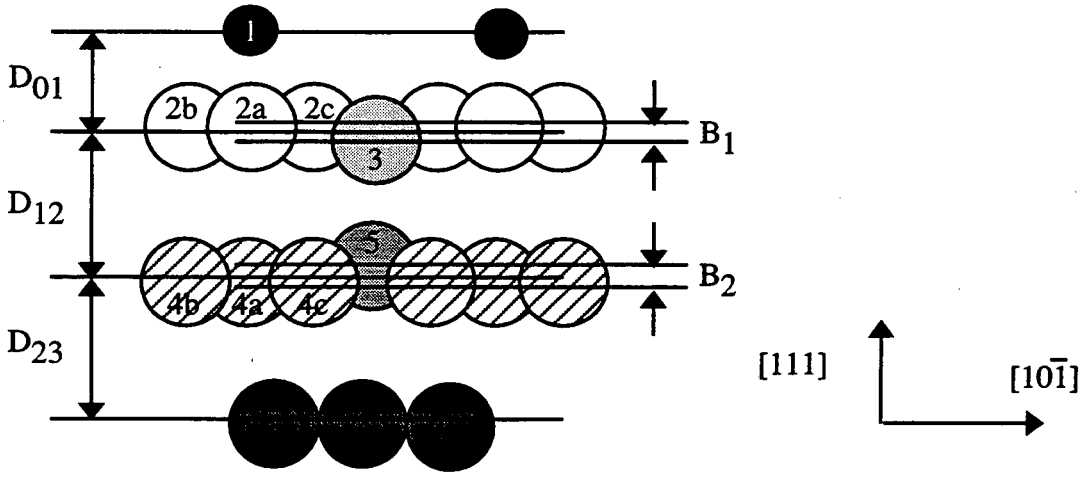

Figure 3.7: Side view of the Pt(111)-$p(2 \times 2)$-O structure. Geometrical parameters are labeled. Inequivalent atoms are shaded differently and numbered; the numbering corresponds to that in Table 3.6.

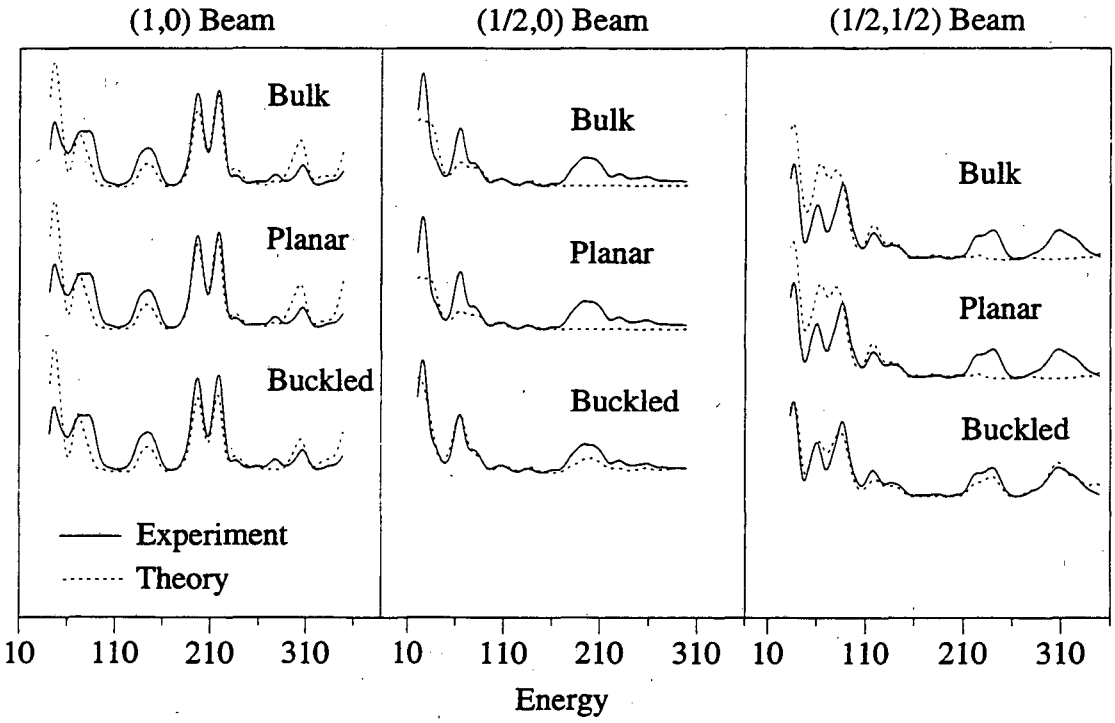

Figure 3.8: Improvements in the Pt(111)-$p(2 \times 2)$-O I-V curves for the fcc-hollow site model with increasing degrees of freedom. By comparing the I-V curves of the "Planar" model with those of the "Buckled" model, one can clearly see the improvement of the fractional order beams, particularly in the higher energy region.

does not reflect the true R_p-factor value of the resulting structure. For example, the bridge site model has an R_p-factor of 0.45 with a large and unrealistic upward displacement of the O atom of 1.6 Å. In this case, a final R_p-factor value of 0.55 is obtained for the bridge site when the first two metal layers are allowed to relax and the O atom is kept fixed at a reasonable distance above the surface.

In both coarse analyses, Pendry's method[47] was used to rule out all sites other than the fcc-hollow. Note that buckling of the metal layers, which is responsible for the considerably lower R_p-factors of the TLEED analysis, was not needed to differentiate between the various possible adsorption sites. Using the best-fit fcc-site structure obtained by the conventional analysis, the normal incidence of the experimental data was verified by computing the R_p-factor values for an incident angle up to 1.0° from normal in the mirror plane. The lowest R_p-factor was obtained for normal incidence and varied by 0.1 over the whole range of angles.

The structure resulting from the initial analysis was used as a starting point for further refinement using the three different schemes. The automated TLEED method (scheme 2) iterated the structural search starting from new reference structures until the resulting structure was within a 0.01 Å radius of the last reference structure, thus eliminating any error caused by the TLEED approximation. We find that iteration, and thus recomputation of the reference structure, is imperative to minimize the errors induced by the TLEED approximation, since they can affect the final structure. Two iterations involving two new reference structures were required to obtain convergence within 0.01 Å. The maximum difference between the initial and final structures after two iterations was 0.02 Å in the second interlayer spacing. The TLEED approximation coupled with a grid search (scheme 1) yielded consistent results. In this analysis the whole available experimental data set, up to 250 eV, was used. A similar structure was obtained by the direct method (scheme 3) using the energy range from 30 to 250 eV. Deviations in the results from the different schemes are restricted to below 0.02 Å for layer distances and 0.06 Å for lateral distances, to which the R_p-factor was less sensitive because of normal incidence data. All parameters, illustrated in Figures 3.6 and 3.7, were always within the error margins.

The three schemes involved searches using models with varying degrees of relaxation. The model (see Figures 3.6 and 3.7) which contains only relaxations consistent with the three-fold rotational axis and the mirror plane symmetry ($p3m1$) of the fcc-hollow site was examined first. Other structural models, in which either the mirror plane was broken

by allowing the triangle of three Pt atoms bonded to the O atom to rotate in-plane ($p3$-symmetry) or the rotational symmetry was broken by allowing two of three Pt atoms bonded to the O atom to move together and the third separately, were also considered. Symmetry in the LEED pattern is regained by averaging beam intensities over the resulting domains. The small decrease in the R_p-factor value with an increasing number of parameters does not allow one to distinguish between these three different models.

The best-fit fcc hollow site structure with lateral relaxations and $p3m1$ symmetry determined by the automated search (scheme 1) has the same number of parameters as does the grid-refined structure (scheme 2). A quantitative comparison of the resulting features shows similar adsorbate-induced relaxations of the metal surface. In both structures, there is an expansion followed by a contraction of the metal-metal interlayer spacings (defined as the distance between the centers of mass of two layers). The buckling of the first and second metal layers does not agree as well, although both structures show the same trend, and the displacements are within the stated error bars. It is important to remember that these structures were obtained using not only different amounts of experimental data and different computational parameters, but also dissimilar search schemes. The agreement of lateral displacements is also good. Comparing the R-factors of two structures obtained by relaxing the mirror plane and restricting the search to vertical displacements only, we find that the vertical displacements are relatively insensitive to the lateral displacements. Due to the normal incidence of the LEED data, it is difficult to distinguish between models which differ only by lateral displacements. This difficulty is evident in the maximum variance of 0.02 between the R_p-factor values obtained with the three different levels of relaxation, as well as in the large error bars for the lateral displacements. Figure 3.9 shows the differences between the plots of the R_p-factor vs. coordinate obtained by schemes 1 and 2 for the first metal-metal interlayer spacing and the lateral expansion of the triangle of three Pt atoms directly below the O.

3.4.3 Conclusions

Detailed LEED analyses of the Pt(111)- $p(2\times2)$-O system carried out with different search schemes arrive at a similar final structure. Three different degrees of freedom ranging from no lateral displacements to displacements which break the rotational symmetry have insignificantly different R_p-factor values. For the final structure, we have chosen to accept

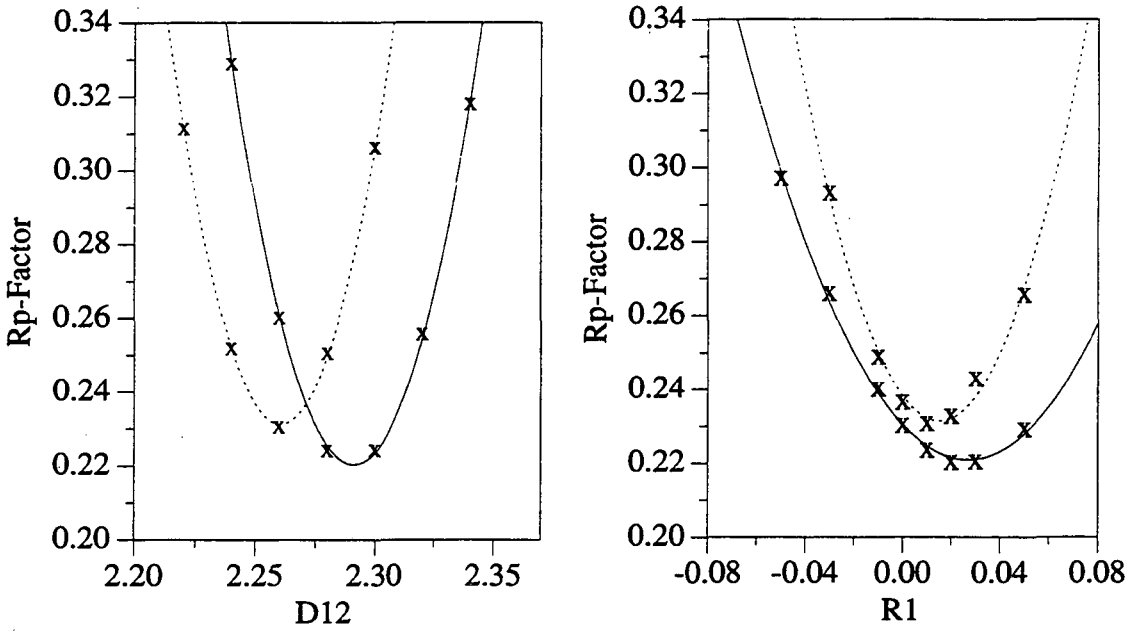

Figure 3.9: R_p-factor vs. coordinate plots obtained from scheme 1 (—) and scheme 2 (···). D_{12} is the first metal-metal interlayer spacing and R_1 is the expansion of the triangle of three Pt atoms directly below the O. Notice the low sensitivity of the R_p-factor to the lateral expansion of the triangle of three metal atoms directly bonded to the O (coordinate R_1 in Figure 3.6) due to normal incidence experimental data.

a model containing lateral displacements consistent with the three-fold rotational axis and the mirror plane symmetry ($p3m1$) of the fcc-hollow site. The reliability of our relaxed fcc-site model for the Pt(111)-$p(2 \times 2)$-O system is illustrated through its reproducibility using three different schemes of structural analysis. Reliability is also assessed by the assignment of error bars. Differences between the fcc-site structures obtained by these LEED analyses are consistent within error bars obtained by Pendry's method.[47]

3.5 Pt(111)-$p(2 \times 2)$-O: Non-structural Parameters

In the structural analysis, we assumed that non-structural parameters have little effect on the resulting structure, as in the case of the clean Pt(111) surface. In this section, we examine the effects of various non-structural parameters on the best-fit structure found by the three optimization schemes. We investigated the changes caused by both the muffin-tin potential and relativistic effects in the phase shift computation. In addition, changes in the final structure caused by varying both the total energy range and the ratio of fractional to integer order beams in the experimental I-V curves used in the R-factor computation are reported. Finally, the effects of smoothing on both the structure and the error bars are discussed. In this way, we quantify the effects of the non-structural parameters on the structure.

3.5.1 Phase Shifts and the Muffin-Tin Potential

The phase shifts used in the three structural optimization schemes were obtained using standard procedures.[6] To examine the effect of the phase shifts on the resulting structure, additional phase shifts were computed using a muffin-tin potential computed from a slab. In this slab, the atomic O potential was arranged in a $p(2 \times 2)$ overlayer and then placed on top of two (1×1) Pt layers. The muffin-tin potential was computed and the zero of this potential was adjusted to match the value found from an fcc Pt crystal. The muffin-tin zero of this slab was then offset to match the value obtained using a Pt fcc crystal and the muffin-tin radius of the O atom was chosen so the potential at this radius was the same as that at the Pt muffin-tin radius. The Pt phase shifts computed in this way were found to be almost identical to the phase shifts obtained from the bulk crystal and were virtually layer independent. It is possible that the reduction of the Pt muffin-tin radius to 0.95 Å is responsible for the insensitivity of the Pt phase shifts to the surrounding

environment.

LEED computations for the Pt(111)-$p(2\times2)$-O system were carried out to examine the effects of the muffin-tin radii of the O and Pt atoms used in the phase shift calculations on both the resulting structures and R-factor values. Using the (1,0), (0,1), (1,1), (1/2,0), (0,1/2) and (1/2,1/2) beams from 100 to 250 eV, which are found to have the highest signal-to-noise ratio experimentally, we find that a Pt muffin-tin radius of 0.95 Å gives an optimal R_p-factor. The O muffin-tin radius of 0.66 Å was chosen so that the potential at this radius was identical to that at the Pt muffin-tin radius. Adjustment of the O muffin-tin radius independently of the Pt muffin-tin radius was found to have little effect on the optimal R_p-factor. In addition, varying the Pt muffin-tin radius from 0.95 Å to 1.38 Å and the O radius from 0.50 Å to 0.90 Å had little influence on the resulting structure. The best-fit Pt muffin-tin radius and the reduction of 0.02 in the overall R_p-factor is in agreement with the result found for clean Pt(111). However, the R_p-factor has lower sensitivity to the muffin-tin radius, as compared to the clean surface; this is most likely due to greater experimental noise. If the optimization is repeated using all available experimental beams, one finds very little change in the R_p-factor value. In addition, the reduction of the Pt muffin-tin radius greatly reduces the number of phase shifts required in the LEED computation. We find that it is possible to generate theoretical I-V curves up to 350 eV using only nine phase shifts ($l_{max}=8$) with a great reduction in the amount of computer time. Using touching spheres, i.e. a muffin-tin radius of 1.38 Å for Pt, eleven phase shifts were required at 350 eV.

The inclusion of relativistic effects in the phase shift calculations has interesting consequences for the Pt(111)-$p(2\times2)$-O system. When relativistic effects are included, the O phase shifts are not affected, due to the low atomic number of O, while the Pt phase shifts are shifted upward as explained in Section 3.3. Thus, the O position changes in order to compensate for the changing Pt phase shifts. We find that the O height is increased by 0.04 Å. Although the surface buckling and the interlayer spacing for the metal are only affected to a small degree, this represents a large systematic error. Correct inclusion of relativistic effects is necessary in the case of a light element adsorbed on a relativistic metal surface.

Table 3.5: Error bars computed using Pendry's method[47] with either the fractional order, integer order, or both beam sets. Notice the low sensitivity of the integer order beams to the surface buckling. The geometrical parameters are illustrated in Figures 3.6 and 3.7.

Parameter	Error Bars		
	R_p-Both	R_p-Fractional	R_p-Integer
D_{01}	±0.02	±0.02	±0.05
D_{12}	±0.02	±0.02	±0.02
D_{23}	±0.03	±0.03	±0.03
B_1	±0.03	±0.03	$\rangle\pm0.1$
B_2	±0.04	±0.04	$\rangle\pm0.1$
R_1	±0.03	±0.03	$\rangle\pm0.1$
R_2	±0.04	±0.04	$\rangle\pm0.1$

3.5.2 Additional Factors

In determining the relaxation of the surface, one important parameter is the ratio of two energy ranges: that of the fractional order beams to that of integer order beams. This importance is due to the greater sensitivity of fractional order beams to the surface relaxation than of integer order beams. This sensitivity is clearly illustrated in Table 3.5. Shown in this table are the error bars computed with Pendry's method[47] for both the integer and fractional, only the integer, or only the fractional order beams. The large differences in the error bars shown in Table 3.5 are a direct result of the buckled atoms' contributions to the intensities of fractional order beams. By comparing the I-V curves of the non-relaxed model with those of the buckled model (Figure 3.8), one can clearly see the improvement of the fractional order beams, particularly in the higher energy region. The stronger scattering power of the buckled Pt atoms with respect to that of the O atom results in increased intensity in the fractional order beams relative to that which would normally be expected from the O atoms alone.

In addition to the importance of the ratio of fractional to integer order beams, we find that the resulting structure is relatively insensitive to the addition of higher order beams. The structure obtained using the (1,0), (0,1), (1,1), (1/2,0), (0,1/2) and (1/2,1/2) beams is virtually identical to the structure obtained using all 14 nonequivalent beams, even though the energy range is increased threefold. Also, error bars assigned with Pendry's method[47] are directly dependent on the curvature of the plot of R_p-factor vs. coordinate and inversely dependent on the square root of the cumulative energy range. Because of

this, our error bars, obtained with Pendry's method, proved insensitive to the addition of relatively noisy higher order beams. This observation supports the value of using a high quality experimental data set in the structural search, as opposed to a larger set that includes regions of greater experimental uncertainty.

As a last refinement we optimized the imaginary part of the inner potential and the surface Debye temperature of the Pt and O atoms using all 14 experimental beams from 30 to 350 eV. The optimal Debye temperature for the Pt atoms was found to be the same as the value for the clean surface. We find a small improvement in the overall R-factor when the Debye temperature of the O atoms is reduced by a factor of 2, which corresponds to an rms vibration amplitude about 2 times greater than that found for the Pt atoms. The optimal imaginary part of the inner potential was found to be -5.5 eV. However, these refinements resulted in very little (less than 0.01 Å) change in the final structure.

3.5.3 The Final Structure

The final structure obtained after including these non-structural refinements has O atoms adsorbed in fcc hollow sites. Details of this final structure can be found in Table 3.6, and a comparison of final theoretical and experimental I-V curves in Figure 3.10. We find the O atoms induce a buckling (see Figure 3.7 for the relative displacements of the metal atoms within the layer) of 0.07 ± 0.03 and 0.10 ± 0.04 Å in the first and second metal layers, respectively. In addition, oxygen induces a probable expansion of 0.01 Å in the first metal-metal interlayer spacing and a possible small contraction of 0.02 Å in the second. A metal-oxygen bond length of 2.02 Å was found. Lateral displacements consistent with the three- fold rotational and mirror plane symmetries yield a possible small lateral expansion of the triangle of three metal atoms bonded to the O. This expansion is within error bars of the bulk positions.

3.5.4 Conclusions

We have examined the effect of various non-structural parameters on the best-fit Pt(111)-$p(2 \times 2)$-O structure. We find that details in the construction of the muffin-tin potential generated from a slab computation do not influence the resulting structure. Although the construction of the muffin-tin potential does not influence the structure markedly, we find that one must use the correct relativistic treatment of the phase shifts in the case of

Table 3.6: Optimal atomic coordinates (in Å) for the best-fit Pt(111)-$p(2 \times 2)$-O fcc-hollow site model after the structural and non-structural optimization. X is defined as positive into the surface. Y and Z are coordinates parallel to the surface. Error bars are given for each set of equivalent atoms.

Atom	X	Y	Z
1 O	0.00 ± 0.02	0.00	0.00
2a Pt	1.19 ± 0.02	0.00	1.63 ± 0.03
2b Pt	1.19	1.41	-0.82
2c Pt	1.19	-1.41	-0.82
3 Pt	1.26 ± 0.03	0.00	-3.20
4 Pt	3.41 ± 0.04	2.77	-1.60
5a Pt	3.51 ± 0.02	0.00	-1.60 ± 0.04
5b Pt	3.51	1.38	0.80
5c Pt	3.51	-1.38	0.80
Bulk repeat vector			
	2.2650	0.0000	1.6016
$2D$ repeat vectors			
		2.7740	4.8048
		2.7740	-4.8048

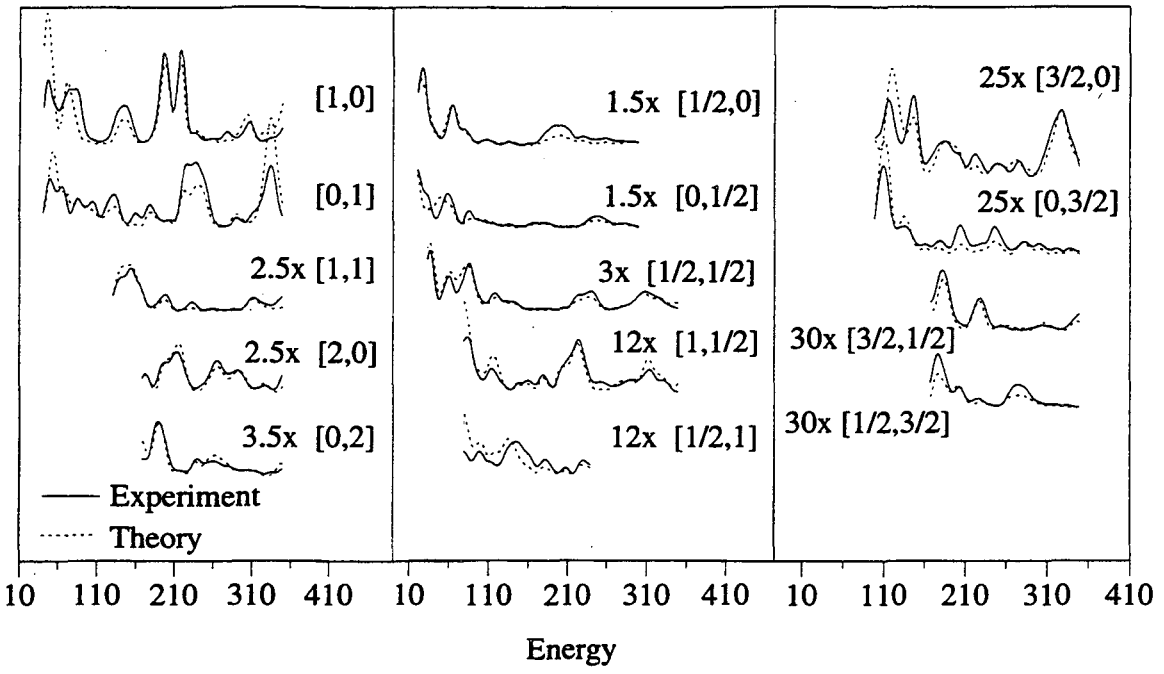

Figure 3.10: I-V curves of the final best-fit Pt(111)-$p(2 \times 2)$-O structure with an R_p-factor of 0.18.

a light element on a relativistic, or high Z, metal surface. Failure to do so will result in a systematic increase in the overlayer's bond length to the metal surface. Finally, we find that the Debye temperature has little effect and the experimental beam selection is more important than the total energy range.

3.6 Summary

LEED I-V analyses of the clean Pt(111) surface show excellent structural agreement with earlier experimental results.[56–60] A detailed study of the scattering potential led to a large improvement in agreement between theoretical and experimental I-V curves as compared to previous LEED studies[56,57] and, correspondingly, a considerable reduction of the error bars. The first and second interlayer spacings of the Pt(111) clean surface were determined to be 2.29 ± 0.01 and 2.27 ± 0.03 Å, respectively, with an R_p-factor of 0.15. This corresponds to a 0.03 ± 0.01 Å expansion of the first metal-metal interlayer spacing of the ideally terminated, clean Pt(111) surface. Within its error bars, the second interlayer spacing of the clean Pt surface agrees with the bulk value of 2.265 Å. Due to the gen-

eral trend of contraction for clean metal surfaces, the question remains as to the cause of this expansion. Possibly, the lateral surface stress is offset by increased electron density or bonding between surface atoms, leading to a weakening of interlayer bonding and therefore an expansion. In addition, the use of spin-averaged phase shifts to model the scattering properties is in question for the low energy range between 50 to 100 eV. Because of this, the energy range between 50 to 100 eV was not used in the final structural analysis. The limitation of using spin-averaged phase shifts for Pt is supported by the excellent agreement in both peak position and height for the clean Ni(111) I-V curves[66] (see Figure 6.5). The R-factor improvement for clean Pt(111) obtained by using the optimized, spin-averaged phase shifts carries over to the analysis of O on this surface.

Detailed LEED analyses of the Pt(111)-$p(2 \times 2)$-O system, carried out by different search methods, arrive at a similar final structure. An R_p-factor of 0.18 was obtained for the final structure. In this structure, O atoms adsorb in fcc hollow sites and induce a buckling (see Figure 3.7 for the relative displacements of the metal atoms within the layer) of 0.07 ± 0.03 and 0.10 ± 0.04 Å in both the first and second metal layers, respectively. In addition, there is a probable expansion of 0.01 Å in the first metal-metal interlayer spacing and possibly a small contraction of 0.02 Å in the second. A metal-oxygen bond length of 2.02 Å was found. Lateral displacements, including symmetry-breaking features, were found to be within error bars; however, we do find a small lateral expansion of the triangle of three Pt atoms directly below the O. The fractional order beams proved to have much greater sensitivity to the surface relaxation than the integer order beams. In addition, relativistic phase shifts for the Pt(111)-$p(2 \times 2)$-O structure were found to have important influences on the resulting metal-oxygen bond length.

Chapter 4

Sulfur on Pt(111): A Combined LEED and STM Study.

Examined in this chapter are the effects of different coverages of sulfur on the relaxation of the Pt(111) surface. This work was done in collaboration with H. A. Yoon. Sulfur is an ideal adsorbate for the study of adsorbate-induced reconstruction, because it forms a relatively large number of stable ordered overlayers[15]. This allows one to examine metal-adsorbate and nearest neighbor interactions. The possibility of many different ordered overlayers suggests a delicate balance of forces between the adsorbates and with the metal surface. Low energy electron diffraction (LEED) provides structural information that can be used to elucidate these interactions. One example of such use of structural information is the continuous order-disorder phase transitions on the Ru(0001) surface[71,72]. LEED structural analyses provided information about the symmetry class of various overlayers on the Ru surface[73].

Sulfur adsorption on platinum is also of interest because sulfur acts as a poison in some catalytic reactions[74]. An understanding of the binding site of sulfur as a function of coverage may be helpful in the study of catalytic properties and in studies of the interaction of sulfur with other adsorbates. One such study is the interaction of sulfur adsorbed with carbon monoxide on the Pt(111) surface[75]. In this study, using both scanning tunneling microscopy (STM) and LEED, J. C. Dunphy et al.[75] found that the $p(2 \times 2)$ sulfur overlayer can be compressed into the $(\sqrt{3} \times \sqrt{3})$R30° overlayer with the additional adsorption of carbon monoxide. The study provides another molecular mechanism for carrying out cat-

alytic reactions on metal surfaces that are covered with a non-reactive chemisorbed layer. Structural information is needed to help understand not only the mechanism but also the energetics of this compression.

This chapter is organized in six sections. First, we examine previous structural determinations of sulfur on close-packed metal surfaces. Next, we describe our experiment and present our STM images from three different ordered overlayers. In the following three sections (Sections 4.3 to 4.5), we report the details of the LEED analyses. Finally, we present our conclusions in the last section.

4.1 Background

LEED patterns of sulfur on Pt(111) have been investigated by both Auger electron spectroscopy (AES)[15] and radiotracers (S^{35})[76] to determine the coverage of sulfur. In the work of W. Heegemann et al.,[15] three ordered LEED patterns were observed at approximately 0.25, 0.33 and 0.43 monolayers (ML). The lowest coverage LEED pattern is a $p(2 \times 2)$ and the next highest is a $(\sqrt{3} \times \sqrt{3})$R30°. Above 0.33 ML, a complex $\begin{pmatrix} 4 & \bar{1} \\ \bar{1} & 2 \end{pmatrix}$ pattern is formed.

Several fcc(111)-$(\sqrt{3} \times \sqrt{3})$R30°-S overlayers have previously been analyzed with LEED. For the Ir,[77] Pd[78] and Rh[79] $(\sqrt{3} \times \sqrt{3})$R30° overlayers, metal-sulfur bond lengths of 2.28, 2.20 and 2.18 Å, respectively, were found. The fcc hollow site adsorption was found in all cases. In addition, sulfur on Pt(111) has been studied by K. Hayek et al.[80,81]. They find fcc adsorption and a Pt-S distance of 2.27 Å. This corresponds to a sulfur height of 1.61 Å above the metal surface. LEED analyses of the Ni(111)-$p(2 \times 2)$,[82] the Re(0001)-$p(2 \times 2)$[83] and the Ru(0001)-$p(2 \times 2)$[73] overlayers yielded hollow sites and bond lengths of 2.00, 2.32 and 2.28 Å, respectively. In the work of D. Jürgens et al. on Ru,[73] the $(\sqrt{3} \times \sqrt{3})$R30° was examined and a bond length identical to that of the Ru-$p(2 \times 2)$ overlayer was found. A. Barbieri et al.[83] also looked at the complex Re(0001)-$(2\sqrt{3} \times 2\sqrt{3})$R30°-6S overlayer. In this overlayer, they found three different Re-S bond lengths of 2.21, 2.24 and 2.51 Å.

4.2 Experiments

Our experiments were carried out in a stainless steel ultrahigh vacuum (UHV) chamber. This chamber was also equipped with an ultrahigh vacuum scanning tunneling microscope (UHV-STM). The sample manipulator allowed the transfer of the crystal from the manipulator to the UHV-STM. The sample was cleaned by repeated cycles of ion bombardment and annealing in oxygen until no impurities could be detected by Auger electron spectroscopy (AES), and the LEED pattern of the clean surface was sharp and free of diffuse background intensities. The UHV instrumentation and sample preparations are described in Section 2.2.

LEED data were collected by Varian 4-grid LEED optics with an off-axis electron gun. A Dage-MTI SIT-68 high-sensitivity video camera interfaced with a PC was used to digitalize the LEED pattern on the fluorescent screen of the Varian LEED optics (see Section 2.3.1). As detailed in Section 2.4, the I-V curves were generated by computing the integrated intensity of each individual diffraction spot in each LEED pattern collected over a range of energies. LEED data acquisition was performed at 90 K and normal incidence was confirmed by comparing I-V curves of symmetrically equivalent beams.

The STM experiments were performed after obtaining the desired LEED pattern. The sample was then transferred from the manipulator to the UHV-STM. The UHV-STM is a double tube design in which the inner piezoelectric tube controls the scanning and the tip-to-sample distance; the outer piezoelectric tube provides inertial sample approach and coarse x and y positioning. This design is similar to the UHV-STM design in Reference 84. All of the UHV-STM experiments were carried out with a positive sample bias from 0.05 to 1.00 eV and a tunneling current varying from 0.5 to 1.0 nA for both the topographic and the current imaging modes.

A solid-state electrochemical source[85] was utilized for sulfur adsorption. A beam of S_2 is produced by the electrochemical decomposition of silver sulfide, thus, allowing direct adsorption of sulfur on the Pt(111) surface. The exposure can be controlled either by the current to the cell or by the exposure time. Use of this source, allows much higher coverages than the use of H_2S. Indeed, unlike H_2S, the electrochemical source allows the formation of multilayers on the Pt(111) surface[15]. Presumably, the S_2 is dissociated during the annealing process required to form the ordered overlayer. In our experiments, we found that all three sulfur overlayers initially studied by W. Heegemann et al.[15] could be reproduced.

Figure 4.1: The LEED pattern of the Pt(111)-$p(2 \times 2)$-S overlayer at 132 eV and normal incidence.

4.2.1 Pt(111)-$p(2 \times 2)$-S

After depositing sulfur at 90 K and annealing to 800 K for 10 seconds, the sharp $p(2 \times 2)$ LEED pattern shown in Figure 4.1 was produced. LEED I-V curves were collected at normal incidence for 14 symmetry inequivalent beams from 90 to 300 eV in 2 eV steps for a total energy range of 2322 eV; they were found to be reproducible. I-V curves for two separate preparations were averaged together for use in the LEED analysis. We found that this surface was more sensitive to background gas adsorption than the $(\sqrt{3} \times \sqrt{3})$R30°, but was still stable for several hours.

At the coverage of 0.25 ML, the $p(2 \times 2)$ overlayer forms very large domains on the Pt(111) surface. Figure 4.2 shows a topographic image of the $p(2 \times 2)$ overlayer. The real space unit cell in this image has a periodicity of 5.54 Å. Almost no effect is seen in the STM images of the same region when bias or tunneling currents are varied. When the sulfur coverage is less than the 0.25 ML required by a complete $p(2 \times 2)$overlayer, our STM images show $p(2 \times 2)$ islands on the terraces about 20 to 30 Å away from the step edges. This is indicative of a weak attractive interaction between the unit cells. We find a height difference of approximately 0.5 Å on and off a $p(2 \times 2)$ island. Assuming that this height is related to the real height difference and not an electronic effect, it supports the idea that there is 2D sulfur gas between the islands. A 2D lattice gas has been seen on the Re(0001) surface by J. C. Dunphy et al[86]. In addition, we find many defects caused by sulfur vacancies in the ordered islands. These vacancies show up as dark regions in the

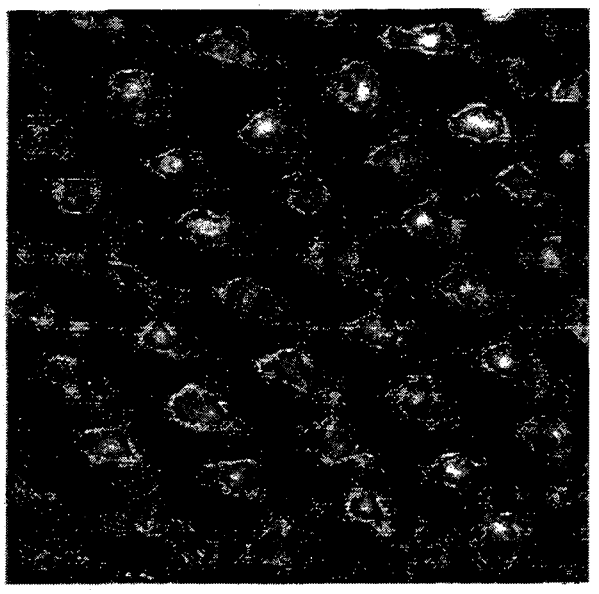

Figure 4.2: The STM image of the Pt(111)-$p(2 \times 2)$-S overlayer in topographic mode. Sulfur has been identified as the bright spots in the image. The image size is approximately 41×41 Å.

STM image; thus, identifying sulfur as the bright spots in the STM images.

4.2.2 Pt(111)-($\sqrt{3} \times \sqrt{3}$)R30°-S

As in the $p(2 \times 2)$ preparation, we deposited sulfur at 90 K and annealed to 500 K for 10 seconds. After this, we obtained the sharp ($\sqrt{3} \times \sqrt{3}$)R30° LEED pattern shown in Figure 4.3. LEED I-V curves were collected at normal incidence for 11 symmetry inequivalent beams from 90 to 300 eV in 2 eV steps for a total energy range of 1616 eV; they were found to be reproducible for two preparations. We found this surface to be very stable; it could even be seen the next day.

The STM image of the ($\sqrt{3} \times \sqrt{3}$)R30° structure is shown in Figure 4.4. As in the $p(2 \times 2)$ images, we were able to identify, using defects, the bright spots in the image as sulfur. The images show a periodicity of 4.80 Å. If the coverage is between 0.25 and 0.33 ML, the STM images contain both the $p(2 \times 2)$ and the ($\sqrt{3} \times \sqrt{3}$)R30° overlayers.

Figure 4.3: The LEED pattern of the Pt(111)-($\sqrt{3} \times \sqrt{3}$)R30°-S overlayer at 132 eV and normal incidence.

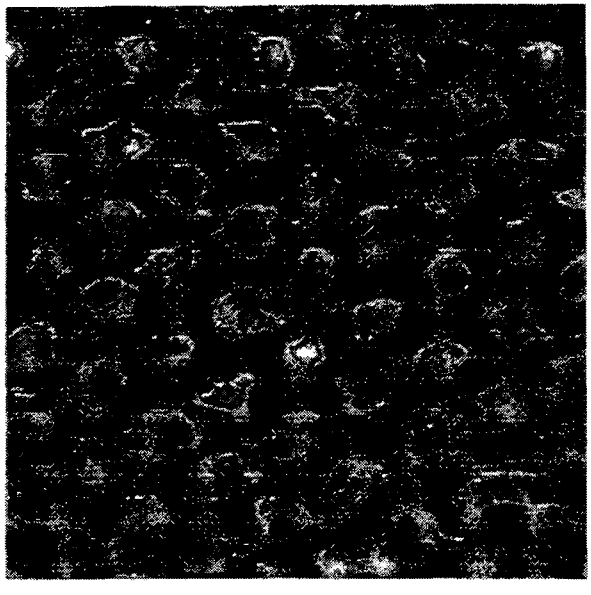

Figure 4.4: The STM image of the Pt(111)-($\sqrt{3} \times \sqrt{3}$)R30°-S overlayer in topographic mode. Sulfur has been identified as the bright spots in the image. The image size is approximately 36 × 36 Å.

Figure 4.5: The LEED pattern of the Pt(111)-Oblique-3S overlayer at 100 eV and normal incidence.

4.2.3 Pt(111)-Oblique-3S

By adsorbing more sulfur at 90 K than in the $p(2\times2)$ and $(\sqrt{3}\times\sqrt{3})$R30° preparations and annealing to 500 K for 5 seconds, the relatively sharp $\begin{pmatrix} 4 & \bar{1} \\ \bar{1} & 2 \end{pmatrix}$ or, for simplicity, oblique LEED pattern shown in Figure 4.5 can be produced. It is believed, based on AES measurements, to contain 3 sulfur atoms per unit cell[15]. LEED I-V curves were taken; however, due to the size of the sample manipulator and the close spacing between diffraction spots, we have not yet been able to analyze the I-V curves.

It was possible to obtain STM images for this overlayer. Figure 4.6 shows one such image. Other studies of high coverage sulfur overlayers on metal surfaces have shown sulfur can form clusters. One STM study of sulfur on the Cu(111) surface has found that three sulfur atoms can come together and form a single bright spot[87]. One must be careful to remember STM probes the electronic structure close to the Fermi level and not the geometrical structure. In the case of Mo(100)-$c(4\times2)$-3S, one finds only one bump in the STM image, however LEED analysis and STM simulations show that there are three non-clustered sulfur atoms at a lower height above the surface which do not appear in the experimental STM images[88]. Due to the size of the single bump in our image, we believe that it results from an unresolved cluster of 3 sulfur atoms. We also find that the real space unit cell does not have a mirror plane or an axis of rotation. The $p3m1$ symmetry in the LEED pattern must be due to domain averaging. In Figure 4.6, one can see two different

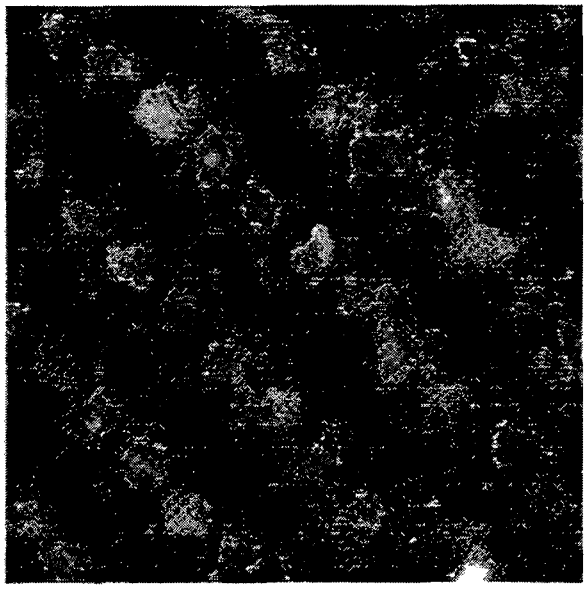

Figure 4.6: The STM image of the Pt(111)-Oblique-3S overlayer in topographic mode. Sulfur clusters have been associated with the bright spots in the image. The real space unit cell does not display the $p3m1$ symmetry of the LEED pattern. The image size is approximately 36×36 Å.

domains within a terrace.

4.3 LEED Theory

In addition to determining the adsorption site with LEED, we wished to investigate adsorbate-induced relaxations in the substrate atoms. An automated search method based on the TLEED approximation[1] was used. Addition information on the search procedure can be found in Section 2.6. Nine spin-averaged phase shifts were generated from a muffin-tin model potential formed using relativistic atomic wavefunctions. Additional phase shifts did not influence our results. Scattering between the layers and towards the bulk was modeled using renormalized forward scattering (RFS). Up to 199 beams were necessary to achieve convergence for the interlayer multiple scattering in RFS. Electron damping was simulated by the imaginary part of the inner potential, which was found to be $V_i = -5.00$ eV. This damping was determined by fitting its value using the initial best-fit model; it was then used for all the models reported in this chapter. Thermal vibrations were modeled using temperature dependent phase shifts. These phase shifts were initially based on isotropic

vibrations of the same amplitude for the S atom and metal atoms. The Debye temperature of platinum was set to 250 K, which was determined by fitting the clean surface data[52] (see Section 3.3). As with the imaginary part of the inner potential, we optimized the vibrational amplitude of the S atom for the initial best-fit model and report further results based on this value. For the sulfur atom, we find a Debye temperature of 417 K which corresponds to a vibrational *rms* enhancement of approximately 1.5 times that determined from identical *rms* vibrational amplitudes for both S and Pt.

The fit between theoretical and experimental I-V curves was quantified by Pendry's R-factor (R_p-factor)[47] which emphasizes peak positions in the spectra at the expense of absolute values. Error bars were estimated using Pendry's method[47]. We have examined the influence of smoothing the experimental I-V curves, quantifying it by examining the resulting error bars for the initial best-fit model. Because Pendry's method depends both on the overall R_p-factor and on R_p-factor sensitivity to variation of the coordinate, an optimal amount of smoothing can be found by minimizing the error bar of a coordinate vs. the amount of smoothing. As smoothing is increased, experimental noise is removed, thus reducing the overall R_p-factor. However, if smoothing is increased until information is lost from the I-V curves, R_p-factor sensitivity to changes in a coordinate will be indirectly decreased. Therefore, by minimizing the error bars vs. amount of smoothing, we can decrease the amount of information lost and lower the R_p-factor. For both the $p(2 \times 2)$ and the $(\sqrt{3} \times \sqrt{3})$R30° experimental I-V curves, we find that four three-point smoothings of both the experimental and theoretical I-V curves, after interpolation onto a common 0.25 eV energy grid, minimize the R_p-factor value and the error bars on all optimized parameters. This smoothing was applied to the I-V curves for all models reported in this chapter.

4.4 LEED Analyses

This section is divided into several parts. The first part deals with the initial coarse structural search over high symmetry adsorption sites for the $p(2 \times 2)$-S and the $(\sqrt{3} \times \sqrt{3})$R30° overlayers. In the next part, we discuss the effect of vertical relaxations, or buckling, in the $p(2 \times 2)$ overlayer on the fractional I-V curves. After this, we investigate possible models containing symmetry-allowed and symmetry-breaking lateral displacements. This section ends with our initial conclusions for the best-fit model which is presented in following section.

Table 4.1: The resulting R_p-factor values for the best-fit structure of each adsorption site and for various degrees of freedom. "Planar" refers to automated TLEED searches which varied only vertical displacements of the S and the two metal layers. "Buckled" refers to all vertical relaxations in the first two metal layers allowed by the local symmetry of the site and determined by automated TLEED searches.

Site	$p(2 \times 2)$		$(\sqrt{3} \times \sqrt{3})$R30°	
	Planar	Buckled	Planar	Buckled
fcc-hollow	0.47	0.21	0.18	—
hcp-hollow	0.69	0.66	0.74	0.73
top	0.80	0.67	0.71	0.71
bridge	0.65	0.57	0.68	0.66

4.4.1 Coarse Searches

The coverage of sulfur in the $p(2 \times 2)$ and $(\sqrt{3} \times \sqrt{3})$R30° systems has been determined by AES[15]. In addition, the $(\sqrt{3} \times \sqrt{3})$R30° overlayer has been the subject of a previous LEED analysis by K. Hayek et al.[80,81]. These studies combined with our STM data support the assumption of only one S atom per unit cell. Given only one S atom in the unit cell, four high symmetry adsorption sites are possible: top, bridge, fcc-hollow and hcp-hollow.

We tested the high symmetry adsorption sites using TLEED analysis coupled with an automated search algorithm. For the $p(2 \times 2)$ overlayer, the initial TLEED search was restricted to the (1,0), (0,1), (1,1), (1/2,0), (0,1/2) and (1/2,1/2) beams between 90 and 300 eV for a total energy range of 1198 eV. These beams have the lowest experimental noise and the largest total energy range. The initial search for the $(\sqrt{3} \times \sqrt{3})$R30° overlayer used all of the experimentally available beams, the (1,0), (0,1), (1,1), (2,0), (2,0), (1/3,1/3), (2/3,2/3), (1/3,4/3), (4/3,1/3), (1/3,7/3), and the (7/3,1/3). For each high symmetry site, automated searches were carried out over trial geometries with varying degrees of freedom. When needed, domain averaging was used to recover the $p3m1$ symmetry of the LEED pattern. In our first structural searches, we allowed only the sulfur height and the first two substrate interlayer spacings to vary (D_{01}, D_{12} and D_{23} of Figure 4.8 and Figure 4.10) for each model and overlayer. Table 4.1 summarizes these results under the heading "Planar." Additional vertical parameters for the first two metal layers are possible in all models with the exception of the $(\sqrt{3} \times \sqrt{3})$R30° fcc-hollow site model. These parameters allow for buckling of the metal surface (as an example, B_1 and B_2 shown in Figure 4.8). The

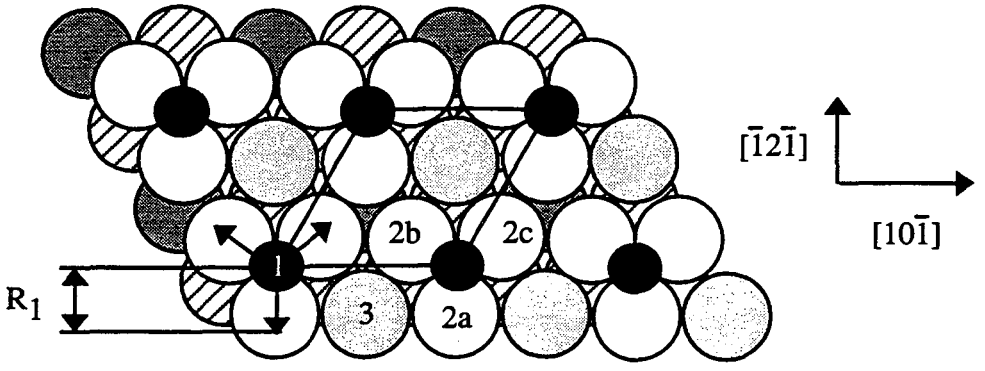

Figure 4.7: Top view of the Pt(111)-$p(2 \times 2)$-S structure. Geometrical parameters are labeled. The parameter which characterizes the second layer lateral expansion of the triangle of three metal atoms directly below the S (R_2) is not shown. Inequivalent atoms are shaded differently and numbered; the numbering corresponds to that in Table 4.3. The unit cell is outlined.

resulting R_p-factors are shown under the heading "Buckled" in Table 4.1. For the fcc-hollow site model, any possible symmetry-allowed relaxation would have to occur in metal layers below the first two layers. Although the R_p-factors for the models under the "Planar" heading have the same number of parameters, the models under the "Buckled" heading, due to differences in adsorption site, do not have the same number of parameters included in the optimization. The addition of lateral parameters in the structural search (for example, R_1 in Figures 4.7 and 4.9), along with symmetry-breaking relaxations, is described later in Section 4.4.3.

4.4.2 Effects of Buckling on the $p(2 \times 2)$ Model

As seen in Table 4.1, relaxation or buckling of the metal surface results in a dramatic improvement in the agreement between the theoretical and the experimental I-V curves for the $p(2 \times 2)$ overlayer. Figure 4.11 illustrates these improvements in the I-V curves of the $p(2 \times 2)$ fcc-hollow site model with increasing degrees of freedom. In this figure, the heading "Bulk" refers to automated TLEED searches in which only the S height above the ideally-terminated substrate was varied. The headings "Planar" and "Buckled" refer to the same structural optimizations described above in Section 4.4.1.

In determining adsorbate-induced relaxation of the surface, it was noted in Chapter 3 that an important consideration in a LEED analysis is the ratio of the energy range of the fractional order beams to that of the integer order beams. This importance is due to

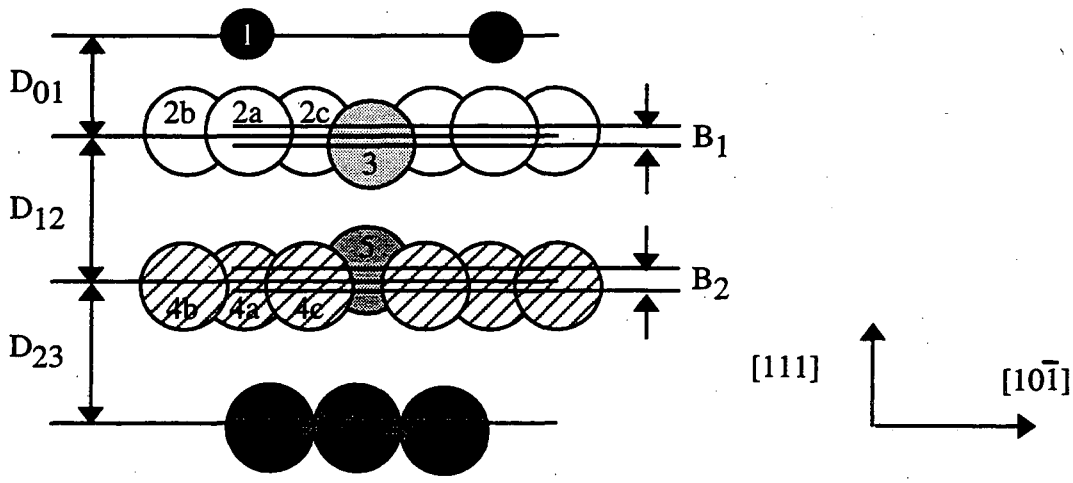

Figure 4.8: Side view of the Pt(111)-$p(2 \times 2)$-S structure. Geometrical parameters are labeled. Inequivalent atoms are shaded differently and numbered; the numbering corresponds to that in Table 4.3.

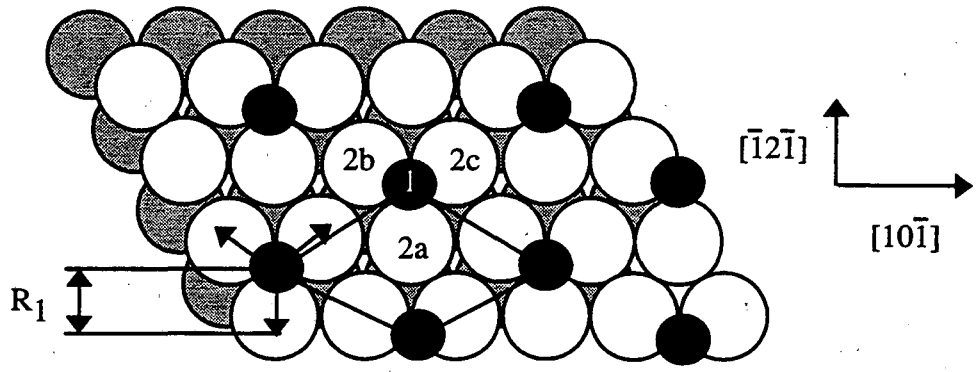

Figure 4.9: Top view of the Pt(111)-$(\sqrt{3} \times \sqrt{3})$R30°-S structure. Geometrical parameters are labeled. The parameter which characterizes the second layer lateral expansion of the triangle of three metal atoms directly below the S (R_2) is not shown. Inequivalent atoms are shaded differently and numbered; the numbering corresponds to that in Table 4.4. The unit cell is outlined.

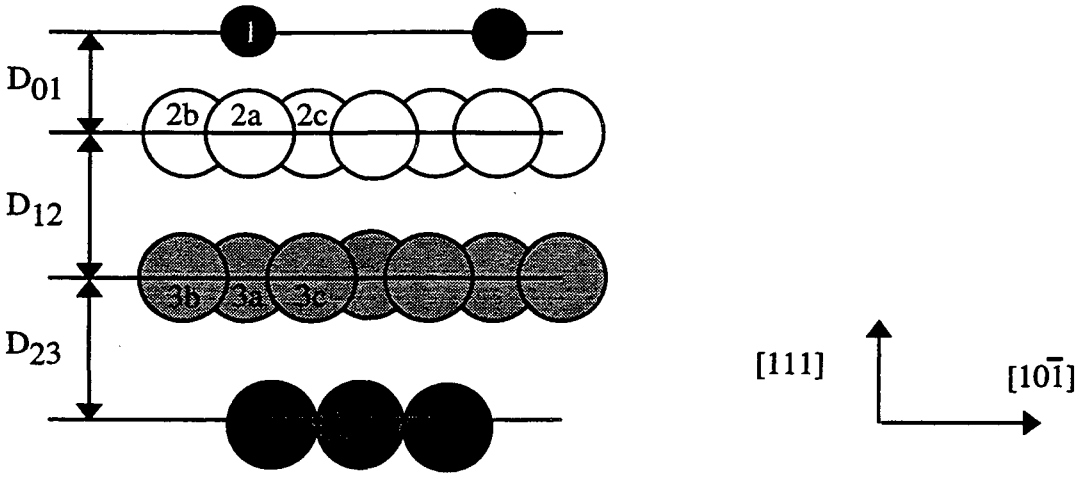

Figure 4.10: Side view of the Pt(111)-($\sqrt{3} \times \sqrt{3}$)R30°-S structure. Geometrical parameters are labeled. Inequivalent atoms are shaded differently and numbered; the numbering corresponds to that in Table 4.4. This figure is similar to Figure 4.8, however, here all Pt atoms within a layer are equivalent.

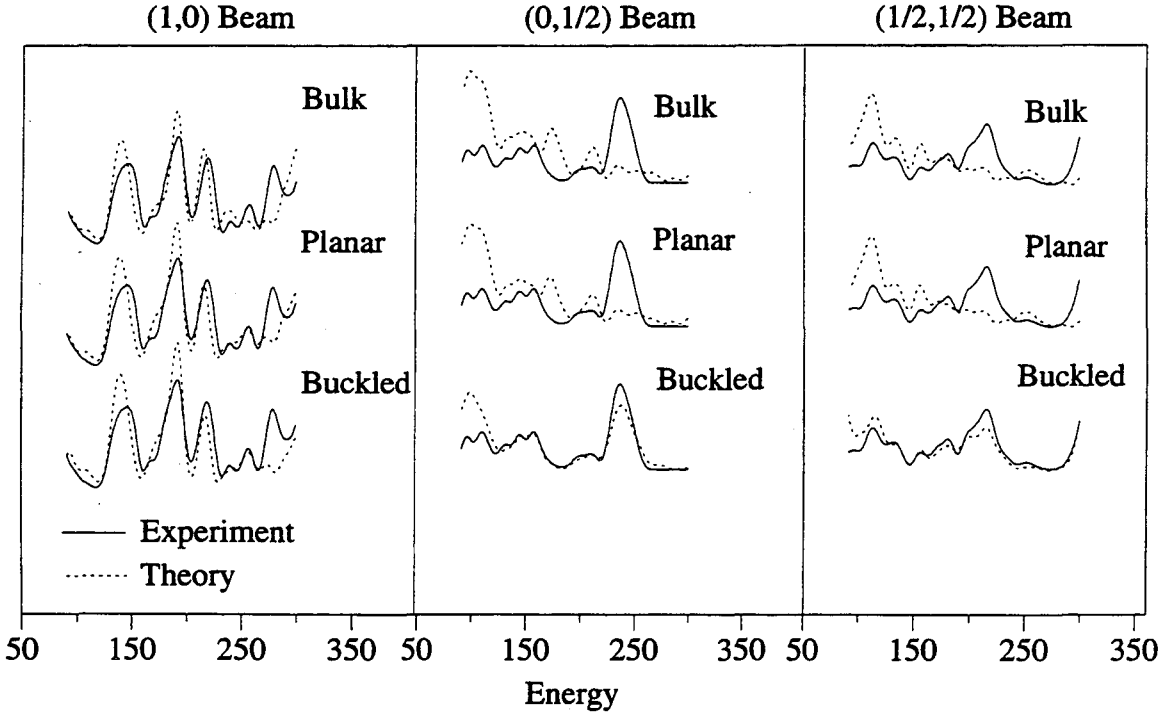

Figure 4.11: Improvements in the Pt(111)-$p(2 \times 2)$-S I-V curves for the fcc-hollow site model with increasing degrees of freedom. By comparing the I-V curves of the "Planar" model with those of the "Buckled" model, one can clearly see the improvement of the fractional order beams, particularly in the higher energy region.

Table 4.2: Error bars computed using Pendry's method[47] with either the fractional order, integer order, or both beam sets. Notice the low sensitivity of the integer order beams to the surface buckling. The geometrical parameters are illustrated in Figures 4.7 and 4.8.

Parameter	Error Bars		
	R_p-Both	R_p-Fractional	R_p-Integer
D_{01}	±0.02	±0.02	±0.03
D_{12}	±0.03	±0.03	±0.03
D_{23}	±0.04	±0.05	±0.03
B_1	±0.04	±0.04	⟩±0.1
B_2	±0.05	±0.06	⟩±0.1
R_1	±0.04	±0.04	⟩±0.1
R_2	±0.06	±0.06	⟩±0.1

the greater sensitivity of fractional order beams to surface relaxation; it is clearly demonstrated for the case of the Pt(111)-$p(2\times2)$-O overlayer in Figure 3.8. This sensitivity is also illustrated for the $p(2\times2)$-S overlayer in Figure 4.11. Shown in Tables 3.5 and 4.2 are the error bars computed with Pendry's method[47] for both the integer and fractional, only the integer, or only the fractional order beams using all of the available experimental beams. The restricted data set used in the coarse search gave rise to large error bars (⟩ ± 0.1 Å) for the lateral displacements, R_1 and R_2. The large differences in the error bars shown in Table 4.2 are a direct result of the buckled atoms' contributions to the intensities of fractional order beams. By comparing the I-V curves of the non-relaxed model with those of the buckled model (Figure 4.11), one can clearly see the improvement of the fractional order beams, particularly in the higher energy region. The stronger scattering power of the buckled Pt atoms with respect to that of the S atoms results in increased intensity in the fractional order beams relative to that which would normally be expected from just the S atoms.

4.4.3 Lateral Displacements and Symmetry-Breaking Models

We have also examined various models, all based on the best-fit fcc-hollow site model, with different degrees of lateral relaxations of the metal atoms for both overlayers. As above, we used all the available experimental beams in these computations. The addition of fractional order beams with larger momentum transfer parallel to the surface than that found in the beam sets used in the coarse search was necessary to obtain the desired

sensitivity to these displacements. The first model contained only relaxations consistent with the three-fold rotational axis and the mirror plane symmetry ($p3m1$) of the fcc hollow site. These symmetry-allowed relaxations result in two additional parameters for both the $p(2\times2)$ and the $(\sqrt{3}\times\sqrt{3})$R30° models. In both cases, a lateral expansion or contraction of the triangle of three metal atoms directly bonded to the sulfur and of the triangle of three metal atoms directly below the adsorption site is possible. One of these two parameters (R_1) is illustrated in Figures 4.7 and 4.9. The next two structural models contain features which break the $p3m1$ symmetry of the fcc hollow site. In the first such model, the mirror plane was broken by allowing the triangle of three Pt atoms bonded to the S atom to rotate in-plane ($p3$ symmetry); in the second the rotational symmetry was broken by allowing two of the three Pt atoms bonded to the S atom to move together and the third to move separately. Symmetry in the LEED pattern was regained by averaging beam intensities over the resulting domains. The small decrease in the R_p-factor value with an increasing number of parameters contained in these last two models does not allow one to distinguish between these models and the symmetry-conserving model. However, because of the large error bars (greater than 0.10 Å) associated with these symmetry-breaking displacements and because of the symmetry of the adsorption site, we believe that there are no symmetry-breaking features in either the $p(2\times2)$ or the $(\sqrt{3}\times\sqrt{3})$R30° overlayer.

4.4.4 Summary of Initial Results

In these initial analyses of the $p(2\times2)$ and the $(\sqrt{3}\times\sqrt{3})$R30° overlayers, the fcc-hollow site model clearly yields the best fit to the experimental data. The resulting R_p-factors for the other sites shown in Table 4.1 were obtained from structures which have large, possibly unrealistic displacements from the reference structures. Because the TLEED approximation becomes increasingly inaccurate as displacements get larger, the R_p-factor does not reflect the true R_p-factor value of the resulting structure. One can use Pendry's method[47] to generate a range of R_p-factor values in which the resulting R_p-factor values of indistinguishable models should fall into. R_p-factor values of all sites other than the fcc-hollow for both structures fall outside this range centered on the fcc-hollow site's R_p-factor value. The buckling of the metal layers which is responsible for the considerably lower R_p-factors of the TLEED analysis of the $p(2\times2)$ overlayer, was not needed to differentiate between the various possible adsorption sites. No buckling of the first two metal layers in

the $(\sqrt{3} \times \sqrt{3})$R30° overlayer was observed in the initial search due to the symmetry of the adsorption site. The third metal layer is the first metal layer in the $(\sqrt{3}\times\sqrt{3})$R30° fcc-hollow site model which can display a symmetry-allowed buckling. Finally, we see no evidence of symmetry-breaking features in either the $p(2 \times 2)$ or the $(\sqrt{3} \times \sqrt{3})$R30° overlayer.

4.5 LEED Results

The $p(2\times2)$ and $(\sqrt{3}\times\sqrt{3})$R30° structures which resulted from the initial analysis were used as a starting point for the final analysis. We optimized all parameters which are consistent with the $p3m1$ symmetry of the overlayer. For the final structures, we initiated automated TLEED structural searches starting from new reference structures until the resulting structure was within a 0.02 Å radius of the last reference structure. In this way, we were able to eliminate any error caused by the TLEED approximation in the final structure. We find that iteration, and thus recomputation of the reference structure, is imperative to minimize the errors induced by the TLEED approximation, which can affect the final structure.

4.5.1 Final $p(2 \times 2)$ Structure

The final structure obtained for the Pt(111)-$p(2 \times 2)$-S has S atoms adsorbed in fcc hollow sites with an R_p-factor of 0.22. Details of this final structure can be found in Table 4.3, and a comparison of final theoretical and experimental I-V curves in Figure 4.12. We find the S atom induces a buckling (see Figure 4.8 for the relative displacements of the metal atoms within the layer) of 0.08 ± 0.04 and 0.08 ± 0.05 Å in the first and second metal layers, respectively. In addition, sulfur induces a probable expansion of 0.03 Å in the first metal-metal interlayer spacing and a possible small contraction of 0.02 Å in the second. A metal-sulfur bond length of 2.24 Å was found. Lateral displacements consistent with the three-fold rotational and mirror plane symmetries yield a possible small lateral expansion (0.03 ± 0.04 Å) of the triangle of three metal atoms directly bonded to the sulfur. This expansion is within error bars of the bulk positions.

Table 4.3: Optimal atomic coordinates (in Å) for the Pt(111)-$p(2 \times 2)$-S fcc hollow site model with an R_p-factor of 0.22. X is defined as positive towards the surface. Y and Z are coordinates parallel to the surface. The "Atom" numbers correspond to inequivalent atoms labeled in Figures 4.7 and 4.8. Error bars are given for each set of equivalent atoms.

Atom	X	Y	Z
1 S	0.00 ± 0.02	0.00	0.00
2a Pt	1.54 ± 0.03	0.00	1.63 ± 0.04
2b Pt	1.54	1.41	-0.82
2c Pt	1.54	-1.41	-0.82
3 Pt	1.62 ± 0.04	0.00	-3.20
4 Pt	3.80 ± 0.05	2.77	-1.60
5a Pt	3.88 ± 0.04	0.00	-1.60 ± 0.06
5b Pt	3.88	1.38	0.80
5c Pt	3.88	-1.38	0.80
Bulk repeat vector			
	2.2650	0.0000	1.6016
$2D$ repeat vectors			
		2.7740	4.8048
		2.7740	-4.8048

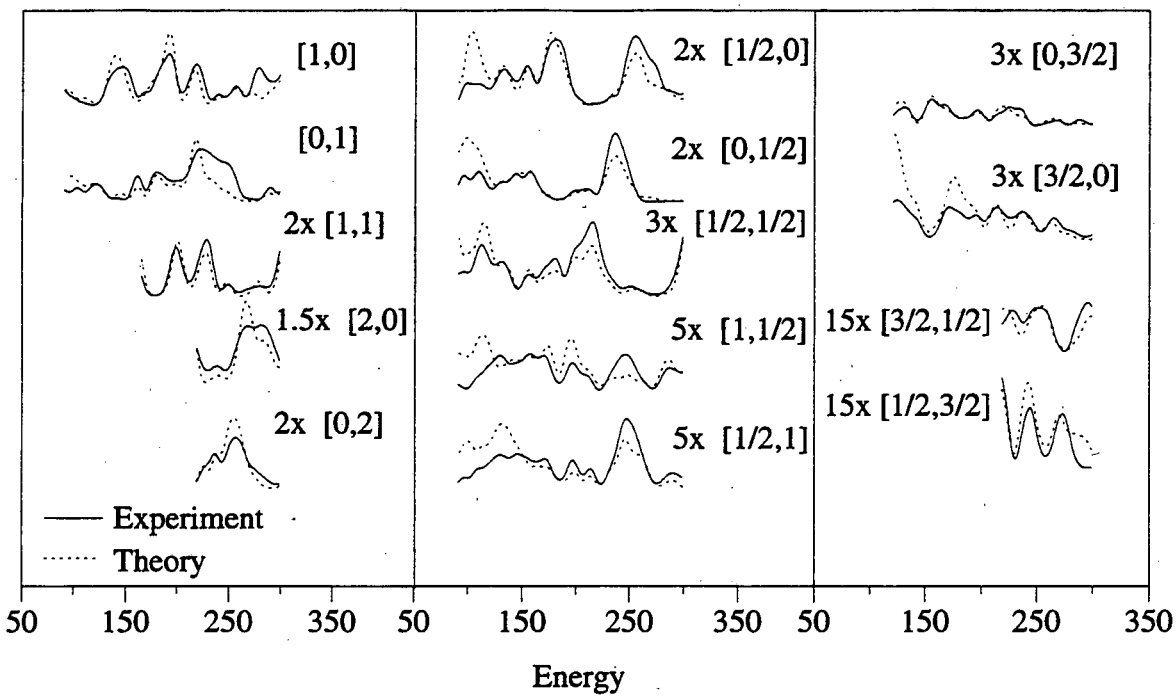

Figure 4.12: I-V curves of the best-fit Pt(111)-$p(2 \times 2)$-S structure with an R_p-factor of 0.22.

4.5.2 Final $(\sqrt{3} \times \sqrt{3})$R30° Structure

The final structure obtained for the Pt(111)-$(\sqrt{3} \times \sqrt{3})$R30°-S has S atoms adsorbed in fcc hollow sites with an R_p-factor of 0.18. Details of this final structure can be found in Table 4.4, and a comparison of final theoretical and experimental I-V curves in Figure 4.13. Sulfur induces a probable expansion of 0.01 Å in the first metal-metal interlayer spacing and a possible small contraction of 0.02 Å in the second. A metal-sulfur bond length of 2.25 Å was found. Lateral displacements consistent with the three-fold rotational and mirror plane symmetries yield a possible small lateral expansion (0.04 ± 0.04 Å) of the triangle of three metal atoms directly bonded to the sulfur. This expansion is within error bars of the bulk positions.

4.6 Conclusions

We studied two of the three ordered overlayers of sulfur on Pt(111) using both LEED and STM. Comparing the $p(2 \times 2)$ and the $(\sqrt{3} \times \sqrt{3})$R30° overlayers, we find

Table 4.4: Optimal atomic coordinates (in Å) for the Pt(111)-($\sqrt{3} \times \sqrt{3}$)R30°-S fcc-hollow site model with an R_p-factor of 0.18. X is defined as positive towards the surface. Y and Z are coordinates parallel to the surface. The "Atom" numbers correspond to inequivalent atoms labeled in Figures 4.9 and 4.10. Error bars are given for each set of equivalent atoms.

Atom	X	Y	Z
1 S	0.00 ± 0.02	0.00	0.00
2a Pt	1.55 ± 0.03	0.00	1.63 ± 0.04
2b Pt	1.55	1.42	-0.82
2c Pt	1.55	-1.42	-0.82
3a Pt	3.83 ± 0.03	0.00	-1.61 ± 0.05
3b Pt	3.83	1.39	0.81
3c Pt	3.83	-1.39	0.81
Bulk repeat vector			
	2.2650	0.0000	1.6016
$2D$ repeat vectors			
		4.1610	2.4024
		0.0000	-4.8047

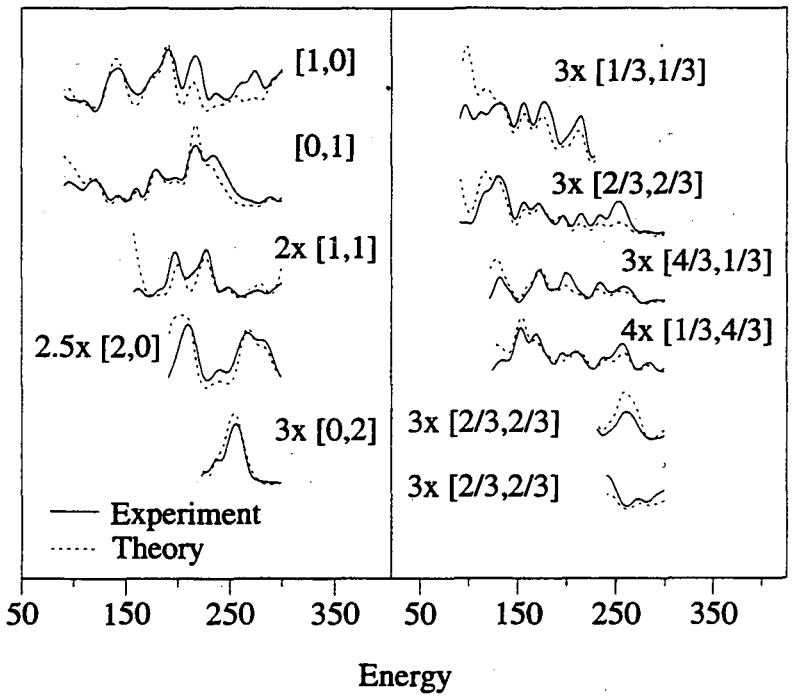

Figure 4.13: I-V curves of the best-fit Pt(111)-($\sqrt{3}\times\sqrt{3}$)R30°-S structure with an R_p-factor of 0.18.

similarity in the local bonding of the S atom. The metal-sulfur bond lengths are practically identical. Examining the center-of-mass interlayer spacings, we again find similarity: a small expansion of the first and subsequent contraction of the second for each system. The lateral expansions of the triangle of three atoms under the adsorbate (R_1 and R_2 in Figures 4.7 and 4.9) are within error bars for both systems. Our structural results for Pt are qualitatively similar to what is found for the $p(2\times 2)$ and ($\sqrt{3}\times\sqrt{3}$)R30° overlayers on Ru(0001)[73] and for the $p(2\times 2)$ overlayer on Re(0001)[83] with the exception that on hcp metal sulfur is found in the hcp site.

As is the case for other fcc(111) surfaces,[77–79,82] we find an fcc hollow site for sulfur adsorption. The Pt-S bond lengths of 2.24 Å for the $p(2\times 2)$ overlayer and 2.25 Å for the ($\sqrt{3}\times\sqrt{3}$)R30° overlayer are also within the range of metal-S bond lengths found on other metal surfaces. Our bond lenths are a little shorter than the values found for the ($\sqrt{3}\times\sqrt{3}$)R30° overlayers on Ir[77] and Pt,[80,81] but are larger than the values for Ni,[82] Pd,[78] and Rh[79]. The Pt-S height found in our analysis is shorter by 0.06 Å than the value found by K. Hayek et al.;[81] however our R_p-factor is less than half of theirs.

Table 4.5: Comparison of various geometrical parameters for the $p(2 \times 2)$ and the $(\sqrt{3} \times \sqrt{3})$R30° sulfur structures on Pt(111). The $p(2 \times 2)$ parameters are shown in Figures 4.7 and 4.8, while the $(\sqrt{3} \times \sqrt{3})$R30° parameters are illustrated in Figures 4.9 and 4.10. Because there are no relaxations of the metal surface for the $(\sqrt{3} \times \sqrt{3})$R30° overlayer, the parameters B_1 and B_2 apply only to the $p(2 \times 2)$ overlayer.

	$p(2 \times 2)$	$(\sqrt{3} \times \sqrt{3})$R30°
D_{01}	1.54 ± 0.02	1.55 ± 0.02
D_{12}	2.30 ± 0.03	2.28 ± 0.03
B_1	0.08 ± 0.04	—
D_{23}	2.25 ± 0.05	2.24 ± 0.03
B_2	0.08 ± 0.05	—
R_1	0.03 ± 0.04	0.04 ± 0.04
R_2	0.00 ± 0.06	0.01 ± 0.05

One difference between our two structures is the lack of buckling in the $(\sqrt{3} \times \sqrt{3})$R30° structure. The $(\sqrt{3} \times \sqrt{3})$R30° structure is the highest coverage structure obtainable without clustering of the sulfur atoms. It is possible that the increased adsorbate-adsorbate interaction is enough to overcome the energy gained through the buckling of the metal atoms and to allow the S atoms to adsorb in every other fcc hollow site. This argument presupposes that the buckling of the metal surface is the most prominent interaction between unit cells and that the energy required to transform the $p(2 \times 2)$ into the $(\sqrt{3} \times \sqrt{3})$R30° is equal to the removal of the buckling. The almost identical Pt-S bond lengths of the $p(2 \times 2)$ and the $(\sqrt{3} \times \sqrt{3})$R30° structures support the assumption that local interactions around the adsorbate do not change, thus, leaving the metal atoms as the only suspected cause for this energy barrier. Total energy calculations are clearly needed to fully understand the energetics of these structural changes.

Our STM images (see Figure 4.6) for the $\begin{pmatrix} 4 & \bar{1} \\ \bar{1} & 2 \end{pmatrix}$ overlayer indicate possible clustering of sulfur on the surface. Clustering at higher coverages results in structures which defy any attempts to understand energetics. In the case of the $(2\sqrt{3} \times 2\sqrt{3})$R30° structure on the Re surface,[83] one finds that clustering results in adsorbate-adsorbate distances which are not quite bonding but definitely closer than the van der Waals distances. Clustering is also believed to take place on Cu(111)[87]. We assume that the same type of S-S bonding takes place in the higher coverage structure on Pt. In contrast to the above examples, no such clustering was found for the $c(4 \times 2)$ overlayers on Ru(0001)[89] or Mo(100)[88]. Strain-

relieving lateral displacements were even found for the Mo structure[88]. Obviously the next question is how the presence of the metal surface affects and is affected by either clustering or repulsion of adsorbed S atoms. This question awaits future research.

Chapter 5

Ethylidyne on Pt(111): Structure and Coverage

The thermal reaction of hydrocarbons on transition metal surfaces has been investigated with a variety of surface science techniques in the past. Probably the most intensively studied system in this respect is ethylene and its decomposition as a function of temperature on Pt(111)[90–111]. This reaction serves as a model system for understanding the interactions involved in heterogeneous catalytic reactions of hydrocarbons over metal catalysts[74]. Of the decomposition products, the relatively stable surface species ethylidyne is present at room temperature on Pt(111) and has also been observed on other metal surfaces[112–120].

In this chapter, which is based on Reference 121, we address the questions of surface relaxation and coverage of ethylidyne on Pt(111). The intimate relationship between surface relaxation and coverage allows LEED to unambiguously determine the correct model from the qualitatively different models which have been proposed. This was not possible in the earlier LEED analysis[92] which did not study the surface relaxations due to the prohibitively large computational requirements of conventional LEED analysis. Before we address these issues, we first describe the experimental preparation of the ethylidyne overlayer and the theoretical methods used to calculate the theoretical I-V curves. Next, we discuss structural results from different structural models obtained with searches which preserve the symmetry of the model. We examine the effect of hydrogen on the best-fit $p(2 \times 2)$ fcc site model. After this, we look at the effect of allowing the structural search to break the symmetry of

the reference model. We end this chapter by comparing our resulting best-fit structure to a similar structure found on the Rh(111) surface.

5.1 Background

Exposure of a Pt(111) surface to ethylene at room temperature or slightly above leads to a well-ordered overlayer showing a (2x2) pattern in low-energy electron diffraction (LEED)[90–92]. Several models were proposed for the adsorbed species in this overlayer[92–95]. LEED,[93] angular resolved ultraviolet photoelectron spectroscopy (ARUPS),[96] and high-resolution electron energy loss spectroscopy (HREELS)[97] identified the adsorbate as ethylidyne (CCH_3, or equivalently, C_2H_3). The HREELS spectra assignment was confirmed through a comparison with infrared adsorption spectroscopy of an organometallic complex, $(CH_3C)Co_3(CO)_9$[122].

The adsorbed species has been identified as ethylidyne, however, the density of the overlayer is still in question. The (2×2) LEED pattern can be interpreted as either a $p(2 \times 2)$ structure or a $p(2 \times 1)$ structure with three equivalent domain orientations. A $p(2 \times 2)$ structure would have either one or two molecules per unit cell (the latter being very tightly packed), corresponding to 0.25 or 0.5 monolayers (ML). A $p(2 \times 1)$ structure would have a coverage of 0.5 ML with one molecule per unit cell. Both coverages have been proposed in the literature. A coverage of 0.25 ML was originally assumed in both the LEED work,[92] and the HREELS study[97]. Several TDS studies,[99,106,107] a radio tracer study[108] and a nuclear reaction analysis[109] have favored the lower coverage of 0.25 ML. The 0.5 ML coverage was first proposed using quantitative X-ray photoelectron spectroscopy (XPS)[104]. Ion scattering investigations came to the same conclusion[101,105]. Yu and Gustafsson[101] proposed a $p(2 \times 2)$ honeycomb model with two molecules per unit cell in different sites. That model would account for a 0.5 ML coverage but would still maintain a $p(2 \times 2)$ periodicity and a three-fold site adsorption for the ethylidyne.

5.2 Experiment

Our experiments were carried out in a stainless steel ultrahigh vacuum (UHV) chamber. The sample was cleaned by repeated cycles of ion bombardment and annealing in oxygen until no impurities could be detected by Auger electron spectroscopy (AES), and

the LEED pattern of the clean surface was sharp and free of diffuse background intensities. The UHV instrumentation and sample preparations are described in Section 2.2. LEED measurements were taken using a digital LEED detector[12] (see Section 2.3.2). During the acquisition of a LEED pattern, the charge deposition is typically only about 10^{-5} electrons per surface unit cell. However, because a total charge of only about 10^{-2} electrons per surface unit cell was deposited during these experiments, the influences of electron beam damage on the results can be ruled out. Electron beam damage of hydrocarbon overlayers has been suggested by Freyer et al.[104] as a possible experimental difficulty. About 100 LEED patterns (at different energies) are necessary for a complete LEED experiment involving measurements of diffraction spot intensities versus electron beam energy (I-V curves). See Section 2.4 for additional experimental details related to the I-V curve measurements.

Different recipes for preparation of the ethylidyne overlayer were tested, and the resulting I-V curves were compared. In agreement with previous findings,[92] no significant difference was found between the I-V curves obtained after low temperature exposure followed by annealing to 400 K and those obtained after exposure at room temperature. The sharpest (2×2) LEED pattern can be generated by exposing the crystal to 1.5 to 2 Langmuir of ethylene at 250 K followed by brief annealing to room temperature (see Figure 5.1). Data acquisition was carried out at a temperature of 90 K. LEED patterns were recorded in the energy range from 30 to 250 eV in steps of 2 eV. I-V curves for diffraction spots that are symmetry equivalent under this condition were compared to verify normal incidence and were averaged to improve the quality of the data and enhance the signal-to-noise ratio. Surface preparation and LEED measurements were repeated and a total of four independent data sets were available to check reproducibility. I-V curves from the different sets showed excellent similarity and were averaged for additional noise reduction. A total of five integer and nine fractional order, symmetrically unrelated beams were generated using this procedure. The structural analysis was restricted to the (1,0), (0,1), (1,1), (1/2,0), (0,1/2) and (1/2,1/2) beams in the energy range from 100 to 250 eV, corresponding to a cumulative energy range of 850 eV. These beams have the largest experimental energy range and the lowest noise level. Following the structural analysis, the best geometry was confirmed using the whole experimental data set.

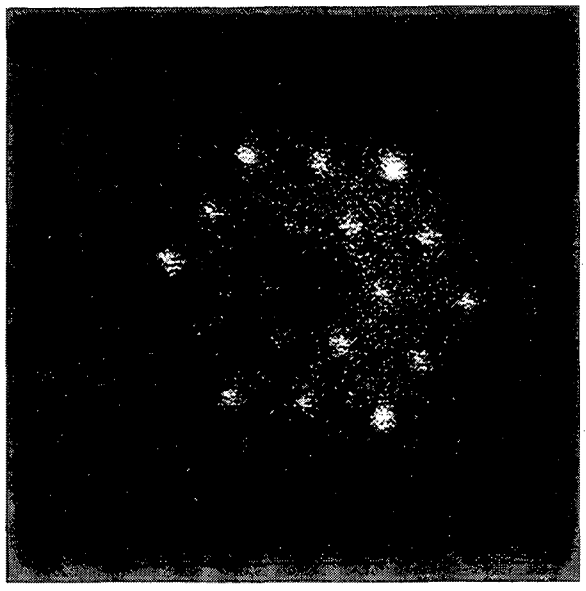

Figure 5.1: The Pt(111)-(2 × 2)-C_2H_3 LEED pattern at 120 eV and normal incidence. The low intensity on the lower left side of the LEED pattern is due to variations in the gain of the channel plates.

5.3 Theory

The main goal of this investigation was to test a variety of possible adsorption models and to allow for substrate atom displacements in order to consider adsorbate-induced relaxations. An automated search method based on the TLEED approximation[1] was used. Additional information on the search procedure can be found in Section 2.6. The model calculations were done using nine phase shifts. Up to 199 beams were necessary to achieve convergence for the interlayer multiple scattering in RFS. Electron damping was simulated by the imaginary part of the inner potential. It was set to $V_{0i} = -4.25$ eV based on a comparison of peak widths in the theoretical and experimental I-V curves. The hydrogen atoms were neglected in most of the models considered in the analysis due to their weak scattering power, except as noted explicitly in the refinement of the fcc hollow-site model. Thermal vibrations were modeled using temperature dependent phase shifts based on isotropic vibrations of the same amplitude for carbon and platinum. The Debye temperature of platinum was set to 250 K, and that of carbon was accordingly determined to be 1000 K. No fit of the Debye temperatures was attempted.

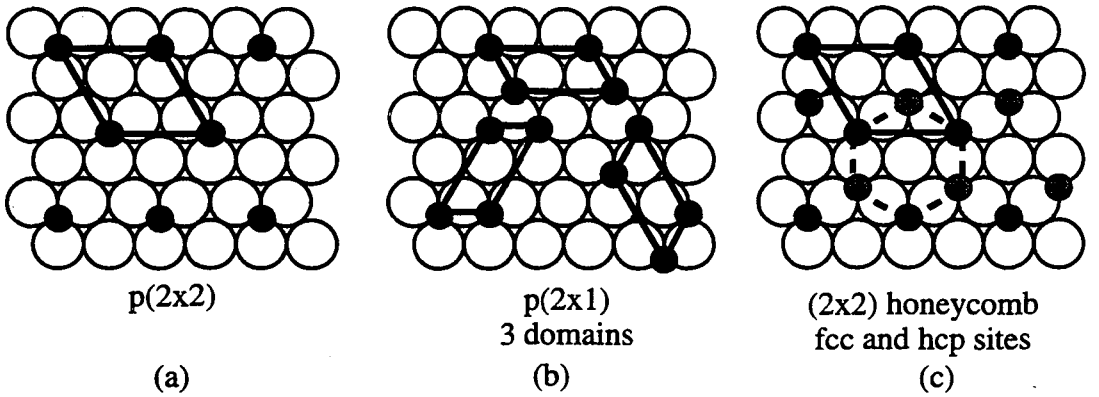

Figure 5.2: Possible unit cells compatible with the (2×2)-C_2H_3 LEED pattern on Pt(111), shown with adsorption in fcc or hcp hollow sites. a) $p(2 \times 2)$ model with one molecule per unit cell at 0.25 ML coverage. b) $p(2 \times 1)$ model with 0.5 ML coverage. Three different domains, rotated by 120°, are possible as displayed. c) $p(2 \times 2)$ honeycomb model[101] with two different sites (fcc and hcp hollows) per unit cell, accounting for a 0.5 ML coverage. The unit cell is indicated by the solid line, the honeycomb hexagon by the dashed line.

5.4 Structural Analysis

The structural analysis concentrated on finding the proper adsorption geometry for ethylidyne aligned normal or near normal to the surface. A variety of different adsorption sites (top, bridge, hcp and fcc hollows) and models representing both 0.25 ML and 0.5 ML coverage were tested. As outlined in Section 2.6, the TLEED search program allows for rapid calculation of many geometries within a certain segment of the parameter space. This capability was used to allow for geometry variations in the top two layers of the substrate for all models under consideration.

5.4.1 Symmetry-Preserving Structures

Models with $p(2 \times 2)$ periodicity were tested assuming a 0.25 ML coverage (see Figure 5.2a for a model with hollow site adsorption). In these models, the surface is constrained to keep the highest symmetry compatible with the superlattice unit cell, e.g. $p3m$ for the $p(2 \times 2)$ fcc hollow-site model. Top and bridge sites could be clearly ruled out based on R_p-factors; the top model yields an R_p-factor of 0.57, while for the bridge model no significant R_p-factor minimum could be found. Three different three-fold hollow site models were included in the analysis: an fcc site for the molecule, an hcp site, and a single carbon adsorbate in an fcc site. This last model was included to test the possibility of either a

completely disordered upper carbon atom or cracking fragments from thermal dissociation, even though the latter may seem unlikely. Calculations for an hcp geometry yielded an R_p-factor of 0.59; the model was therefore eliminated. The single carbon model in an fcc site resulted in an R_p-factor of 0.35. The fcc hollow site for a molecule turned out to be the overall best model with an R_p-factor of 0.288. To the upper carbon of this fcc best-fit geometry, three hydrogen atoms were added, but only a slight improvement of 0.014 in the R_p-factor could be achieved. Further refinements of this model, including the addition of hydrogen atoms, are discussed later.

Two models for a 0.5 ML coverage were tested, a $p(2 \times 1)$ fcc hollow-site model and a $p(2 \times 2)$ honeycomb structure. The $p(2 \times 1)$ hcp hollow-site model was not tested, because the structure of I-V curves is dominated by the local adsorption geometry and is, to a lesser extent, influenced by the periodic arrangement[123]. Due to this, a $p(2 \times 1)$ model with hcp hollow adsorption sites cannot be expected to yield a substantially better fit than the $p(2 \times 2)$ fcc hollow-site model. The $p(2 \times 1)$ overlayer can be ordered in 3 different domains rotated by 120° (see Figure 5.2b), producing a symmetrical (2x2) LEED pattern. Analysis of such a model with ethylidyne in fcc hollow sites yielded an R_p-factor of 0.42. The honeycomb model with a $p(2 \times 2)$ periodicity as suggested by Yu et al.[101] contains one fcc and one hcp hollow site in each unit cell due to packing requirements. The two sites form a honeycomb of six-fold rings with alternating types of sites separated by 3.20 Å (see Figure 5.2c). This model maintains a three-fold site for the ethylidyne and is consistent with HREELS results[122]. The best R_p-factor obtained for this model was 0.39.

Selected I-V curves calculated for the best-fit geometries in the different models are displayed and compared to the experimental data in Figure 5.3. We believe the discrepancy between theoretical and experimental curves in the region of high energy for the (1/2,0) and (0,1/2) beams, including those of the best-fit model, might be caused by experimental uncertainties due to the proximity of these beams to the edge of the detector. Table 5.1 lists R_p-factors obtained for the best-fit structures for the different models. Comparison with values assuming an unrelaxed substrate structure (labeled "R_p-C_2H_3 only") shows the extent of the improvements in I-V curves gained from allowing substrate relaxations (labeled "R_p-best fit"). A comparison of different models without actually fitting the substrate geometry would lead to the right conclusion in this particular study, but a distinction based on such high R_p-factors is ambiguous and might be misleading in some cases. Using Pendry's statistical estimate[47] we obtain $\Delta R_p = 0.056$ as range of uncertainty, or error bar, using

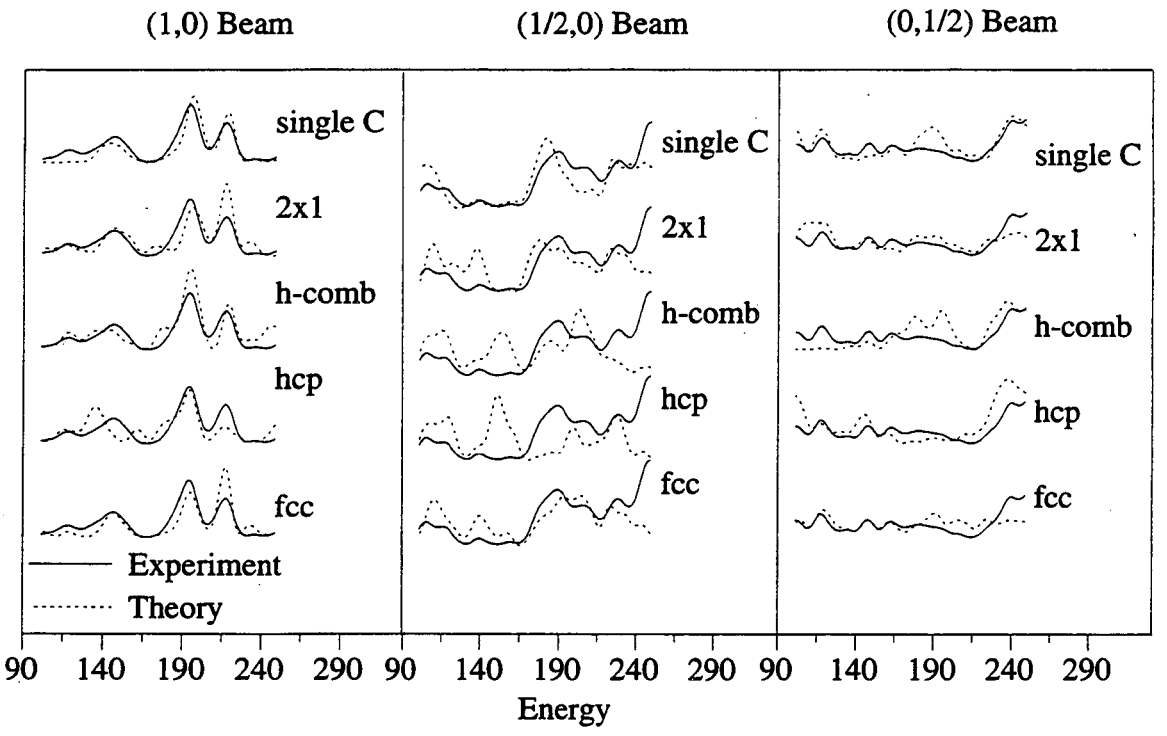

Figure 5.3: Selected best-fit Pt(111)-(2 × 2)-C_2H_3 I-V curves for the (1,0), (1/2,0) and (0,1/2) beams obtained for various models. Experimental curves (solid lines) are displayed on the same intensity scale together with the theoretical best-fit curves (dashed lines). The models shown are, from the bottom: $p(2 \times 2)$ fcc hollow-site ("fcc"), $p(2 \times 2)$ hcp hollow-site ("hcp"), $p(2 \times 2)$ honeycomb ("h-comb"), $p(2 \times 1)$ fcc hollow-site ("2x1"), and a single carbon $p(2 \times 2)$ fcc hollow-site ("single C").

Table 5.1: Resulting R_p-factor values for various ethylidyne models. The "R_p-best fit" column refers to models in which symmetry-allowed displacements of the molecule and symmetry-allowed relaxations of the first two metal layers were included. The "R_p-C_2H_3 only" of the fcc + hydrogen model is based on the $p(2 \times 2)$ fcc hollow-site best-fit geometry. Aside from this model all the R_p-factors in this column assume an unrelaxed substrate. The two values given for the fcc + hydrogen model are with hydrogen positions as displayed in Figures 5.8a and 5.8b, respectively.

Periodicity	Model	R_p-best fit	R_p-C_2H_3 only
0.25 ML coverage			
$p(2 \times 2)$	fcc	0.29	0.47
	fcc + H	0.27	0.30, 0.35
	fcc (Single C)	0.35	0.61
	hcp	0.59	0.71
	top	0.57	0.70
	bridge	no stable fit	0.71
0.50 ML coverage			
$p(2 \times 2)$	honeycomb	0.39	0.66
$p(2 \times 1)$	fcc	0.42	0.62

an R_p-factor of 0.29 as the reference. Hence the fcc hollow-site model for 0.25 ML (with or without hydrogen) is clearly favored over the $p(2 \times 1)$ fcc, the honeycomb and the single carbon species models.

The intrinsically lower symmetry of the $p(2 \times 1)$ model allows not only for the variation of more parameters, but also for a tilted geometry of the adsorbate. In fact, in the corresponding best fit, the carbon-carbon bond is tilted away from the surface normal by 8°. Comparing the $p(2 \times 1)$ and $p(2 \times 2)$ models in full symmetry by means of the R_2-factor actually slightly favors the $p(2 \times 1)$ with an R_2-factor of 0.122 as compared to 0.166. However, with the $p(2 \times 1)$ model, the tilt of the carbon-carbon bond goes in opposite directions for the R_2- and R_p-factor fits. Visual inspection of best-fit I-V curves reveals the different effect of the two R-factors on the search. The R_2-factor reproduces one (or a few) large peaks very well at the expense of several smaller peaks and peak positions, while the R_p-factor does just the opposite. (Compare "R2 $p(2 \times 1)$" and "Rp $p(2 \times 2)$" in Figure 5.4.) As a result, the best-fit I-V curves look much better for the $p(2 \times 2)$ model obtained using the R_p-factor than for the $p(2 \times 1)$ model obtained using the R_2-factor. Another way one can judge the quality of a structural fit is by comparing different subsets of data[6,124]. The structural difference between the resulting geometries should be small, indicating a correct structure. The searches directed by R-factor comparisons of the I-V curves were carried out separately for the fractional and integer order beam sets. The difference in geometry between structures obtained with different subsets is less than 0.05 Å in the $p(2 \times 2)$ model. The $p(2 \times 1)$ model yielded structural differences of up to 0.18 Å for perpendicular parameters. Even the lateral position of the top carbon atom changes by 0.56 Å between the two subsets. In the case of the $p(2 \times 2)$ model, for a fit corresponding to one set of beams the R_p-factor for the other set was around 0.4. However, in a similar analysis of the $p(2 \times 1)$ model, the unused beams yielded an average R_p-factor of 0.8. Altogether this is strong evidence that the $p(2 \times 1)$ model is incorrect, while the $p(2 \times 2)$ fcc hollow-site model corresponds to the correct geometry.

Figures 5.5 and 5.6 show the best-fit, symmetry-preserving geometry, while Table 5.2 lists the corresponding atomic coordinates. In this structure, the carbon-carbon bond length is 1.49 Å. The adsorption height is 1.21 Å as measured between the lower carbon atom and the average plane of the first layer. The first layer also contains a perpendicular buckling of 0.11 Å with the hollow site (three atoms) lifted outwards, so that the local adsorption height is 1.19 Å. Additionally, a lateral contraction of the hollow triangle

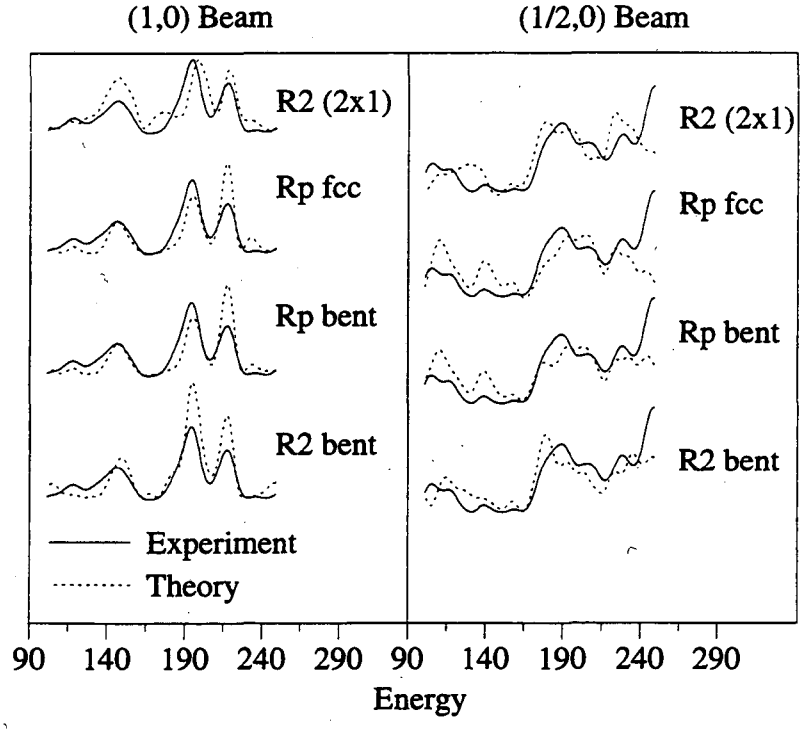

Figure 5.4: Pt(111)-(2 × 2)-C_2H_3 I-V curves showing the effect of a tilted carbon-carbon bond in the $p(2 \times 1)$ and $p(2 \times 2)$ fcc hollow-site models. Top I-V curves correspond to the best fit for the $p(2 \times 1)$ periodicity allowing a molecular tilt obtained with the R_2-factor ("R2 (2x1)"). The second set of I-V curves shows the best R_p-factor fit for a $p(2 \times 2)$ model with no tilt allowed ("Rp fcc"). The final two rows of I-V curves show a low symmetry model in $p(2 \times 2)$ periodicity with a tilt allowed for the molecule and first layer obtained with either the R_p-factor ("Rp bent") or the R_2-factor ("R2 bent").

Table 5.2: Cartesian coordinates of the best-fit, symmetry-preserving $p(2\times2)$ fcc hollow-site model. X and Y are coordinates parallel to the surface; Z is perpendicular to the surface and positive towards the bulk. Error bars in terms of center of mass distances and buckling are shown in Figures 5.5 and 5.6.

		X	Y	Z
1	C	0.00	0.00	0.00
2	C	0.00	0.00	1.49
1a	Pt	0.00	1.49	2.68
1a	Pt	-1.29	-0.75	2.68
1b	Pt	1.29	-0.75	2.68
2	Pt	0.00	-3.20	2.79
3a	Pt	0.00	-1.16	5.02
3b	Pt	-1.39	0.80	5.02
3c	Pt	1.39	0.80	5.02
4	Pt	0.00	3.20	4.94
5	Bulk	0.00	0.00	7.26

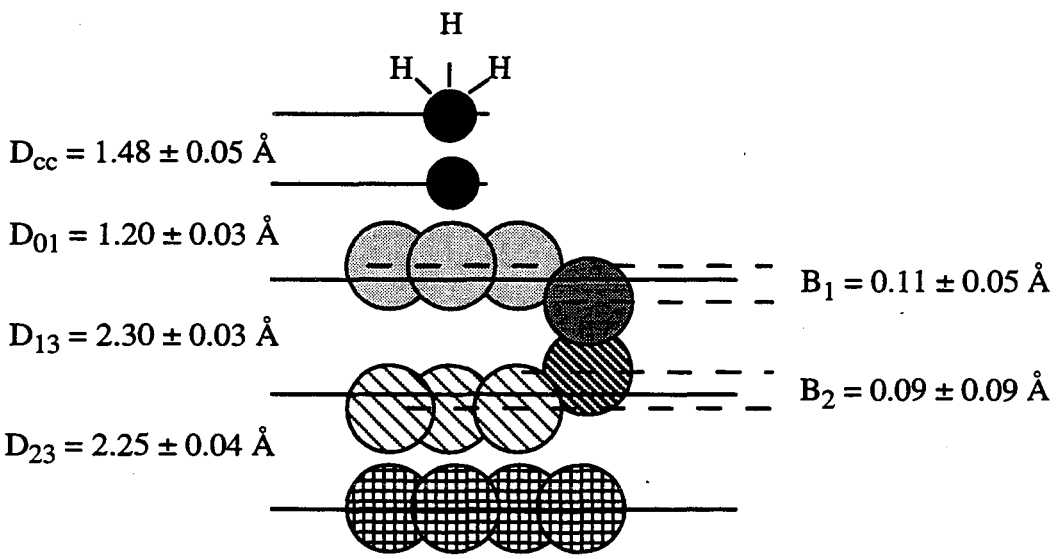

Figure 5.5: Side view of the best-fit, symmetry-preserving, fcc hollow-site model in $p(2\times2)$ periodicity for CCH_3 on Pt(111) with a coverage of 0.25 ML. Shading distinguishes the two types of atoms in each substrate layer due to buckling in the ethylidyne model. The buckling is exaggerated for visual representation. The distance between the lower carbon and the first metal layer (d_{01}) and interlayer spacings (d_{12} and d_{23}) are measured between average perpendicular positions of the planes (solid lines). The total buckling amplitudes within the first two metal layers are represented by b_1 and b_2, respectively.

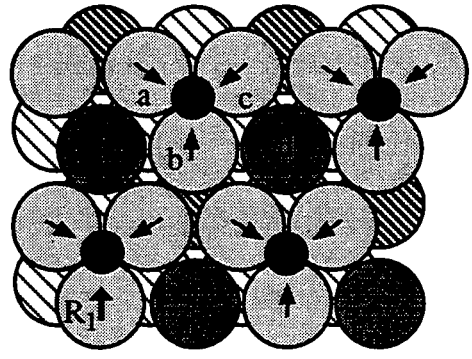

$R_1 = 0.1 \pm 0.08$ Å $\quad R_2 = 0.0 \pm 0.09$ Å

Figure 5.6: Top view of the best-fit, symmetry-preserving, $p(2 \times 2)$ fcc hollow-site model for ethylidyne on Pt(111), exhibiting a radial contraction (R_1) of the metal triangle that makes up the hollow site. The radial displacement of the three metal atoms in the second layer (R_2) is not shown. Atoms are shaded corresponding to those in Figure 5.5. No rotation in the first layer and no lateral motion in the second layer were detected. The hydrogen positions are not depicted.

is observed with radial displacements of 0.11 Å giving a carbon-platinum bond length of 1.91 Å. The average first-to-second layer spacing is 2.30 Å. In the second layer a buckling of 0.08 Å in the opposite direction is observed, with the three atoms underneath the molecule being pushed into the substrate. This corresponds to a local expansion of the substrate underneath the adsorbate by 0.08 Å from the bulk value of 2.26 Å. In Figure 5.7, I-V curves are displayed for fits allowing different degrees of relaxation. A significant improvement, particularly visible in the fractional order I-V curves, is achieved due to the addition of buckling. This addition lowers the R_p-factor from 0.40 to 0.33. The improvement due to lateral displacement is $\Delta R_p = 0.04$ and is possibly significant, as the lateral displacement is slightly larger than the estimated error bar. Using the complete experimental data set of five integer and nine fractional order beams, a calculation was done for this model allowing full relaxation. The structural result obtained stays within 0.01 to 0.02 Å of the geometry obtained with 6 beams, which is inside the error margin.

5.4.2 Addition of Hydrogen

The $p(2 \times 2)$ fcc hollow-site model was found to be the best-fit structure among all sites and coverages under consideration. However, the improvement in the R_p-factor from the addition of hydrogen is not large enough to unambiguously determine the H positions. In

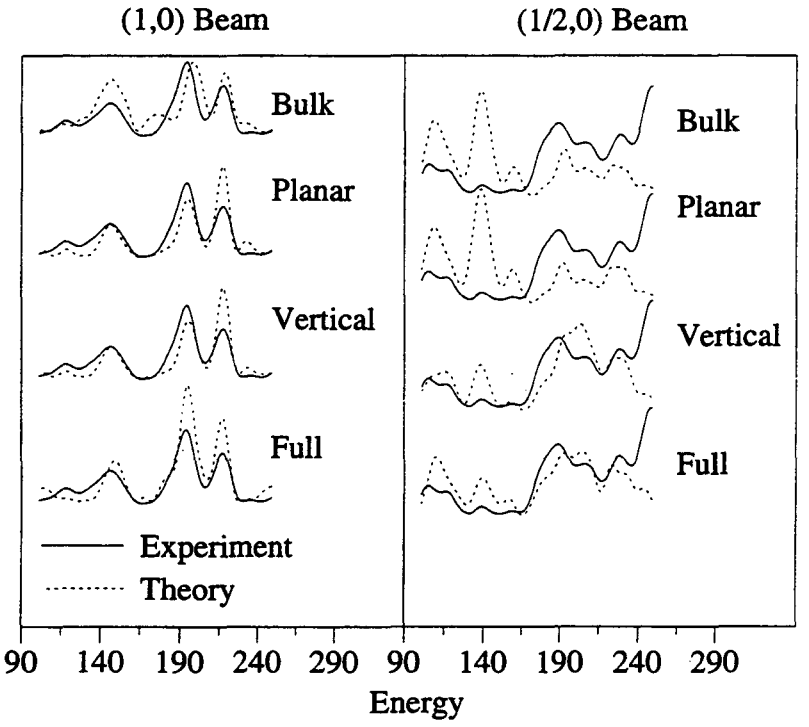

Figure 5.7: Pt(111)-$p(2 \times 2)$-C_2H_3 I-V curves of the (1,0) and (1/2,0) beams for different degrees of relaxation. The top I-V curves correspond to an unrelaxed bulk geometry for the substrate and an ethylidyne molecule added at a carbon-carbon distance corresponding to hard core radii ("bulk"). The second set of I-V curves is obtained with layer distances (d_{CC}, d_{01}, d_{12} and d_{23} in Figure 5.5) relaxed in the search but without layer buckling ("planar"). The third set of I-V curves corresponds to a best-fit model which additionally includes buckling (b_1 and b_2 in Figure 5.5) within the layers ("Vertical"). In the final set of I-V curves, radial lateral displacements (r_1 and r_2 in Figure 5.5) were included ("Full"). The corresponding R_p-factors for the four different models are 0.47, 0.40, 0.33 and 0.29, respectively.

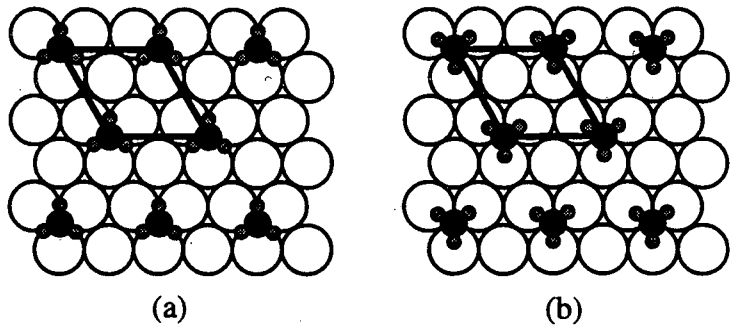

Figure 5.8: Orientation of the carbon-hydrogen bond in each model used as a reference structure to analyze hydrogen presence and position. The projection of one carbon-hydrogen bond points in the $[\bar{1}\bar{1}2]$-direction of the crystal in (a) and in the $[1\bar{2}1]$-direction in (b).

fact, the addition of hydrogen to the best-fit structure obtained for the fcc model with bond lengths and angles comparable to an expected sp^3-like CH_3 group initially leads to a rise in the R_p-factor. Two high-symmetry arrangements were tested. In one case, the hydrogen atoms are pointing toward the bridge (the projection of the carbon-hydrogen bond parallel to the surface points in the $[\bar{1}\bar{1}2]$-direction of the crystal). In the other, they are pointing toward the next atom top (in the $[1\bar{2}1]$-direction), as illustrated in Figure 5.8. The carbon-hydrogen bond angle is 109.3° with a bond length equal to 1.09 Å. The hydrogen is tilted 19.3° away from the surface. The R_p-factors obtained for those reference structures are 0.35 for the $[\bar{1}\bar{1}2]$-oriented H and 0.30 for the $[1\bar{2}1]$-oriented H, respectively. Corresponding I-V curves are shown as the two upper curves in Figure 5.9 for the (1/2,0) and (0,1/2) beams. Small changes in peak heights and shoulders are responsible for the poorer fit. It should be noted that hydrogen visibly affects the calculated fractional order I-V curves up to 250 eV. Integer order I-V curves are basically insensitive to the additional hydrogen atoms. Search runs with and without hydrogen included as a parameter reduce the R_p-factor to 0.274. However, the hydrogen positions are not stable in this fit, and cannot be determined with certainty. Furthermore, as Figure 5.9 shows, the I-V curves of the resulting fit come remarkably close to those obtained for the model without hydrogen (see "3H" vs. "No H" plots) where the R_p-factor was 0.288. There is no specific feature in the curves that is convincingly improved by the inclusion of hydrogen; the fitting procedure removes all new features introduced by the addition. This seems to indicate that the experimental curves contain no hydrogen contribution, implying that the hydrogen atoms are not contributing to the ordered $p(2\times2)$ periodicity and are relatively free to rotate around the carbon-carbon

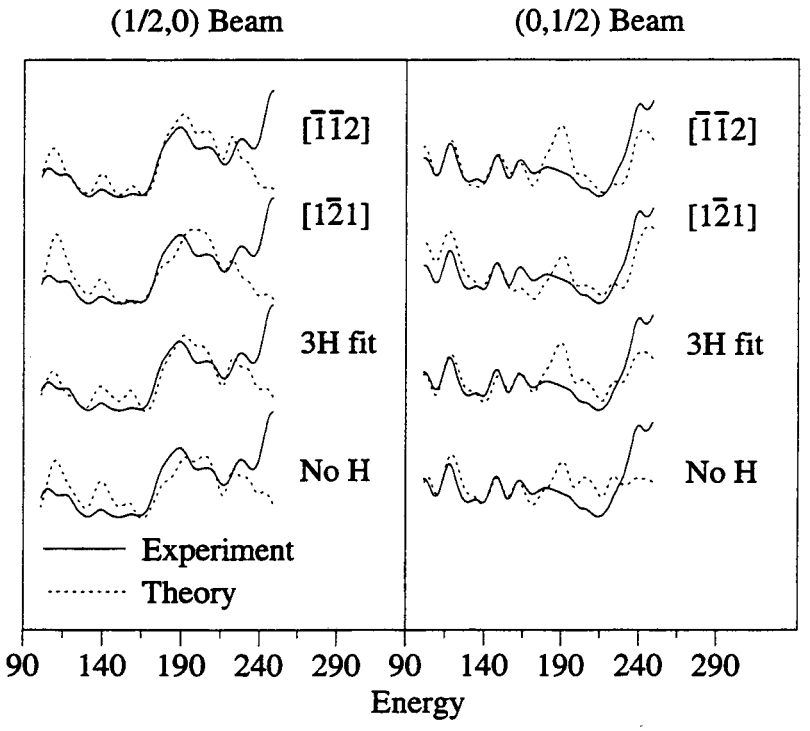

Figure 5.9: Fractional (1/2,0) and (0,1/2) beam I-V curves with and without hydrogen included in the calculations. The top two sets of I-V curves correspond to the initial hydrogen positions displayed in Figure 5.8 ("[$\bar{1}\bar{1}$2]" and "[1$\bar{2}$1]"). The third set of I-V curves shows the best fit obtained with fitted hydrogen positions ("3H fit"). The best fit without hydrogen is plotted at the bottom ("No H") for comparison.

bond axis at 90 K.

5.4.3 Symmetry-Breaking Features

In all models discussed so far, symmetry was constrained as much as possible. For the $p(2 \times 2)$ fcc hollow-site model, for example, this means that the carbon-carbon bond must be oriented strictly normal to the surface. The three Pt atoms forming the triangular hollow site are treated identically. In Figures 5.5 and 5.6 they are the lightly shaded atoms, labeled a, b, and c. They can have a different perpendicular position than the fourth atom in the unit cell (shaded darker and labeled d in Figures 5.5 and 5.6). The hollow site can be contracted or expanded laterally as indicated by the arrows and label r_1 in Figure 5.6. But a rotation of the triangle or an asymmetric buckling is not allowed, as it would reduce the symmetry of the model. Second-layer atoms (dashed atoms in Figures 5.5 and 5.6) are restrained in the same way.

Displacements which lowered the symmetry were included in the search for the $p(2 \times 2)$ fcc hollow-site model by averaging with equal weights over as many differently oriented domains as necessary to recover the symmetrical (2x2) LEED pattern. First, an off-normal carbon-carbon bond was considered but restricted to motions within a mirror plane of the crystal. Second, with the same symmetry, both carbon atoms and the first layer were allowed to move. Third, symmetry was given up completely for the molecule and the first layer. The second layer was included last. One feature which was observed in the first step is that the carbon-carbon bond tilts by 7° in the $[1\bar{2}1]$-direction, or towards the top site. The angle value is only slightly altered to 6° and 8°, respectively, in the other two steps. In step 2, a buckling of 0.06 Å is found for the three nearest-neighbor Pt atoms (a, b, and c in Figure 5.6), corresponding to a tilt in the same direction as the molecular tilt. Note that the average normal position of the triangle changes by less than 0.01 Å. The R_p-factor drops from 0.29 for the fully symmetric $p(2 \times 2)$ fcc hollow-site model to 0.28 in step 1 and 0.25 in step 2. The third and last step changes the R_p-factor by less than 0.01 although many more parameters are made available to the fitting procedure. Hence, step 2 seems to contain all significant features of the model. In Figure 5.4 the improvement in the I-V curves is shown (indicated as "Rp bent"). For comparison a fit obtained with the R_2-factor is also shown ("R2 bent"). Table 5.3 lists the corresponding atomic coordinates of the R_p-bent geometry.

Table 5.3: Cartesian coordinates of the best-fit, symmetry-breaking $p(2 \times 2)$ fcc hollow-site model. Error bars for vertical displacements of C_1, C_2, first-layer platinum atoms (1a-c and 2) and second-layer platinum atoms (3a-c and 4) are 0.10, 0.04, 0.07 and 0.08 Å, respectively. The typical error bar for lateral displacements is 0.15Å.

		X	Y	Z
1	C	-0.06	0.22	0.00
2	C	0.05	0.03	1.47
1a	Pt	0.07	1.63	2.59
1a	Pt	-1.27	-0.82	2.72
1b	Pt	1.25	-0.78	2.62
2	Pt	-0.03	-3.23	2.76
3a	Pt	0.02	-1.59	4.98
3b	Pt	-1.38	0.84	5.00
3c	Pt	1.38	0.83	4.99
4	Pt	-0.02	3.11	4.90
5	Bulk	0.00	0.00	7.26

A similar molecular tilt was reported recently for CO on Ru(0001)[40]. The tilt was interpreted as an anharmonic wagging vibration. In that study, scattering from molecules tilted in three directions according to the symmetry of the substrate was averaged coherently to simulate the average positions of the molecule in the anharmonic vibration. Using coherent (amplitude) or incoherent (intensity) averaging we find the same tilt angle of the ethylidyne molecule and the coordinated tilt in the substrate. We assume our findings indicate the presence of an anharmonic wagging mode vibration for ethylidyne on Pt(111). The R_p-factor value slowly decreases as one moves away from the surface normal and then sharply increases after the R_p-factor minimum, which occurs at a tilt angle of 6°. This asymmetrical nature leads to an asymmetric error bar of 5° in the direction of smaller values of the tilt angle and 2° in the direction of larger values.

It should be noted that the R_2-factor for the low symmetry $p(2 \times 2)$ model has dropped to the level obtained for the $p(2 \times 1)$ model, so that the previous difference can be attributed to the difference in the number of fit parameters rather than a preference for one model over the other. Again, by visual judgment, the I-V curves obtained using the R_2-factor do not seem to reproduce the experiment as well as the I-V curves obtained from a fit with the R_p-factor. The R_2-factor seems to be less efficient in the refinement procedure than the R_p-factor according to our experience in this study.

5.5 Conclusions

The present LEED crystallography study of ethylidyne adsorbed on Pt(111) strongly favors the fcc hollow adsorption site in a $p(2 \times 2)$ rather than a $p(2 \times 1)$ periodicity, corresponding to a 0.25 ML coverage and confirming the site determination found in an earlier LEED study[92]. Additionally, we have found adsorbate-induced relaxations of the substrate in the form of buckling, where the three Pt atoms nearest to the adsorbate site move upward in the first layer and downward towards the bulk in the second layer. This is equivalent to a local expansion of the metal-metal interlayer spacing underneath the adsorbate. A corresponding analysis of ethylidyne on Rh(111),[11] also with a $p(2 \times 2)$ periodicity, yielded an hcp hollow site; it involves essentially the same buckling in the first layer, but an outward displacement of the atom directly below the adsorbate in the second metal layer. In addition, the triangle of first-layer metal atoms which forms the hollow site contracts laterally for ethylidyne on Pt(111), but expands on Rh(111).

The structural refinement found no hydrogen contributions in the experimental data, although hydrogen can visibly affect theoretical I-V curves. This indicates that the hydrogen atoms are relatively free to rotate around the carbon-carbon bond axis and do not contribute to the ordered structure. In the best-fit, symmetry-breaking model the carbon-carbon bond tilts towards the top site (in the $[1\bar{2}1]$-direction) by 6°. This tilt is accompanied by a slight buckling of the three-fold site. We interpret this tilt to be the result of thermal wagging vibrations of the ethylidyne about the surface normal. Similarly, Over et al.[40] have reported a wagging of the carbon-oxygen axis for CO adsorption on Ru(0001).

Models with 0.50 ML coverage can clearly be ruled out, as can all alternative sites under consideration. It is unclear how the discrepancies in coverage measured in a variety of investigations can be resolved, especially since the accuracy of the coverage determinations leaves no room for overlap between the two values of 0.25 ML and 0.50 ML. However, a recent joint study using nuclear reaction analysis and XPS supports the 0.25 ML model.[125] They believe that the earlier XPS measurements[104] underestimated the C_{1s} intensity of the CO, resulting in an incorrect finding of higher coverage for the ethylidyne. The large shake-up intensity for CO requires a larger energy range than used in earlier measurements in order to reliably measure the total quantity of the adsorbate on the surface.[125] There remains a discrepancy between the present results and the ion beam result.[101,105] However, in light of our results and the new XPS and nuclear reaction analysis,[125] we believe that

the $p(2 \times 2)$ 0.25 ML model for ethylidyne is correct.

Chapter 6

Surface Structures of NO on Pt(111) and Ni(111)

The sensitivity of low energy electron diffraction (LEED) to the position of the surface atom's atomic core allows one to unambiguously assign the correct adsorption site. In this chapter, which is based on References 126 and 66, we use LEED to address the controversial adsorption site for ordered nitric oxide (NO) overlayers on the Pt(111) and Ni(111) surfaces. Determining the interaction of NO with metal surfaces is important not only for understanding the catalytic reduction of NO, but also from a more fundamental standpoint due to the molecular similarities between NO and CO. Structural analysis of the surface geometry of such systems is the first step in this understanding. We have determined hollow-site adsorption for the Pt(111)-$p(2\times2)$-NO and the Ni(111)-$c(4\times2)$-2NO structures and have found that NO induces surface relaxation in both metals.

In this chapter, we first focus on the experimental preparation of the NO structures on Pt(111) and Ni(111). After an introduction to the theory, the structural analysis of the LEED intensity vs. energy (I-V) curves using an automated search method based on the TLEED approximation is described. This discussion is followed by a comparison of the two resulting structures with other LEED structures and an explanation of the reasons behind the discrepancy between LEED results and vibrational site assignments.

6.1 Introduction

A variety of experimental techniques have been used to determine the adsorption geometry and behavior of NO on Pt(111) and on Ni(111)[16,55,127–147]. Vibrational spectroscopy, both high resolution electron loss spectroscopy (HREELS)[134–136] and infrared reflection spectroscopy (IRS),[137–139] has identified top and bridge sites as possible NO adsorption sites based on a comparison of the stretching frequency of NO on the surface to that of NO in inorganic nitrosyl compounds. Hollow-site adsorption is therefore unexpected based on current interpretations of vibrational spectroscopy data[134–139]. However, direct interpretation of the binding geometry based on vibrational spectroscopy is problematic due to the strong correlation between stretching frequency and the effective charge on the NO group[141,142]. In addition, vibrational coupling between NO molecules can complicate the interpretation of vibrational spectra[131,137]. Electron stimulated desorption ion angular distributions (ESDIAD),[141] angular-resolved ultraviolet photoelectron spectroscopy (ARUPS),[142] photoelectron diffraction (PD),[143–145] and Auger photoemission[146] experiments on the Ni(111)-$c(4 \times 2)$-2NO structure all indicate a molecular arrangement in which the NO is perpendicular to the surface. Unfortunately, these experiments were unable to yield complete or convincing structural information. Our hcp+fcc model for Ni(111) confirms a recent site determination by surface extended x-ray adsorption fine structure (SEXAFS)[16] and by a concurrent LEED analysis.[147] No additional structural information has been available for Pt(111).

Expectation of a top or bridge bonded NO on Pt(111) and on Ni(111) also arises from the similarities between NO and CO. In inorganic chemistry, the similarity of molecular orbitals leads to bonding in metal nitrosyl complexes which is comparable to that in many metal carbonyl complexes.[148] Furthermore, when coadsorbed with ethylidyne on Rh(111), NO and CO occupy the hollow adsorption sites[149] In addition, NO and CO form almost identical 0.75 ML coverage (2×2) structures on Rh(111)[150]. However, the additional unpaired electron of the NO molecule enables it to assume a bent geometry in nitrosyl complexes which is not found in metal carbonyls. One striking example of the difference between NO[127,136] and CO[151] adsorption on metal surfaces is the significant lack of richness in LEED patterns resulting from NO adsorption as a function of coverage.

6.2 Experiments

The experiments were carried out in two separate stainless steel ultrahigh vacuum (UHV) chambers. The samples were cleaned by repeated cycles of ion bombardment and annealing in oxygen until no impurities could be detected by Auger electron spectroscopy (AES), and the LEED pattern of the clean surface was sharp and free of diffuse background intensities. The UHV instrumentation and sample preparations are described in Section 2.2. LEED data were collected for the Pt crystal using a digital LEED detector[12] (see Section 2.3.2). For the Ni(111) experiment, LEED data were collected by Varian 4-grid LEED optics with an off-axis electron gun. A Dage-MTI SIT-68 high-sensitivity video camera interfaced with a PC was used to digitalize the LEED pattern on the fluorescent screen of the Varian LEED optics (see Section 2.3.1). Additional information related to the I-V curve measurements can be found in Section 2.4.

6.2.1 NO Adsorption on Pt(111)

For the adsorption of NO on Pt(111), NO was introduced into the chamber through a stainless steel gas manifold connected to a leak valve. The gas purity was analyzed using a quadrupole mass spectrometer. Initially the NO gas was contaminated by CO from the oxidation of carbon in the gas line. However, after flushing the gas line and the leak valve several times, the CO concentration was reduced below detection limits. Because of conflicting studies of the (2×2) overlayer, several preparation methods for the overlayer were tried. Adsorption at room temperature gave a fair (2×2) LEED pattern; however, the presence of additional diffuse intensities indicated some disorder or dissociated NO. Above 290 K, but below the desorption temperature, the ordered pattern disappears. The pattern reappears once the crystal is cooled below 290 K, indicating a surface order to disorder phase transition. The best preparation was achieved by adsorbing 1 Langmuir (L) of NO at 90 K followed by annealing to 250 K, giving the sharp (2×2) LEED pattern shown in Figure 6.1. After the preparation, the crystal was cooled to 90 K and the I-V curves were measured from 90 to 250 eV at normal incidence. Four different LEED experiments were performed and the resulting I-V curves were compared and averaged. Normal incidence was confirmed by the agreement between symmetry equivalent beams. A total of three integer order symmetry-averaged beams, the (1,0), (0,1) and (1,1), and three fractional order symmetry-averaged beams, the (1/2,0), (0,1/2) and (1/2,1/2), were used in the structural search for a total

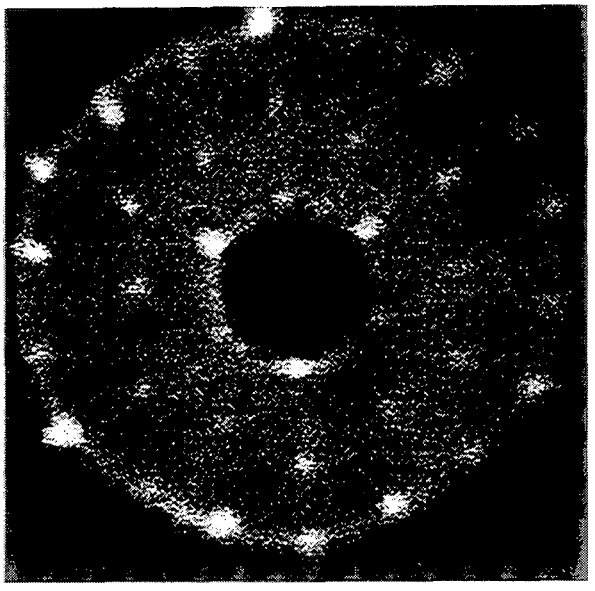

Figure 6.1: The LEED pattern of the Pt(111)-$p(2 \times 2)$-NO overlayer at 120 eV and normal incidence.

energy range of 800 eV. The energy range of the (1/2,0), (0,1/2) and(1/2,1/2) fractional order beams was limited by their low intensities at higher energies. Higher order fractional beams were too weak to collect. In addition, I-V curves for the (1,0), (0,1), (1,1), (2,0) and (0,2) beams of the clean surface were measured from 100 to 250 eV at normal incidence.

6.2.2 NO Adsorption on Ni(111)

For the Ni(111) surface, a complex LEED pattern (shown in Figure 6.2) was initially formed after exposure to 6 L of NO at 190 K. After heating to 330 K, the complex LEED pattern became a $c(4 \times 2)$ pattern (See Figure 6.3). AES showed a loss of approximately 10% of surface NO upon heating. In about 30 minutes, the $c(4 \times 2)$ LEED pattern began to degrade due to electron beam damage. Additional heating to 420 K yielded another complex LEED pattern shown in Figure 6.4. The pattern is currently interpreted to be a reconstruction of the (111) surface into the (100) surface[152]. Following the preparation of a sharp $c(4 \times 2)$ LEED pattern, the crystal was cooled to 190 K and I-V curves were measured from 30 to 350 eV at normal incidence. A total of two integer order symmetry-averaged beams, the (1,0) and the (0,1), and eleven fractional order symmetry-averaged beams, the (-1/4,3/4), (3/4,-1/4), (1/2,1/2), (3/4,-3/2), (1/4,1/4), (-1/4,-3/2), (3/4,3/2),

Figure 6.2: Initial LEED pattern for NO adsorption on Ni(111) at 83 eV and normal incidence.

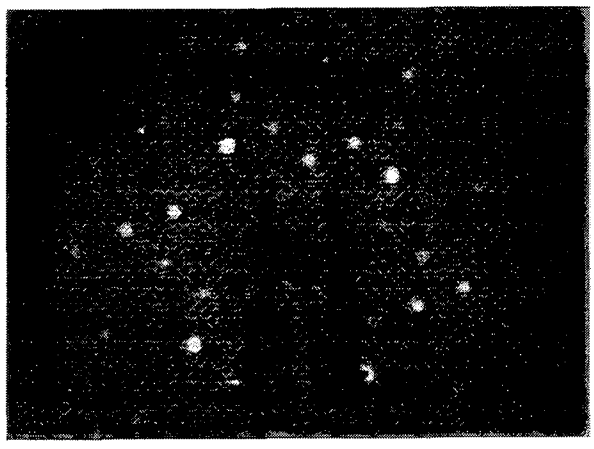

Figure 6.3: The LEED pattern of the Ni(111)-$c(4 \times 2)$-2NO overlayer at 82 eV and normal incidence.

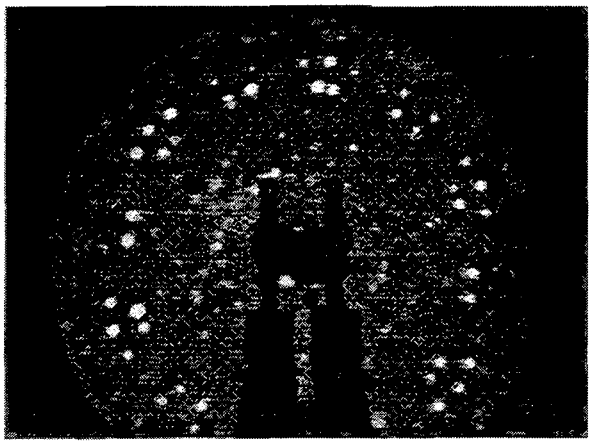

Figure 6.4: The LEED pattern at 77 eV and normal incidence formed by heating the NO layer to 420 K.

(-1/2,3/2), (3/2,-1/2), and (1/2,-1/2), were used in the structural search for a total energy range of 2400 eV. In addition, I-V curves for the (1,0), (0,1) and (1,1) beams of the clean surface were measured from 70 to 300 eV at normal incidence.

6.3 Theory

In addition to determining the adsorption site, we wished to investigate adsorbate-induced relaxations in the substrate atoms. An automated search method based on the TLEED approximation[1] was used. Additional details on the search procedure can be found in Section 2.6. Nine spin-averaged phase shifts, generated from muffin-tin model potentials formed from relativistic atomic wavefunctions, were used to compute multiple scattering within a layer. Scattering between the layers and towards the bulk was modeled using renormalized forward scattering (RFS). Up to 199 beams were necessary to achieve convergence for the interlayer multiple scattering in RFS. Electron damping was simulated by the imaginary part of the optical potential and was set to $V_o = -4.25$ eV. Thermal vibrations were modeled using temperature dependent phase shifts. These phase shifts were based on isotropic vibrations of the same amplitude for the NO molecule and metal atoms. The Debye temperature of platinum was set to 250 K, which was determined by fitting the clean surface data[52] (see Section 3.3), and that of the NO molecule was determined to be 640 K accordingly. For the nickel atoms a bulk Debye temperature of 380 K was used; implying a

Debye temperature of 520 K for the NO molecule. Due to the agreement between theoretical and experimental I-V curves for the clean Ni(111) surface, this value was not optimized. No further fit of the Debye temperatures for the NO molecules or the metal atoms was attempted.

6.4 Results

This section is divided into two parts. The first deals with the Pt(111)-NO structure, the second with the Ni(111)-2NO structure. In each case, different structural models are first discussed, followed by a description of the best-fit structure along with refinements. For both models, the fit between the theoretical and experimental I-V curves was quantified by Pendry's R-factor (R_p-factor)[47] which emphasizes peak positions in the spectra at the expense of absolute values. Error bars were estimated using Pendry's method[47].

Analysis of the Pt(111)-$p(2\times2)$-NO and the Ni(111)-$c(4\times2)$-2NO overlayers began by optimizing the NO bond length, the height of the molecules above the surface, the buckling of the topmost metal layer and the relaxation of the topmost metal-metal interlayer spacing for various adsorption sites. After the best structure was identified, we refined the buckling of the second metal layer, the relaxation of the second metal-metal interlayer spacing and the lateral displacements consistent with the symmetry of the overlayer.

6.4.1 Clean Surfaces: Pt(111) and Ni(111)

Before the structural analyses of NO on Pt(111) and Ni(111) were performed, an I-V analysis of each clean surface was carried out. The results show excellent agreement with other experimental results[57,59,67,153,154]. The first and second interlayer spacings of the Pt(111) clean surface were determined to be 2.29 ± 0.01 and 2.27 ± 0.03 Å, respectively, with an R_p-factor of 0.15. This corresponds to a 0.03 ± 0.01 Å expansion of the first metal layer of the ideally terminated Pt(111) clean surface. Within its error bars, the second interlayer spacing of the Pt clean surface agrees with the bulk value of 2.265 Å. Additional details can be found in Section 3.3; the best-fit I-V curves are shown in Figure 3.2, and the side view of the surface is illustrated in Figure 3.3. For the Ni(111) clean surface the first and second interlayer spacings were 2.01 ± 0.01 and 2.02 ± 0.02 Å, respectively, with an R_p-factor of 0.08. This corresponds to a 0.02 ± 0.01 Å contraction of the ideally terminated, clean Ni(111) surface. Again, within its error bars, the second interlayer spacing agrees

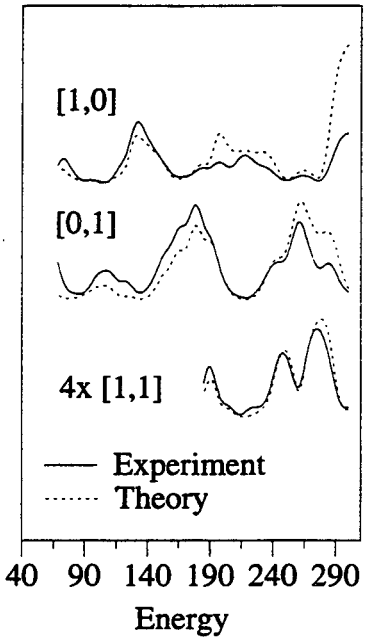

Figure 6.5: Experimental and theoretical I-V curves for the best-fit clean Ni(111)(1 × 1) surface with an R_p-factor of 0.08. The side view of this surface is shown in Figure 6.6.

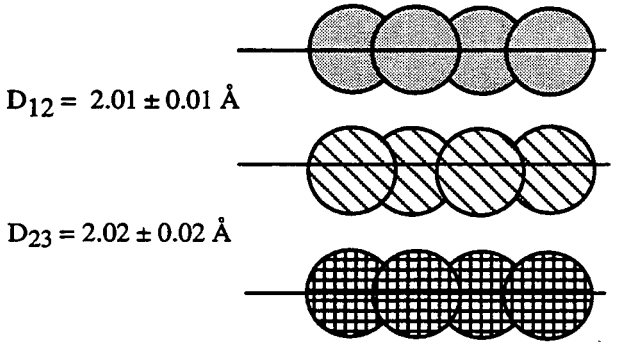

Figure 6.6: The side view of the best-fit clean Ni(111)-(1 × 1) surface with an R_p-factor of 0.08.

with the bulk value of Ni, 2.03 Å. The best-fit I-V curves for the clean Ni(111) surface are shown in Figure 6.5; the side view of the surface is illustrated in Figure 6.6. Notice the good agreement between the theoretical and experimental I-V curves below 100 eV, as compared to the curves for Pt(111).

Table 6.1: R_p-factor values for various Pt(111)-$p(2 \times 2)$-NO models. "NO only" refers to optimization of the NO bond length and height. "1D" refers to the addition of perpendicular displacements of the first metal layer consistent with the symmetry of the overlayer.

Periodicity	NO only	1D
$p(2 \times 2)$ 0.25 ML coverage		
fcc	0.35	0.32
hcp	0.63	0.62
bridge	0.59	0.58
top	0.69	0.69
O in fcc	0.59	0.52
N in fcc	0.61	0.48
$p(2 \times 1)$ 0.50 ML coverage		
fcc	0.42	0.40

6.4.2 Pt(111)-$p(2 \times 2)$-NO

Four different high-symmetry adsorption sites, the hcp, fcc, top and bridge, were tried for the $p(2 \times 2)$ overlayer on Pt(111) assuming 0.25 ML coverage and a perpendicular NO molecule. The NO molecule and the first metal layer were included in the structural search. Only displacements consistent with the three-fold rotational and mirror plane symmetries ($p3m$) of the overlayer were allowed. As a check for decomposition, O or N atoms adsorbed in the fcc hollow site were also tried assuming 0.25 ML coverage. In addition, we tested a $p(2 \times 1)$ fcc hollow site model with 0.5 ML coverage, which would yield a (2×2) diffraction pattern after averaging over the three possible domains. Displacements preserving the mirror plane were allowed for the NO molecule and the first metal layer for the $p(2 \times 1)$ model. This model is unlikely due to the agreement on the 0.25 ML coverage for NO on Pt(111) in previous experiments[55,129,130]. Indeed, the R_p-factor for this model is larger than that for the $p(2 \times 2)$ fcc-site model. The R_p-factors for the different models are shown in Table 6.1. The R_p-factor for the fcc site is considerably better than that for all other sites. In addition, there is a very small difference between the R_p-factors for optimization including only the vertical coordinates of the NO molecule and optimization when the vertical coordinates of the first metal layer are added. This is reflected by the 0.06 Å error bar for the buckling of this layer.

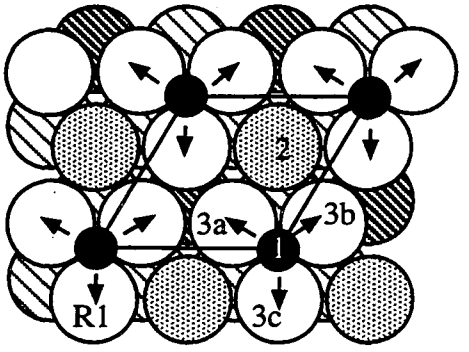

$R_1 = 0.03 \pm 0.10$ Å

Figure 6.7: Top view of the best-fit Pt(111)-$p(2 \times 2)$-NO surface structure with an R_p-factor of 0.28. A unit cell is outlined for clarity. The labeling of the NO molecules and of the top metal layer atoms corresponds to that in Table 6.2.

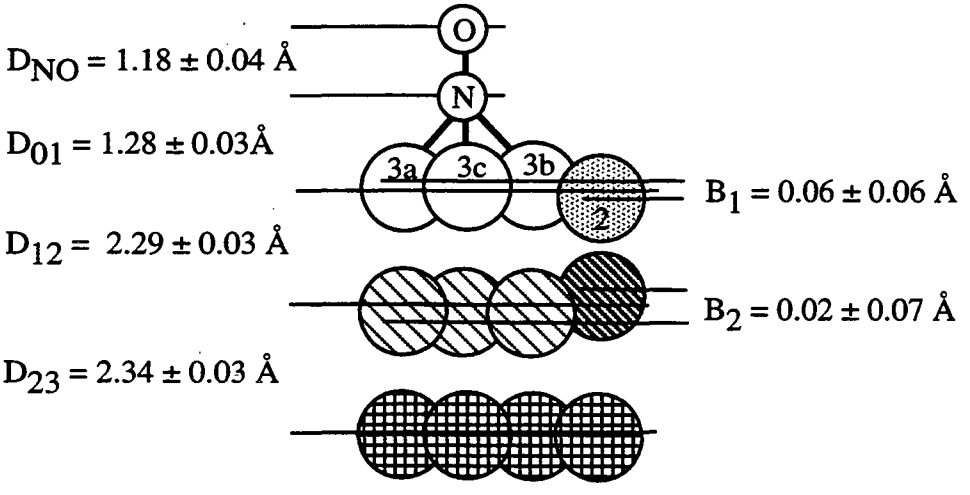

Figure 6.8: Side view of the best-fit Pt(111)-$p(2 \times 2)$-NO structure with an R_p-factor of 0.28. The labeling of the NO molecules and of the top metal layer atoms corresponds to that in Table 6.2.

Additional optimization of the second metal layer resulted in the final structure (Figures 6.7, 6.8) with I-V curves shown in Figure 6.9 and an R_p-factor of 0.28. Labeling of the inequivalent atoms in Figure 6.7 corresponds to the labeling in Table 6.2, where atomic coordinates of the best-fit geometry are shown. A total of eight structural parameters, consistent with the three-fold rotational and mirror plane symmetries ($p3m$) of the overlayer, were included in the fit. The R_p-factor of 0.28 is comparable with R_p-factor values obtained with recent extensive LEED analyses for structures of similar complexity which

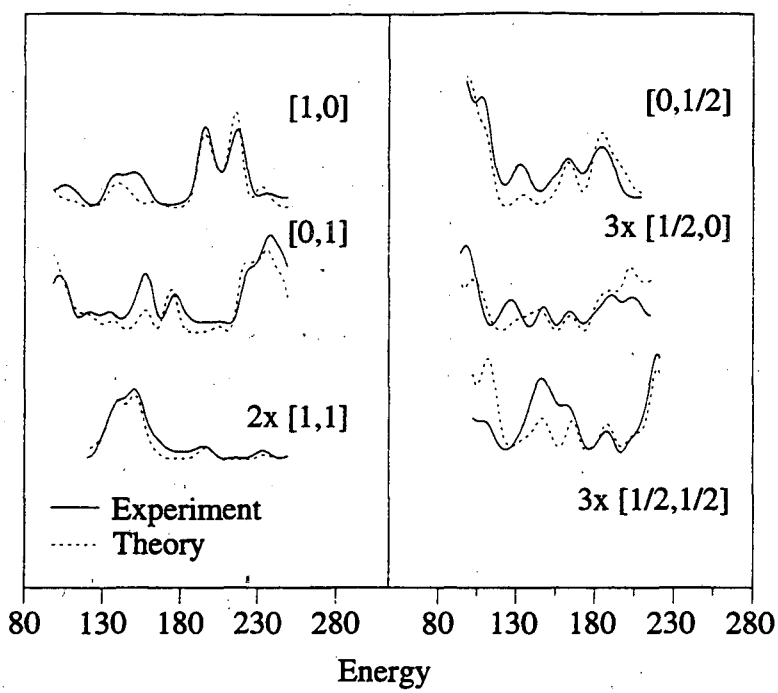

Figure 6.9: I-V curves for the best-fit Pt(111)-$p(2 \times 2)$-NO surface, which illustrate overall agreement between theory and experiment for all beams. An R_p-factor of 0.28 was obtained.

Table 6.2: Atomic coordinates of the best-fit geometry of Pt(111)-$p(2 \times 2)$-NO with an R_p-factor of 0.28. These coordinates are consistent with the $p3m$ symmetry of the overlayer. 8 structural parameters were optimized. X and Y are coordinates parallel to the surface; Z is perpendicular to the surface and positive towards the bulk. Top view of the structure in Figure 6.7; side view in Figure 6.8. Atoms labeled with the same number are symmetry equivalent (e.g. 3a, b and c). NO is constrained by symmetry to a position perpendicular to the surface.

		X	Y	Z
1	O	0.00	0.00	0.00
	N	0.00	0.00	1.18
2	Pt	0.00	3.20	2.51
3a	Pt	1.42	0.82	2.44
3b	Pt	-1.42	0.82	2.44
3c	Pt	0.00	-1.64	2.44
4	Pt	2.77	1.60	4.74
5a	Pt	0.00	1.51	4.76
5b	Pt	1.31	-0.75	4.76
5c	Pt	-1.31	-0.75	4.76
6	Bulk	0.00	0.00	7.08
7	Bulk	0.00	-1.60	9.34

are supported by additional experimental techniques and therefore not controversial. For instance, an R_p-factor of 0.28 was obtained for the Pt(111)-$p(2 \times 2)$ ethylidyne structure[121] (see Chapter 5) and a R_p-factor of 0.32 for the Rh(111)-$p(2 \times 2)$ ethylidyne structure[11]. In the best-fit, symmetry-restricted Pt(111)-$p(2 \times 2)$-NO structure, the NO has a bond length of 1.18 ± 0.04 Å with N at a height of 1.28 ± 0.04 Å above the center of mass plane of the first metal layer. This gave an NO-Pt bond distance of 2.07 Å. The first and second Pt interlayer spacings measured from the center of mass positions of the respective layers were determined to be 2.30 ± 0.03 and 2.32 ± 0.04 Å, respectively, as compared to the bulk value, 2.26 Å. The first interlayer spacing is very close to the value of 2.29 Å found for the clean surface and corresponds to an expansion of the first interlayer spacing. The second interlayer spacing also corresponds to an expansion and is within error bars of the clean surface value. The first and second layer bucklings were 0.06 ± 0.06 and -0.02 ± 0.07 Å, respectively. Here buckling is defined as the height difference between the three symmetry equivalent atoms and the inequivalent atom in a surface unit cell (see Figure 6.8). Lateral displacements were within error bars.

Analysis of the Tilt Angle

In the best-fit structure, the three-fold rotational symmetry of the model constrains NO to a position perpendicular to the surface. NO has been found in a bent configuration in inorganic nitrosyl compounds[148]. Due to this, we allowed the three-fold rotational symmetry to be broken in the structural search. The three-fold rotational symmetry of the LEED pattern was recovered by averaging either the intensity or amplitude of the resulting inequivalent beams. Intensity averaging of inequivalent beams is appropriate for surface domains in which the NO molecules tilt together; amplitude averaging simulates independent or uncorrelated tilting of the molecules[40]. Both averaging techniques lead to a tilt of approximately 10° with a reduction of the R_p-factor by 0.04. This reduction is mainly due to the R_p-factor improvement of 0.12 for the (1/2,0) beam. In addition, searches starting from tilted reference structures with NO bond lengths and angles typical of inorganic nitrosyl compounds resulted in structures identical to the best-fit structure. Bent NO molecules could be possible within lateral error bars; however, because of the 1.28 ± 0.04 Å height, accurately determined in the LEED analysis, a tilt typical of a bent NO molecule,[148] would lead to a highly improbable bond length for the molecule. Accordingly, the fact that LEED

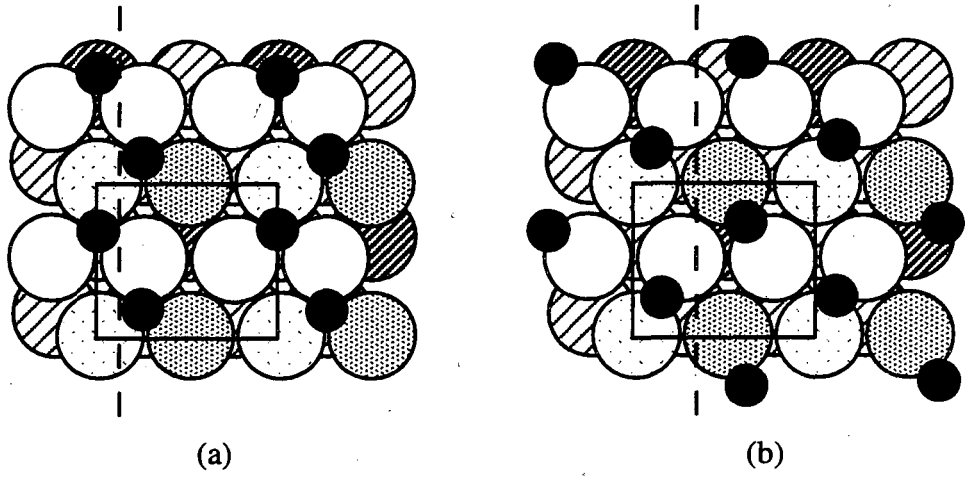

Figure 6.10: Suggested models for the Ni(111)-$c(4 \times 2)$-2NO structure with glide planes parallel to the short side of the unit cell (illustrated by the dashed line) which were not observed in the LEED patterns.

has high sensitivity to the vertical distance between the N and O atoms strongly supports a linearly bonded molecule. Because of the symmetrical environment of the NO molecule on Pt(111), we interpret its tilt, as in the case of CO on Ru(0001),[40] to be an anisotropic wagging vibration rather than a static tilt.

6.4.3 Ni(111)-$c(4 \times 2)$-2NO

Turning to NO on Ni(111), a recent SEXAFS analysis[16] supports hollow-site adsorption, but was not able to distinguish between fcc and hcp hollow sites. The authors of Reference 16 determined the correct model using a symmetry argument based on the observed LEED patterns. A photoelectron diffraction study[144,145] also supports the hollow site, however normal N 1s photoemission was not sensitive to the difference between the hollow and bridge sites. Assuming hollow-site adsorption and 0.5 ML coverage, three simple models are possible due to the three inequivalent hcp and three inequivalent fcc hollow sites available to the two NO molecules in the $c(4 \times 2)$ unit cell. The first possible model is one in which both molecules adsorb in fcc hollow sites (fcc+fcc model). The fcc+fcc model is shown in Figure 6.10a. The second possible model, one in which both molecules are adsorbed in hcp hollow sites (hcp+hcp model), is formed by a simple translation of the NO overlayer. For either of these models there are two different NO-NO distances, 2.49 Å and 4.31 Å. The third possibility is one molecule adsorbed in an fcc hollow site

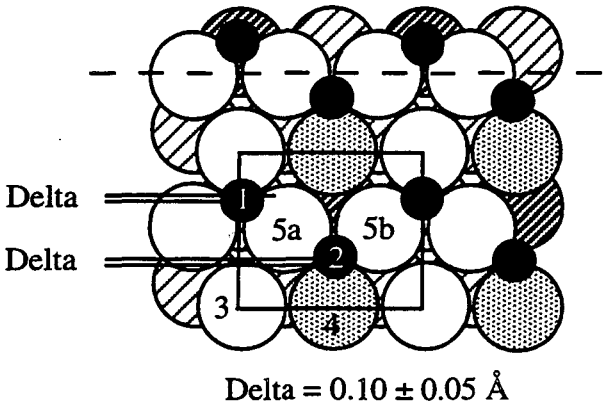

Figure 6.11: Top view of the best-fit Ni(111)-$c(4 \times 2)$-2NO surface structure with an R_p-factor of 0.13. The side view is shown in Figure 6.12. A unit cell is outlined for clarity. The labeling of the NO molecules and of the top metal layer atoms corresponds to that in Table 6.4. The glide plane symmetry of the overlayer and first metal layer is parallel to the long side of the unit cell and is illustrated by a dashed line. Delta is the lateral shift of 0.10 ± 0.05Å of the NO molecules from the hollow site toward the top site. I-V curves are shown in Figure 6.13.

and the other in an hcp hollow site (fcc+hcp model) as illustrated in Figure 6.11, leading to more favorable NO-NO distances of 2.87 and 3.80 Å. In addition to these models, we examined a 0.5 ML coverage bridge+bridge site model with NO-NO distances of 3.29 Å shown in Figure 6.10b, and a 0.25 ML coverage fcc site model similar to the Pt(111) fcc site model. As with the Pt(111) structural search, only displacements of the NO molecules and the first metal layer which were consistent with the symmetry of each model were allowed. The fcc+fcc, hcp+hcp, and bridge+bridge models exhibit a glide plane symmetry shown in Figures 6.10a and 6.10b. This symmetry would lead to systematic beam extinctions at normal incidence which were not observed in the LEED pattern. Due to this, the structural searches for these models were allowed to break the glide plane symmetry. The need to break this glide plane symmetry is one strong argument against the bridge+bridge model suggested by vibrational spectroscopy data[135,138,139]. Only the six beams which had the lowest experimental noise, two integer order and four fractional order beams, were fit for each model selection. R_p-factor values for the various models are shown in Table 6.3. Due to the excellent agreement between theory and experiment for the fcc+hcp hollow site model, no additional models were investigated. Interestingly, the resulting vertical displacements, or relaxations of the first layer metal atoms, were almost identical for the different models,

Table 6.3: R_p-factor values for various Ni(111)-$c(4 \times 2)$-2NO models. "NO only" refers to optimization of the NO bond length and height. "1D" refers to the addition of perpendicular displacements of the first metal layer consistent with the symmetry of the overlayer. "Full" refers to the additional optimization of symmetry-allowed lateral displacements.

Model	NO only	1D	Full
hcp+fcc	0.44	0.23	0.15
fcc+fcc	0.71	0.70	0.52
hcp+hcp	0.64	0.64	0.41
bridge	0.55	0.36	0.28
fcc	0.70	0.52	0.37

even though these displacements were consistent only with the molecular arrangement of the fcc+hcp overlayer. The additional improvement in the R_p-factor of the fcc+hcp model when lateral displacements were included is due to the 0.1 Å shift of the NO molecules off the hollow site towards the top site, which increases the shortest NO-NO distance by 0.1 Å.

Refinements were made to the fcc+hcp model by allowing relaxation of two metal layers and lateral displacements consistent with a mirror plane symmetry (pm). Atomic coordinates of the best-fit geometry are shown in Table 6.4. Labeling of the inequivalent atoms in Figures 6.12 and 6.11 corresponds to the labeling in Table 6.4. A total of twenty-two structural parameters, consistent with the mirror plane symmetry (pm) of the overlayer, were included in the fit. All thirteen experimental beams were included in this refinement. The analysis resulted in a final structure (see Figures 6.11 and 6.12) with an R_p-factor of 0.13; I-V curves are shown in Figure 6.13. This value is similar to R_p-factors of 0.11[155] and 0.16[156] obtained in recent extensive LEED analyses for atomic adsorption of oxygen on Ni(111), indicating remarkable agreement for a molecular system. In the final structure, the NO molecules on Ni(111) have a bond length of 1.17 ± 0.04 Å with N at a height of 1.24 ± 0.04 Å above the center of mass plane of the first metal layer. This gives an average NO-Ni bond distance of 1.18 Å. Both molecules are shifted approximately 0.10 ± 0.05 Å from the center of the hollow site towards the top site as illustrated in Figure 6.11 and tilted $4 \pm 4°$ in the same direction, thereby increasing the distance between neighboring N molecules to 2.98 Å. Unlike the Pt(111)-$p(2 \times 2)$-NO structure, the NO molecules on Ni are not in a symmetric environment and are therefore not constrained to a position perpendicular to the surface. The tilting of the molecules does not break the symmetry of the overlayer and may be either a static tilt or an anisotropic wagging vibration. Our

Table 6.4: Atomic coordinates of the best-fit geometry of Ni(111)-$c(4 \times 2)$-2NO structure with an R_p-factor of 0.13. These coordinates are consistent with the *pm* symmetry of the overlayer. 22 structural parameters were optimized. X and Y are coordinates parallel to the surface; Z is perpendicular to the surface and positive towards it. Top view of the structure in Figure 6.11; side view in Figure 6.12. Atoms labeled with the same number are symmetry equivalent. NO is not constrained by symmetry to a position perpendicular to the surface.

		X	Y	Z
1	O	0.00	3.10	0.00
	N	0.00	2.98	1.17
2	O	2.49	1.29	0.00
	N	2 .49	1.34	1.17
3	Ni	0.00	-0.01	2.49
4	Ni	2.49	0.06	2.49
5a	Ni	1.24	2.15	2.34
5b	Ni	3.74	2.15	2.34
6	Ni	0.00	1.47	4.46
7	Ni	2.49	1.53	4.51
8a	Ni	1.26	3.60	4.49
8b	Ni	3.72	3.60	4.49
9	Bulk	0.00	-1.14	6.49
10	Bulk	0.00	0.00	8.52

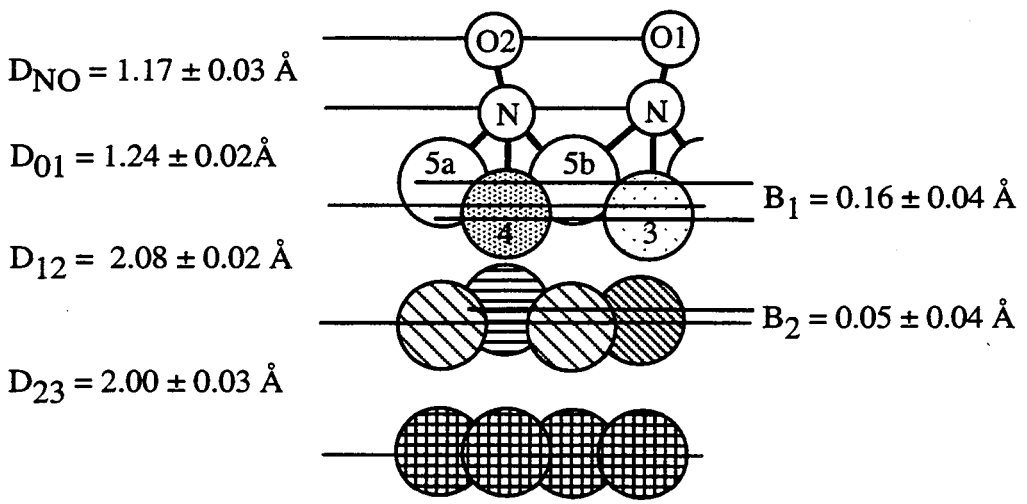

Figure 6.12: Side view of the Ni(111)-$c(4\times2)$-2NO structure of Figure 6.11 with an R_p-factor 0.13. I-V curves are shown in Figure 6.13.

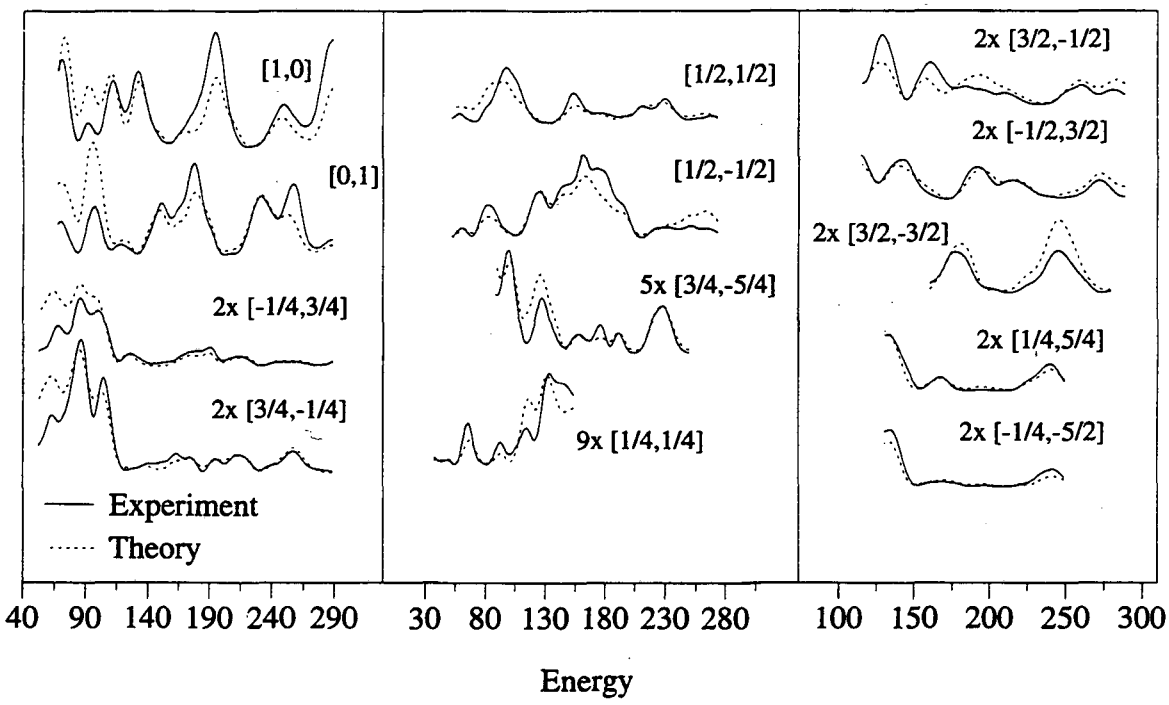

Figure 6.13: I-V curves for the best-fit Ni(111)-$c(4\times2)$-2NO surface, which illustrate overall agreement between theory and experiment for all beams. An R_p-factor of 0.13 was obtained.

results are consistent with other studies[142–146] which find NO perpendicular to within 10° of the surface normal. As in the case of NO on Pt(111), the large error bar for the tilt angle precludes further interpretation as to the nature of the tilt. A recent PD study[143] finds a peak at 0° in the polar angle scan of the N 1*s* intensity with a FWHM of less than 20°. Unfortunately, the resolution does not allow one to rule out tilt angles as small as 4°. Our NO tilt is in the opposite direction but within error bars of the tilt away from the top site found in a concurrent LEED analysis[147]. However, this concurrent analysis obtained an R_p-factor of more than twice the value of our R_p-factor of 0.13 and optimized a greater number of parameters for a smaller energy range.

The first and second Ni interlayer spacings of the best-fit Ni(111)-$c(4 \times 2)$-2NO structure measured from the center of mass planes of the respective layers were determined to be 2.08 ± 0.02 and 2.00 ± 0.03 Å, respectively, as compared to the bulk value of 2.03 Å. These values correspond to an expansion followed by a contraction of the first and second interlayer spacings of the ideally terminated surface. The first interlayer spacing also indicates an expansion of the clean surface. A total buckling of 0.16 ± 0.04 Å was found for the first layer. It is possible that this large relaxation of the first metal layer along with the lateral relaxation of the overlayer is the reason why theoretical analysis of PD spectra[145] found only an fcc hollow site. The two equivalent atoms in the first layer are displaced upward, while the two inequivalent atoms are displaced downward by the same amount. In the second layer no significant buckling was found. The lateral displacements of the metal atoms were within error bars.

6.4.4 Unexpected Sensitivity of the (1/4,1/4) Beam

In the initial hcp+fcc model, one without buckling of the metal atoms, lateral displacements or tilting of the molecules, the overlayer and the first metal layer have a glide plane symmetry, as shown in Figure 6.11, which would lead to zero intensity for the (1/4,1/4) beam, if it were not broken by the second metal layer. In addition to having this symmetry, the intensity of this beam should also be zero according to kinematic, or single, scattering theory, because of the particular positions of the atoms in the unit cell. Only multiple scattering paths, connecting the overlayer and the first relaxed metal layer with deeper metal layers, contribute to the intensity of this beam. Because of the limited mean free path of the LEED electron in the metal surface, these scattering paths are necessarily

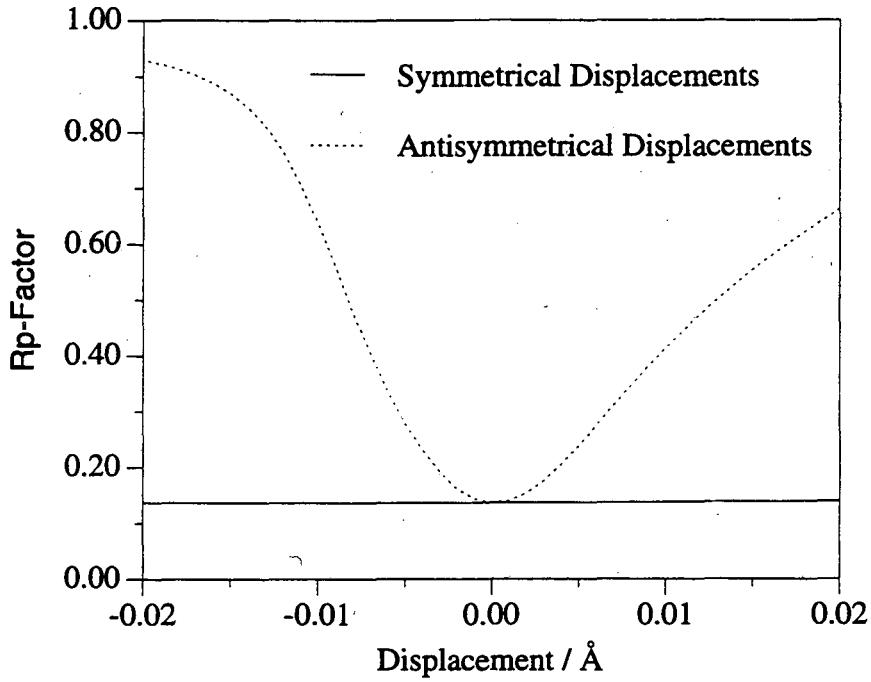

Figure 6.14: This graph shows the slow variation in the Ni(111)-$c(4 \times 2)$-2NO overlayer's (1/4,1/4) beam R_p-factor when the two NO molecules are displaced together (symmetrically) and the rapid variation when they are displaced in opposite directions (antisymmetrically).

weak when compared to scattering paths which include scattering in the overlayer or first metal layer. Experimentally, the intensity of this beam is relatively weak when compared to that of other beams in Figure 6.13; however, it is significantly above the background noise. Displacements in the overlayer or first metal layer which break the glide plane symmetry, disrupt the delicate balance, which leads to the cancellation of strong scattering paths and dramatically changes the I-V curve of this beam. These displacements include different heights and bond lengths for the NO molecules and different vertical heights for the two inequivalent Ni atoms in the first layer (3,4 in Figure 6.11 and Table 6.4). Displacements which do not break this symmetry do not cause these drastic results.

These effects can be seen in the variation of the R_p-factor value for the (1/4,1/4) beam shown in Figure 6.14. In this figure, NO molecules displaced in opposite directions (antisymmetrically) perpendicular to the surface lead to a curve which shows rapid variation resulting from very small displacements (on the scale of thousandths of angstroms).

In contrast, NO molecules displaced in the same direction (symmetrically) perpendicular to the surface lead to an almost flat curve which indicates little variation for very small displacements. The difference between these two curves graphically illustrates the effect of breaking the glide plane symmetry of the overlayer and first metal layer and thereby introducing additional strong scattering paths for the (1/4,1/4) beam. The sensitivity of the (1/4,1/4) beam to the addition of these paths results in extremely small error bars for displacements which break the glide plane symmetry of the overlayer and first metal layer. This is demonstrated in error bars for the relative difference in NO bond lengths, the relative height difference above the surface, and the different vertical heights for the two inequivalent Ni atoms in the first layer (3 and 4 in Figure 6.11 and Table 6.4); these error bars are ±0.005, ±0.008 and ±0.02 Å, respectively. In the best-fit structure, small lateral displacements break the glide plane symmetry for the first metal layer and the overlayer. However, these displacements are within error bars. If this symmetry is imposed in the structural search– –a reduction of 6 parameters– –an R_p-factor increase of only 0.01 above that of the best-fit structure is obtained.

6.5 Discussion

The NO bond length and height above the surface are almost identical for the Pt(111) and Ni(111) systems. The NO bond lengths are close to the average value of 1.19 Å and within the range of 1.15 to 1.22 Å found for nitrogen-oxygen compounds[148]. Our value of 1.88 Å for the NO-Ni bond length in the Ni(111)-$c(4 \times 2)$-2NO structure compares well with an NO-Ni bond length of 1.83 Å determined by PD[144,145]. In addition, the average Ni-O distance in the Ni structure of 2.70 Å compares well with the value of 2.68 Å found with SEXAFS[16]. The relaxations induced in the Ni substrate are larger than those of Pt; this may be due either to the NO coverage on Ni being twice that on Pt or possibly to a stronger NO-metal bond with Ni than with Pt, as suggested by temperature programmed desorption (TPD)[127,134]

A concurrent LEED analysis of the Ni(111)-$c(4 \times 2)$-2NO structure[147] obtains a similar best-fit model. The R_p-factor quoted in reference 147 was twice that of our analysis using a smaller energy range and optimizing a greater number of parameters. We believe the difference in the two R_p-factors is due to the quality of the experimental data. The NO bond lengths and the average Ni-O distance are in good agreement with our values and

the values obtained with PD[145] and SEXAFS[16]. Their NO-metal bond length is a little larger but still within error bars of our result. Lateral relaxations of the overlayer and the relaxation of the first metal layer were not reported even though such displacements were allowed in the structural search. Also, their first interlayer spacing shows a contraction of 0.05 Å of the ideally terminated surface, as opposed to our expansion of 0.05 Å. However, their error bar of ±0.09 Å for this measurement is larger than ours (0.03 Å). In addition, many LEED analyses find that adsorption leads to a local expansion of the first interlayer spacing as determined in our analysis of NO adsorption on Pt and on Ni[157].

On both Ni(111) and Pt(111) surfaces, CO adsorption forms a variety of complex LEED patterns. On the Pt(111) surface four distinct LEED patterns are observed at different coverages; on Ni(111) three patterns are formed. In contrast with CO, NO on Pt(111) forms a $p(2 \times 2)$ structure first and with increasing coverage forms a diffuse (2×2) pattern. On Ni(111), NO adsorption gives a diffuse (2×2) pattern, followed by the $c(4 \times 2)$ pattern. The antiphase domain model for CO-metal systems which involves strong molecule-metal interaction coupled with molecule-molecule interaction, favors top and bridge site adsorption at the expense of regular intermolecular distances;[151] it has been successful in explaining the vibrational spectroscopy data and the complex LEED patterns on both Pt(111) and Ni(111). Due to the unpaired electron in the antibonding $2\pi^*$ orbital, NO adsorption energy is about 10 to 20 kcal/mol lower than the CO adsorption energy[74]. This lower adsorption energy could possibly disrupt the delicate balance of molecule-molecule and molecule-metal interactions and lead to the limited number of ordered LEED patterns obtained for NO. In addition, the lack of complexity in the patterns obtained for NO adsorption may be related to the similar adsorption site symmetry, unlike CO adsorption which can occur in sites of different symmetry.

TPD results[127] and the identical NO-Ni heights for the two adsorption sites in the Ni(111)-$c(4 \times 2)$-2NO structure support similar fcc and hcp hollow-site adsorption energies. In addition, if the difference in adsorption energies of the fcc and hcp hollow sites was small compared to the thermal energies, entropy could possibly disorder a $p(2 \times 2)$ structure by randomly filling both sites. This may be the reason that Ni(111) forms a well-ordered, higher coverage $c(4 \times 2)$ structure and not a lower coverage $p(2 \times 2)$ structure. The formation of a $p(2 \times 2)$ structure on Pt(111) might suggest a larger adsorption energy difference between the fcc and hcp hollow sites than on Ni(111). NO in excess of 0.25 ML on Pt(111) does not produce a $c(4 \times 2)$ but adsorbs in a disordered fashion[130]. The lack of fundamental

understanding of these structural differences illustrates the need to further analyze the NO-metal bond and the intermolecular interactions in these systems.

Our results contradict earlier assignments of adsorption sites from vibrational spectroscopy data[134–139] and X-ray photoelectron spectroscopy (XPS) data[129,130]. Unlike CO, NO does not have nearly the number of extensively studied cluster compounds as references on which to base site assignments. In addition, the possible structural complexity in inorganic nitrosyl compounds is much greater than that found in metal carbonyl complexes. As mentioned above, NO has an additional electron in the $2\pi^*$ orbital; this electron allows the molecule to bond to a metal in a bent or linear fashion[148]. These different bonds occur because the additional electron allows the NO to either accept another electron forming a lone pair on the N atom or to donate this electron forming a bond to the metal. In metal complexes, the ability to accept or donate electron density leads to complex charge transfer between the NO and the metal. Due to this complexity, interpretation of vibrational spectroscopy and XPS data in metal nitrosyl complexes has been found to be unreliable.[140] Correct interpretation of such data requires detailed knowledge of the effects of charge transfer in NO-metal bonding. One example of this effect on the Ni(111) surface is the 200 cm^{-1} change in the NO vibration frequency observed for NO coadsorbed with oxygen, which reduces the $2\pi^*$ electron density[141]. In addition to this effect, which has analogs in inorganic chemistry, vibrational coupling between NO molecules on the surface can also complicate the vibrational spectra by shifting vibrational frequencies. Since LEED is sensitive to the positions of atomic cores rather than details of bonding, it provides adsorption sites with much greater reliability.

6.6 Conclusions

The surface structures of the Pt(111)-$p(2 \times 2)$-NO and Ni(111)-$c(4 \times 2)$-2NO systems have been solved by LEED. For both metal surfaces, a hollow site adsorption model was determined to give the best fit between theory and experiment. An hcp+fcc hollow site model proved to be the optimal structure in the case of NO on Ni(111). In this structure a total buckling of the first metal layer was found to be 0.16 Å. Both structures cast doubt on current vibrational and XPS site assignments and demonstrate a need for understanding the influence of vibrational coupling and charge transfer on the NO molecule. The subtle effects of charge transfer on the NO-metal chemical bond in inorganic complexes are reflected in

the surface bonding of NO. This study shows that examination of such problems associated with inorganic reference clusters is essential to determine the reliability of sites assigned by indirect methods.

Chapter 7

Molecular Surface Structure of Ice(0001)

Ice plays a pervasive role in many daily phenomena, particularly through its surface. For example, the unusual slipperiness of ice is possibly due to surface premelting or melting of the surface below the bulk melting point (for reviews, see References 158 and 159). In addition, ice is thought to catalyze chemical reactions in the Earth's ozone layer and it can play a role in cloud-seeding and thunderstorms. Ice also causes many optical effects in the atmosphere due to the refraction of light from ice surfaces. However, there have been relatively few structural studies of the ice surface at the molecular level. In this chapter, we examine the ice surface both experimentally, using low energy electron diffraction (LEED), and theoretically, using both molecular dynamics and total energy computations, in order to provide a structural model for the surface. The molecular dynamics (MD) simulations were performed in collaboration with G.-J. Kroes (Theoretical Chemistry, Department of Chemistry, Vrije Universiteit, Amsterdam, The Netherlands) and the total energy calculation in collaboration with C. Minot (Laboratoire de Chimie Organique Théorique, Université Pierre et Marie Curie, Paris, France). A brief report of our results can be found in Reference 160.

One question also addressed in this chapter is to what extent ice surfaces may show either disordering behavior or larger amplitudes of vibrations at temperatures as low as 90 K. At this temperature, surface melting is not expected to occur. Most experiments investigating surface melting of ice put the temperature at which a liquid-like layer may

exist on the ice at no lower than about 243 K (-30° C). At low temperatures, one still might expect larger amplitudes of motion and a greater extent of disordering in the surface layer, due to disruption of the hydrogen bonding network at the surface. In the bulk, H_2O molecules are held in place by four hydrogen bonds, whereas, in their ideal bulk-like arrangement, surface molecules can form no more than three hydrogen bonds. The issues of surface disorder and enhanced vibrational amplitudes are especially important for structural determinations of molecular surfaces where the bonding is much weaker than in metals or semiconductors.

We will first briefly introduce previous experimental and theoretical investigations of the surface of bulk ice and of water adsorption on metal surfaces. A description of our thin film approach, used to study the bulk ice surface, follows in Section 7.2. Provided in Section 7.3 is a short description of our theoretical methods, while Section 7.4 contains the LEED results. In this section a detailed description of the various surface models and their relative agreement with the experimental intensity vs. voltage curves (I-V curves) can be found. Because it was not possible to distinguish between models which result in an apparent half-bilayer termination, we address these issues with both total energy computations and molecular dynamics simulations. Section 7.5 describes total energy computations used to obtain the relative energy differences between various surface models. In this section, we also examine the potential energy surfaces along selected vibrational coordinates to obtain an idea of the surface vibrational amplitudes within a harmonic model. To investigate the possible influence on the LEED experiments of either a disordered top layer (due to thermal motions which result in the loss of lateral order) or enhanced vibrational amplitudes of the surface molecules, MD simulations of the basal plane or (0001) face of ice at the experimental temperature ($T = 90$ K) were carried out. Section 7.7 refines the LEED analysis of the full-bilayer termination model with enhanced vibrational amplitudes. This model is supported by both the total energy computations and MD simulations. Finally, our conclusions are summarized in Section 7.8.

7.1 Motivation and Background

Previous experimental and theoretical investigations of the surface of bulk ice have focused on adhesion and friction,[161] on surface premelting,[158,159,162–167] on vaporization mechanisms,[168] and on the adsorption of non-water molecules on ice clusters and amorphous

ice[169,170]. In other studies, measurements of O-H vibrations in ice clusters and amorphous ice can identify hydrogen atoms not participating in hydrogen bonds and thus characterize the surface[171]. Most studies so far were performed at temperatures well above 240 K and report the presence of a liquid or quasi-liquid layer on ice, above (but not below) this temperature. In one particular study, x-ray crystal truncation rod scattering was used to determine the possibly preparation-dependent surface morphology of the (0001) surface of the common ice phase Ih at 266 K, but the surface crystallography[164] was not determined.

UHV studies of water adsorption on single crystal surfaces have utilized a variety of surface science techniques.[172] Electron stimulated desorption ion-angular distribution (ESDIAD) and vibrational spectroscopy have provided orientational information for submonolayer to saturation coverages of water molecules. High-resolution electron energy loss spectroscopy (HREELS), and more recently infrared reflection adsorption spectroscopy (IRS), experiments on Pt(111) support clustering of the water molecules even in the submonolayer regime.[173] On Ru(0001), a detailed structural study of water adsorption has been conducted.[174] This study found that deuterated water molecules form a single ordered bilayer, which fits the substrate 2D lattice in a $(\sqrt{3} \times \sqrt{3})$R30° pattern and that the oxygen positions could be determined with automated tensor LEED. In their final structure, the outermost water molecules, which are hydrogen-bonded to the molecules underneath, were found to be almost coplanar with the innermost metal-bonded molecules.

7.2 The LEED Experiment

Our LEED experiments were carried out in a stainless steel ultrahigh vacuum chamber (see Section 2.2.1) which was kept at or below 10^{-10} torr throughout the experiments. An exposure of 20 Langmuir of water vapor at 140 K resulted in the ordered six-fold symmetric LEED pattern shown in Figure 7.1.[175,176] On the Pt(111) surface, no ordered water adsorption structures are formed with the exception of a multilayer ice film.[175,176] Comparing both the LEED spots and the background intensity of the LEED pattern shown in Figure 7.1 to the LEED pattern obtained from the clean Pt(111) surface, one can see the relatively larger spot size and higher background intensity in the ice film LEED pattern (see Figures 2.12 and 2.11). These features indicate a larger degree of disorder than that found for the clean metal surface. The background could also be indicative of diffuse thermal scattering due to surface vibrations. Using the Debye temperature for bulk ice, we find

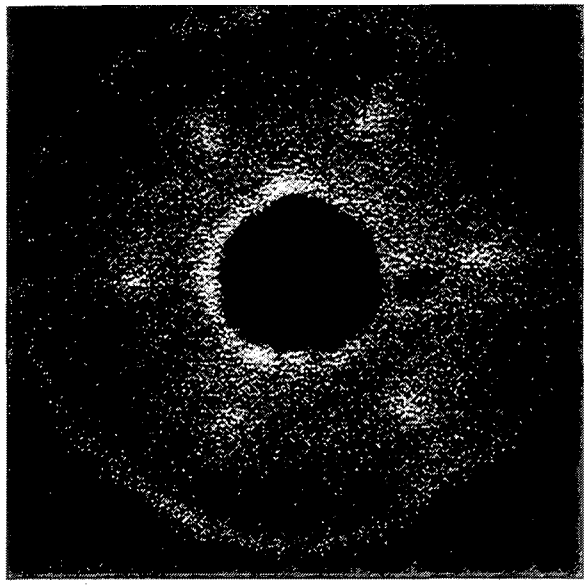

Figure 7.1: The LEED pattern of the Ih(0001) film grown on the Pt(111) surface at 48 eV and normal incidence.

that at 90 K the surface *rms* vibrational amplitudes of the water molecules are an order of magnitude greater than those of the substrate metal atoms. The LEED patterns measured from the ice film showed no contributions from the Pt(111) substrate; also, the 2D lattice constant computed from the LEED patterns matches the lattice constant of bulk ice within the LEED uncertainty of a few percent.

The film thickness seen by the LEED electron can be estimated from the electron attenuation length, λ, or the length required for the intensity of an outgoing beam to decrease by $1/e$. From these considerations we have determined that the thickness of the film, as seen by the LEED electron, must be at least 10 Å.

After the preparation of the ice film, the crystal was cooled to 90 K. A digital LEED detector[12] (see Section 2.3.2) was used to measure the impact position of single diffracted electrons and digitally generate the diffraction pattern. We exclude the influence of electron-beam-induced damage, a definite possibility with water molecules and ice,[172] on our diffraction patterns since our experiment used an extremely weak electron beam current that deposits only about 10^{-2} electrons per experiment per surface unit cell[12]. Intensity vs. energy (I-V) curves were measured for 18 beams from 30 to 150 eV. The symmetrically-equivalent beams in the six-fold symmetric pattern were averaged, resulting

in three non-equivalent beams, the (1,0), (1,1) and (2,0), for use in the LEED analysis. The collection of higher-energy I-V data was prevented by the rapid fall of intensity with increasing energy. This rapid fall of intensity was also reproduced in the theoretical I-V curves and is due to the decreasing cross-section for backscattered electrons with increasing energy. The curves were repeatedly measured after four separate surface preparations and found to be reproducible.

7.3 Theory

7.3.1 LEED Theory

The LEED simulations utilized the automated tensor LEED method.[177] We modeled the ice surface as a semi-infinite ice sample using composite bulk and surface bilayers which were combined using renormalized forward scattering.[177] For ice, seven scattering phase shifts were computed utilizing a potential obtained, within the muffin-tin approximation, from overlapping atomic wave-functions on an Ih ice lattice. Inelastic damping of the electrons was represented by the imaginary part of the inner potential of -4 eV. Thermal vibrations were represented by temperature dependent phase shifts based on a Debye-Waller model. The rms vibrational amplitudes used to construct the temperature dependent phase shifts were fit to the experimental I-V curves and will be discussed along with the LEED results.

7.3.2 Total Energy Theory

Total energy calculations were performed at the Hartree-Fock level utilizing CRYSTAL[178]. This program carries out total energy calculations for finite slabs made up of two-dimensional layers which are of infinite extent. We have used two basis sets: the 631G* and the 631G**[179–182]. The main difference between these two basis sets is that the G31G** allows for some polarization of each H atom's charge density by the addition of a p-orbital function. All energies reported in this chapter are energy gains with respect to the free molecule(s):

$$\mathrm{E}_{reported} = n\mathrm{E}_{molecule} - \mathrm{E}_{computed} \tag{7.1}$$

where n is the number of water molecules in the calculated unit cell.

For the free water molecule, these basis sets give OH distances of 0.947 and 0.943 Å, while for the HOH angles they give 105.5 ° and 106 °. Most of the published total energy calculations concern the proton-ordered phases that are stable at high pressure and low temperature.[183,184] However, an MD simulation[163] found that the outermost molecules on an Ih(0001) surface moved slightly inward. Because the atomic positions and the affects of the hydrogen positions on the total energy are not known, we perform geometry optimizations on several different slab geometries to estimate the energy difference between surface different terminations.

7.3.3 MD Theory

Ice surface simulations were carried out in essentially the same manner used in a previous study by Kroes[163] for a higher range of temperatures (between 190 and 250 K). Briefly (see Reference 163 for further details), in these MD simulations, the (0001) surface is modeled using 12 layers of "moving" H_2O molecules which form a slab of thickness 21.83 Å. The moving molecules are held in place by four layers of fixed H_2O molecules underneath. An infinite surface is simulated by replicating the "MD box" containing the H_2O molecules in the directions parallel to the surface, using periodic boundary conditions. The MD box has the dimensions $x = 22.35$ Å and $y = 23.23$ Å parallel to the surface, and contains 480 H_2O molecules, 360 of which move according to Newton's equations of motion.

The simulations are started from a configuration generated using a scheme suggested by the work of Cota and Hoover;[185] this configuration has a zero dipole moment and obeys the "ice rules".[186] We use the TIP4P potential model[187,188] for the interaction between the H_2O molecules. An advantage of this potential is that it yields stable hexagonal ice.[189] In the TIP4P model, the water molecule is treated as a rigid rotor, disallowing intramolecular (vibrational) motion. As was previously done,[163] the potential is switched off at long range (between 9.5 and 10 Å), because, for a slab of molecules in a semi-infinite lattice, it would be both difficult and computationally expensive to calculate the long range interaction using an Ewald-like scheme.[190] The switching function is such that it yields a potential with continuous first and second derivatives. Additional discussions of the TIP4P potential applied to the surface of ice can also be found in Reference 163. In the simulations, the temperature (90 K) is imposed using a computational analog of a thermostat[191] during an initial 10 *ps* run. The equations of motion are solved using an improved leapfrog

algorithm,[192] with a timestep of 1 fs. After imposing the temperature of 90 K, the surface was propagated in time in four runs all lasting 20 ps. The results presented below are (converged) averages of the last run. Comparisons with results using 16 layers of moving water molecules showed that the results presented below are also converged with respect to the number of layers used in the simulations.

The rms amplitude of motion of the water molecules perpendicular to the surface was calculated by computing, for each layer, the average value of

$$\sigma(Z) = \sqrt{(\bar{Z}_o^2) - (\bar{Z}_o)^2} \tag{7.2}$$

where Z_o is the Z-coordinate associated with the oxygen atom of a water molecule and Z is the coordinate perpendicular to the surface. To assess the disorder associated with the vertical displacements of the molecules, density profiles were made by partitioning the sample along the direction perpendicular to the surface into bins 0.1 Å wide, and summing the number of oxygen atoms in each bin at each time step. To monitor disorder associated with translational motion parallel to the surface, a translational order parameter (S_T) was calculated by averaging the three order parameters given by equation 2 in Reference 163. This order parameter measures to what extent the O-atoms in a given layer remain in their ideal lattice positions parallel to the surface (relative to one another). For a perfectly ordered surface, $S_T = 1$, while for a perfectly disordered (liquid-like or amorphous) surface, S_T is equal to one divided by the number of molecules per layer (30 in the present calculation).

Rotational disorder was monitored quantitatively by calculating a rotational order parameter (S_R) (equation 3 of Reference 163). The order parameter S_R measures to what extent the orientations of the dipole vectors of the H_2O molecules in a given layer deviate from the ideal orientations, of which there are six for each layer. For a perfectly ordered solid, $S_R = 1$, while for a liquid $S_R = 0$. More qualitatively, rotational disorder was calculated by computing distributions ("densities") of $\cos\theta$ and ϕ, where θ and ϕ are the polar angles that the dipole vector of a water molecule makes with the crystal axes system. The distributions were calculated by partitioning $\cos\theta$ into 100 bins and ϕ into 200 bins, and by summing the number of $\cos\theta$ and ϕ of each water molecule in each bin at each timestep.

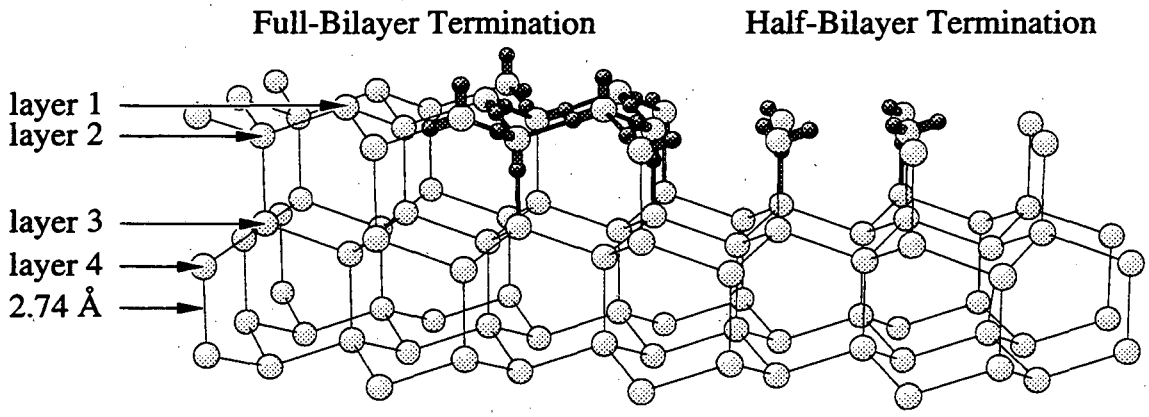

Figure 7.2: Perspective grazing view of the ice Ih (0001) surface with two ideal terminations: full-bilayer termination at left, and half-bilayer termination at right. Large atoms are oxygen, with some hydrogen included as small atoms with assumed bulk-like positions and randomness to form H_2O molecules (covalent bonds are drawn white and thick, hydrogen bonds dark and thin).

7.4 Initial LEED Results

7.4.1 Surface Models

The LEED pattern only fits the two simplest phases among the many different bulk ice phases:[193,194] the unreconstructed (0001)-(1x1) surface of hexagonal ice Ih, the most commonly occurring form, and the (111)-(1x1) surface of cubic ice Ic, a metastable phase that has been obtained by condensation on metals at about 140 K[172]. Both bulk ice Ih and bulk ice Ic consist of bilayers of tetrahedrally bonded H_2O molecules connected by hydrogen bonds. The O layers have hexagonal symmetry and the O planes are spaced by about 2.76 Å between bilayers and 0.92 Å within bilayers. The O atoms in Ic form the diamond lattice while those in Ih form the corresponding hexagonal lattice shown in Figure 7.2. The O layers have an ...ABBAABBA... stacking sequence in ice Ih, and an ...ABBCCAAB... sequence in ice Ic, so the distinction only appears after three or four O layers, or about 7 Å under the ideally-terminated surface. Each oxygen is surrounded by four other hydrogen-bonded oxygens about 2.76 Å away at RT and 2.74 Å at 90 K. The H atoms are located between adjacent O atoms in the hydrogen bond, but are off-set asymmetrically by about 0.38 Å from the midpoint in a largely random fashion and are most likely slightly off-axis.[193] Each O atom is covalently bonded to two nearby H atoms

and weakly bonded to two other, more distant H atoms.

We have investigated models based on two different terminations of the ice Ih(0001) and Ic(111) surfaces, as shown in Figure 7.2 for the Ih(0001) model. In the full-bilayer termination model each outermost O atom is hydrogen-bonded to 3 neighboring O atoms, while in the half-bilayer termination model each is hydrogen-bonded to only one neighboring O atom. For the full-bilayer Ih and Ic models, we also allowed the outermost O to have an enhanced vibrational amplitude. Enhanced vibrational amplitudes were not tried for the half-bilayer model because this feature, due to the Debye-Waller factor, would for large amplitudes, effectively make the model equivalent to the full-bilayer termination model. In section 7.7.2, we will discuss the optimization of these enhanced vibrational amplitudes. In an attempt to simulate a surface with a mixture of full- and half-bilayer termination, an incoherent average of the scattered intensities resulting from the two terminations was also investigated. In addition, a collapsed bilayer was tried, in which the water molecules forming the outermost bilayer are nearly coplanar. For all models, domain averaging was applied to recover the six-fold symmetry observed in the LEED pattern .

For each model, our calculations explored different lateral lattice constants from 4.33 to 4.99 Å parallel to the surface – – the bulk ice value being 4.52 Å – – with proportional lattice constants perpendicular to the surface, and various spacings between the two outermost oxygen layers. This is equivalent to assuming that each oxygen atom, with the exception of the atoms on the surface, is surrounded by four tetrahedral oxygen atoms at identical O-O distances. Although, in bulk hexagonal ice, the O-O distances for the molecules in the bilayer are slightly different than the O-O distances between bilayers,[193] we have assumed they are identical in the initial model computations. In Section 7.7.1, we attempt to examine the effect of relaxing this constraint on the best-fit structure. Hydrogen was omitted in most of the LEED calculations, since its contribution is small, partly due to its small scattering cross-section, but primarily in view of the inherent disorder present in its asymmetric positions. However, in Section 7.7.3, we attempt to extract some information, even if only averaged, about the position of the hydrogen.

7.4.2 Single Termination Models

The fit between theory and experiment I-V curves for the full- and half-bilayer termination models was quantified by means of the Pendry R-factor (R_p-factor)[47]. The results

Table 7.1: R_p-factor values for different single termination surface models with the first two interlayer spacings optimized as a function of lattice constant d (parallel to the surface, with proportional lattice changes perpendicular to surface): full- and half-bilayer termination of bulk Ic (cubic) and bulk Ih (hexagonal), with $\sigma(Z)$ (the perpendicular rms vibrational amplitude) of the top oxygen atoms equal to 0.10 or 0.28 Å for the full-bilayer model. All other layers have $\sigma(Z)$ set to 0.10 Å. See Section 7.7.2 for additional details related to the vibrational amplitudes used in these LEED optimizations.

d Å	Ic-full		Ic-Half	Ih-full		Ih-half
	0.10	0.28		0.10	0.28	
4.33	0.58	0.56	0.43	0.52	0.42	0.44
4.49	0.47	0.43	0.36	0.42	0.26	0.28
4.66	0.47	0.40	0.35	0.40	0.27	0.29
4.99	0.63	0.45	0.62	0.40	0.50	0.52

of structural optimization as a function of the "bulk" lattice constant d, are summarized in Table 7.1. Three parameters were fit in each case, the inner potential and the perpendicular positions of the first two topmost oxygen atoms in the surface unit cell. A Debye temperature of 300 K ($\sigma(Z)$ of 0.10 Å) was used for all O atoms with the exception of the topmost atom in the enhanced vibrational amplitude model. In the case of the full-bilayer model, these two topmost oxygen atoms correspond to layers 1 and 2 of Figure 7.2. For the half-bilayer model, because there is no layer 1, we fit the perpendicular positions of the oxygen atoms in layers 2 and 3. Deeper layers were tried but not included in the fit due to the relatively small improvements they made in the resulting R_p-factor. In the model with the enhanced vibrational amplitudes ($\sigma(Z)$ in layer 1 of 0.28 Å), the topmost atom (layer 1) was held fixed, due to the lack of sensitivity to its position in the R_p-factor, and the next two oxygen atoms (layers 2 and 3) were included in the search. These parameters are identical to the parameters fit in the half-bilayer model. Assuming bulk-like vibrations ($\sigma(Z)$ of 0.10 Å), our analysis clearly favors the half-bilayer termination and systematically favors the Ih form of ice (R_p-factor between 0.28 and 0.29). The R_p-factor can be improved somewhat with a large vibrational amplitude, i.e. $\sigma(Z)$ of the outermost O atoms in the full-bilayer termination of Ih ice (R_p-factor between 0.26 and 0.27). The similarity of R_p-factors for the half-bilayer and the full-bilayer termination with enhanced vibrational amplitudes indicates that for these large vibrational amplitudes, the outermost O atoms in the full-bilayer model become essentially undetectable by LEED. However, the presence of these O

atoms does have a small influence on the resulting R_p-factor values. The optimization of the perpendicular rms vibrational amplitude, i.e. $\sigma(Z)$ of the outermost oxygen atoms for the full-bilayer model will be discussed in Section 7.7.2.

The Ih and Ic forms of ice have close R_p-factor values (differences of 0.08 to 0.06), since they differ mainly in the lateral positions of the third and deeper O layers. This structural difference between the two forms is approximately 7 Å under the surface, which is close to the 10 Å limit imposed by the imaginary part of the inner potential. We used Pendry's method[47] to generate the range of R_p-factor values into which all models that are indistinguishable from each other should fall. In doing so, we find that the R_p-factors for the cubic model are just outside this range of values. One should note that the 10 Å thickness is based on a decay of $1/e$ in the electron's wavefunction; thus it is indeed a lower limit. Another consideration in determining whether we have Ih or Ic ice is the six-fold symmetry of the LEED pattern. The Ic model requires averaging rotated domains which possibly could have been formed in the initial growth phase of the film in order to produce six-fold symmetrical LEED patterns, while similar averaging comes more naturally for the Ih model due to the different orientations of successive terraces. Studies of bulk ice grown on cold metal surfaces have found the Ic form of ice at low temperatures; however, the irreversible transition of the Ic form to the Ih form depends on the thermal history of the sample and is found for a range of temperatures around our growth temperature[193]. For these reasons, we favor the Ih over the Ic form.

7.4.3 Coexistence of Two Terminations

One possible way to explain the relatively good agreement between the experimental and theoretical I-V curves for the half-bilayer model is a kinetically limited process during the film growth. This includes condensation on the ice surface or sublimation of water molecules before the sample has had time to cool down to 90 K. At the low measurement temperature of 90 K, diffusion along the surface is probably too slow to anneal of the remaining half-bilayer into a full-bilayer, possibly resulting in a mixed termination.

To test this idea, we have carried out automated TLEED searches in which the diffracted intensities from both the half- and the full-bilayer termination models were added in several predetermined ratios. This addition of diffracted intensities simulated a surface which contained a mixture of half- and full-bilayer terminated domains. The results of

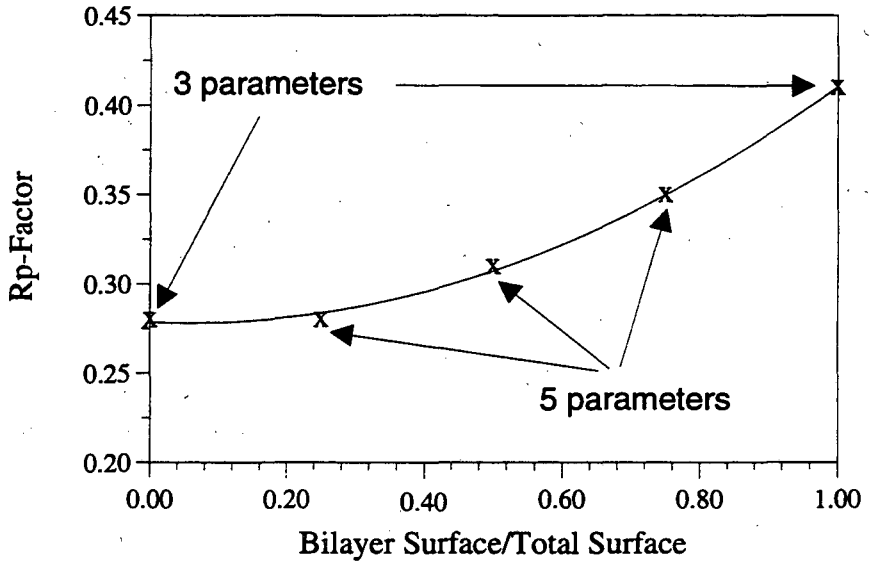

Figure 7.3: Automated TLEED searches in which the diffracted intensities from both the half- and the full-bilayer termination models of Ih(0001) were added in a predetermined ratio in order to simulate a surface which contained a mixture of half- and full-bilayer domains. The curve is a best fit parabola.

these calculations are illustrated graphically in Figure 7.3. In this figure, the left and right endpoints represent surfaces containing only the half- or the full-bilayer termination, representing for these, only the three parameters described in Section 7.4.2 were optimized. Between the two endpoints, a surface which is a mixture of the half- and the full-bilayer termination is simulated. Because the model contains a mixture of two surface terminations, the number of parameters increases to five: the inner potential and the positions of two oxygen atoms per surface. As one increases the concentration of the full-bilayer termination past 25%, the R_p-factor increases to the value of the full-bilayer termination model. Below 25%, the R_p-factor is approximately equal to the R_p-factor of the half-bilayer termination model. However, one must remember that twice the number of structural parameters were optimized for these mixed models; thus one would expect a significant drop in the R_p-factor as seen in the case of disordered CO on Pt(111).[195] The complete lack of a definite minimum between the two terminations strongly supports single termination and not a mixture.

The possibility of either condensation on the ice surface as the surface cools or sublimation before the sample has had time to cool down, seems unlikely for other reasons. One might expect the molecules in any half-bilayer portion of the surface to preferentially desorb leaving only the more stable full-bilayer portions. This expectation is based on TPD

studies of a full-bilayer of water molecules on the Ru(0001) surface, in which the whole bilayer desorbs at the same temperature.[196] For the ice surfaces, it is not clear why the top half of the bilayer would continue to evaporate faster than the bottom half, since the exposed bottom half has much lower coordination. Instead, one might expect that if sublimation was occurring as the sample cooled, it would help to maintain a full- bilayer termination over most of the surface at all times.

7.4.4 Possible Models

Our LEED computations support the Ih ice phase over the Ic phase. These are consistent with either the half-bilayer termination model with bulk-like vibrational amplitudes or the full-bilayer termination model with enhanced vibrational amplitudes. We have eliminated models which contain mixed termination. The addition of hydrogen, as discussed in Section 7.7.3, does not affect this conclusion. It is thus not possible, with the use of R_p-factors alone, to distinguish between the two termination models. A third possible model, which is also indistinguishable from these models, is a full-bilayer termination model covered by a disordered top layer or film. Previous MD simulations have shown that the topmost layer of ice is disordered ($S_T < 0.5$) at temperatures down to 180 K[163]. We now examine the results of both total energy calculations and MD simulations, in order to distinguish between these models.

7.5 Total Energy Calculations

We examined the relative stability of two of the aforementioned models using total energy calculations. The full-bilayer termination model with a disordered top layer and enhanced vibrational amplitudes will be addressed in the next section using MD simulations. In this section, we compare the energy difference between the half- and the full-bilayer terminations. To distinguish between the two models with different terminations, we need to understand the importance of the H-bonds in the slabs of the ice structure. Since the geometry of the surface bilayers differs from bilayers within a bulk ice crystal, we must perform geometry optimizations to minimize the total energy. All energies reported in this chapter are energy gains with respect to the free molecules (see Equation 7.1).

7.5.1 Lattices with Hexagonal Symmetry

A Single Bilayer

We begin our geometry optimizations using the 631G* basis set to minimize the total energy of a single bilayer. Because the CRYSTAL program benefits from periodicity, we must order the hydrogen atoms in the slab even though these atoms should be arranged in a disordered fashion. In an attempt to estimate the consequences of this localization, we have varied the size of the two dimensional unit cell to allow for different ordered arrangements. The first arrangement is the (1x1) arranged bilayer. In this bilayer all the water molecules have identical orientations in each unit cell. On one face, H atoms point outward from the slab's surface and on the other face, an oxygen lone pair points outward. The face with external hydrogen atoms is acidic while the face with external electron pairs is basic. Another way to look at this situation is that the non H-bonded OH bonds are aligned along the *c*-axis (the (0001) direction) in the (1x1) bilayer. The other arrangement is a $(\sqrt{3}\times\sqrt{3})$R30° arranged bilayer. The larger unit cell allows adjacent non H-bonded OH bonds to point in opposite directions along the *c*-axis, thus reducing dipole-dipole repulsion between water molecules. In this model, one third of the external H atoms belong to one face and the remaining two thirds to the opposite face.

For the (1x1) arrangement, we start optimizing the single bilayer slab by varying the O-O distance between the water molecules. By doing so, we vary the lateral lattice constant of the slab with proportional changes between the two oxygen layers. This optimization is very similar, in terms of geometrical parameters, to that of the LEED lattice constant optimization of Section 7.4. At the minimum, each oxygen atom is at the center of an incomplete tetrahedron formed by its nearest-neighbor oxygen atoms which are at a distance of 2.91 Å (Table 7.2: row labeled "(1x1)"). Next, keeping the lateral cell dimensions constant, we allow the variation of spacing between the oxygen planes within the bilayer, forming a (1x1) arranged compressed bilayer. The optimal spacing, 0.592 Å instead of 0.97 Å as above, corresponds to an O-O distance of 2.81 Å (Table 7.2: row labeled "(1x1) compressed"). This reduction of the O-O distances between the layers is associated with a increase of the cohesive energy within the bilayer. Indeed, the energy per H-bond increases from 4.2 to 5.1 kcal/mol. This value is comparable to that for the water dimer, 5.6 kcal/mol, or to that of the bulk, 6.3 kcal/mol.

We now turn to the $(\sqrt{3}\times\sqrt{3})$R30° arrangement of water molecules in a single

Table 7.2: Total energies computed with the 631G* basic set for the dimer, the various bilayer models with hexagonal symmetry, and the bulk structure. The values labeled with a "†" are optimized. The geometry of the oxygen atoms in the bulk is tetrahedral. Two different HOH angles were tried for the bulk. When this angle differs from 109.5° the H atoms do not point toward the oxygen atoms but are off the bond axis. "*d*" is the O-O distance in Å; "H-Bonds" is the total number of H-bonds; "Energy" is the total energy gained with respect to the free H_2O molecules (see Equation 7.1).

	d (Å)	H-Bonds	Energy (kcal/mol)
Dimer	2.97†	1	5.6
Bilayers			
(1x1)	2.91†	3	12.7
(1x1) compressed	2.91/2.81†	3	15.4
$(\sqrt{3} \times \sqrt{3})$R30°	2.91	3	15.9
4 Layers-(1x1)			
bilayer+bilayer	2.91	7	27.0
mono+bi+mono	2.91	5	13.2
4 Layers-$(\sqrt{3} \times \sqrt{3})$R30°			
bilayer+bilayer	2.91	7	39.4
mono+bi+mono	2.91	5	20.0
Bulk			
HOH = 109.5°	2.835†	4	24.9
HOH = 107.1°	2.835	4	25.1

bilayer. In the previous system, the (1x1) arrangement, the H atoms on the two faces either all point outward or all point inward. Because of this, the interaction between two coupled (1x1) arranged bilayers is asymmetric. For the $(\sqrt{3}\times\sqrt{3})$R30° structure, the larger unit cell allows adjacent OH groups to point in opposite directions and the two faces of the bilayer are more similar to each other (both are amphoteric) when compared to the (1x1) bilayers. This structure is more stable than the (1x1) bilayer but only by 3.2 kcal/mol. In the case of truly disordered hydrogen bonding, the total energy should be between the (1x1) and $(\sqrt{3}\times\sqrt{3})$R30° energies; each one representing an extreme created by the orientation of the OH groups in the lattice.

Coupling of the Bilayers

Now that we have optimized the geometry of the (1x1) and the $(\sqrt{3}\times\sqrt{3})$R30° arranged bilayers, we examine thicker slabs formed from these two basic units. Presented in Table 7.2 are the results for four layers using the 631G* basis, arranged either as two full bilayers or as one bilayer flanked on both sides by half bilayers, i.e. monolayers. In both cases, stacks formed using the $(\sqrt{3}\times\sqrt{3})$R30° arranged unit cell have a lower energy than the (1x1) arranged stacks. The most notable result is that the slabs made from coupling two bilayers are much more stable (by 13.8 to 19.4 kcal/mol) than those where a bilayer is flanked on both sides by half bilayers. The energy resulting from the coupling of the bilayers is weak (1.6 kcal/mol) for the (1x1) arrangement, but for the $(\sqrt{3}\times\sqrt{3})$R30° arrangement it is of the order of the H-bond of the bulk (7.6 kcal/mol).

7.5.2 Distorted Hexagonal Lattices

We are interested in the relative energy difference between various slab geometries which differ in their terminations, but not in small and difficult to compute energy differences which give rise to the various ice phases and to the exact bulk geometry. The importance of the H-bonds can be illustrated by keeping all the oxygen atoms at the same positions as in the regular bulk ice (assumed to have perfectly tetrahedral coordination) and placing the H atoms opposite the neighboring oxygen atoms, thus minimizing H-bonding. One loses 27.7 kcal/mol. This calculation gives an idea of the repulsion between the water molecules, which is only approximately 10% of the energy obtained though H-bonding.

The importance of the H-bonds in determining the total energy suggests a geom-

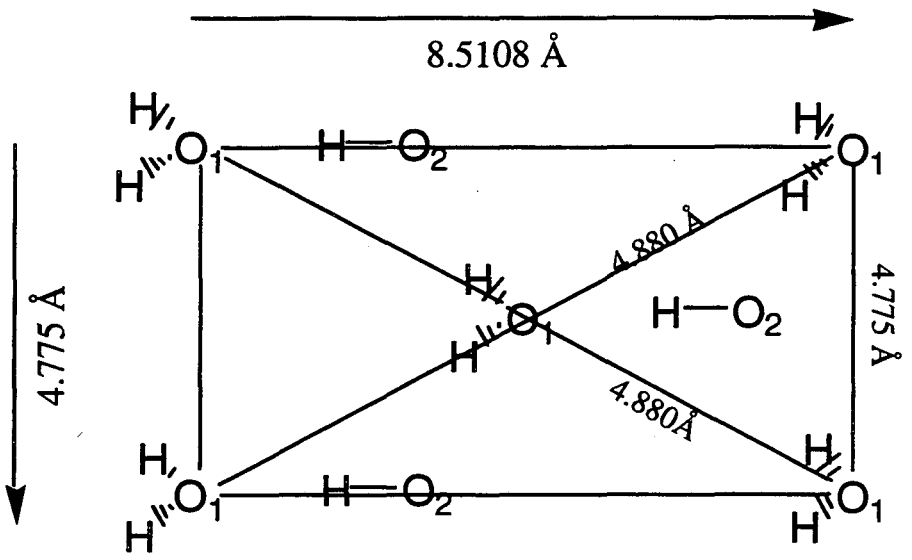

Figure 7.4: Top view of the $cm11$ unit cell for the distorted ice model.

etry in which every OH···O bond has the same local geometry as that of the dimer. In the dimer using the 631G** basis set, we calculate the OH bond length to be 0.943 Å and the OH···O distance is 2.979 Å. The H-bond energy for the dimer is 5.5 kcal/mol. Assuming these constraints for the slab geometry, one must make a small distortion in the layer which contains the water molecules that make up a half-bilayer. In addition, the c-axis will no longer be perpendicular to this layer, but must be oriented with an angle of 86°. These distortions allow the formation of equivalent H-bonds similar to that of the dimer. The resulting system has $cm11$ symmetry but remains close to the hexagonal system. The resulting lattice of oxygen atoms formed from this $cm11$ unit cell is shown in Figure 7.4. The cell vectors for the corresponding bulk structure are $a=b=4.88$ Å, $c=4.755$ Å with angles $\alpha=\beta=118°$ and $\gamma=59°$. In the calculations below, we have also used the 631G** basis set.

Results for the bilayer (see Table 7.3: row labeled "2L") confirm that the H-bond energy of 4.7 kcal/mol within the bilayer is close to that of the dimer (5.5 kcal/mol) or to that of the bulk (6.25 kcal/mol). The energies in Table 7.3 are results for the dimer, several different bilayer geometries and the bulk $cm11$ ice. The H atoms are arranged in a (1x1) manner. The energies for the four-layer (4L) and the six-layer (6L) systems show that the couplings of the bilayers are weak (1.9 kcal/mol and 1.85 kcal/mol respectively). It is possible, as in the case of the hexagonal bilayers, that this energy could become

Table 7.3: Total energies computed with the 631G** basic set for the dimer, various models with the distorted hexagonal symmetry derived from the dimer geometry and the *cm*11 bulk model. In slab calculations, these structures have *cm*11 symmetry. For the bulk geometry (labeled as "H on bond axis"), the cell vectors are $a = b = 4.80$ Å and $c = 4.755$ Å with angles $\alpha = \beta = 118°$ and $\gamma = 59°$. The values labeled with a "†" are optimized. We have not distinguished between the two possible orderings of H-bonds in the slabs due to the similarity of the total energies. "*d*" is the O-O distances in Å; "H-Bonds" is the total number of H-bonds; "Energy" is the total energy with respect to the free H_2O molecules.

	d (Å)	H-Bonds	Energy (kcal/mol)
dimer	2.98†	1	5.5
2L: bilayer	2.98	3	14.1
3L: mono+bilayer	2.91	5	16.0
4L: 2 bilayers	2.91	7	30.1
6L: 3 bilayers	2.91	11	46.0
Bulk *cm*11 Ice			
H on bond axis	2.900†	4	25.4
HOH = 109.5°	2.887†	4	25.2

comparable to that of the H-bond of the dimer and to that of the H-bond of the bulk if a $(\sqrt{3} \times \sqrt{3})$R30° arrangement of the H atoms is used. The comparison of the 6L energy with those for 4L+2L or 3L+3L systems gives the energy for cleavage occurring between bilayers or within a bilayer. The energy of the $cm11$ bulk geometry resulting from the adaptation of the ice geometry to the H-bonds of a dimer is slightly more stable than the regular ice with equivalent O-O distances. However, the energy difference is very small and may disappear when the proton exchanges are considered. Nevertheless, these calculations show the importance of the H-bonds in determining the total energy of the system.

7.5.3 Conclusions from Total Energy Computations

In this section, we have examined the two possible surface terminations discussed in the last section, using total energy calculations. One would expect the ice surface to maximize the number of hydrogen bonds. Such maximization of course occurs within bulk ice,[193] and also appears to occur at water surfaces and water/molecule interfaces.[197] Qualitatively, one would expect an energy difference equal to one hydrogen bond between the half- and full-bilayer termination. When the bulk lattice is cleaved such that both surfaces terminates in the full-bilayer, one hydrogen bond per surface unit cell is broken, as can be seen by examining Figure 7.2. However, if the lattice is cleaved such that both surfaces terminate in the half-bilayer, three hydrogen bonds are broken. Thus, this simple computation gives an energy difference of one hydrogen bond per surface unit cell per surface in favor of the full-bilayer termination. Our calculations also show that hydrogen bonding is the main factor in the determination of the surface structure. This is true even within liquid water where, on average, each molecule makes 2 to 3 hydrogen bonds to neighboring molecules, forming a random network, such that strings of hydrogen bonds extend uninterrupted throughout the liquid.[198]

The total energy computations confirm this simple argument for the energetic stability of the full-bilayer termination over the half-bilayer termination. The calculation of the energetic stabilization of full- vs. half-bilayer termination gives about 14 kcal/mol (total for both sides), which is indeed approximately double the H-bond energy of about 7 to 8 kcal/mol. In these calculations, we also found that the arrangement of molecular orientations contributes noticeably to the total energy through dipole-dipole interactions, but not to the extent of changing our conclusions.

Table 7.4: Resulting MD *rms* amplitudes of motion of the O-atoms perpendicular to the surface, $\sigma(Z)$ in Å for the first 8 layers, or the first 4 bilayers. The translational order parameter, S_T, and the rotational order parameter, S_R, are also shown.

Layer	$\sigma(Z)$	S_T	S_R
1	0.24	0.90	0.66
2	0.20	0.91	0.86
3	0.19	0.92	0.87
4	0.16	0.92	0.88
5	0.16	0.94	0.89
6	0.15	0.94	0.90
7	0.15	0.95	0.90
8	0.14	0.95	0.91

7.6 Molecular Dynamics Simulations

Given the $T=0$ K Hartree-Fock results, we now examine the results of the molecular dynamics (MD) simulations. With these simulations we can obtain dynamic information about the water molecules on the ice surface. In addition, MD simulations also allow us to examine any possible effect of temperature on the relative stability of the two differently terminated models. Using the translational order parameter S_T, it is also possible to address the full-bilayer model which has disordered, but not vibrationally enhanced, topmost water molecules.

For the upper eight layers, we collect in Table 7.4 the *rms* amplitudes $\sigma(Z)$ of motion perpendicular to the surface, translational order parameters (S_T) and rotational order parameters (S_R) calculated using the MD method. The most important result of this table is that $\sigma(Z)$ of the first layer is much larger than that of the other layers and also much larger than the bulk value of the zero-point uniaxial *rms* vibrational amplitude (0.1 Å at 90 K).[193] Thus, the MD simulations lend support to the assumption that, in the full bilayer termination, the water molecules in the upper layer of the first bilayer are essentially "invisible" in the LEED experiments (in the sense of Table 7.1 and Figure 7.9), due to their enhanced amplitude of motion perpendicular to the surface.

The $\sigma(Z)$ value calculated for the first layer is not quite as large as the value needed ($\approx$ 0.25 Å) to make the upper layer molecules "invisible" in the LEED experiment. However, close examination of Table 7.1 and Figure 7.9 shows that the upper layer is not

completely "invisible." The R_p-factor value of 0.24 for $\sigma(Z)$ in the upper layer is only $\approx$ 0.01 larger than the best-fit R_p-factor of Section 7.7. In addition, the MD result for $\sigma(Z)$ is likely to be a lower bound for $\sigma(Z)$ of the "experimental ice," for several reasons. In the MD simulations, the contribution of the intramolecular vibrations to the oxygen amplitudes is absent (the water molecules are treated as rigid rotors). Furthermore, the lattice constant parallel to the surface which fits the experimental results best is enhanced over the bulk value, indicating the presence of some strain in the surface: apparently the ice layer is not yet thick enough for the surface molecules to be unaware of the presence of the metal surface underneath. In the presence of such strain, one may expect the hydrogen bonds to be somewhat weakened, resulting in increased amplitudes of motion.

According to the MD simulations, the *rms* amplitude $\sigma(Z)$ slowly decreases when going into the bulk (see Table 7.4). Note that the amplitude in layer 2 is similar to that in layer 3, and the same is true for layers 4 and 5, and so on. The amplitudes of motion perpendicular to the surface are more or less the same for the molecules of the lower layer or half-bilayer within a given bilayer as those for the molecules in the upper layer or half-bilayer of the bilayer below. Because the hydrogen bonds between these molecules (for example the molecules in layers 2 and 3 of Figure 7.2) are in the direction direction perpendicular to the surface, the motions of the molecules perpendicular to the surface is highly correlated in these half-bilayers.

The enhanced vibrational amplitude in the upper layers is also visible in Figure 7.5, where we show a density profile along the Z-direction (see also Section 7.3.3). As is clearly evident, the two layers in the first bilayer have started to merge. From a dynamical perspective, it will no longer be possible to make the assignment of a given molecule to one of the layers within the first bilayer on the basis of the instantaneous position of the molecule only. In contrast, the layers within the third, fourth and fifth bilayers are basically distinct. The molecules in the sixth bilayer are clearly affected by the presence of the rigid layers underneath, as is evinced by the sharp peak produced by the lower layer.

Turning our attention to the translational and rotational order parameters (see also section 7.3.3) presented in Table 7.4, we find that the surface of ice is much more ordered at 90 K than it is at 190 K and higher.[163] The translational order parameters for the first and second layers at 90 K are 0.90 and 0.91, respectively; at 190 K they are in the range of 0.4 to 0.6 (see Reference 163). At 90 K, the rotational order parameter S_R is 0.66 for the first layer; it is in the range of 0.2 to 0.3 at 190 K. Nevertheless, S_R is much lower for the

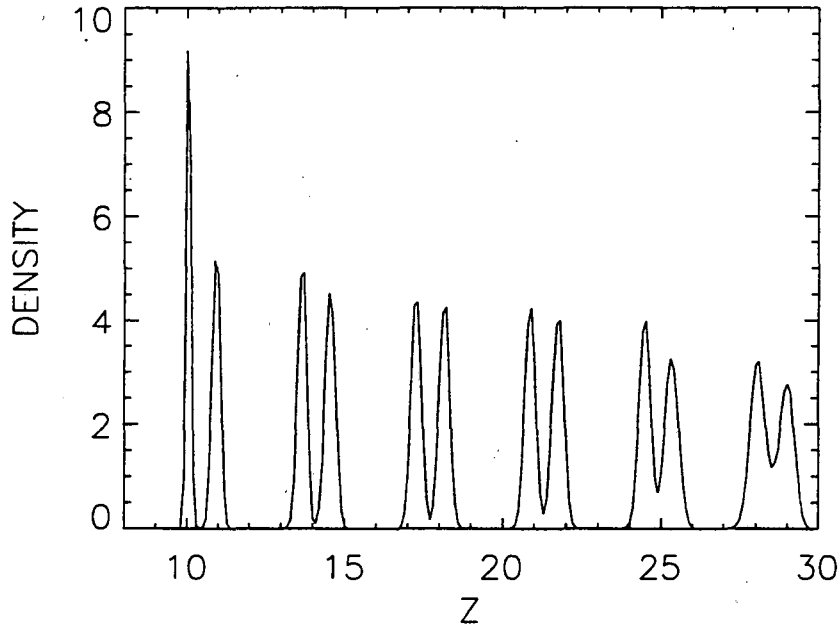

Figure 7.5: Density profile along the direction perpendicular to the Ih(0001) surface at $T = 90$ K. The density is in a.u., and the distance is in Å. Only the moving layers are shown.

first layer (0.66) than it is for the second and lower layers (0.86 and higher), indicating that the extent of rotational disorder is much larger in the first layer. The rotational disordering is visualized in Figures 7.6 and 7.7, where we plot distributions ("densities") of $\cos\theta$ and ϕ (see section 7.3.3). As can be seen from Figure 7.6, the distribution of $\cos\theta$ about the ideal lattice values (0.5 and -0.5) is much wider for the first layer than for the second. Likewise, the ϕ-distribution, shown in Figure 7.7, is also broader for the first layer.

The increased amplitude of motion $\sigma(Z)$ and the enhanced rotational disorder in the first layer should be a consequence of the disruption of the hydrogen bonding network at the surface.[199] In bulk ice, the molecules are firmly held in place by a strongly directional tetrad of hydrogen bonds, which is disrupted at the surface. In the ideal (0001) surface with full bilayer termination, the molecules in the outermost layer only participate in three hydrogen bonds. As a consequence, they may try to move inwards to form an extra hydrogen bond. This may lead to strains and some disruption of the hydrogen bonding network. At $T = 190$ K, Kroes[163] found that this strain also leads to high rotational mobility of the molecules, as is evident from the small value calculated for the NMR correlation time (τ_{NMR} of the order of 100 ps[163]). We found it impossible to calculate a converged value for τ_{NMR} (it should be larger than 1 ns) at a temperature of 90 K. Nevertheless, the low value of S_R for the first layer and the wide angular distributions indicate an enhanced rotational mobility of the molecules in the first layer. Of course, the most important consequence of the strain in the surface layer for the present experiments is still the enhanced value of $\sigma(Z)$.

7.7 Refinements to the LEED Structure

After combining the LEED results with the total energy and molecular dynamics results, the Ih(0001) model, with full-bilayer termination and enhanced vibrational amplitudes for the top oxygen atoms is clearly the best model for our ice film. The half-bilayer model is ruled out due to total energy arguments and the stability of the full-bilayer is supported by MD simulations (see Table 7.4 column S_T). Due to the stability of the full-bilayer termination, we do not believe that the apparent half-bilayer termination is due to a disordered top layer. This reasoning does not assume that the whole surface is perfectly ordered as indicated by the high background in the LEED pattern (Figure 7.1), but, instead it implies that the ordered portion which contributes to the diffraction pattern is a well

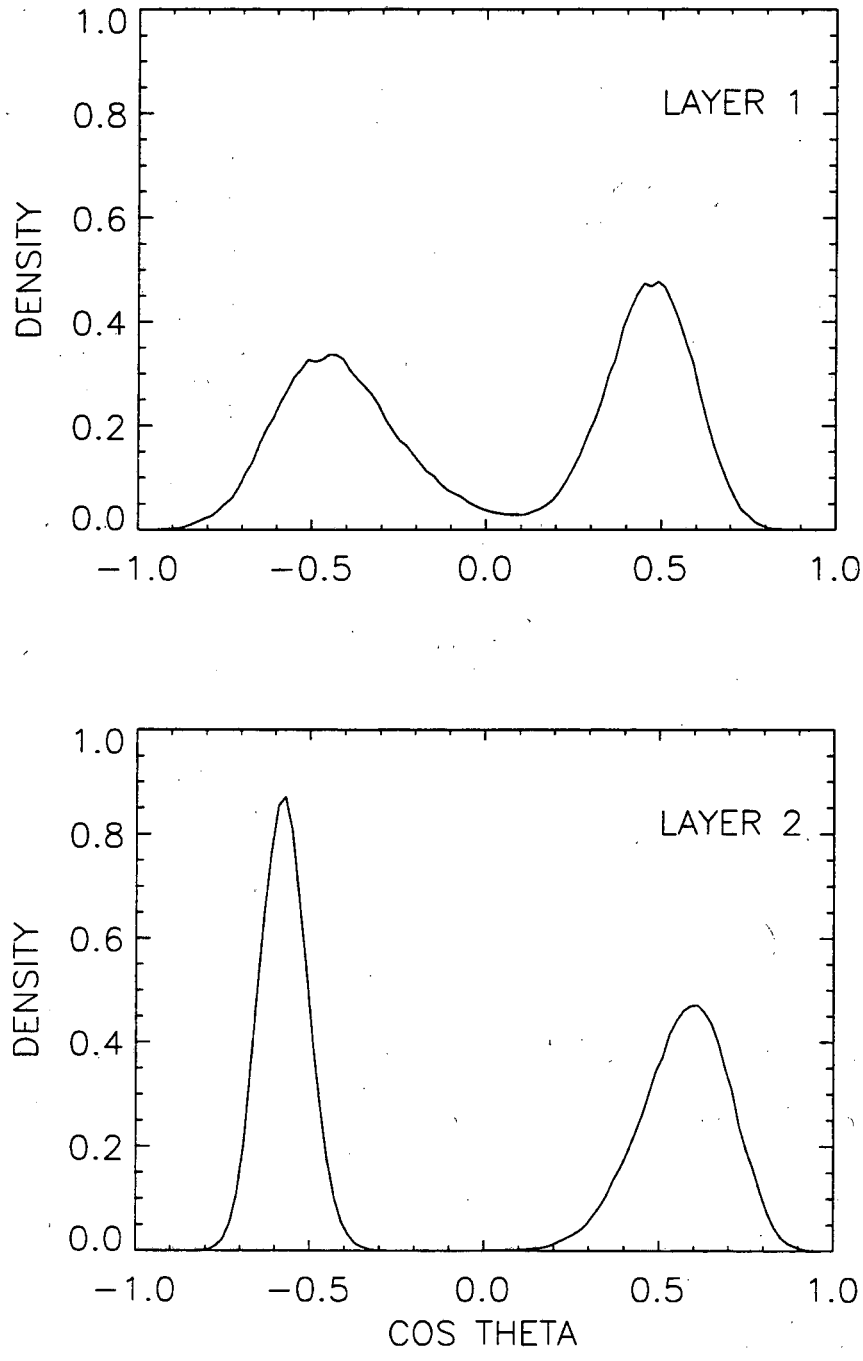

Figure 7.6: The resulting MD distribution of $\cos\theta$ (in a.u.) for the water molecules in the first two layers at $T = 90$ K. θ is the polar angle the dipole vector of water makes with the surface normal.

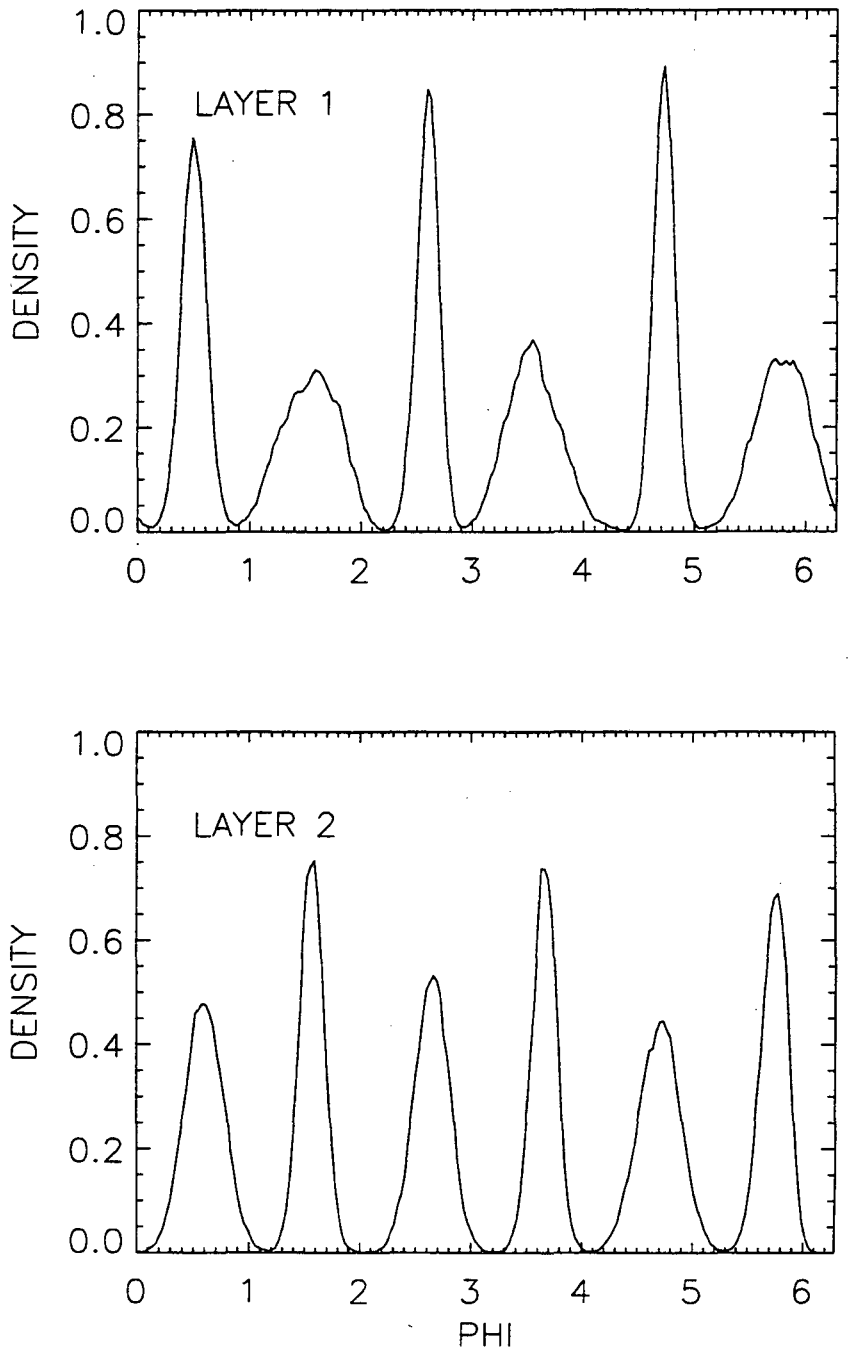

Figure 7.7: The resulting distribution of ϕ (in a.u.) for the water molecules in the first two layers at $T = 90$ K. ϕ is the azimuthal polar angle which defines the projection of the dipole vector of water on the surface.

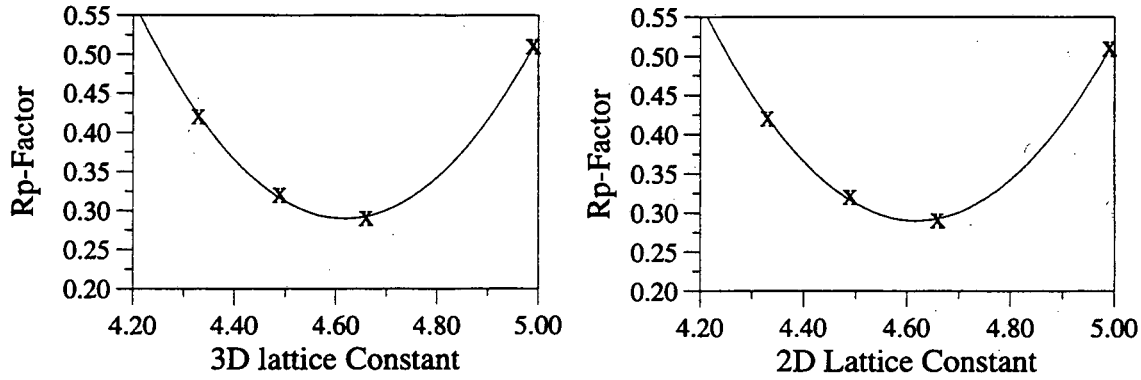

Figure 7.8: R_p-factor variation of Ih(0001) with the 2D and 3D lattice constants. For each lattice constant value (marked by a "x'), the outermost two interlayer spacings were optimized. In the 3D lattice constant determination, the lateral lattice constant was varied from 4.33 to 4.99 Å parallel to the surface with a proportional lattice constant perpendicular to the surface, while for the 2D lattice constant determination, the lateral lattice constant was varied from 4.33 to 4.99 Å parallel to the surface with the lattice constant perpendicular to the surface fitted at its optimal value. For bulk ice, the lateral lattice constant is 4.52 Å. The solid lines are a best-fit parabola.

ordered full-bilayer. Therefore in this section, we refine the initial full-bilayer termination model of Section 7.4 to obtain the best-fit structural parameters.

7.7.1 Refinement of the Lattice Parameters

In bulk ice, the O-O distances within the bilayer are slightly different from those between bilayers[193]. In the LEED computations (see Table 7.1 in Section 7.4) we have assumed that all O-O distances are identical. We now attempt to examine the effect of relaxing this artificial constraint on the best-fit structure. For the best-fit Ih(0001) model, with full-bilayer termination and enhanced vibrational amplitudes, we have explored different lateral lattice constants from 4.33 to 4.99 Å parallel to the surface (Table 7.1), the bulk ice value being 4.52 Å, with proportional lattice constants perpendicular to the surface, and various spacings between the two outermost oxygen layers. The resulting R_p-factors vs. the lattice constants are shown in Figure 7.8 (labeled "3D Lattice Constant") with the minimum at 4.62 Å. By allowing the lateral lattice constant to change proportionally to the lattice constant perpendicular to the surface, we have enhanced the sensitivity of the R_p-factor to changes in its value. Because fitting does not take into account that the O-O distances for the molecules in the bilayer are slightly different from those between bilay-

ers in bulk ice, we have also performed LEED calculations for models in which we varied only the lateral lattice constant with the perpendicular lattice constant equal to the above value. Figure 7.8 (labeled "2D Lattice Constant") shows the resulting R_p-factor variation as the lateral lattice constant took on values between 4.33 and 4.99 Å with the minimum also at 4.62 Å. This optimization scheme has the effect of varying both the in-plane O-O bond distance and bond angle. Unfortunately, the R_p-factor has low sensitivity to further refinements of the lattice constants, due to the relatively small energy range of the LEED data. For the final structure, we have assumed that all O-O bond distances are identical.

7.7.2 Enhanced Vibrations

In Section 7.4.2, we used a bulk *rms* vibrational amplitude of 0.10 Å and an enhanced amplitude of 0.28 Å without justification. With the full-bilayer termination model with enhanced vibrational amplitudes supported by both the total energy computation and the MD simulations, we can examine these parameters in more detail. Figure 7.9 shows the R_p-factor variation of the topmost oxygen (lightly shaded in Figure 7.2) vs. the inverse *rms* perpendicular amplitude. The value of zero for the inverse *rms* amplitude corresponds to the half-bilayer termination model. The minimum value is within the range of values predicted by the MD simulations of Section 7.6. However, the error bar on this determination is relatively large. The R_p-factor was relatively insensitive to the vibrational amplitudes of deeper layers. We have chosen 0.10 Å for the bulk *rms* perpendicular amplitude because it corresponds to experimental values for bulk Ih ice.[193]

7.7.3 Addition of Hydrogen

As mentioned Section 7.4, hydrogen was omitted in most LEED calculations because of its small contribution to the LEED intensities. This is not only because of its small scattering cross-section, but also primarily in view of the inherent disorder present in its asymmetric positions. We now attempt to investigate the influence of hydrogen in the LEED computations in the hope of obtaining some information, if only averaged, about the hydrogen positions.

In a first calculation, we modeled the H atom positions by occupying the midpoints of all O-O bonds with H atoms having large vibrational amplitudes (Debye temperature of 1200 K) in order to represent the averaged smeared-out H positions. In addition to

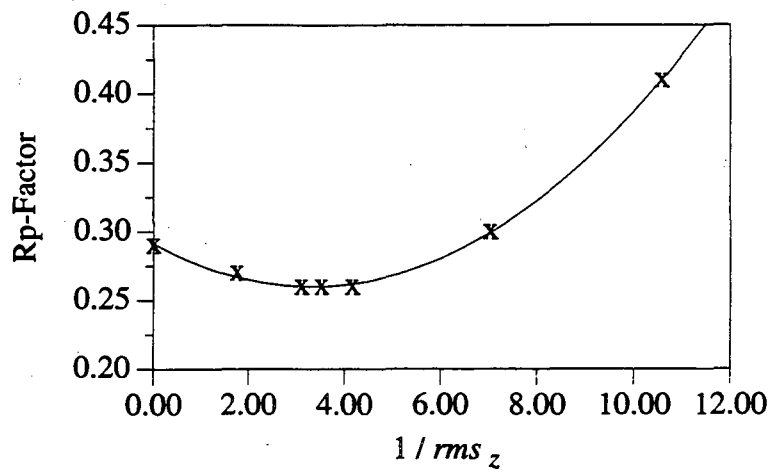

Figure 7.9: The R_p-factor variation of the topmost water layer vs. the inverse rms perpendicular amplitude. The value of zero for the inverse rms amplitude corresponds to the half-bilayer termination model, and the minimum value is within the range of values predicted by the MD simulations. The data points are marked with an "x" and the curve is a best fit parabola.

hydrogen atoms at the midpoints, calculations were also performed with H in "top" sites on the outermost O's of a full bilayer termination to represent surface H atoms not involved in hydrogen bonding. These calculations resulted an in R_p-factor value of approximately 0.40 when only the interlayer spacings between the first two oxygen layers were optimized, and 0.30 when the hydrogen positions were included in the R_p-factor minimization. The last value (0.30) was between the values obtained for the half-bilayer termination and for the full-bilayer termination, but the hydrogen atoms were found to be optimized at unrealistic positions. However, because this model has many more fitted parameters, it should yield a much better fit than the half-bilayer Ih model without hydrogen; therefore, since this change in the R_p-factor is so small, the introduction of H actually worsens the agreement with experiment. A final calculation was done on a model with H atoms occupying only the top sites to simulate detectable top-site H atoms on the surface with undetectable disordered H atoms in the bulk. The addition of hydrogen atoms at these top sites in the full-bilayer model results in an R_p-factor value of 0.40 and therefore also worsens the agreement with experiment. Thus, not surprisingly in the view of the MD simulations, our results suggest disordered hydrogen on the surface as well as in the bulk.

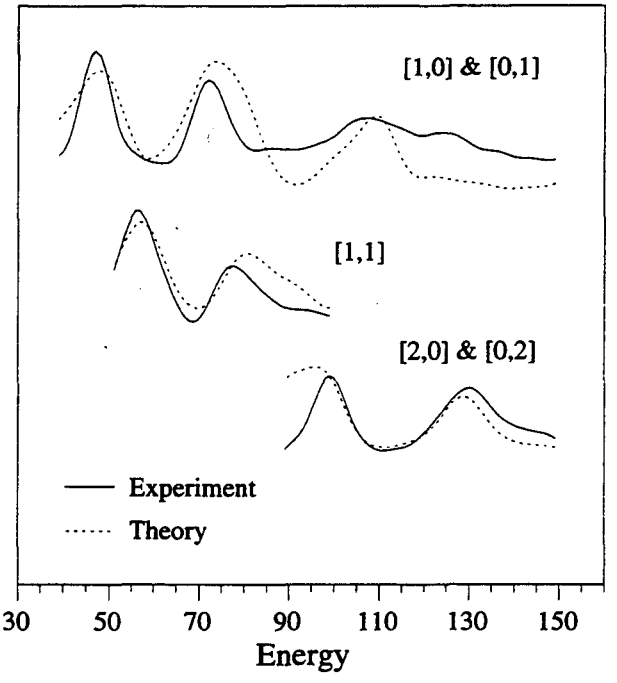

Figure 7.10: The best-fit intensity vs. energy (I-V) curves for the Ih(0001) full-bilayer termination model with the strongly vibrating (or otherwise disordered) molecules in the top half of the bilayer. The coordinates of the final best-fit structure, which yields an R_p-factor of 0.26, are given in Table 7.5.

7.7.4 The Final Structure

For the best-fit full-bilayer termination with enhanced vibrational amplitudes we obtain an R_p-factor of 0.26. The lattice constant parallel to the surface, with proportional lattice changes perpendicular to the surface, was varied to obtain an optimal value of 4.62 ± 0.10 Å. This corresponds to a hexagonal unit cell with edges $a = 4.62$ and $c = 7.56$ Å, within the ice film, compared with bulk values of 4.52 and 7.37 Å, respectively. Thus, the lattice of the ice film may be slightly expanded parallel to the surface by $2 \pm 3\%$, possibly due to the mismatch between the ice film and the Pt substrate; a match would require a 6.4% lateral expansion of the ice. The coordinates of the final best-fit structure are given in Table 7.5; the corresponding best fit I-V curves are shown in Figure 7.10.

Table 7.5: Oxygen coordinates [in Å] for one 2D unit cell of the best-fit full-bilayer termination with enhanced vibrational amplitudes for the top oxygen atoms model of ice Ih(0001). X and Y are coordinates parallel to the surface (repeating with the given 2D lattice vectors) while Z is perpendicular to surface. One unit cell is given by its 2D lattice vectors along with its repeat vector for the bulk. Due to the enhanced vibrational amplitudes, the R_p-factor was insensitive to variations in the position of the top oxygen atom; thus, its position was not optimized.

X	Y	Z	
0.00	0.00	0.00	(insensitive)
1.33	2.31	0.99	±0.05
1.33	2.31	3.79	±0.06
0.00	0.00	4.80	
Repeating Bulk Atoms			
0.00	0.00	7.63	
1.33	2.31	8.57	
1.33	2.31	11.40	
0.00	0.00	12.34	
Bulk Repeat Vector			
0.00	0.00	7.55	
2D lattice vectors			
4.00	-2.31	0.00	
4.00	2.31	0.00	

7.8 Conclusion

We find the ice surface at 90 K to be terminated by strongly vibrating molecules in the top half of the outermost bilayer, such that the molecules would be undetectable by LEED. This model results in the best agreement between the theoretical and experimental intensity vs. energy (I-V) curves and is consistent with total energy considerations based on maximizing the number of hydrogen bonds. In addition, the stability of the Ih(0001) surface with bilayer termination and bulk-like interlayer spacings is clearly illustrated by our molecular dynamics simulations. The top bilayer has much higher translational and rotational order than found previously at 190 K. While the previous calculations found a much enhanced rotational mobility of the top layer molecules, little enhancement of the rotational mobility was found for 90 K. On the other hand, for the O atoms large amplitudes of motion perpendicular to the surface were found in the top layers. The simulations do indicate a more gradual decay of amplitudes into the substrate than that found by LEED.

The possibility that the molecules of the top half-bilayer vibrate with relatively large amplitudes perpendicular to the surface as low as 90 K is also reasonable for molecules held in place by only three almost coplanar hydrogen bonds, the bonds being only 19.5° out-of-plane in an ideal tetrahedral geometry. The weak dependence of the bond energy on the O-O bond angle is supported by total energy calculations.[198] In the ice structure, the perpendicular vibrations of the outermost water molecules are not obstructed due to the relatively open Ih structure, although these molecules are needed to stabilize the lower half of the bilayer.

Chapter 8

Iron Surface: A First Step

The catalytic synthesis of ammonia over an iron catalyst has been both an important technological problem and a scientific challenge.[200] Despite the large amount of successful research into the qualitative aspects of this catalytic process, very little is known about the detailed atomic structure of atoms and molecules on the catalytically active Fe(111) surface. On this surface there has been no LEED structural determinations of either atomic or molecular adsorbates.[2]

In this chapter, we have addressed two of the major difficulties which must be overcome as a first step in investigations of adsorbates on this surface. The first is the inherent difficulty in cleaning these surfaces due to the bcc to fcc phase transition at 910°C. The second difficulty involves the close interlayer spacing (≈ 0.8 Å) present on the Fe(111) surface. This close spacing requires major modifications to the "standard" automated tensor LEED analysis programs.

8.1 Background

The clean iron surfaces have been studied in great detail by the group of F. Jona and P. M. Marcus[17]. However, very little quantitative structural work has been done with adsorbates on any iron surface.[2] Focusing on the Fe(111) surface, a number of clean surface determinations have been performed.[201,202] These determinations result in a structure in which the first and second interlayer spacings contract by 16.9 ± 3.0 and 9.8 ± 3.0 %, respectively. The third spacing shows a small expansion followed by a small contraction of the fourth. These calculations were performed with a specialized LEED program. In

addition, the surface has been investigated using total energy calculations by R. Wu et al.[203] and their results agree within 0.2 Å with the LEED result.

Ordered atomic nitrogen overlayers have been reported on the Fe(100), Fe(110) and Fe(111) surfaces. For the Fe(100) surface, the Fe(100)-$c(2 \times 2)$-N LEED structure has been determined by R. Imbihl et al.[204] and the structural results have been interpreted as showing a surface nitride. The surface structure is similar to that of the (002) plane of bulk Fe_4N. Similar arguments have been made for nitrogen absorbed on the Fe(110) surface;[205] however, no LEED determination has been performed. The Fe(111) surface is more complex. Several qualitative LEED studies have been performed.[206,207] F. Bozso et al.[207] found LEED structures with (3×3), $(\sqrt{19}\times\sqrt{19})$R23.4°, $(3\sqrt{3}\times3\sqrt{3})$R30° and (2×2) periodicities. These LEED patterns are interpreted as being formed by a reconstruction and subsequent rotation of the first metal layer. The decomposition of hydrocarbons forms very similar overlayers on this surface.[206]

In addition to the LEED work, there has been many non-structural studies of this surface. Thermal desorption spectroscopy (TDS) has shown that the sticking probability of N_2 on the Fe(111) surface is an order of magnitude larger than that of the Fe(110) or the Fe(100) surfaces.[205] Reaction studies have also shown that the Fe(111) surface has a much higher rate constant than the Fe(110) or the Fe(100) surfaces.[200] These studies illustrate the importance of this face for the catalytic synthesis of ammonia. Vibrational spectroscopy[208] and angle resolved photoemission[209] support a bonding model in which N_2 is bonded to the metal surface on its side.

8.2 Cleaning

8.2.1 UHV Cleaning

Our first attempts at cleaning the Fe(111) surface followed the procedure used for other clean surfaces (see Section 2.2). Sputtering followed by annealing has been successful in cleaning a Fe(100) sample of K. O. Legg et al.[210]. We found their procedure sufficient to form a metastable clean surface, but not one which was clean enough for further studies. Although they were able to form a clean surface which was satisfactory for their LEED study, we found that heating the sample to temperatures required for adsorption studies resulted in the segregation of sulfur to the surface. Figure 8.1 shows the typical Auger

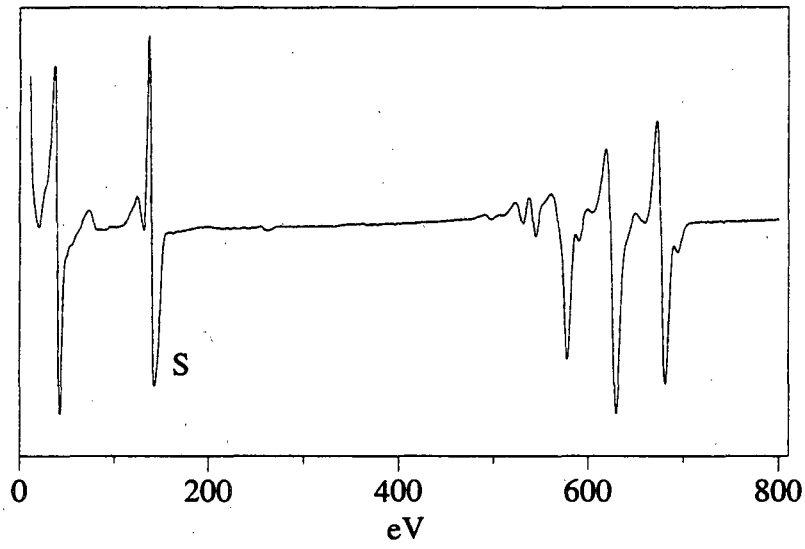

Figure 8.1: AES spectrum of a sulfur covered iron sample. The spectrum resulted after heating a UHV cleaned iron crystal to 650° C. The peak due to sulfur is labeled while the remaining peaks can be assigned to iron.

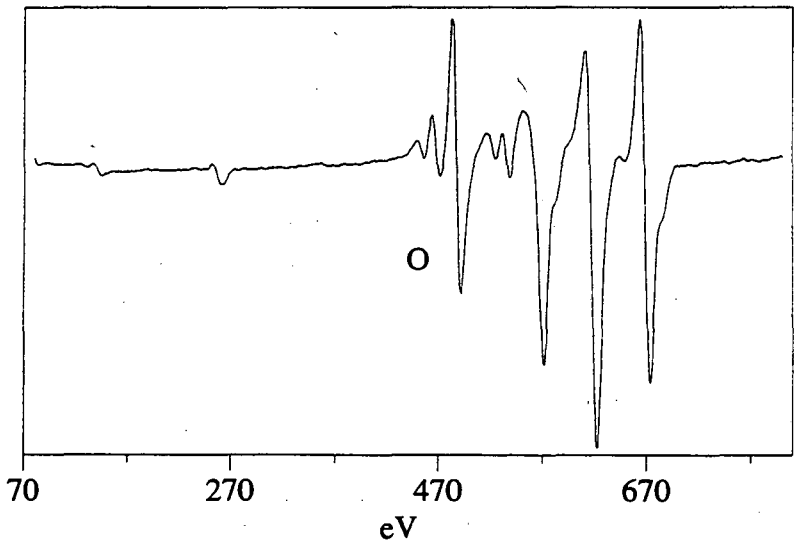

Figure 8.2: AES spectrum of an oxygen covered Fe sample. The oxygen overlayer forms during the oxidation of carbon deposits on the iron surface and is removed when the sample is heated between 650 and 700° C. The peaks due to oxygen are labeled, and the remaining peaks can be assigned to iron.

electron spectroscopy (AES) spectrum of our iron sample after heating to approximately 650° C.

We found that is was possible to remove carbon from the surface by heating in an

oxygen background. After this procedure, the Fe(111) surface forms a disordered surface oxide which must be removed by heated between 650 and 700° C. We found this process highly successful for removing carbon if sulfur is not present on the sample. Any trace of sulfur poisoned the reaction of oxygen with carbon. In addition, the subsequent annealing to remove the oxide layer segregates sulfur to the surface.

8.2.2 High-Pressure Cell

High-pressure cells[200] have been used in the G. A. Somorjai group to perform reaction studies under atmospheric conditions with UHV prepared samples. We used a high-pressure cell to remove the sulfur conditions by heating the sample to 700° C under an atmosphere of flowing H_2 gas for several days. The high-pressure cell consists of a tube which closes over the sample and sample manipulator, sealing it from the UHV environment. Because the inner diameter of the tube is quite small, the sample mounting was done by spot welding the sample to metal wires which were connected to electrical feedthroughs for resistively heating the sample. Several metal wires were used in an attempt to hold the sample during heating. Gold wires were too difficult to spot weld and iron wires failed after several hours of sample heating. Platinum wires seemed to provide contact for several days before finally failing.

One iron sample was heated to 700° C under an atmosphere of flowing H_2 gas for three days. The sample appeared clean when transferred into the UHV system. However, after several hours of UHV cleaning, sulfur returned to the surface. Thus, hydrogen treatment works, but one needs to allow more time to remove all of the sulfur from the sample. Figure 8.3 shows the gradual increase of sulfur on the surface when the sample was held at 600° C. Higher temperatures increased the rate. After several surface diffusion experiments, we found that further cleaning was clearly necessary.

8.2.3 Hydrogen Furnace

Our experiences with the UHV and the high-pressure cell cleaning procedures convinced us to design a hydrogen furnace. E. Hassold et al.[211] used a similar procedure to clean an Fe(211) sample. The requirements of the system are high temperatures, freedom from additional contaminants and stability. The high stability is needed because if either the hydrogen flow or the temperature changes over a month, sample cleaning would be

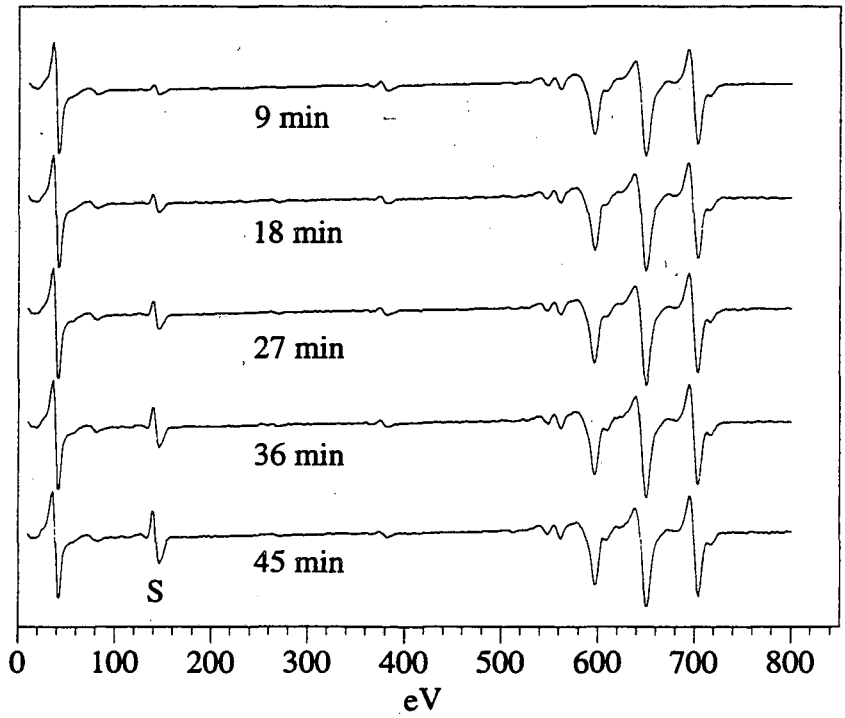

Figure 8.3: The time dependence of the surface segregation of sulfur monitored by AES. The sample was held at 600° C during the experiment. The peak due to sulfur is labeled, and the remaining peaks can be assigned to iron.

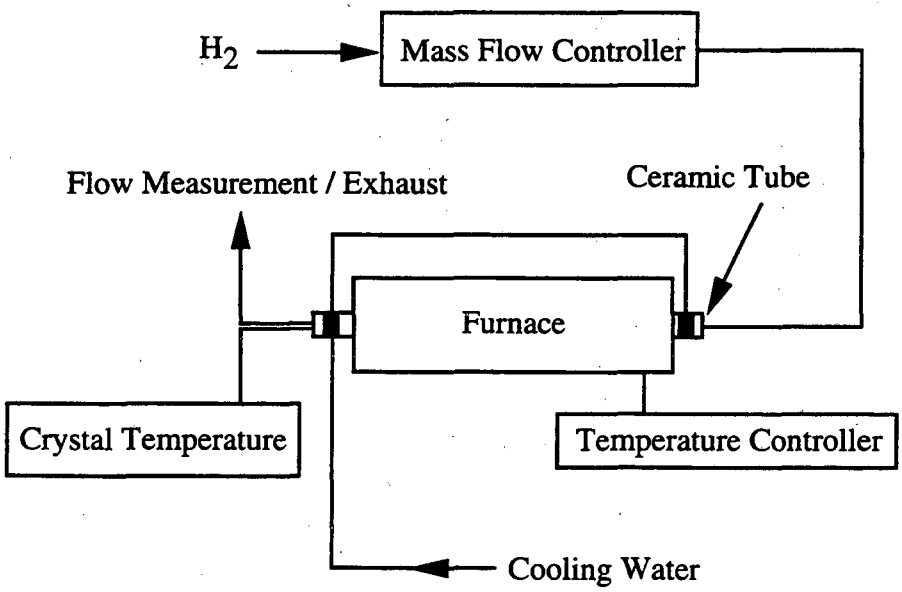

Figure 8.4: Outline of the construction plan for the hydrogen furnace. It is capable of heating the sample to 700° C and maintaining a constant flow rate of approximately 1mL/min for periods of up to a month.

compromised. In addition, it is not possible to keep watch over the system over this time scale. The overall design of the furnace is illustrated in Figure 8.4. H_2 gas flow was controlled by a mass flow controller which provided low flow rates with very little variance. The reactor tube was a ceramic tube which had been precleaned with flowing hydrogen gas and high temperatures. The connections to the tube were made with a pressed Teflon seal on one side and an o-ring seal for quick release on the other. These connections were cooled by flowing water to prevent failure due to melting. The hydrogen was allowed to escape through a manual flow meter as a double check. The furnace temperature was controlled by a thermocouple placed in the center of the heating elements. Using a small ceramic spacer, an additional thermocouple was held in the center of the iron wire to which the iron samples were spot welded. This additional thermocouple provided a direct measure of the sample temperature.

Several crystals were placed in this furnace for a period of one mouth. The sample temperature was held at 700° C. From the high-pressure cell experiences, it was determined that 600° C was not high enough to allow rapid enough mass transfer of sulfur from the bulk to the surface. 700° C was chosen, but not optimized. After spending a month in this environment, some of the samples required repolishing due to discoloration of the surface. After repolishing and introduction into the UHV chamber, several sputter-anneal cycles were needed to remove any remaining sulfur atoms along with annealing in an oxygen background to remove carbon. However, after these procedures, the samples appeared to be atomically clean. Additional carbon buildup from background gases could be easily removed by oxygen treatments. Further experiments still need to be performed, but these initial results seem promising.

8.2.4 UHV Sample Mounting

As in the high-pressure cell, the sample mounting was also found to be a problem for the UHV manipulator. The initial sample mounting was done by spot welding the sample to Ta strips which were connected to electrical feedthroughs for resistively heating the sample. In all cases, these spot welds failed after prolonged heating to 700° C. To alleviate this problem a new sample manipulator was designed in order in implement e-beam heating, thus, solving the mounting problem.

In this new manipulator, the sample was mounted using Ta strips spot welded to a

Mo plate screwed onto a Cu block. This block was cooled with flowing liquid-N_2-cooled N_2 gas. The sample was heated using an e-beam filament placed 1 mm under the metal sample through a hole in both the Mo plate and the Cu block. The sample temperature could be measured using a chromel-alumel thermocouple spot welded to the side of the sample.

8.3 LEED Computations

In addition to the cleaning, a second difficulty involves the close interlayer spacing ($\approx$ 0.8 Å) of the Fe(111) surface. This spacing presents a problem for our "standard" LEED analysis programs. The dynamical calculations have been addressed in the earlier studies of H. D. Shih et al.[201] and J. Sokolov et al.;[202] however, their programs did not implement TLEED. In this section, we discuses our development of an ATLEED program which can perform these calculations on the iron surface.

8.3.1 Layer Doubling

Our "standard" automated tensor LEED analysis program uses Renormalized-Forward-Scattering (RFS)[6,18] to compute the diffracted amplitudes in a series of steps composed of only one backscattering event, thus, relying on the fact that backscattering is weak compared to forward scattering. When two layers are placed close to one another, the number of evanescent-waves increases and the backscattering amplitude of high order beams becomes large. The first effect decreases the stability of the method, while the other causes the method to diverge.

For interlayer spacings between 1.0 and 0.5 Å, Layer-Doubling (LD)[6,18] has been shown to provide an effective solution. For smaller spacings, one must rely on a number of specialized methods specifically designed to address the close interlayer spacings on stepped surfaces[212,213]. The LD method computes the reflectivity of the bulk by solving multiple scattering exactly between two layers in the plane wave representation by matrix inversion, forming a single new layer. Once this is done, one solves for multiple scattering between two of these new layers. Thus in an iterative process, one continues joining pair of even increasing layers until the reflectivity does not change. The result gives the reflectivity for an ideal unrelaxed substrate. After this, the non-bulk-like surface layers are stacked one by one onto the surface, using the same method. New LD routines were written which allow

this process to be transparent from the point of view of the user. The new code was able to calculate the theoretical I-V curves of the Fe(111) surface under 200 eV.

8.3.2 Generation of the Tensor

One problem with LD is that local information about the plane wave amplitudes is lost during the process. The result of the RFS method provides the plane wave amplitudes for each layer while in LD one only obtains the amplitudes at the surface. These amplitudes are needed in order to generate the tensor ($\mathcal{F}^n_{LL'}$ of Equation 2.18) from Equation 2.20. This problem can easily be solved once one realizes that the outgoing wave can be back-propagated into the crystal. Effectively, this procedure is related to the transfer matrix approach[6] to the LEED problem. This procedure was implemented. An additional complication is that LD must be used multiple times to generate the outgoing LEED state for each exit beam for which one wants a TLEED tensor. This is important because LD uses matrix inversion and can be solved by saving the inverted diffraction matrices.

8.4 General Conclusions

We addressed both sample cleaning and LEED computations as a first step in the investigation of adsorbates on the Fe(111) surface. It was found that it was not possible to clean this surface using standard UHV cleaning procedure. In addition, we found that the sample mounting required to resistively heat the sample proved to be prone to failure. This difficulty was removed by switching to a design which allows e-beam heating. For the cleaning procedure, a specialized hydrogen reactor has been constructed to allow carefully controlled heating to 700° under a flow of H_2 gas at atmospheric pressures. In this reactor, the sample is to be heated in hydrogen for month-long periods without supervision or damage to the crystal. During this time period, the sulfur impurities diffuse to the surface and are removed by reactions with the H_2 gas. The atomically clean surfaces were obtained from crystals first treated in this manner and then cleaned in UHV.

We have shown that the layer doubling technique[6] can be used to perform conventional LEED calculations at the close interlayer spacing (≈ 0.8 Å) present on this surface. We have integrated this technique into our automated TLEED program. The ground work has now been completed for new structural determinations on this surface.

Chapter 9

General Conclusions

In Chapters 3 through 6 of this work, we have investigated the relaxation of the Pt(111) surface in the presence of various adsorbates (O, S, C_2H_3 and NO) with LEED. In addition to the work on the Pt(111) surface, we have presented two other systems: the surface structure of NO on the Ni(111) surface (Chapter 6) and an ordered ice film (Chapter 7). In this final chapter, we step back to examine general features which connect these various surface structures.

In the first section, we summarize the results of Chapter 3 and discuss these results in terms of our structural determinations. Next, in Section 9.2, we examine the structural similarities of various $p(2 \times 2)$ overlayers on Pt(111). One additional structural feature of molecules on surfaces, not present in the case of atomic adsorption, is a possible tilt of the molecule. Such a tilt can be interpreted as either a static tilt or as a wagging vibration. Our evidence supporting wagging vibrations for C_2H_3 and NO will be the subject of Section 9.3. Following this, drawing from material in Chapter 4, the effect of sulfur coverage on the surface structure and relaxations is briefly summarized. We then compare the structure of NO on Ni(111) with that of NO on Pt(111) in Section 9.5. After this, we summarize our structural results for an ordered ice film. Finally, we end with a discussion of our initial results on the Fe(111) surface and discuss future directions.

9.1 Reliability of a LEED Structure

As discussed in the introduction, detailed structural analysis has only recently been possible due to computational enhancement of tensor LEED (TLEED). To under-

stand the reliability of our structural determinations, in Chapter 3 we have undertaken a comprehensive study of various non-structural parameters used in LEED computations. In this section, we summarize what we have learned and how this knowledge was applied in our analyses.

One should not underestimate the importance of the clean surface data. On the experimental side, the overall performance of the equipment and the quality of the crystal can be quickly assessed using the clean surface I-V curves. By examination of the I-V curves of symmetry equivalent beams, one can also determine at which energies the I-V curves are the most sensitive to normal incidence. For the LEED analysis, the investigation of the clean surface, at least in the case of those clean surfaces which remain unreconstructed, provide a simple system on which to investigate various non-structural parameters used in the LEED computation. Most of all, by obtaining a low R-factor for the clean surface, one gains the confidence to move on to more complex overlayers.

We have investigated two clean metal surfaces. Our results in Chapter 3 for the clean Pt(111) surface and in Chapter 6 for the clean Ni(111) surface show excellent agreement with other experimental results[57,59,67,153,154]. In obtaining our clean surface results for Pt, we examined the scattering potential used in the atomic phase shift computation. We find that relativistic effects must be included in both the potential and the scattering portions of the phase shift computation for the Pt(111) surface. Another factor which we have found to constantly improve the agreement between theory and experiment is the use of a smaller muffin-tin radius in the phase shift computation than one would normally use in a band structure computation, where the crystal potential is solved self-consistently. By decreasing the muffin-tin radius, one removes charge density that is possibly inaccurate anyway, because the muffin-tin potential was not solved self-consistently. This charge density seems to be better described by a constant, the real part of the inner-potential, which is then fit in the analysis. As an additional benefit of reducing the muffin-tin radius, the number of phase shifts required in the LEED computation decreases. In particular, for the Pt(111) surface, the results of this phase shift study lead to a large improvement in agreement between theoretical and experimental I-V curves; the agreement represents a 50% improvement over older LEED results.[56,57]

We have also examined the effect of various non-structural parameters on the best-fit Pt(111)-$p(2\times2)$-O structure. We find that details in the construction of the muffin-tin potential do not influence the resulting structure. However, one must use the correct

relativistic treatment of the phase shifts in the case of a light element on a relativistic or high Z metal surface. Failure to do so will result in a systematic increase in the overlayer's bond length to the metal surface. We also optimized both the imaginary part of the inner potential and the surface Debye temperatures of the Pt and O atoms. However, these refinements resulted in very slight (less than 0.01 Å) changes in the final structure.

In the case of clean Pt(111), we find that the R_p-factor[47] can vary by factors of two due to modifications in the non-structural parameters, with little change in the final structure. In adsorbate systems, particularly O and S, reasonable variations in either the Debye temperature of the adsorbate or the imaginary part of the inner potential have little effect on the best- fit structure. This is an important result because it implies that the desired structural results can be trusted without detailed independent knowledge of the values of these parameters. The structural parameters related to the relaxations of the metal surface proved to be much more sensitive to fractional order beams than to integer order beams (see Figures 3.8 and 4.11). This indicates the importance of evaluating the fractional order beams both during the experimental measurement and in the analysis.

The identification of the relative importance of various factors establishes a foundation which was applied in the analysis of the S, C_2H_3 and NO structures on the Pt(111) surface. In all cases we have obtained good agreement between the experiment and theory. In fact, our agreement for these adsorbate systems is better than that for previous clean surface results.[56,57] Thus, our confidence in the structural results obtained from these systems is reinforced by the reliable quality of the fit.

9.2 General Features of Pt(111)-$p(2 \times 2)$ Overlayers

The resulting surface structures of the $p(2 \times 2)$ overlayers of O, S, C_2H_3 and NO on Pt(111) exhibit similar adsorbate-induced relaxations, or displacements of the metal atoms away from their positions in the clean metal surface. In all cases the adsorbate occupies the fcc hollow site, even in the case of NO where one might predict top or bridge bonding based on vibrational spectroscopy. Therefore, we do not have to worry about the effect of differences in metal coordination. The fcc hollow site is the site which would be occupied by a metal atom if there were an additional layer of the bulk. Because of the structural similarities between these overlayers, local bonding is identical; thus it is possible to focus on the general effect of different adsorbates on the metal, without worrying about effects of

Table 9.1: Comparison of vertical relaxations for $p(2 \times 2)$ overlayers on Pt(111). "Buckling" refers to the total buckling of the first layer. "Spacing" refers to the center of mass distance between the first and second metal layers. "Local Spacing" refers to the distance between the three metal atoms which are bonded to the adsorbate and the triangle of three metal atoms below the adsorbate in the second layer. For side views of the best-fit structures see: Figure 3.7 for O, Figure 4.8 for S, Figure 6.8 for NO, and Figure 5.5 for C_2H_3.

Adsorbate	Buckling	Spacing	Local Spacing
O	0.07 ± 0.03 Å	2.28 ± 0.03 Å	2.30 ± 0.03 Å
S	0.08 ± 0.04 Å	2.30 ± 0.03 Å	2.32 ± 0.03 Å
NO	0.06 ± 0.06 Å	2.30 ± 0.03 Å	2.32 ± 0.03 Å
C_2H_3	0.11 ± 0.05 Å	2.30 ± 0.03 Å	2.34 ± 0.03 Å

differences in coordination number. In addition, the adsorbate-adsorbate interaction should also be small due to the relatively large intermolecular distance in these $p(2 \times 2)$ overlayers.

The adsorption of these species induces an approximately 0.1 Å buckling of the metal surface. For all four different adsorbates, the buckling of the metal surface consists of the three metal atoms directly bonded to the adsorbate being "pulled" out of the surface and the metal atom which is not bound to the adsorbate being "pushed" inward, toward the second layer. For each of the four systems, Table 9.1 compares the total buckling of the first layer, the center of mass distance between the first and second metal layers, and the distance between the three metal atoms which are bonded to the adsorbate and the triangle of three metal atoms below the adsorbate in the second layer. The various adsorbates induce remarkably similar buckling. Each distance between the center of mass of the first layer and the center of mass of the second layer is not too different from the value of 2.29 ± 0.03 Å found for the clean metal surface. Due to the buckling, for each system, the distance between the three metal atoms directly bonded to the adsorbate and the center of mass of the second layer is expanded even as compared to the clean surface value. At this point it is not clear why the buckling of these adsorbates always causes an expansion and, in data collected up to now, never a contraction. It is possible that apparent interaction between the adsorbates is mediated through the metal buckling or relaxation. The main lateral interaction in these ordered $p(2 \times 2)$ overlayers may be between the metal atoms and have little contribution from adsorbate-adsorbate interactions.

Some differences between these systems are apparent in the lateral relaxations. Table 9.2 compares these lateral displacements. In the cases of O and S, we find a small

Table 9.2: Comparison of lateral relaxations for $p(2 \times 2)$ overlayers on Pt(111). The relatively large error bars in the case of NO and C_2H_3 are due to the lack of LEED data for higher order fractional beams. The direction of the displacement of the three metal atoms which are bonded to the adsorbate is indicated in the table. For top views of the best-fit structures see: Figure 3.6 for O, Figure 4.7 for S, Figure 6.7 for NO, and Figure 5.6 for C_2H_3.

Adsorbate	Displacement	
O	0.03 ± 0.03 Å	expansion
S	0.03 ± 0.04 Å	expansion
NO	0.04 ± 0.10 Å	expansion
C_2H_3	0.10 ± 0.08 Å	contraction

lateral expansion on the order of 0.03 ± 0.03 Å. For NO, the large error bars exclude any possibility of obtaining lateral information. C_2H_3 is an exception, in that we find a definite contraction of 0.10 ± 0.08 Å. In this structure the metal atoms are drawn closer to the C atom in order to optimize the Pt-C bond length and satisfy atomic repulsion between the atom and the surface. The relatively larger S atom, as compared to the C atom in C_2H_3, seems to require an expansion to optimize bond length and atomic repulsion. The same arguments could also be made in the case of O.

9.3 Tilting of Molecules

One additional structural feature of molecules on surfaces, not present in the case of atomic adsorption, is a possible tilt of the molecule. C_2H_3 and NO on the Pt(111) surface sit in three-fold symmetrical environments. In both cases the $p3m1$ symmetry does not allow the molecule to tilt; rather it constrains the molecules to an orientation perpendicular to the surface. However, this symmetry constraint can be broken if one then averages over all possible tilt angles, three angles if the tilt is toward the bridge sites, to regain the symmetry of the LEED pattern. There are two additional possibilities for the tilt. In the first possibility, the tilt angle of each molecule is independent of its neighbors; in the second, all the molecules in a single large domain tilt together. Modeling the first possibility requires coherent (amplitude) averaging, while modeling the second results in incoherent (intensity) averaging over the tilt angle. In addition to a static tilt, it is also possible that the molecule is wagging in an anharmonic potential. If this is true, the molecule will appear to be tilted

due to an effective averaging over the vibrational displacements.

A molecular tilt was reported recently for CO on Ru(0001)[40]. In this study, the tilt was interpreted as an anharmonic wagging vibration. Scattering from molecules tilted in three directions according to the symmetry of the substrate was averaged. Using either coherent or incoherent averaging, we find a similar tilt angle for ethylidyne molecules on Pt(111) (see Chapter 5). We assume our findings indicate the presence of an anharmonic wagging mode vibration for the ethylidyne. In the case of the NO structure on Pt(111) (see Chapter 6), the bent form of NO was eliminated based on the accurately determined N and O heights. Allowing the molecule to tilt yielded a small tilt angle, which again, because of the symmetrical environment of the molecule, we interpret as a wagging vibration. NO molecules on the Ni(111) surface also tilt away from each other; however, in the $c(4 \times 2)$ overlayer there is no symmetry constraint on the molecules and we assume that this tilt is a static tilt, not a wagging vibration.

Before ending this section, we must point out some possible difficulties with the determination of a tilt. For each case, we must include an additional parameter which necessarily lowers the R-factor. In our studies, we were careful to add the tilt angle only after all other structural features had been determined. By examining the variation of the R-factor vs. the tilt angle, we were able to assign error bars to the possible tilt. Unfortunately, due to the large lateral error bars, we cannot, without some degree of arbitrariness, determine if there is a small tilt. Another difficulty is the assignment of the tilt as a static tilt or as a wagging vibration. In our work we have associated the wagging vibration with structures in which the possible tilt would break the symmetry of the LEED pattern. We assigned the static tilt in cases where the tilt is allowed by symmetry. This assignment does have some arbitrary character to it. The precise analysis of the adsorbed molecule's tilt angle should prove to be an interesting topic in the future.

9.4 Coverage-Dependent Relaxations and Clustering

In Chapter 4, we studied two of the three ordered overlayers of sulfur on Pt(111) using both LEED and STM. Comparing the $p(2 \times 2)$ and the $(\sqrt{3} \times \sqrt{3})$R30° overlayers, we find similarity in the local bonding of the S atom. We find practically identical metal-sulfur bond lengths and similar center-of-mass interlayer spacings. The lateral expansions of the triangle of three atoms under the adsorbate are within error bars for both systems.

The structural results on Pt are qualitatively similar to what is found on the $p(2 \times 2)$ and $(\sqrt{3} \times \sqrt{3})$R30° overlayers on Ru(0001)[73] and on the $p(2 \times 2)$ overlayer on Re(0001)[83] with the exception that on an hcp metal sulfur is found in the hcp site.

One difference between our two structures is the lack of buckling in the $(\sqrt{3} \times \sqrt{3})$R30° structure. The $(\sqrt{3} \times \sqrt{3})$R30° structure is the highest coverage structure obtainable without clustering of the sulfur atoms. It is possible that the increased adsorbate-adsorbate interaction is enough to overcome the energy gained through the buckling of the metal atoms and to allow the S atoms to adsorb in every other fcc hollow site. Further discussion can be found in Chapter 4; however, total energy calculations are clearly needed to fully understand the energetics of these structural changes.

Clustering at higher coverages results in structures which defy any attempts to understand energetics. Our STM images (see Figure 4.6) for the high coverage overlayer indicate the possible clustering of sulfur on the surface. STM also supports clustering on the Cu(111) surface[87]. In the case of the $(2\sqrt{3} \times 2\sqrt{3})$R30° structure on the Re surface,[83] one finds that clustering results in adsorbate-adsorbate distances which are not quite bonding but definitely closer than the van der Waals distances. In contrast to the above examples, no such clustering was found for the $c(4 \times 2)$ overlayers on Ru(0001)[89] or on Mo(100)[88]. The Mo structure[88] even contained strain-relieving lateral displacements which may indicate repulsive S-S interactions. How the presence of the metal surface affects and is affected by either clustering or repulsion of adsorbed S atoms awaits future research.

9.5 NO on Ni(111) and Pt(111)

In addition to the work on the Pt(111) surface, we have also studied NO on the Ni(111) surface as reported in Chapter 6. This system is in many ways analogous to the NO on Pt(111) system. Due to the sensitivity of LEED to the position of the surface atom's atomic core, we were able to unambiguously assign the adsorption site and address the controversial adsorption site for ordered NO overlayers on Ni(111) surfaces. In both systems, NO occupies the hollow site and the N-O bond distances are practically identical. The relaxations induced in the Ni substrate (0.16 Å total buckling in the first layer) are larger than those induced in Pt; this may be due either to the NO coverage on Ni being twice that on Pt or to a stronger NO-metal bond in the case of Ni than in that of Pt.

9.6 The Ordered Ice Film

In a study of water adsorption on the Pt(111) surface (see Chapter 7), we have grown an ordered ice film. The surface of this film is the basal, or (0001), face of a common hexagonal ice crystal, the Ih form. We find the ice surface at 90 K to be terminated by strongly vibrating molecules in the top half of the bilayer, such that the molecules are almost undetectable by LEED. This model results in the best agreement between theory and experiment and is consistent with total energy considerations based on maximizing the number of hydrogen bonds. These undetected molecules would provide the additional hydrogen bonds needed to stabilize the detected lower half of the bilayer. Molecular dynamics simulations also support large vibrational amplitudes. The molecular dynamics simulations also allow us to rule out other types of disordered arrangements for the surface molecules which would render them undetectable by LEED; therefore, we believe that their apparent invisibility is primarily due to large vibrational amplitudes.

9.7 Iron Surfaces

Very little is known about the detailed atomic structure of atoms and molecules on the catalytically active Fe(111) surface. In Chapter 8, we addressed two of the major difficulties which must be overcome as a first step in the investigation of adsorbates on this surface. The first is the inherent difficulty in cleaning these surfaces due to the bcc to fcc phase transition at 900°C. A specialized hydrogen reactor has been constructed to allow carefully controlled heating to 700° under a flow of H_2 gas at atmospheric pressures. In this reactor, the sample is to be heated in hydrogen for month long periods without supervision or damage to the crystal. Atomicly clean surfaces were obtained from crystals first treated in this manner and then UHV cleaned. The second difficulty involves the close interlayer spacing ($\approx$ 0.8 Å) present on the Fe(111) surface. This close spacing requires major modifications to the "standard" LEED analysis programs. To handle this problem, a new automated TLEED program was developed based on a layer doubling approach.

9.8 Future Directions

The main thrust of this dissertation is the examination of several ordered overlayers using LEED. Advancements in the LEED theory, mainly the introduction of tensor LEED, have allowed us to efficiently analyze a large number of similar systems. By doing so, we have compiled a relatively complete structural overview of the $p(2 \times 2)$ overlayers on Pt(111). As more and more of these relatively simple structures are solved in such detail, we will move closer to having a complete, detailed picture of metal relaxation induced by simple overlayers. The ability to analyze these structures and to provide meaningful results brings hope to the idea that one will eventually be able to analyze more complex systems. As an example, in the study of S adsorption on Pt(111) (Chapter 4) we analyzed only the two simplest overlayers and skipped the high coverage structure. To fully understand, or to at least determine, the effect of coverage on the relaxations, it is imperative that one be able to solve high coverage structures with large unit cells. In addition to examining the relaxations on these high coverage surfaces, one will also be able to investigate the interaction between adsorbates in increasingly compressed layers. Another direction LEED is taking, is to examine different materials, for example, the surface structures of oxide surfaces[214] and molecular crystals (see Chapter 7). Each of these tasks has its own list of pitfalls and difficulties, both experimental and theoretical. This work is a step in overcoming these difficulties and moving in new directions.

Bibliography

[1] M. A. Van Hove, W. Moritz, H. Over, P. J. Rous, A. Wander, A. Barbieri, N. Materer, U. Starke, D. Jentz, J. M. Powers, G. Held, and G. A. Somorjai, *Surf. Sci. Rep.*, vol. 19, p. 191, 1993.

[2] P. R. Watlson, M. A. Van Hove, and K. Hermann, *NIST Surface Structure Database Ver. 1.0.* Gaithersburg, MD: NIST Standard Reference Data Program, 1993.

[3] A. Zangwill, *Physics at Surfaces.* Cambridge University Press, 1988.

[4] R. Hoffmann, *Solids and Sufaces: A Chemist's View of Bonding in Extended Structures.* VCH, 1988.

[5] S. Holloway and J. Nϕrskov, *Bonding at Surfaces.* Liverpool University Press, 1991.

[6] M. A. Van Hove, W. H. Weinberg, and C.-M. Chan, *Low Energy Electron Diffraction.* Berlin, Heidelberg, New York: Springer-Verlag, 1986.

[7] A. R. Sandy, S. G. J. Mochrie, D. M. Zehner, G. Grübel, K. G. Huang, and D. Gibbs, *Phys. Rev. Lett.*, vol. 68, p. 2192, 1992.

[8] G. A. Somorjai, *Annu. Rev. Phys. Chem.*, vol. 45, p. 721, 1994.

[9] C. J. Davisson and L. H. Germer, *Phys. Rev.*, vol. 30, p. 705, 1927.

[10] U. Starke and M. A. Van Hove, *Prog. Surf. Sci.*, vol. 46, p. 305, 1994.

[11] A. Wander, M. A. Van Hove, and G. A. Somorjai, *Phys. Rev. Lett.*, vol. 67, p. 626, 1991.

[12] D. F. Ogletree, G. S. Blackman, R. Q. Hwang, U. Starke, G. A. Somorjai, and J. E. Katz, *Rev. Sci. Instrum.*, vol. 63, p. 104, 1991.

[13] G. Ertl and J. Küppers, *Low Energy Electrons and Surface Chemistry.* VCH, 2nd ed., 1985.

[14] D. P. Woodruff and T. A. Delchar, *Modern Techniques of Surface Science.* Cambridge University Press, 2nd ed., 1994.

[15] W. Heegemann, K. H. Meister, E. Bechtold, and K. Hayek, *Surf. Sci.*, vol. 49, p. 161, 1975.

[16] S. Aminpirooz, A. Schmalz, L. Becker, and J. Haase, *Phys. Rev. B*, vol. 45, p. 6337, 1992.

[17] J. Sokolov, F. Jona, and P. M. Marcus, *Solid State Comm.*, vol. 49, p. 307, 1984.

[18] J. B. Pendry, *Low-Energy Electron Diffraction.* London: Academic Press, 1974.

[19] E. A. Wood, *J. Appl. Phys.*, vol. 35, p. 1306, 1964.

[20] R. L. Park, J. Houston, and D. G. Schreiner, *Rev. Sci. Instrum.*, vol. 42, p. 60, 1971.

[21] G. Comsa, *Surf. Sci.*, vol. 81, p. 57, 1979.

[22] M. Henzler, *Appl. Surf. Sci.*, vol. 11/12, p. 450, 1982.

[23] B. E. Warren, *X-Ray Diffraction.* Dover, 1990.

[24] J. F. O'Hanlon, *A User's Guide to Vacuum Thechnology.* John Wiley & Sons, 1989.

[25] W. Heppler, *Crystal Preparation at LBL 1976 to 1986.* LBL.

[26] R. G. Musket, W. McLean, C. A. Colmenares, D. M. Makowiecki, and W. J. Siekhaus, *Appl. Surf. Sci.*, vol. 10, p. 143, 1982.

[27] D. F. Ogletree. PhD thesis, UC Berkeley, 1986.

[28] Omicron Associates, *LEED-Star Video LEED System.*

[29] K. O. Legg, M. Prutton, and C. Kinniburgh, *J. Phys. C*, vol. 7, p. 4236, 1974.

[30] S. K. Kim, F. Jona, and J. A. Strozier, *Phys. Rev. B.*, vol. 51, p. 13837, 1995.

[31] S. Y. Tong, *Prog. Surf. Sci.*, vol. 7, p. 1, 1975.

[32] L. F. Mattheiss, *Phys. Rev. A*, vol. 133, p. 1399, 1964.

[33] T. L. Loucks, *Augmented Plane Wave Method.* New York, Amsterdam: W.A. Benjamin, Inc., 1967.

[34] I. P. Grant, *Adv. Phys.*, vol. 19, p. 747, 1970.

[35] F. Herman and S. Skillman, *Atomic Structure Calculations.* Englewood Cliffs, New Jersey: Prentice-Hall, Inc., 1963.

[36] V. L. Moruzzi, J. F. Janak, and A. R. Williams, *Calculated Electronic Properties of Metals.* Pergamon Press, 1978.

[37] R. Feder, "The role of relativistic intensity corrections and of spin polarization analysis for LEED surface structure determination," in *Determination of Surface Structure by LEED* (P. M. Marcus and F. Jona, eds.), p. 173, New York: Plenum, 1984.

[38] C. B. Duke and G. E. Laramore, *Phys. Rev. B*, vol. 2, p. 4765, 1970.

[39] C. B. Duke and G. E. Laramore, *Phys. Rev. B*, vol. 2, p. 4783, 1970.

[40] H. Over, W. Moritz, and G. Ertl, *Phys. Rev. Lett.*, vol. 70, p. 315, 1993.

[41] U. Löffler, R. Döll, K. Heinz, and J. B. Pendry, *Surf. Sci.*, vol. 301, p. 346, 1994.

[42] V. Fritzsche, *Phys. Rev. B*, vol. 50, p. 1922, 1994.

[43] P. J. Rous, *Prog. Surf. Sci.*, vol. 39, p. 3, 1992.

[44] P. J. Rous and J. B. Pendry, *Surf. Sci.*, vol. 219, p. 355, 1989.

[45] P. J. Rous and J. B. Pendry, *Comp. Phys. Comm.*, vol. 54, p. 137, 1989.

[46] D. P. Woodruff and B. W. Holland, *Phys. Lett. A*, vol. 31, p. 207, 1970.

[47] J. B. Pendry, *J. Phys. C*, vol. 13, p. 937, 1980.

[48] W. J. Press, S. A. Teukolsky, W. T. Vetterling, and B. P. Flannery, *Numerical Recipes in Fortran.* Cambridge University Press, 2 ed., 1992.

[49] J. B. Pendry and K. Heinz, *Phys. Rev. Lett.*, vol. 61, p. 2953, 1988.

[50] J. B. Pendry, K. Heinz, and W. Oed, *Surf. Sci.*, vol. 230, p. 137, 1990.

[51] P. J. Rous, *Surf. Sci.*, vol. 296, p. 358, 1993.

[52] N. Materer, U. Starke, A. Barbieri, R. Döll, K. Heinz, M. A. Van Hove, and G. A. Somorjai, *Surf. Sci.*, vol. 325, p. 207, 1995.

[53] H. Steininger, S. Lehwald, and H. Ibach, *Surf. Sci.*, vol. 123, p. 1, 1982.

[54] K. Mortensen, C. Klink, F. Jensen, F. Besenbacher, and I. Steensgaard, *Surf. Sci.*, vol. 220, p. L701, 1989.

[55] W. Ranke, *Surf. Sci.*, vol. 209, p. 57, 1989.

[56] D. L. Adams, H. B. Nielsen, and M. A. Van Hove, *Phys. Rev. B*, vol. 20, p. 4789, 1979.

[57] K. Hayek, H. Glassl, A. Gutmann, H. Leonhard, M. Prutton, S. P. Tear, and M. R. Welton-Cook, *Surf. Sci.*, vol. 152, p. 419, 1985.

[58] L. L. Kesmodel and G. A. Somorjai, *Phys. Rev. B*, vol. 11, p. 630, 1975.

[59] J. F. van der Veen, R. G. Smeenk, R. M. Tromp, and F. W. Saris, *Surf. Sci.*, vol. 79, p. 219, 1979.

[60] J. A. Davies, D. P. Jackson, P. R. Norton, D. E. Posner, and W. N. Unertl, *Solid State Comm.*, vol. 34, p. 41, 1980.

[61] P. J. Jennings and B. K. Sim, *Surf. Sci.*, vol. 20, p. 18, 1970.

[62] P. J. Jennings and R. O. Jones, *Surf. Sci.*, vol. 71, p. 101, 1978.

[63] K. Schwarz, *Phys. Rev. B*, vol. 5, p. 2466, 1972.

[64] M. N. Read and G. J. Russell, "Effect of the choice of exchange-correlation and the inner potential on the structure determination of the clean Mo(001) (1x1) surface," in *Determination of Surface Structure by LEED* (P. M. Marcus and F. Jona, eds.), p. 535, New York: Plenum, 1984.

[65] H. L. Davis and J. R. Noonan, "Sensitivity of structural conclusions in non-structural parameters," in *Determination of Surface Structure by LEED* (P. M. Marcus and F. Jona, eds.), p. 215, New York: Plenum, 1984.

[66] N. Materer, A. Barbieri, D. Gardin, U. Starke, J. D. Batteas, M. A. Van Hove, and G. A. Somorjai, *Surf. Sci.*, vol. 303, p. 319, 1994.

[67] R. Feder, H. Pleyer, P. Bauer, and N. Müller, *Surf. Sci.*, vol. 109, p. 419, 1981.

[68] R. C. Cammarata, *Surf. Sci.*, vol. 279, p. 341, 1992.

[69] R. J. Needs, M. J. Godfrey, and M. Mansfield, *Surf. Sci.*, vol. 242, p. 215, 1991.

[70] C. Teichert, M. Hohage, T. Michelt, and G. Comsa, *Phys. Rev. Lett.*, vol. 72, p. 1682, 1994.

[71] R. Dennert, M. Sokolowski, and H. Pfnür, *Surf. Sci.*, vol. 271, p. 1, 1992.

[72] M. Sokolowski and H. Pfnür, *Phys. Rev. B*, vol. 49, p. 7716, 1994.

[73] D. Jürgens, G. Held, and H. Pfnür, *Surf. Sci.*, vol. 303, p. 77, 1994.

[74] G. A. Somorjai, *Chemistry in Two Demensions: Surfaces.* Ithaca, NY: Cornell Univerity Press, 1981.

[75] J. C. Dunphy, B. J. McIntyre, J. Gomez, D. F. Ogletree, G. A. Somorjai, and M. B. Salmeron, *J. Chem. Phys.*, vol. 100, p. 6092, 1994.

[76] Y. Berthier, M. Perdereau, and J. Oudar, *Surf. Sci.*, vol. 36, p. 225, 1973.

[77] C.-M. Chan and W. H. Weinberg, *J. Chem. Phys.*, vol. 71, p. 3988, 1979.

[78] F. Maca, M. Scheffler, and W. Berndt, *Surf. Sci.*, vol. 160, p. 467, 1985.

[79] P. C. Wong, M. Y. Zhou, K. C. Hui, and K. A. R. Mitchell, *Surf. Sci.*, vol. 163, p. 172, 1985.

[80] K. Hayek, H. Glassl, A. Gutmann, H. Leonhard, M. Prutton, S. P. Tear, and M. R. Welton-Cook, *Surf. Sci.*, vol. 172/173, p. 419, 1985.

[81] K. Hayek, H. Glassl, A. Gutmann, H. Leonhard, M. Prutton, S. P. Tear, and M. R. Welton-Cook, *Surf. Sci.*, vol. 175, p. 535, 1986.

[82] J. E. Demuth, P. M. Marcus, and D. W. Jepsen, *Phys. Rev. Let.*, vol. 32, p. 1182, 1974.

[83] A. Barbieri, D. Jentz, N. Materer, G. Held, J. Dunphy, D. F. Ogletree, P. Sautet, M. Salmeron, M. A. Van Hove, and G. A. Somorjai, *Surf. Sci.*, vol. 312, p. 10, 1994.

[84] D. A. Zeglinski, D. F. Ogletree, T. Beebe, R. Q. Hwang, G. A. Somorjai, and M. Salmeron, *Rev. Sci. Instrum.*, vol. 61, p. 3769, 1990.

[85] C. Wagner, *J. Chem. Phys.*, vol. 21, p. 1819, 1953.

[86] J. Dunphy, P. Sautet, D. F. Ogletree, O. Dabbousi, and M. B. Salmeron, *Phys. Rev. B*, vol. 47, p. 2320, 1993.

[87] K. Motai, T. Hashizume, H. Lu, D. Jeon, and T. Sakurai, *App. Surf. Sci.*, vol. 67, p. 246, 1993.

[88] D. Jentz, S. Rizzi, A. Barbieri, D. Kelly, M. A. Van Hove, and G. A. Somorjai, *Surf. Sci.*, vol. 329, p. 14, 1995.

[89] C. Schwennicke, D. Jürgens, G. Held, and H. Pfür, *Surf. Sci.*, vol. 316, p. 81, 1994.

[90] P. C. Stair and G. A. Somorjai, *J. Chem. Phys.*, vol. 66, p. 2036, 1977.

[91] L. L. Kesmodel, L. H. Dubois, and G. A. Somorjai, *Chem. Phys. Lett.*, vol. 56, p. 267, 1978.

[92] L. L. Kesmodel, L. H. Dubois, and G. A. Somorjai, *J. Chem. Phys.*, vol. 70, p. 2180, 1979.

[93] L. L. Kesmodel, P. C. Stair, R. C. Baetzold, and G. A. Somorjai, *Phys. Rev. Lett.*, vol. 36, p. 1316, 1976.

[94] J. E. Demuth, *Chem. Phys. Lett.*, vol. 45, p. 12, 1977.

[95] H. Ibach and S. Lehwald, *J. Vac. Sci. Thechnol.*, vol. 15, p. 407, 1978.

[96] M. R. Albert, L. Sneddon, W. Eberhardt, F. Greuter, T. Gustafsson, and E. W. Plummer, *Surf. Sci.*, vol. 120, p. 19, 1982.

[97] H. Steininger, H. Ibach, and S. Lehwald, *Surf. Sci.*, vol. 117, p. 685, 1982.

[98] A. Cassuto, J. Kiss, and J. M. White, *Surf. Sci.*, vol. 255, p. 289, 1991.

[99] M. Salmeron and G. A. Somorjai, *J. Chem. Phys.*, vol. 86, p. 341, 1982.

[100] J. R. Creighton and J. M. White, *Surf. Sci.*, vol. 129, p. 327, 1983.

[101] R. Yu and T. Gustafsson, *Surf. Sci. Lett.*, vol. 182, p. L234, 1987.

[102] X.-L. Zhou, X.-Y. Zhu, and J. White, *Surf. Sci.*, vol. 193, p. 387, 1988.

[103] T. A. Land, T. Michely, R. J. Behm, J. C. Hemminger, and G. Comsa, *Surf. Sci.*, vol. 264, p. 261, 1992.

[104] N. Freyer, G. Pirug, and H. P. Bonzel, *Surf. Sci.*, vol. 125, p. 327, 1983.

[105] T. Masson, C. S. Sass, O. Grizzi, and J. W. Rabalais, *Surf. Sci.*, vol. 125, p. 327, 1983.

[106] J. R. Creighton, K. M. Ogle, and J. M. White, *Surf. Sci. Lett.*, vol. 138, p. L137, 1984.

[107] M. Abon, J. Billy, and J. C. Bertolini, *Surf. Sci. Lett.*, vol. 171, p. L387, 1986.

[108] S. M. Davis, F. Zaera, B. E. Gordon, and G. A. Somorjai, *J. Catalysis*, vol. 92, p. 24, 1985.

[109] I. V. Mitchell, W. N. Lennard, G. R. M. K. Griffith, and J. W. Huppertz, *Surf. Sci.*, vol. 256, p. L598, 1991.

[110] J. E. Demuth, *Surf. Sci.*, vol. 80, p. 367, 1979.

[111] P. D. Ditlevsen, M. A. Van Hove, and G. A. Somorjai, *Surf. Sci.*, vol. 292, p. 267, 1993.

[112] L. H. Dubois, D. G. Castner, and G. A. Somorjai, *J. Chem. Phys.*, vol. 72, p. 5234, 1980.

[113] B. E. Koel, B. E. Bent, and G. A. Somorjai, *Surf. Sci.*, vol. 146, p. 211, 1984.

[114] M. M. Hills, J. E. Parmeter, C. B. Mullins, and W. H. Weinberg, *J. Am. Chem. Soc.*, vol. 108, p. 3554, 1986.

[115] J. A. Gates and L. L. Kesmodel, *Surf. Sci. Lett.*, vol. 120, p. L461, 1982.

[116] J. A. Gates and L. L. Kesmodel, *Surf. Sci.*, vol. 124, p. 68, 1982.

[117] T. S. Marinova and K. L. Kostov, *Surf. Sci.*, vol. 181, p. 573, 1987.

[118] M. A. Bartea, J. Q. Broughton, and D. Menzel, *Appl. Surf. Sci.*, vol. 19, p. 92, 1984.

[119] H. Ibach in *Proc. Intern. Conf. on Vibrations in Adsorbed Layers*, p. 64, KFA Jülich, 1978.

[120] R. Levis and N. Winograd, *J. Am. Chem. Soc.*, vol. 109, p. 6873, 1987.

[121] U. Starke, A. Barbieri, N. Materer, M. A. Van Hove, and G. A. Somorjai, *Surf. Sci.*, vol. 286, p. 1, 1993.

[122] P. Skinner, M. W. Howard, I. A. Oxton, S. F. A. Kettle, D. B. Powell, and N. Sheppard, *J. Chem. Soc. Faraday Tran. II*, vol. 77, p. 397, 1981.

[123] K. Heinz, U. Starke, and F. Bothe, *Surf. Sci. Lett.*, vol. 243, p. L70, 1991.

[124] K. Heinz, *Prog. Surf. Sci.*, vol. 27, p. 239, 1988.

[125] K. Griffiths, W. N. Lennard, I. V. Mitchell, P. R. Norton, G. Pirug, and H. P. Bonzel, *Surf. Sci. Lett.*, vol. 284, p. L389, 1993.

[126] N. Materer, A. Barbieri, D. Gardin, U. Starke, J. D. Batteas, M. A. Van Hove, and G. A. Somorjai, *Phys. Rev. B*, vol. 48, p. 2859, 1993.

[127] H. Conrad, G. Ertl, J. Küppers, and E. E. Latta, *Surf. Sci.*, vol. 50, p. 296, 1975.

[128] C. M. Comrie, W. H. Weinberg, and R. M. Lambert, *Surf. Sci.*, vol. 57, p. 619, 1976.

[129] M. J. Breitschafter, E. Umbach, and D. Menzel, *Surf. Sci.*, vol. 109, p. 493, 1981.

[130] M. Kiskinova, G. Pirug, and H. P. Bonzel, *Surf. Sci.*, vol. 136, p. 285, 1984.

[131] W. Erley and B. N. J. Persson, *Surf. Sci.*, vol. 218, p. 494, 1989.

[132] V. K. Agrawal and M. Trenary, *Surf. Sci.*, vol. 259, p. 116, 1991.

[133] C. T. Campbell, G. Ertl, and J. Segner, *Surf. Sci.*, vol. 115, p. 309, 1982.

[134] H. Ibach and S. Lehwald, *Surf. Sci.*, vol. 76, p. 1, 1978.

[135] D. A. Degras and M. Costa, eds., *IVC-8, ICSS-4, ECOSS-3, Cannes*, vol. p. 221, 1980.

[136] J. L. Gland and B. A. Sexton, *Surf. Sci.*, vol. 94, p. 355, 1980.

[137] B. E. Hayden, *Surf. Sci.*, vol. 131, p. 419, 1983.

[138] W. Erley, *Surf. Sci.*, vol. 205, p. L771, 1988.

[139] J. G. Chen, W. Erley, and H. Ibach, *Surf. Sci.*, vol. 224, p. 215, 1989.

[140] J. E. Enemark and R. D. Feltam, *Coordination Chem. Rev.*, vol. 13, p. 339, 1974.

[141] F. P. Netzer and T. E. Madey, *Surf. Sci.*, vol. 110, p. 251, 1981.

[142] H.-P. Sheinrück, C. Schneider, P. A. Heimann, T. Pache, E. Umbach, and D. Menzel, *Surf. Sci.*, vol. 208, p. 136, 1989.

[143] L. S. Caputi, R. G. Agostino, A. Amoddeo, E. Colavita, and A. Santaniello, *Surf. Sci.*, vol. 282, p. 62, 1993.

[144] M. C. Asensio, D. P. Woodruff, A. W. Robinson, K.-M. Schindler, P. Gardner, D. Ricken, A. M. Bradshaw, J. C. Conesa, and A. R. González-Elipe, *J. Vac. Sci. Technol. A*, vol. 10, p. 2445, 1992.

[145] M. C. Asensio, D. P. Woodruff, A. W. Robinson, K.-M. Schindler, P. Gardner, D. Ricken, A. M. Bradshaw, J. C. Conesa, and A. R. González-Elipe, *Chem. Phys. Lett.*, vol. 192, p. 259, 1992.

[146] H.-P. Steinrünck, T. Pache, and W. Huber, *Phys. Scr.*, vol. 41, p. 177, 1990.

[147] L. D. Mapledoram, A. Wander, and D. A. King, *Chem. Phys. Lett.*, vol. 209, p. 409, 1993.

[148] F. Cotton and G. Wilkinson, *Advance Inorganic Chemistry*. New York: Wiley, 5th ed., 1988.

[149] G. S. Blackman, C.-T. Kao, B. E. Bent, C. M. Mate, M. A. Van Hove, and G. A. Somorjai, *Surf. Sci.*, vol. 207, p. 66, 1988.

[150] C.-T. Kao, G. S. Blackman, M. A. Van Hove, and G. A. Somorjai, *Surf. Sci.*, vol. 224, p. 77, 1989.

[151] J. P. Bibérian and M. A. Van Hove, *Surf. Sci.*, vol. 138, p. 361, 1984.

[152] D. E. Gardin, J. D. Batteas, M. A. Van Hove, and G. A. Somorjai, *Surf. Sci.*, vol. 296, p. 25, 1993.

[153] J. E. Demuth, P. M. Marcus, and D. W. Jepsen, *Phys. Rev. B*, vol. 11, p. 1460, 1975.

[154] T. Narusawa, W. M. Gibson, and E. Tφrnquist, *Phys. Rev. Lett.*, vol. 47, p. 417, 1987.

[155] M. Mendez, W. Oed, A. Fricke, L. Hammer, K. Heinz, and K. Müller, *Surf. Sci.*, vol. 253, p. 99, 1991.

[156] D. T. Vu Grimsby, Y. K. Wu, and K. A. R. Mitchell, *Surf. Sci*, vol. 232, p. 51, 1990.

[157] G. A. Somorjai and M. A. Van Hove, *Prog. Surf. Sci.*, vol. 30, p. 201, 1989.

[158] H. H. G. Jellinek, *J. Colloid Interface Sci.*, vol. 25, p. 192, 1967.

[159] J. G. Dash, *Contemp. Phys.*, vol. 30, p. 89, 1989.

[160] N. Materer, U. Starke, A. Barbieri, M. A. Van Hove, G. A. Somorjai, G.-J. Kroes, and C. Minot, *J. Chem. Phys.*, vol. 99, p. L6267, 1995.

[161] F. P. Dowben and D. Tabor, *The Friction and Lubrication of Solids*, ch. Part II, Chap. VII. Oxford: Clarendon Press, 1964.

[162] M. Elbaum and M. Schick, *Phys. Rev. Lett.*, vol. 66, p. 1713, 1991.

[163] G.-J. Kroes, *Surf. Sci.*, vol. 275, p. 365, 1992.

[164] A. Goto, K. Akiya, T. Hondoh, Y. Furukawa, T. Shimura, I. Takahashi, and J. Harada, *J. Crystal Growth*, vol. 129, p. 491, 1993.

[165] M. Elbaum, S. G. Lipson, and J. G. Dash, *J. Crystal Growth*, vol. 129, p. 491, 1993.

[166] A. Lied, H. Dosch, and J. H. Bilgram, *Phys. Rev. Lett.*, vol. 72, p. 3554, 1994.

[167] H. Dosch, A. Lied, and J. H. Bilgram, *Surf. Sci.*, vol. 327, p. 145, 1995.

[168] J. G. Davy and G. A. Somorjai, *J. Phys. Chem.*, vol. 55, p. 3624, 1971.

[169] V. Buch and J. P. Devlin, *J. Phys. Chem.*, vol. 98, p. 4195, 1993.

[170] J. D. Graham and J. T. Roberts, *J. Phys. Chem.*, vol. 98, p. 5974, 1994.

[171] B. Rowland, M. Fisher, and J. P. Devlin, *J. Phys. Chem.*, vol. 97, p. 2485, 1993.

[172] P. A. Thiel and T. E. Madey, *Surf. Sci. Rep.*, vol. 7, p. 211, 1987.

[173] H. Ogasawara, J. Yoshinobu, and M. Kawai, *Chem. Phys. Lett.*, vol. 231, p. 188, 1994.

[174] G. Held and D. Menzel, *Surf. Sci.*, vol. 316, p. 92, 1994.

[175] U. Starke, K. Heinz, N. Materer, A. Wander, M. Michl, R. Döll, M. A. Van Hove, and G. A. Somorjai, *J. Vac. Sci. Technol. A*, vol. 10, p. 2521, 1992.

[176] U. Starke, N. Materer, A. Barbieri, R. Döll, K. Heinz, M. A. Van Hove, and G. A. Somorjai, *Surf. Sci.*, vol. 287, p. 432, 1993.

[177] M. A. Van Hove, W. Moritz, H. Over, P. J. Rous, A. Wander, A. Barbieri, N. Materer, U. Starke, D. Jentz, J. M. Powers, G. Held, and G. A. Somorjai, *Surf. Sci.*, vol. 287, p. 431, 1993.

[178] R. Dovesi, C. Pisani, C. Roetti, M. Causà, and V. R. Saunders, *CRYSTAL 88, QCPE program No 577.* Bloomington, Indiana, 1989.

[179] P. C. Hariharan and J. A. Pople, *Theoret. Chim. Acta. (Berl.)*, vol. 28, p. 213, 1973.

[180] W. J. Hehre, R. Ditchfield, and J. A. Pople, *J. Chem. Phys.*, vol. 56, p. 2257, 1972.

[181] W. J. Hehre, R. F. Stewart, and J. A. Pople, *J. Chem. Phys.*, vol. 51, p. 2567, 1969.

[182] J. S. Binkley, R. A. Whiteside, R. Kishnan, R. Seeger, H. B. Schlegel, D. J. Defrees, and J. A. Pople, *Gaussain 80, QCPE No 406.* Bloomington, Indiana.

[183] L. Ojamäe, K. Hermansson, R. Dovesi, C. Roetti, and V. Saunders, *J. Chem. Phys.*, vol. 100, p. 2128, 1994.

[184] J. M. Besson, P. Pruzan, S. Klotz, G. Hamel, B. Silvi, R. J. Nelmes, J. S. Loveday, R. M. Wilson, and S. Hull, *Phys. Rev. B*, vol. 49, p. 12540, 1994.

[185] E. Cota and W. G. Hoover, *J. Chem. Phys.*, vol. 67, p. 3839, 1977.

[186] J. D. Bernal and R. H. Fowler, *J. Chem. Phys.*, vol. 1, p. 515, 1933.

[187] W. L. Jorgensen, J. Chandrasekhar, J. D. Madura, R. W. Impey, and M. L. Klein, *J. Chem. Phys.*, vol. 79, p. 926, 1983.

[188] W. L. Jorgensen and J. D. Madura, *Mol. Phys.*, vol. 56, p. 1381, 1985.

[189] O. A. Karim and A. D. J. Haymet, *J. Chem. Phys.*, vol. 89, p. 6889, 1988.

[190] S. W. de Leeuw and J. W. Perram, *Mol. Phys.*, vol. 37, p. 1313, 1979.

[191] H. J. C. Berendsen, J. P. M. Postma, W. F. van Gunsteren, A. DiNola, and J. R. Haak, *J. Chem. Phys*, vol. 81, p. 3684, 1984.

[192] D. Fincham, *Mol. Simul.*, vol. 8, p. 165, 1992.

[193] D. S. Eisenberg and W. Kauzmann, *The Structure and Properties of Water.* New York: Oxford University Press, 1969.

[194] E. Walley in *The Hydrogen Bond* (P. Schuster, G. Zundel, and C. Sandorfy, eds.), p. 1425, Amsterdam: North-Holland, 1976.

[195] G. S. Blackman, M.-L. Xu, D. F. Ogletree, M. A. Van Hove, and G. A. Somorjai, *Phys. Rev. Lett.*, vol. 61, p. 2353, 1988.

[196] G. Pirug, C. Ritke, and H. P. Bonzel, *Surf. Sci.*, vol. 241, p. 289, 1991.

[197] Y. R. Shen private communication.

[198] F. H. Stillinger, *Science*, vol. 209, p. 451, 1980.

[199] T. A. Weber and F. H. Stillinger, *J. Phys. Chem.*, vol. 87, p. 1983, 1983.

[200] D. R. Strongin. PhD thesis, UC Berkeley, 1988.

[201] H. D. Shih, F. Jona, D. W. Jepsen, and P. M. Marcus, *Surf. Sci.*, vol. 104, p. 39, 1981.

[202] J. Sokolov, F. Jona, and P. M. Marcus, *Phys. Rev. B*, vol. 33, p. 1397, 1986.

[203] R. Wu and A. J. Freeman, *Phys. Rev. B*, vol. 47, p. 3904, 1993.

[204] R. Imbihl, R. J. Behm, G. Ertl, and W. Moritz, *Surf. Sci.*, vol. 123, p. 129, 1982.

[205] F. Bozso, G. Ertl, and M. Weiss, *J. Catal.*, vol. 49, p. 18, 1977.

[206] K. Yoshida and G. A. Somorjai, *Surf. Sci.*, vol. 75, p. 46, 1978.

[207] F. Bozso, G. Ertl, and M. Weiss, *J. Catal.*, vol. 50, p. 519, 1977.

[208] M.-C. Tsai, U. Seip, I. C. Bassignana, J. Küppers, and G. Ertl, *Surf. Sci.*, vol. 155, p. 387, 1985.

[209] H.-J. Freund, B. Bartos, R. P. Messmer, M. Grunze, H. Kuhlenbeck, and M. Neumann, *Surf. Sci.*, vol. 185, p. 187, 1987.

[210] K. O. Legg, F. Jona, D. W. Jepsen, and P. M. Marcus, *J. Phys. C*, vol. 10, p. 937, 1977.

[211] E. Hassold, U. Löffler, R. Schmiedl, M. Grund, L. Hammer, K. Heinz, and K. Müller, *Surf. Sci.*, vol. 326, p. 93, 1995.

[212] X.-G. Zang, P. J. Rous, J. M. MacLaren, M. A. Van Hove, and G. A. Somorjai, *Surf. Sci.*, vol. 239, p. 103, 1990.

[213] P. Pinkava and S. Crampin, *Surf. Sci.*, vol. 233, p. 27, 1990.

[214] A. Barbieri, W. Weiss, M. A. Van Hove, and G. A. Somorjai, *Surf. Sci.*, vol. 302, p. 259, 1994.

LAWRENCE BERKELEY LABORATORY
CENTER FOR ADVANCED MATERIALS
1 CYCLOTRON ROAD
BERKELEY, CALIFORNIA 94720